UNIVERSITÀ
DEGLI STUDI
DI PADOVA

Sede Amministrativa: Università degli Studi di Padova

Dipartimento di Scienze Chimiche

CORSO DI DOTTORATO DI RICERCA IN: Scienza e Ingegneria dei Materiali

CICLO XXIX

Development of metal/ceramic membranes for hydrogen purification at medium/high temperatures

Tesi redatta con il contributo finanziario: Consiglio Nazionale delle Ricerche (CNR)

Coordinatore: Ch.mo Prof. Gaetano Granozzi

Supervisore: Ch.ma Prof.ssa Lidia Armelao

Co-Supervisore: dott.ssa Simona Barison (CNR-ICMATE)

Dottorando: Matteo Romano

To my Family

Table of Contents

Abstract 10

1 - Hydrogen: an energy carrier

1.1. Hydrogen economy 12

1.2. Hydrogen today 13

1.3. Hydrogen production 13

1.3.1. Steam reforming 14

1.3.2. Production from biomass 15

1.4. Distribution of hydrogen 17

1.5. Hydrogen separation technologies 18

1.5.1. Pressure swing absorption 18

1.5.2. Cryogenic separation 19

1.5.3. Membranes 19

References 20

2 - Membranes for hydrogen separation

2.1. General features of membranes for hydrogen separation 22

2.2. Dense metallic membranes 26

2.2.1. General features of metallic membranes 26

2.2.2. Commercial membranes 27

2.3. Palladium and palladium – based membranes 28

2.3.1. Absorption of hydrogen in palladium and palladium alloys 31

2.3.2. Diffusion of hydrogen in palladium and palladium alloys 32

2.4. Alternatives to Palladium based alloys 34

2.4.1. Hydrogen in vanadium 36

2.4.2. Promising alloys 38

2.4.2.1. $V_{90}Pd_{10}$ 38

2.4.2.2. V-Ni-Ti ternary system 39

2.5. Implementation of dense metallic membranes 40

References 41

3 - Thin films deposition techniques

3.1. Introduction 49
3.2. Thin films preparation 49
3.2.1. Electroless Plating 49
3.2.2. Sputtering 51
3.3. The sputter deposition 52
3.3.1. DC diode sputtering 53
3.3.2. Radio frequency (RF) sputtering 53
3.3.3. Magnetron sputtering 54
3.3.4. Bias sputtering 56
3.4. Film structure 56
3.5. HiPIMS (High Power Impulse Magnetron Sputtering) 58
References 62

4 - Porous substrates for hydrogen separation membranes

4.1. Introduction 67
4.2. Ceramic porous substrates preparation 68
4.2.1. Partial sintering 69
4.2.2. The sintering process 69
4.2.3. Pore former agents 70
4.2.4. Replica templates 70
4.2.5. Direct foaming 71
4.3. Types of porous ceramic substrate 71
4.3.1. Tubular 71
4.3.2. Planar 72
References 72

5 - Hydrogen permeation in metallic membranes

5.1. Introduction 75
5.2. Hydrogen permeation in metal membranes 76
5.2.1. H_2 permeation through composite membranes 78
5.2.2. Permeation through porous substrate 79
5.2.3. The leak model 81

References 82

6 - Zeolite membranes for gas separation

6.1. Zeolites 85

6.2. Preparation of zeolite membranes 86

6.2.1. Hydrothermal synthesis 87

6.3. Permeation of gas through a zeolite membrane 88

References 90

7 - Experimental part

7.1. Thin metallic membranes preparation 92

7.1.1. Deposition details 92

7.2. Zeolite membrane preparation 94

7.3. Ceramic porous substrates 95

7.4. Characterization techniques 97

7.4.1. SEM/EDS 97

7.4.2. X-ray diffraction – XRD 99

7.4.2.1 Rietveld refinement 100

7.4.3. Thermal analyses 102

7.4.4. Adhesion properties 103

7.4.5. Permeation apparatus 104

References 106

8 - Porous ceramic substrates preparation

8.1. Alpha alumina partial sintering 108

8.2. PMMA 110

8.2.1. PMMA / alpha alumina powder mixtures 112

8.2.2. Graded porosity 117

8.3. Starch 119

8.3.1. Characterization 119

8.3.2. Alumina / starch powder mixtures 120

8.3.3. Graded porosity 121

9 - Pd-Ag(23wt%)

9.1. DC magnetron sputtering - DCMS 123
9.1.1. Targets calibration 123
9.1.2. Influence of temperature and substrate on alloy morphology 124
9.1.3. Influence of bias voltage and pressure on alloy morphology 127
9.1.4. EDS/XRD 129
9.1.5. Thermal treatment 130
9.2. HiPIMS 132
9.2.1. Influence of deposition parameters on alloy morphology 132
9.2.2. EDS/XRD 137
References 139

10 - Vanadium based alloys

10.1. $V_{90}Pd_{10}$ 140
10.2. Ternary Alloy $V_{84.2}Ni_{5.3}Ti_{10.5}$ 143
10.2.1. Stainless steel substrate 143
10.2.2. Porous alumina substrate 147
10.2.3. EDS/XRD 151
References 153

11 - Zeolite membranes for hydrogen separation

11.1. Powder 155
11.2. Membranes 160
References 166

12 - Hydrogen permeation tests

12.1. Permeation through porous ceramic substrate 167
12.2. Permeation tests of Pd-Ag(23wt%) membranes 169
12.2.1. Post permeability characterization 174
12.3. Permeation tests of vanadium based membranes 176
12.3.1. V-Pd post permeability characterization 178
12.4. Permeation tests of zeolite membrane 180
References 183

13 - Closing remarks and future work

13.1. Closing remarks 185

13.2. Future works 187

Acknowledgments 188

Abstract

The aim of the PhD activity (completely developed at CNR-ICMATE, Padova Research Area) was the development of planar and thin membranes for hydrogen separation for high temperature processes (400°C, metal membranes) and medium temperature processes (< 150°C, zeolite membranes), supported by porous ceramic substrates. Metallic membranes were deposited by PVD processes and zeolite membranes were grown onto ceramic substrate by hydrothermal synthesis. Advantages of PVD techniques are exposed in the PVD chapter of the thesis. PVD deposition is particularly useful in case of metal alloys, since co-sputtering of metals can hinder the intermetallics formation in the alloy and allows a fine tuning of the chosen stoichiometry.

A goal of the work was to develop new composite membranes combining porous substrates, having fine pore size and smooth surfaces, with a new deposition technique, HiPIMS (High Power Impulse Magnetron Sputtering), to deposit very thin and dense palladium-based membranes (Pd-Ag 77-23 wt%) to reduce the thickness and thus the palladium content, in order to fulfil the targets of the U.S. Department of Energy (DoE), in term of costs of membranes and hydrogen flux.

A further goal of the activity was the investigation of new and promising alloys, mainly palladium-free alloys, with a focus on vanadium based alloys, to meet the new guidelines established by European Community about critical elements. We studied a binary alloy ($V_{90}Pd_{10}$) and a ternary alloy ($V_{84.2}Ni_{10.5}Ti_{5.3}$, an alloy whose properties have been predicted by a computational screening approach), both prepared for the first time by PVD processes (the main preparation process involve arc melting).

In order to compare different membranes and flow mechanism, a parallel research activity involved the preparation of thin membranes of zeolites, grown directly onto a porous ceramic substrate. Among the various zeolite structures available, hydroxy-sodalite is the best choice to prepare hydrogen separation membranes, thanks to the pore size compatible with the size of hydrogen molecule. Hydroxy-sodalite membranes are already reported in literature, but our aim was the preparation of reliable zeolite membranes in only one hydrothermal step, simplifying the synthetic approach.

Once membranes were prepared, hydrogen permeation measurements were performed in test station entirely developed at CNR-ICMATE (experimental layout and Labview interface), to gather information about the hydrogen permeance and H_2/N_2 selectivity of membranes.

1. Hydrogen: an energy carrier

1.1. Hydrogen economy

Fossil fuels have powered human civilization since the beginning of the industrial era, but their extensive use threatens future energy supply and increases environmental concerns (pollution and emission of greenhouse gases). Moreover, the energy demand is thought to double by 2050, due to population growth and industrialization of developing countries[1]. Transportation and heating require the two-thirds of the primary energy demand, provided by fossil fuels feedstocks (petroleum and natural gas), but, in the same time, they are the source of over half of all greenhouse gases and air pollutants emissions. The research concerning alternative fuels is necessary not only for human health-care, but even for the development of a new and sustainable energy market. Inexhaustibility, cleanliness, convenience and independence from foreign control are the main properties of the ideal fuel. Hydrogen[2] combines all these criteria and it is promoted worldwide as an environmentally-friendly replacement for the traditional fossil fuels, both in transportation and not transportation applications. Hydrogen is versatile: it can be used in stationary applications (power plants and fuel cells), mobile applications (boats, airplanes and cars) and backup facilities (portable generators). Hydrogen is at the heart of the hydrogen economy, a new energy system combining hydrogen as energy carrier and electricity.

Compared to conventional fuels[3] (Tab. 1.1), hydrogen has the highest energy content per unit mass of any fuel, but its energy density is affected by the physical nature of the fuel, liquid or a gas.

Fuel	LHV* (MJ/kg)	HHV** (MJ/kg)	Stoichiometric air/fuel ratio (kg)	Combustible range (%)	Min. Ignition Energy (MJ)	Auto ignition temperature (°C)
Methane	50.0	55.5	17.2	5-15	0.30	540-630
Propane	45.6	50.3	15.6	2.1-9.5	0.30	450
Octane	47.9	15,1	0.31	0.95-6.0	0.26	415
Methanol	18.0	22.7	6.5	6.7-36.0	0.14	460
Hydrogen	119.9	141.6	34.3	4.0-75.0	0.017	585
Gasoline	44.5	47.3	14.6	1.3-7.1	0.29	260-460
Diesel	42.5	44.8	14.5	0.6-5.5	-	180-320

* = lower heating value ** = higher heating value

Fuel	Energy density (MJ/m^3 at 1 atm, 15°C)	Energy density (MJ/m^3 at 200 atm, 15°C)	Energy density (MJ/m^3 at 690 atm, 15°C)	Energy density (MJ/m^3 of liquid)	Gravimetric energy density (MJ/kg)
Hydrogen	10.0	1825	4500	8491	140.4
Methane	32.6	6860	-	20920	43.6
Propane	86.7	-	-	23488	28.3
Gasoline	-	-	-	31150	48.6
Diesel	-	-	-	31435	33.8
Methanol	-	-	-	15800	20.1

Tab. 1.1: comparison between hydrogen and other fuels (from [4])

1.2. Hydrogen today

The three main hydrogen producers are captive producers (production for direct customers or their own use), by-product hydrogen producers (production from chemical processes) and merchant companies (trading of only 5% of total production). Almost the entire production (≈ 95%) comes from fossil fuels (mainly natural gas), while water electrolysis and other new processes still account for less than 5%. Hydrogen is mainly used as reactant in chemical and petroleum industries (ammonia production, crude-oil processing and methanol production). In addition, hydrogen is used for reduction processes in metallurgy and steel production. On-site produced hydrogen costs approximately $0.70/kg, which raises up to $3.08/kg (liquid hydrogen) if not produced on site. It is clear that, for cost-competitive transportation, hydrogen price must be comparable to conventional fuels.

1.3. Hydrogen production

Hydrogen is commonly extracted from chemical compounds[5], mainly fossil fuels. They are a readily available hydrogen source in the present and near-term, but their employment leads to a further depletion of the limited cheap fossil fuels reserves. To reduce the anthropogenic contribution to greenhouse emissions, the use of a CO_2 neutral energy carrier as biomass could resolve the problem in the near, mid-term.

Nowadays, the most important production processes that require membrane purification are steam reforming and biomass gasification.

1.3.1. Steam reforming

Most of hydrogen is produced by steam reforming of methane (SRM)[6], followed by hydrogen separation. SRM is a relatively simple, efficient and well-proven technology; it provides a cost-effective product and can operate with different hydrocarbon feedstocks[7]. First of all, the sulphur level is reduced below 2 ppm (hydrodesulphurization and H_2S removal), in order to protect the catalysts used in the downstream reforming process. SMR is carried out at 800–900°C and 25–35 atm, using an alkali promoted Ni-based catalyst supported on alumina. The first reaction is the hydrocarbon dissociation on the metal surface and the hydrocarbon fragments reaction with adsorbed steam to produce CO and H_2 (reforming process):

$$C_nH_m + nH_2O \rightarrow nCO + (n + m/2)\ H_2 \qquad \text{(for } CH_4\text{: } \Delta H\ 298\ ^\circ = +206 \text{ kJ/mol)}$$

Equilibrium concentration of CO, H_2, CH_4, CO_2 and H_2O are established according to the reaction equilibria for the methanation and the water gas shift (WGS) reactions:

$$\underline{\text{Methanation:}}\ CO + 3H_2O \leftrightarrows CH_4 + H_2O \qquad (\Delta H\ 298\ ^\circ = +206 \text{ kJ/mol})$$

$$\underline{\text{WGS:}}\ CO + H_2O \leftrightarrows CO_2 + H_2 \qquad (\Delta H\ 298\ ^\circ = -41.2 \text{ kJ/mol})$$

In case of heavy hydrocarbon feedstocks, a pre-reformer (at 400-500°C) is used upstream to first convert the heavy hydrocarbons to CH_4. In the SMR process the final gas mixture depends on pressure, temperature and steam/CH_4 ratio used. For SMR conducted at 800°C, 300 psig and a steam/CH_4 ratio of 3, the gas mixture is (dry basis): 75% H_2, 7% CO_2, 12% CO and 6% CO_2. The amount of H_2 in the synthesis gas may be further increased by reacting CO with steam in the WGS reaction. The WGS reaction is an equilibrium-limited reaction favoured at lower temperatures and it is typically conducted in two steps: high-temperature shift (HTS) and low-temperature shift (LTS). Converted gases are cooled outside of the reactor by producing steam and sent to the LTS converter at about 200–215°C to complete the shift reaction. The exit gas typically contains about 87.3% H_2, 10.7% CO_2, 0.70% CO and 1.3% CH_4 (dry basis) and is further purified by CO_2 removal. The as-prepared hydrogen may need a further purification to meet the requirements of the specific application.

1.3.2. Production from biomass

Biomass[8] is the fourth largest source of energy in the global context and it accounts for 15% of world's primary energy consumption. A variety of biomass sources can be converted for energy supply: energy crops, agricultural residues and wastes, forestry wastes and residues, industrial and municipal wastes. Production of hydrogen from biomass is considered to be a viable option for the near and mid-term future[9]. The worldwide biomass energy potential in 2050 has been estimated to be in the range of 150-450 exajoule/year, with an energy equivalence of $7.6 \cdot 10^{10}$ barrels of oil energy equivalent[10]. Lignocellulosic biomass is a potential feedstocks for the production of biofuel and bio-H_2. It is obtained as nonedible residues from agriculture, forestry, municipal, industrial and urban refuse.

Biomass has a relatively low hydrogen content, a disadvantage compared to, for example, natural gas and the moisture content is widely variable, ranging from 10% to 70%. The water content influences the thermochemical conversion and the volume of gases produced per energy unit.

The main drawbacks of biomass use are: a low mass and energy density, requirement of large storage facilities, expensive transportation and limitation of fuel-conversion technologies[11]. Densification of biomass is well known to overcome these issues and the three most commonly used techniques are baling, briquetting and pelletization.

Here is reported a short overview of the main processes employed to produce hydrogen[12]:

- Pyrolysis: thermal or thermocatalytic decomposition of lignocellulosic biomass in the absence of air and oxygen. The gas production (CO, H_2, CO_2 and CH_4) can be increased by increasing the pyrolysis temperature range above 550°C-750°C (the gaseous yield can increase to 45-50%, compared with the conventional yield of 30-35% below 500°C). The major challenge in this process is the minimization of CO and methane formation.

$$C_xH_yO_z \rightarrow (1\text{-}x)CO + (y/2)H_2 + C \qquad \Delta H = 180\ KJ/gmol\ (27°C,\ x = 6)$$

$$C_xH_yO_z \rightarrow (1\text{-}x)CO + ((y\text{-}4)/2)H_2 + CH_4 \qquad \Delta H = 300\ KJ/gmol\ (27°C,\ x = 6)$$

- Supercritical water gasification: it produces hydrogen from high moisture content biomass. This process has the advantage of processing any kind of biomass with any moisture availability (>50%), by avoiding operations such as drying and pelletization.

In the high temperature process (>500°C), decomposition of biomass proceeds without the presence of catalyst (Ru or Ni metals), whereas in the low temperature process (<500°C) the use of catalysts is necessary. The cost associated with hydrogen production from this process is higher than the present cost of production from steam reforming of methane. With an increase in the temperature, the hydrogen and carbon dioxide yield increase, while the methane yield gradually decreases.

$$CH_xO_y + (2-y)H_2O \rightarrow CO_2 + (2-y + x/2)H_2$$

X and y are the elemental molar ratios of H/C and O/C in biomass, respectively. Reaction is endothermic. High temperature and pressure (>220 atm) is required for higher H_2 yield.

- Aqueous phase reforming: it produces hydrogen from aqueous phase carbohydrates generated from fruit processing and sugar industry. The water gas shift reaction is favoured by the availability of controlled pressure (5-50 bar) and desired temperature, which drives the outcome with lower amounts of CO and higher yields of hydrogen.

$$C_xH_{2x+2}O_x + xH_2O \rightarrow (2x+1)H_2 + xCO_2$$ Reaction needs high T and P for H_2 yield

APR has several advantages:

- Energy consumption is less in APR than in steam reforming;
- Most raw materials are non-flammable and non-toxic. Low grade purity feedstocks can be used;
- APR can be coupled with existing technologies concerning the purification of hydrogen (pressure swing adsorption or membrane technology, see next section) to separate the CO_2 for sequestration or further industrial use;
- Multistage reactor configuration can be eliminated.

- Autothermal reforming: is a combination of both steam reforming and partial oxidation of hydrocarbons. The exothermic heat generated by oxidation/partial oxidation of bio-oil or oxygenates can compensate the heat requirement for endothermic reforming reaction steps. Addition of oxygen through the feed can be well managed to match the heat required for steam reforming or both for preheating and steam reforming as well. The O_2/feed molar ratio is approximately > 0.3-0.5 for ATR, whereas

H_2 yields are high comparable to that of steam reforming (O_2/feed > 7) and are in the range of 71-80% of the stoichiometric yield with a good reproducibility.

$$C_xH_yO_z + (x - z/2)2O_2 \rightarrow xCO + (y/2)H_2 \quad \text{Lower } H_2 \text{ yield}$$

$$C_xHyOz + [(x - z + y/2)/2]O_2 \rightarrow xCO + (y/2)H_2O$$

$$C_xH_yO_z + [(2x - z + y/2)/2]O_2 \rightarrow xCO + (y/2)H_2$$

1.4. Distribution of hydrogen

To achieve the final user, the distribution network should allow a fast and reliable delivery of hydrogen. Production and distribution are correlated, because the distribution system depends directly from the production facility. Distribution[13] is one of the key elements for a successful implementation of hydrogen economy.

Different options are available for hydrogen transport and distribution: 1) compressed gaseous and liquid hydrogen by trucks[3], 2) gaseous hydrogen by pipelines[3].

For a short distance, a pipeline can be economically advantageous, but, since the cost of the pipeline increases with the distance, the economics will depend on the quantity of hydrogen, and pipelines will be favoured in case of large quantities of hydrogen. For small quantities of hydrogen, at some point the capital cost of the pipeline will be higher than the operational costs associated with delivering and liquefying the hydrogen. Pipelines have been used to transport hydrogen for more than 50 years; the denser networks are between Belgium, France and the Netherlands, in the Ruhr area in Germany and along the Gulf coast in the U.S. Liquid hydrogen has a high operating cost (electricity needs for liquefaction) but lower capital cost, depending on the quantity of hydrogen and delivery distance. The break-even point between liquid hydrogen and a pipeline will vary depending on the distance and quantity. Truck delivery of liquid hydrogen results in lower costs per distance, owing to considerably higher hydrogen capacity and, therefore, longer distances can be covered between production and final user.

Compared with liquid hydrogen, compressed gas has lower power requirements and slightly lower capital costs for the tube trailers, but many more tube trailers are required to deliver the same quantity of hydrogen. At long distances, the capital and transport costs of the number of trucks required to deliver a given quantity of compressed hydrogen will be greater than the increased energy cost associated with liquefaction and fewer trucks. If the

distance is relatively short and the quantity of hydrogen transported is small, compressed gas is likely to be the preferred option.

1.5. Hydrogen separation technologies

The three main technologies commonly used for hydrogen separation/purification are:

- Pressure swing absorption (PSA)[14]: the most commonly used technology;
- Membranes[15]: they are used to recover H_2 from a variety of waste streams containing a high content of hydrogen;
- Cryogenic separation[15a, 16]: it is now largely replaced by PSA systems; it is only used for specific applications to produce multiple pure products.

The choice of the most suitable H_2 separation technology often depends on the feedstock and the resulting synthesis gas composition. PSA has been mostly employed for H_2 produced from natural gas. For feedstocks having high carbon/hydrogen ratio, membranes may become attractive, either as stand alone or in hybrid configurations.

1.5.1. Pressure swing absorption

In the PSA process, impurity gas species are adsorbed onto an adsorbent material (mainly zeolite) at high gas partial pressures and are desorbed at lower partial pressures. The impurities are removed by swinging the system pressure from the feed to the tail gas (exhaust) pressure. The process is cyclic and more than one adsorber is used, in order to maintain a constant flow for the feed, product and tail gas. The driving force is the impurity gases partial pressure difference (typically a 4:1 pressure ratio) between the feed and tail gas. The main advantage of PSA is the ability to produce high purity H_2 (99–99.999%). The tail gas from PSA is usually utilised as a fuel at low pressures, with an economical benefit; however, compressing the tail gas is expensive, comparable to the cost of the PSA unit. Hence, selection of a tail gas pressure is highly important. The H_2 recovery from the PSA system is greatly reduced upon increasing the tail gas pressure, which gives rise to a trade-off between H_2 purity and tail gas compression costs. Another drawback is the scale of operation and infrastructure: PSA can be adapted only from a medium to large industrial scale.

1.5.2. Cryogenic separation

Cryogenic separation uses the difference in boiling points of the components of a mixture of gases to separate the components by partial condensation of the gas stream. Although cryogenic separation can be used for producing pure H_2 from synthesis gas, along with other fractionated products, primarily CO, earlier cryogenic systems have largely been replaced by PSA systems thanks to purer H_2 production.

1.5.3. Membranes

Membrane technology has been relentlessly studied in the last 50 years thanks to:

- low energy consumption;
- ability to carry out separation continuously;
- mild process conditions;
- ease of scaling up;
- combination with other technologies in hybrid configurations.

There are, however, important disadvantages, depending on the membrane type:

- fouling tendency;
- low membrane lifetime;
- low selectivity or flux.

Palladium and its numerous alloys have high H_2 permeability values, producing an ultra-pure gas (99.9999%)[17]. The main drawback is the high cost of the metal, so there is a strong interest to investigate new alloys having low Pd content, maintaining the same hydrogen flux and selectivity. Commercial dense metal membranes are commonly based on the Pd/Ag binary alloy system and are usually produced by cold-rolling or drawn into a tube with an approximate thickness of 50 µm. The H_2 flux through such membranes is roughly an order of magnitude lower than that targeted by the U.S. Department of Energy[18], which have listed the goals for H_2 separation metal membranes (Tab. 1.2):

Performance target	Units	2003 status	2006 status	2010 status	2015 status
Flux rate	$m^3/h/m^2$	18.3	30.5	61	91.5
Cost	$\$/m^2$	1940	1620	1080	<1080
Durability	Years	<1	1	3	>5
Operating temperature	°C	300-600	400-700	300-300	250-500
ΔP operating capability	MPa	0.69	1.38	<2.76	2.76-6.89
H_2 recovery	% of total gas	60	70	80	90
H_2 purity	% of total (dry) gas	>99.9	>99.9	>99.95	99.99

Tab. 1.2 : metal membrane separation targets[18].

Using Pd alloy membranes, the U.S. DoE flux target can be reached only decreasing the thickness of the membranes to few μm. The next chapter will offer a wide overview about the membrane technology used for H_2 separation and purification.

References

1. Hoffert, M. I.; Caldeira, K.; Jain, A. K.; Haites, E. F.; Harvey, L. D. D.; Potter, S. D.; Schlesinger, M. E.; Schneider, S. H.; Watts, R. G.; Wigley, T. M. L.; Wuebbles, D. J., Energy implications of future stabilization of atmospheric CO2 content. *Nature* **1998,** *395* (6705), 881-884.

2. Turner, J. A., Sustainable hydrogen production. *Science* **2004,** *305* (5686), 972-974.

3. Wietschel, M.; Ball, M., *The hydrogen economy: Opportunities and challenges*. 2009.

4. Gupta, R. B., *Hydrogen Fuel - Production, Transport and Storage*. CRC Press: 2009.

5. Holladay, J. D.; Hu, J.; King, D. L.; Wang, Y., An overview of hydrogen production technologies. *Catalysis Today* **2009,** *139* (4), 244-260.

6. (a) Hydrogen Production. In *Lecture Notes in Energy*, 2013; Vol. 3, pp 89-111; (b) Abbas, H. F.; Wan Daud, W. M. A., Hydrogen production by methane decomposition: A review. *International Journal of Hydrogen Energy* **2010,** *35* (3), 1160-1190; (c) Iulianelli, A.; Liguori, S.; Wilcox, J.; Basile, A., Advances on methane steam reforming to produce hydrogen through membrane reactors technology: A review. *Catalysis Reviews - Science and Engineering* **2016,** *58* (1), 1-35; (d) Moon, D. J., Hydrogen production by catalytic reforming of gaseous hydrocarbons (methane & LPG). *Catalysis Surveys from Asia* **2008,** *12* (3), 188-202; (e) Qi, X.; Dong, X.; Lin, W., Steam reforming and partial oxidation of methane to produce syngas. *Tianranqi Gongye/Natural Gas Industry* **2005,** *25* (6), 125-127+17-18.

7. Steinberg, M.; Cheng, H. C., Modern and prospective technologies for hydrogen production from fossil fuels. *International Journal of Hydrogen Energy* **1989,** *14* (11), 797-820.

8. (a) Hosseini, S. E.; Abdul Wahid, M.; Jamil, M. M.; Azli, A. A. M.; Misbah, M. F., A review on biomass-based hydrogen production for renewable energy supply. *International Journal of Energy Research* **2015,** *39* (12), 1597-1615; (b) Hosseini, S. E.; Wahid, M. A., Hydrogen production from renewable and sustainable energy resources: Promising green energy carrier for clean development. *Renewable and Sustainable Energy Reviews* **2016,** *57*, 850-866; (c) Navarro, R. M.; Peña, M. A.; Fierro, J. L. G., Hydrogen production reactions from carbon feedstocks: Fossil fuels and biomass. *Chemical Reviews* **2007,** *107* (10), 3952-3991; (d) Ni, M.; Leung, D. Y. C.; Leung, M. K. H.; Sumathy, K., An overview of hydrogen production from biomass. *Fuel Processing Technology* **2006,** *87* (5), 461-472.

9. (a) Demirbas, A., Biohydrogen generation from organic waste. *Energy Sources, Part A: Recovery, Utilization and Environmental Effects* **2008,** *30* (5), 475-482; (b) Demirbas, A., Hydrogen production from carbonaceous solid wastes by steam reforming. *Energy Sources, Part A: Recovery, Utilization and Environmental Effects* **2008,** *30* (10), 924-931.

10. (a) Rioche, C.; Kulkarni, S.; Meunier, F. C.; Breen, J. P.; Burch, R., Steam reforming of model compounds and fast pyrolysis bio-oil on supported noble metal catalysts. *Applied Catalysis B: Environmental* **2005,** *61* (1-2), 130-139; (b) Huber, G. W.; Iborra, S.; Corma, A., Synthesis of transportation fuels from biomass: Chemistry, catalysts, and engineering. *Chemical Reviews* **2006,** *106* (9), 4044-4098.

11. Werther, J.; Saenger, M.; Hartge, E. U.; Ogada, T.; Siagi, Z., Combustion of agricultural residues. *Progress in Energy and Combustion Science* **2000,** *26* (1), 1-27.

12. Mohanty, P.; Pant, K. K.; Mittal, R., Hydrogen generation from biomass materials: Challenges and opportunities. *Wiley Interdisciplinary Reviews: Energy and Environment* **2015,** *4* (2), 139-155.

13. Ball, M.; Weindorf, W.; Bunger, U., Hydrogen distribution. In *The Hydrogen Economy: Opportunities and Challenges*, 2009; pp 322-347.

14. (a) Ritter, J. A.; Ebner, A. D., State-of-the-art adsorption and membrane separation processes for hydrogen production in the chemical and petrochemical industries. *Separation Science and Technology* **2007,** *42* (6), 1123-1193; (b) Step, G. K.; Petrovichev, M. V., Pressure swing adsorption for air separation and purification. *Chemical and Petroleum Engineering* **2002,** *38* (3-4), 154-158.

15. (a) Adhikari, S.; Fernando, S., Hydrogen membrane separation techniques. *Industrial and Engineering Chemistry Research* **2006,** *45* (3), 875-881; (b) Al-Mufachi, N. A.; Rees, N. V.; Steinberger-Wilkens, R., Hydrogen selective membranes: A review of palladium-based dense metal membranes. *Renewable and Sustainable Energy Reviews* **2015,** *47*, 540-551.

16. Helen McCay, M., Hydrogen. An Energy Carrier. In *Future Energy: Improved, Sustainable and Clean Options for our Planet*, 2013; pp 495-510.

17. Grashoff, G. J.; Pilkington, C. E.; Corti, C. W., PURIFICATION OF HYDROGEN. *Platinum Metals Review* **1983,** *27* (4), 157-169.

18. Phair, J. W.; Donelson, R., Developments and design of novel (non-palladium-based) metal membranes for hydrogen separation. *Industrial and Engineering Chemistry Research* **2006,** *45* (16), 5657-5674.

2. Membranes for hydrogen separation

2.1. General features of membranes for hydrogen separation

The two sides of a membrane for hydrogen separation (Fig. 2.1) are called “feed side” (where the gas mixture arrives) and “permeate side” (the pure hydrogen extraction side). The driving force is a pressure gradient: a high pressure gas mixture is applied at the feed side, keeping a relatively low pressure on the permeate side. The driving force is helped by a “sweep gas”, an inert flow which gathers the separated hydrogen. Membranes should have the following characteristics: high selectivity towards hydrogen, high flux, low cost and high mechanical, chemical and thermal stability.

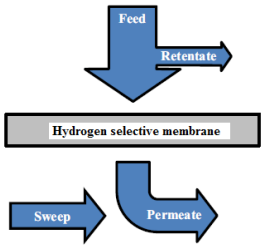

Fig. 2.1: representation of the gas flows through a H_2 selective membrane (from [1]).

Membranes can be classified according to nature (dense, porous), geometry (flat, tubular), separation regime[2] and material (polymeric, metal, ceramic). The most important parameters are selectivity and flux.

Polymeric membranes have relatively low flux and selectivity and work at low temperatures (< 100°C). HCl, SO_x and CO_2 can reduce their effectiveness, but their main advantages are low cost and the ability to withstand high pressure differences.

Dense metallic and ceramic membranes are the most suitable membranes to separate high purity hydrogen, thanks to the high hydrogen selectivity. Metallic membranes are discussed separately in the next sections of the chapter. As to ceramic membranes, microporous membranes, made of silica[3,4,5] or carbon[6,7], are promising for high purity hydrogen separation, but their selectivity is lower compared to dense inorganic membranes. Microporous

silica membranes have low cost, high permeability, good thermal and chemical stability, but low H_2 selectivity[8].

Several ceramics have been examined for hydrogen separation, including zeolites[9,10,11], alumina and other oxides[12], in a dense or asymmetric configuration[13,14,15,16,17,18] (thin dense layer supported by a porous substrate). Dense ceramic membranes, having a combination of electronic and protonic conductivity, can separate high purity hydrogen, but they operate at temperatures typically higher than 700-800°C. The main drawbacks are low fluxes and instability with CO_2 and H_2S. Dense ceramic can be classified into perovskite-type and non-perovskite type membranes:

- **Perovskite type:** the most studied materials are doped $SrCeO_3$[19,20,21,22], $BaCeO_3$[23,24,25,26] and $BaZrO_3$[27]. These perovskites have high protonic conductivity but low electronic conductivity, so a cations doping (Y[28], Eu[21] and Gd[29a]) is required;
- **Non-perovskites type:** there are lots of different doped rare earth metal oxides that may be interesting (fluorite-related-type lanthanum tungsten oxide and aragonite-structure lanthanum borate)[29b, 29c].

An alternative way to increase the electronic conductivity in materials like $SrCeO_3$, $BaCeO_3$ and $BaZrO_3$ is the preparation of composites with a metallic phase, usually Ni, or an electron conducting ceramic. The former materials are called cer-met[30,31,32,33], the latter cer-cer. Cer-cer resulted in having among the highest hydrogen permeabilities of ceramic membranes and good chemical and mechanical stability[34].

Membranes can be further classified into unsupported and supported membranes. Unsupported membranes should be thick enough (> 50 μm) to have sufficient mechanical stability. The main drawbacks of these membranes are their low hydrogen flux, and, in case of expensive materials, the cost of the whole membrane. Supported membranes consist of a dense, thin selective layer deposited onto a porous substrate, which provides mechanical stability. Two main types of porous substrate materials are employed:

- **Ceramic:** they are the most common materials, thanks to the very low cost. Common materials are employed (alumina), but they can give low mechanical stability. Tubes and hollow fibers are commercially available. In general, tubular ceramic substrates

consist of at least two layers, one macroporous, with mechanical strength purposes and fast gas flow, and a microporous low roughness ceramic top layer. Hollow fibers are usually prepared by spinning[35,36]. One of the main drawbacks of the ceramic substrates is the different coefficient of thermal expansion in case of coupling with a metallic thin selective layer.

- **Metallic:** they are mechanically stronger than ceramic but commercial products, mainly tubular, have lower surface qualities. In some cases, where interdiffusion phenomena can alter the selective layer composition, an inter-metallic diffusion barrier has to be deposited between the substrate and the hydrogen selective layer. The most common materials used as barrier are zirconia, yttria-stabilized zirconia (YSZ), titania, ceria and alumina, deposited mainly by atmospheric plasma spraying[37,38] and wet powder spraying[39,40,41].

The most commonly used geometries are planar (early laboratory research and development studies) and tubular (medium scale and industrial scale, thanks to higher surface area-to-volume ratio and easy sealing). Tab. 2.1 reports the main membranes types and parameters.

	Dense polymer	**Micro porous ceramic**	**Dense metal**	**Porous carbon**	**Dense ceramic**
Temperature range (°C)	< 100	200-600	300-600	500-900	600-900
H_2 selectivity	Low	5-139	>1000	4-20	>1000
H_2 flux (x 10^{-3} mol m^{-2} s^{-1} at ΔP=100 kPa)	Low	60-300	60-300	10-200	6-80
Stability issues	Swelling, compaction, mechanical strenght	Stability in H_2O	Phase transition	Brittle, oxidising	Stability in CO_2
Poisoning issues	HCl, SOx, CO_2	-	H_2S, HCl, CO	Strong adsorbing vapours, organics	H_2S
Materials	Polymers	Silica, zirconia, alumina, titania, zeolites	Pd alloy, III-V group metals	Carbon	Proton conducting ceramics (mainly perovskites)

Transport mechanism	Solution / diffusion	Molecular sieving	Solution / diffusion	Surface diffusion; molecular sieving	Solution/diffusion (proton conduction)
Development status	Commercially Linde, BOC, Air Liquide	Prototype tubular silica membranes available up to 90 cm. Other materials only small samples (cm^2)	Commercially by Johnson Matthey; prototype membrane tubes available up to 60 cm	Small membrane modules commercial, mostly small samples (cm^2) available for testing	Small samples available for testing

Tab. 2.1: properties of the various H_2 selective membrane types (from [1]).

According to the membrane nature and the size of pores, six mechanisms[42,43] can be described for the gas separation phenomenon (Fig. 2.2):

- Poiseuille (or viscous flow): it takes place when the mean pore diameter is greater than the mean free path (MFP) of the molecules; it has no utility in gas separation processes;
- Knudsen diffusion: it occurs when the pore diameter of the membrane is smaller than the MFP of the gas being separated (2-100 nm). Small molecules with small MFPs pass through the membrane pores more easily than the bigger ones with larger MFPs. It is useful for the separation of small molecules but selectivity is generally low;
- Molecular sieving: it relies on the difference in kinetic diameter of the molecules, allowing permeation of small molecules;
- Surface diffusion: it relies upon the active sites in the membrane, enhancing the adsorption to the pores. It occurs simultaneously with Knudsen diffusion, increasing selectivity since it does not allow the transfer of non-adsorbed components through the membrane;
- Capillary condensation: it occurs when the pore is filled by a condensed phase, allowing the transport of only those species that are soluble in the condensed phase. The selectivity is high but the effectiveness of the mechanism depends on several factors (composition, pore size and uniformity);
- Solution-diffusion: the first step is the absorption of the gas species into the membrane on the upstream surface. Once absorbed, the gas/atom must diffuse through

the membrane and then desorb from the downstream surface. The permeation rate for this process is controlled by both the solubility of the gas species in the membrane and the diffusion coefficient of the absorbed species through the membrane. As to dense metal membrane, since the hydrogen molecule is dissociated and then re-associated, this process is sometimes called reactive or catalytic solution-diffusion.

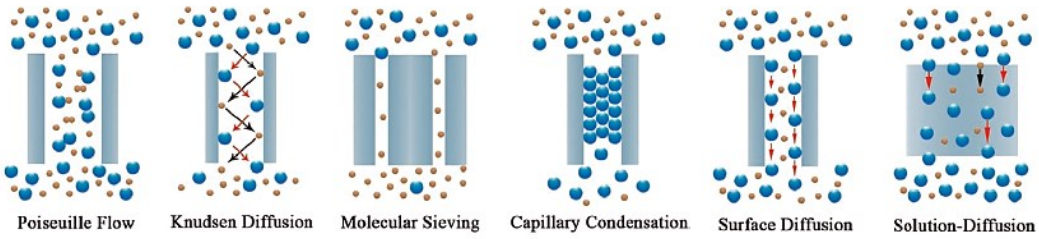

Fig. 2.2: gas transport mechanisms in gas separation membranes (from [44]).

2.2. Dense metallic membranes

2.2.1. General features of metallic membranes

Many metals (pure or alloys) are permeable to hydrogen and the most employed are Pd (face-centered cubic, FCC) and the metals in the groups III-V (body-centered cubic, BCC). BCC metals have 3 times more octahedral (O) and tetrahedral (T) sites than FCC[1]; the T sites surrounding the BCC O sites are severely distorted and they are larger than the O sites, whereas the reverse is true in the FCC crystal structure[45]. According to theoretical calculations, hydrogen prefers to occupy the T interstices in BCC metals[46,47] while in the FCC metals hydrogen will preferentially inhabit the O sites since they are far more stable[48,49].

The palladium ability was discovered by Thomas Graham in 1866, who noticed that palladium was capable of absorbing more than 600 times its own volume in hydrogen (retaining its physical properties / structural integrity), and, of more practical importance, only hydrogen would permeate through the palladium if pure gas was substituted by a coal gas[50].

The non-noble metals of the IVB and VB groups (pure and alloys), even if they show very high hydrogen permeability values, develop a tenacious oxide layer on their surface, reducing the surface ability in hydrogen dissociation, re-association and permeation[51,52]. The most common solution to this problem is the deposition of a very thin Pd based layer on the sur-

faces of these membranes[53], having protective and catalytic purposes. However, metallic membranes can have several drawbacks:

- H_2 embrittlement and fatigue fractures due to absorption/desorption cycles;
- In case of supported membranes, mismatch in the thermal expansion coefficient (CTE) of the metal and the substrate and intermetallic diffusion[54];
- contamination of the H_2 selective layer by oxide formation or CO, CO_2 and H_2S;
- preferential segregation of the element with the lower surface free energy[55];
- diffusion of carbonaceous impurities into the bulk of the membrane[8].

H_2 embrittlement can occur when hydrogen forms a hydride with the metal. The hydride formation causes a discontinuous and abrupt change of the lattice parameters, with a large internal strain and a severe lattice deformation, leading to membrane failure. When hydrogen dissolves in a metal, the lattice expansion far exceeds the thermal expansion. The maximum temperature at which the hydride phase is stable under expected hydrogen pressures is defined as the critical temperature (T_C).

2.2.2. Commercial membranes

Dense metallic membranes are already available on markets and Tab. 2.2 reports a short summary of them[56].

Company name	Architecture	H_2 permeability	H_2 flux	H_2 selectivity	H_2 purity / lifetime
CRI/ Criterion	Pd - Pd alloy tubular membranes deposited onto sintered porous metal substrates	40-70 $Nm^3\ m^{-2}\ h^{-1}\ bar^{-0.5}$	Stable at temperatures of 300-500°C and differential pressures of 26-42 bar		> 99%
Energy Research Center of the Netherlands	Palladium composite membrane, 3-9 µm, deposited by ELP onto porous alumina	-	-	-	99.5% - 99.995% / thousands of hour
Eltron research	Alloy based membranes (6.8 kg/day of hydrogen)	-	809 mL min^{-1} cm^{-2} - 400°C, 6.9 bar ΔP with H_2 pure gas feeding	-	> 300h

Green hydrotech	Pd and Pd-Cu membranes onto porous stainless tubes	-	-	H_2/N_2 selectivity > 100.000	99.996
Media and Process technology	Pd-based membrane module; 2 µm thick layer of Pd deposited on a ceramic substrate	-	0.575 mol m^{-2} s^{-1}	H_2/N_2 selectivity > 1000	-
Membrane reactor technology	Rolled foils or supported thin layers (8-15 µm)	-	95 Nm^3 m^{-2} h^{-1} (5 µm Pd membrane at 550°C and hydrogen ΔP of 3.4 bar)	-	-
Pall Corporation	Pd alloy composite membranes on a pre-commercial basis	-	295-354 mL min^{-1} cm^{-2} (400°C and feed pressure of 1.38 barg)	H_2/Ar selectivity 10,000 – 20,000	-
REB Research and Consulting	Metal membranes of Pd coated refractory metal tubes Metal-metal matrix membranes consisting of a high permeable H_2 metal layer coated with Pd alloys on each side	V-Ti: 0.15 mol m m^{-2} s^{-1} $Pa^{-0.5}$ (600°C) and 0.015 mol m m^{-2} s^{-1} $Pa^{-0.5}$ (300°C) V-Nb: 0.2 mol m m^{-2} s^{-1} $Pa^{-0.5}$ (429°C) and 0.19 mol m m^{-2} s^{-1} $Pa^{-0.5}$ (340°C)	Pd-Cu: 0.2 mol m^{-2} s^{-1} (membrane thickness 0.5 µm; 400°C and 3.03 bar ΔP)	-	-
United technology research center	Palladium-copper-transition metal trimetallic alloy hydrogen separators	-	0.230 mol m^{-2} s^{-1} (400°C, feed pressure of 6.9 bar)	-	99.5%

Tab. 2.2: membranes for hydrogen separation already available on markets.

2.3. Palladium and palladium – based membranes

Palladium is a transition metal with FCC crystal lattice, but, despite the high hydrogen permeability, pure palladium is not appropriate. The palladium-hydrogen system has two immiscible FCC phases: α (interstitial solid solution) and β (hydride). At room temperature, α phase exists up to an approximate H/Pd ratio of 0.02. Above this composition both phases coexist up to the β_{min} composition of 0.6. The lattice parameters are very different: 3.890 Å for pure palladium, 3.895 Å for α_{max} and 4.025 Å for β_{min}. The volume increase for the transition from α to β phase causes internal stresses, deformation and failure of the membrane.

Cycling the membrane in the phase transition range (miscibility gap) produces very large dislocation densities[57], thus the need to operate above 300°C and 2 MPa, where the β phase is not present. Another drawback of pure palladium is the poisoning coming from reactions with H_2S[58], CO, CO_2 and H_2O[59].

Alloying of palladium can solve many of these problems, and several elements (including Ag, Au, Cu, Y and Pt) can be used to form substitutional solid solutions. These alloys have a lower critical temperature for α → β transition, suppressing the miscibility gap below room temperature. Moreover, several Pd alloys demonstrate superior hydrogen permeance and often possess substantially greater mechanical properties.

The Pd-Ag alloy is the most widely studied alloy. Pd and Ag are miscible in all proportions (Fig. 2.3), forming an interstitial solid solution with FCC structure. Ag enlarges the Pd lattice (Fig. 2.4) and reduces the compactness of the unit cell (at 25°C, the lattice parameter varies from 3.889 Å of pure Pd to 3.907 Å with 10% Ag), reducing the variation of lattice expansion that accompanies the phase transition. The α/β miscibility gap is closed to room temperature when the concentration of Ag reaches 24 at%. This alloy absorbs hydrogen more quickly and is approximately twice as permeable as pure palladium[60]. Increasing the Ag content the solubility of hydrogen increases and the critical temperature decreases, but the hydrogen diffusion coefficient decreases. Maximum permeance (approximately twice that of pure Pd) is reached for a Ag content between 20 and 25 wt%, but decreases when the content of Ag is further increased[61]. According to more accurate measurements, the optimum is obtained for Pd-Ag(23 wt%), a composition employed in commercial purifiers, though they exhibit short life cycles due to significant lattice expansion upon hydrogen absorption and undergo grain coarsening at high temperature[62]. Pd-Ag alloy has relatively low strength when compared to other Pd alloys, such as Pd-Y and Pd-Cu, and is soft and ductile for high-pressure applications.

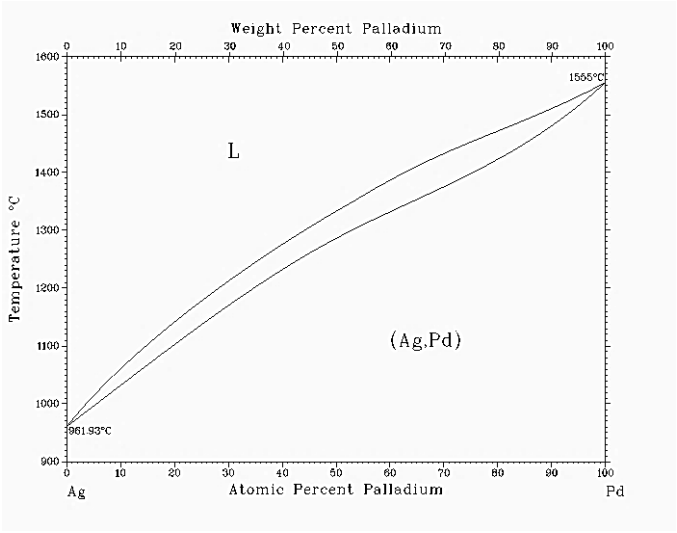

Fig. 2.3: Pd-Ag phase diagram (ASM Handbook, Alloy phase diagram, Vol 3).

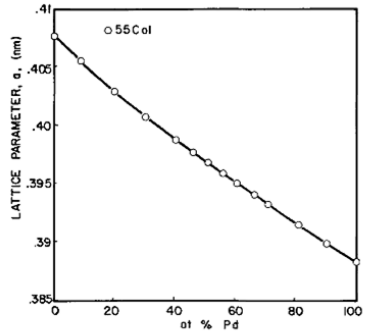

Fig. 2.4: effect of composition on Pd-Ag solid solution lattice parameter (from [63]).

In addition to Pd-Ag alloy, a large variety of binary alloys have been investigated: Pd-Au[64,65], Pd-Cu[66], Pd-Y[67] (Tab. 2.3), although Pd-Ag, Pd-Au and Pd-Cu based alloys are the most studied also in term of long term stability. These alloys are chemically more stable than pure Pd and the critical temperature is significantly reduced.

Alloy	Permeability (x 10^{-8} mol m^{-1} s^{-1} $Pa^{-0.5}$)	Alloy	Permeability (x 10^{-8} mol m^{-1} s^{-1} $Pa^{-0.5}$)
Pd	1.20	**$Pd_{45}Au_{55}$**	0.13
Pd	0.80	**$Pd_{60}Cu_{40}$**	1.42
Pd	0,73	**$Pd_{80}Cu_{20}$**	0.17
$Pd_{75}Ag_{25}$ *	3.21	**$Pd_{47}Cu_{53}$**	0.04
$Pd_{90}Ag_{10}$	2.44	**$Pd_{90}Cu_{10}$**	0.68
$Pd_{60}Ag_{40}$	0.68	**$Pd_{92}Gd_{8}$ ***	5.33
$Pd_{48}Ag_{52}$	0.10	**$Pd_{90}Ni_{10}$**	0.27
$Pd_{95}Au_{5}$	1.49	**$Pd_{90}Y_{10}$ ***	5.69
$Pd_{80}Au_{20}$	1.35	**$Pd_{92}Y_{8}$ ***	3.82
$Pd_{60}Au_{40}$	0.59		

Tab. 2.3: H_2 permeabilities for some Pd based membranes at 350°C (from [1]) - * = at%

2.3.1. Absorption of hydrogen in palladium and palladium alloys

Hydrogen can diffuse in the metal lattice only as atom, so the hydrogen molecule must first dissociate ($H_2 \rightarrow 2H$). The dissociation takes place on the metal surface. This reaction is characterized by a specific activation energy and in some metal hydride systems the overall reaction kinetics of hydride formation is limited by slow dissociation. Hydrogen atoms affect the host lattice mainly in these ways[68, 69]:

- they distort the palladium lattice due to the elastic strain energy and this distortion is independent of the host material[68];
- the interstitial hydrogen changes the local electron density as its electron is taken into the "electron cloud" of the host, screening the charge of the proton.

The thermodynamic properties of a metal-hydrogen system can be evaluated using a series of pressure-composition-temperature (PCT) isotherm diagrams, which correlates hydrogen concentration at a given temperature to the pressure. From PCT diagram of Pd-H reported in Fig. 2.5, three distinct regions can be distinguished: α solid solution, α + β region (miscibility gap, given by the length of the plateau) and the β hydride region.

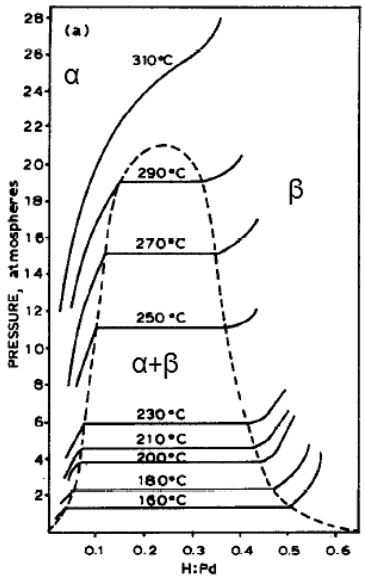

Fig. 2.5: Pd-H system (from [69]).

Hydrogen atoms are uniformly distributed inside the metal lattice and the concentration of hydrogen, or solubility, is directly proportional to the square root of the external hydrogen pressure. This relationship is summarized in the Sieverts' law of ideal dilute solubility:

$$\sqrt{P_{H_2}} = K_S X$$

where P_{H_2} is the hydrogen pressure, X is the hydrogen concentration (also known as c(H)) and K_S is Sieverts constant. K_S is defined as an equilibrium constant under conditions where the hydrogen concentration X is << 1. At low hydrogen concentrations Sieverts' law is valid for many experimentally observed systems, but when X increases deviations from the ideal occur, due to changing nature of the metal-hydrogen system. Deviation from Sieverts' law can occur at high H_2 pressures and also in thin foil membranes when the selective layer is defective and allows the passage of other gases and when the surface of the foil has been poisoned by contaminants, reducing the activity for the dissociation of H_2.

However, the assumption of a low hydrogen concentration (X << 1) has been shown to be a reasonable approximation for most Pd membrane operating conditions[70]. Therefore, Sieverts' law is assumed to be valid and forms the basis of several hydrogen permeation models.

2.3.2. Diffusion of hydrogen in palladium and palladium alloys

Diffusion takes place thanks to a gradient or difference in chemical potential. In case of membranes, this is a hydrogen partial pressure gradient across the membrane. It has not yet fully understood the precise mechanism of hydrogen diffusion through a metal lattice and a lot of models, based on classical[71] or quantum theory[72], have been proposed. Kehr[73] proposed four different diffusion mechanisms:

- at very low temperatures there are virtually no thermal vibrations (phonons). Hydrogen atoms, "self-trapped" due to the relaxation of the surrounding lattice, are thought to proceed to the next interstitial site via a quantum mechanical tunnelling process termed "band propagation";
- as temperature rises, transport mechanisms involving phonons may take place and hydrogen atoms move via thermally activated tunnelling. A phonon brings the occupied low energy site and the neighbouring high energy site into coincidence, allowing the transition of the hydrogen atom between the sites. The lattice then relaxes around the atoms new position;

- at higher temperatures, hydrogen atoms can be regarded as classical particles executing over-barrier jumps between neighbouring sites via thermal excitation;
- at much higher temperatures the hydrogen atoms no longer remain within potential wells of interstitial sites. In this region diffusion occurs via free motion, similar to that in gases and liquids.

At a given temperature, diffusion can occur by a combination of all four mechanisms[74]. At the typical operating temperatures (200 – 600°C), the most suitable mechanism should be the thermally activated over-barrier jumps, adequately described using classical theory[71]. The jump rate of an interstitial hydrogen atom (Γ) can be written as[75]:

$$\Gamma = n\nu \exp\left(\frac{-E_A}{K_B T}\right)$$

where n is the number of nearest neighbour interstitial sites, ν is the vibrational frequency of the hydrogen atom, E_A is the thermal activation energy and K_B is Boltzmann's constant.
The theoretical diffusion coefficient (D) for interstitials in a cubic lattice can then be calculated as:

$$D = a^2 \alpha \Gamma$$

where a is the lattice parameter and α is a coefficient determined by the geometric relationship between interstitial sites (1/12 for octahedral site in an FCC lattice).
The diffusion in metals is a non-classical process and a quantum theory of diffusion is therefore needed[74], but, until now, no model has yet been proposed which accurately determines diffusion in all regimes.
The addition of substitutional alloying elements almost always decreases hydrogen diffusivity, with no regards as to the effect of the alloying element on the host lattice (expansion, as in the case of Ag and Au, or contraction, as in the case of Cu and Fe). Barlag et al.[76] investigated the room temperature hydrogen diffusivity in a range of FCC Pd alloys: small additions of Ag (≤ 20 at.%) were shown to have little effect on the diffusivity, showing good agreement with diffusion data reported by Holleck[77], who found little change in the activation energy from Pd to Pd-Ag20. Barlag et al.[76] found that above 20 at% the diffusivity sharply dropped to a minimum value at approximately Pd-Ag60. The diffusivity progressively increased with further Ag additions until the value for pure Ag was reached.

They proposed a simple two sites model[76] to explain the shape of the curve: two different octahedral sites (Pd and Ag) are assumed to exist, both possessing a different hydrogen occupation probability. Small silver additions to palladium partly block the energetically favoured diffusion paths in the palladium matrix, leading to round-about way diffusion. At high silver concentrations, palladium atoms act as traps for hydrogen in a silver matrix. If Ag is substituted by Ni or Cu a similar trend is observed, although small additions reduce the diffusivity to a greater extent. This was attributed to the lattice contraction experienced by Pd-Cu and Pd-Ni as opposed to the lattice expansion of Pd-Ag.

2.4. Alternatives to Palladium based alloys

The wide use of Pd alloys is limited by excessive cost and availability of the metal, so there is a strong interest in developing non Pd-based (or with a low Pd content) alloys[45,78] (Tab 2.4). The cost reduction can be fulfilled by using a metal cheaper than Pd, limiting Pd only in very thin surface layers, for protection and catalytic purposes. Metals belonging to the groups IV and V show high hydrogen permeability (Fig. 2.6) and have been studied as possible Pd alternatives.

Refractory metals have a permeability that increase reducing the temperature, as a consequence of the prevalent effect of solubility on the hydrogen mass-transfer process. The rate of hydrogen transport through the lattice of group V metals is orders of magnitude higher than that through any other metallic lattice including palladium[79] and the transcrystalline hydrogen transfer through vanadium is the fastest among the group V metals[79b].

In order to promote the dissociative absorption of hydrogen molecules and associative desorption of absorbed H atoms, both sides of the membrane have to be plated with a thin layer of palladium or palladium alloy[79a,79b,80]. This layer also protects the membrane from oxidation. An important drawback of such multilayer is the limited thermal stability, caused by interdiffusion between coatings and core membrane material[79a,79b,80]. In order to avoid this, temperature should not exceed 400°C but, even at this temperature, the hydrogen solubility is so high that it may exceed the limit admissible from the viewpoint of mechanical stability, giving rise to several problems:

- failure of connection tightness between the membranes and the structural parts, with the risk to seriously damage the sealing;

- destructive mechanical stress inside the membrane;
- hydrogen embrittlement in case of high concentration of hydrogen[81].

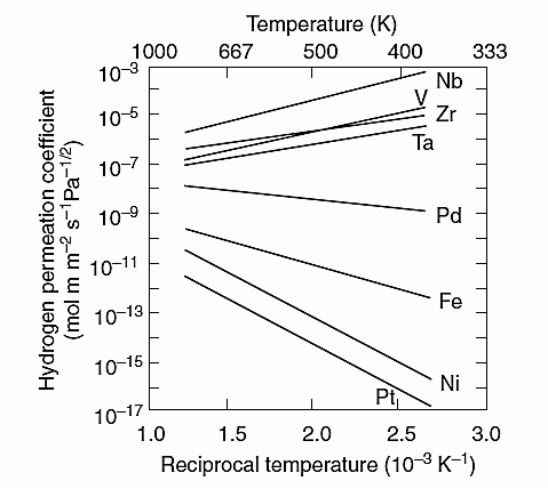

Fig. 2.6: hydrogen permeability of various metals (from Handbook of Membrane Reactors, Vol 1).

However, these metals have some drawbacks: H_2 embrittlement and surface reactivity with gases, in particular oxygen.

Thanks to their relatively high H_2 permeability and low cost, most of the alloys considered for H_2 separation are Ni and V based:

- Ni-based membranes[82]: the Ni-H system has been widely studied due to its important applications in chemical catalysis and in H_2 storage. The difference in lattice size between the α and β hydride is slightly larger than that of the Pd-Ag alloy, thus generating wider expansion/contraction under the hydrogenation/dehydrogenation cycling;
- V-based membranes[83]: they are a possible alternative to palladium membranes thanks to vanadium lower cost and higher hydrogen permeability. A number of binary and ternary alloys were tested and some of them demonstrated rather good properties as to hydrogen solubility and permeability[81, 84]. The improvement of the resistance to embrittlement of vanadium has been studied for the ternary alloy of V and Ni with a third metal (M), according to the formula $V_{85}Ni_{10}M_5$, where M = Ti, Si, Mn, Fe, Co Cu, Pd, Ag or Al[85]. Other studies of vanadium alloys have been carried out on membranes consisting of V - 15% Ni covered by thin layers of Pd[78a,86]. Promising alloys with a low amount of Pd have been reported[87]. In this thesis we focused on

two different vanadium based alloys (described in the following sections) to find alternative to the benchmark Pd-Ag alloy.

As the number of possible combinations of these metals is huge, a modelling approach can be useful in identifying the most suitable combination of metals. An interesting approach is given by density functional theory (DFT) calculations[88].

Alloy	Permeability (mol m^{-1} s^{-1} $Pa^{-0.5}$)	T(°C)	Alloy	Permeability (mol m^{-1} s^{-1} $Pa^{-0.5}$)	T(°C)
$V_{99.98}Al_{0.02}$	0.7-1.8 x 10^{-9}	250-400	$Nb_{95}Ru_5$	1.3 x 10^{-7}	300
$V_{99.1}Al_{0.9}$	0.7-1.8 x 10^{-9}	250-400	$Nb_{95}Pd_5$	1.3 x 10^{-7}	300
$V_{97.1}Al_{2.9}$	0.7-1.8 x 10^{-9}	250-400	$V_{90}Ti_{10}$	2.7 x 10^{-7}	400
$V_{81.3}Al_{18.7}$	3.7-6 x 10^{-9}	250-400	$V_{85}Ti_{15}$	3.6 x 10^{-7}	435
$V_{71.8}Al_{28.2}$	0.7-1.8 x 10^{-9}	250-400	$V_{85}Ni_{15}$	3 x 10^{-8}	400
$Nb_{95}Zr_5$	1.3 x 10^{-7}	300	$V_{90}Co_{10}$	1.2 x 10^{-7}	400
$Nb_{95}Mo_5$	1.3 x 10^{-7}	300	$V_{85}Al_{15}$	6 x 10^{-8}	435

Tab. 2.4: H_2 permeabilities for some non Pd-based alloys (from [89]).

2.4.1. Hydrogen in vanadium

The mechanism of hydrogen absorption in vanadium starts with the formation of vanadium-hydrogen solid solution (α phase). The hydrogen concentration exceeding the terminal solid solubility precipitates as the hydride phase. Initially, the β ($V_{2-x}H_x$) phase forms at low temperature, as shown in the V–H phase diagram (Fig. 2.7), with a composition close to V_2H. The volume increase due to hydrogen absorption is pressure independent. Pauling[90] described the β structure as containing linear V-H-V complexes, with V-H half-bonds with a bond length of about 1.76 Å.

The ε ($V_{3-x}H_{2+x}$) phase is another high temperature phase formed by the modification of β phase. When the metal is fully hydrogenated, γ phase (VH_2) forms[91], but it is not stable and hydrogen absorption and desorption take place at moderate temperature and pressure according to the equation $\mathrm{VH_2} \leftrightarrows \mathrm{VH}$. Thus, only half the amount of hydrogen absorbed in vanadium metal could be used in the subsequent hydrogen absorption-desorption process, but this amount is not enough for practical applications of vanadium as a hydrogen storage material[92].

Another low temperature phase is δ phase[93], which has a composition V_3H_2. In this hydride the octahedral interstitials (holes) are occupied. On further hydrogenation, γ phase forms. TG-DTA study on fully hydrogenated vanadium[94] revealed the order of dehydrogenation: γ → β → α → BCC V (H free), with decomposition temperatures of 300 K, 450 K and 750 K respectively[94]. V-H phases are summarized in Tab 2.5.

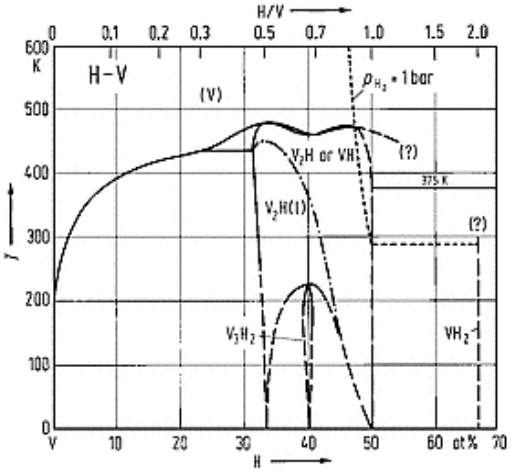

Fig. 2.7: V-H system.

Phases
α: BCC extending to $VH_{0.05}$ / a = 3.037 Å / H randomly distributed in tetrahedral sites
β: BCT with c/a = 1.1, but also reported to be monoclinic (α = 91°) / exists in the range $VH_{0.41}$ – $VH_{0.61}$ below 175°C
ε (β_2): range $VH_{0.40}$ – $VH_{0.80}$ / a = 3.01 Å, c = 3.295 Å / the high – temperature form of β (BCT)
γ: FCC from $VH_{0.90}$ – $VH_{2.00}$ / a = 4.27 Å
δ: ordered V_3H_2 phase in low-temperature region of β phase below -49°C
ζ: VH superstructure achieved by filling empty sites in ε
η: probably similar to β but with higher degree of order

Tab. 2.5: V-H crystal structures data [95].

The alloying elements have a great effect on phase stability, absorption-desorption kinetics as well as the hydrogen absorption capacity[96]. To improve the activation process of vanadium based alloys, the alloying element must have atomic radii at least 5% smaller than that of vanadium matrix[97]. Alloying elements have strong effects on the stability of γ phase[98], and

the effect of alloying on the absorption-desorption from the γ hydride phase was studied by Yukawa et al.[96c].

2.4.2. Promising alloys

Among the alloys available, we focused our attention on $V_{90}Pd_{10}$[87] and V-Ni-Ti[99].

2.4.2.1. $V_{90}Pd_{10}$

$V_{90}Pd_{10}$ is a promising alloy[87a], with an optimal hydrogen permeability and good ductility. Though palladium is a stronger absorber of hydrogen than Ni, it suppresses the hydrogen solubility in binary alloy with V much stronger than Ni, as well as than Cr[100] and W[81], even when palladium concentration is as low as 5 at% (Fig. 2.8).

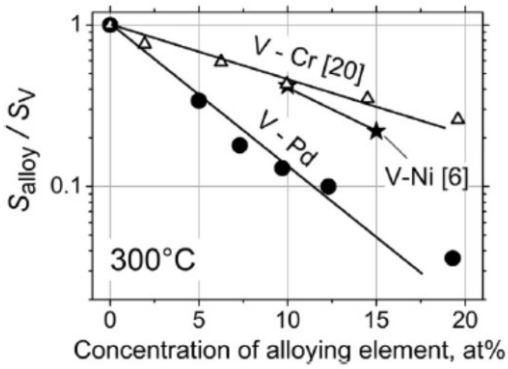

Fig. 2.8: hydrogen solubility for different vanadium based alloys[87b].

Membranes prepared from non-noble metals need a thin layer of palladium[79b, 87a,101], with protective and catalytic purposes; the interdiffusion of palladium in the non-noble core material is considered the main cause of degradation[79b,80,102].

In the V-Pd alloys, the peculiar feature is the validity of Sieverts' law up to a substantially higher concentration of absorbed hydrogen than pure vanadium. As explained by Alimov[87b] and Sakamoto[103], the concept of site blocking could be able to explain this phenomenon. In short, palladium decreases hydrogen solubility due to reduction of the number of possible sites of sorption of H. According to the experimental data[87b, 87c], hydrogen diffusivity in the substitutional V-Pd alloys is only slightly lower than that in pure V.

V-Pd alloys are promising materials for selective membranes, even with relatively small amounts of Pd. This gives two benefits: the first is the lower the concentration of alloying element the more ductile the alloy; the second is a cost-related benefit. Fig. 2.9 reports the

phase diagram of the V-Pd system: it shows several intermetallics, thus limiting the amount of palladium to 18 at%. Up today, no papers report the study of membranes based on $V_{90}Pd_{10}$ thin layer onto porous substrates.

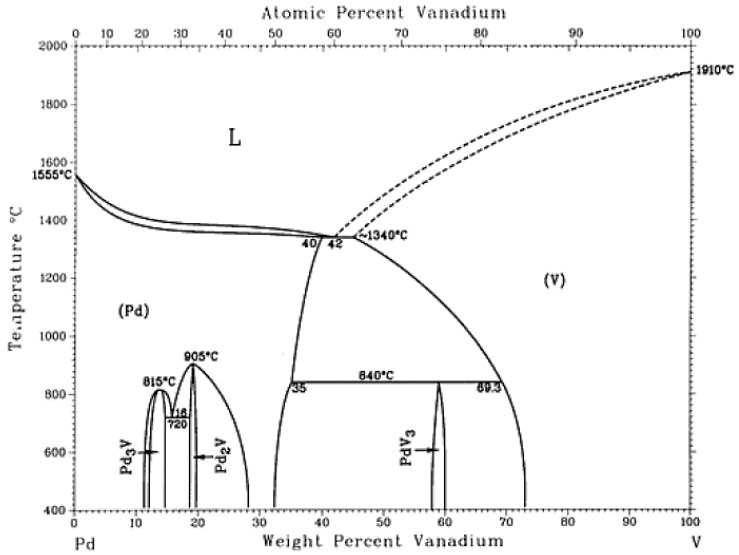

Fig. 2.9: V - Pd phase diagram.

2.4.2.2. V-Ni-Ti ternary system

The ternary system V-Ni-Ti is one of the best known for the development of composite membranes. Ni and Ti form a V-rich BCC phase along with NiTi and $NiTi_2$[104]. Ni and Ti are specifically chosen because addition of Ni to V decreases the H_2 solubility, and therefore reduces the embrittlement susceptibility[105], while Ti enhances the solubility of V both by expanding the metal lattice and by forming stable hydrides[106]. Together they constitute a multi-phase microstructure, containing a primary BCC solid solution (vanadium matrix) and weakly absorbing phases with low volume fraction[107]. NiTi, with a crystal structure differing from the parent BCC solid solution, increases the overall mechanical stability of the material while the dominant V rich phase promotes hydrogen permeability[95]. Hashi et al.[108] were the first to report multi-phase V-Ni-Ti alloys in the context of hydrogen permeation, but the permeabilities measured in alloys with < 50 at.% V were lower than Pd. Adams and Mickalonis[109] reported that the low-temperature permeability of the $V_{53}Ti_{26}Ni_{21}$ alloy was an order of magnitude greater than Pd at the same temperature. Song et al.[107b] examined alloys with a greater proportion of the vanadium solid solution (VSS) phase, reporting significantly greater hydrogen permeabilities for alloys, exceeding 1.0 x 10^{-7} mol m^{-1} $s^{-1}Pa^{-0.5}$ for the

$V_{55}Ti_{30}Ni_{15}$ (containing > 80% of the VSS phase) alloy at 400°C. The overall permeability increased with increasing Ti content.

A miscibility gap between the vanadium α-hydride (a BCC solid solution) and β-hydride (a body-centered tetragonal - BCT - solid solution) exists below 200°C[110]. Addition of Ni increases the critical temperature (T_C) for β-hydride formation to > 400°C[83c] which has major implications for mechanical stability, especially during thermal cycling. Titanium decreases the plateau pressure of β-V-H[111], and the critical temperature for the Ti-H α + β miscibility gap lies well above 700°C[112]. It could therefore be expected that the T_C for a V solid solution containing Ti and Ni would lie significantly above 200°C, increasing the importance of a stabilising composite microstructure. In literature several works about V-Ni-Ti alloy can be found[113,114,115], but they report detailed studies about membranes prepared by arc melting and no papers concerning the deposition of V-Ni-Ti film onto a porous substrate were found.

2.5. Implementation of dense metallic membranes

H_2 flux in Pd-based membranes is highly limited by the membrane thickness, but we have to take into account other parameters, such as mechanical strength and membrane durability. High selectivity and high fluxes can be attained together by the deposition of one or more thin layers of a highly selective membrane material onto a porous substrate (ceramic or metallic), having little or no resistance to fluxes[82c, 116]. The requirement for a thin and defect free metal layer puts strong demand on the quality of the substrate in terms of narrow size pore distribution and surface defects[117]. Pore size and surface roughness of the macroporous substrate surface are often reduced by the application of mesoporous intermediate layers prior to deposition of the permselective metal layer[118]. Substrates with large pores require thicker metal layers, which leads to low permeation and high costs. As to metallic substrates, interdiffusion of metals between the substrate and the H_2 selective layer for operations above the 400°C-450°C have to be reduced. Barrier layers, such as porous silica, zirconia, titania, TiN and porous Pd-Ag have been developed for this purpose[39, 66, 119]. The use of ceramic substrates, such as pure alumina, is not believed to cause significant interdiffusion problems even though only one recent study has reported diffusion of Al from the alumina substrate into the Pd layer at temperatures as high as 650°C, resulting in a decrease in H_2 permeability[120]. Other factors that must be considered include adhesion of the func-

tional coating and the coating defects. These phenomena often lead to failure in membrane performance including lack of mechanical strength and reduced permeability or selectivity. Another approach currently under development is the fabrication of composite, or multi-layer, membranes structure by applying a thin H_2 dissociation catalyst layer (often Pd-based) onto a super-permeable core, with Nb, Ta, V and/or Zr as major components[83a,83f,121,106a,122]. Currently, composite membrane display superior perm-selectivity in comparison to other membrane configurations but long-term chemical and mechanical stability is difficult to achieve. Composite membranes can be implemented in the thin film technology, by deposition of a composite membrane directly on a porous substrate.

References

1. Al-Mufachi, N. A.; Rees, N. V.; Steinberger-Wilkens, R., Hydrogen selective membranes: A review of palladium-based dense metal membranes. *Renewable and Sustainable Energy Reviews* **2015,** *47*, 540-551.

2. Basile, A.; Blasi, A.; Fiorenza, G.; Iulianelli, A.; Longo, T.; Calabrò, V., Membrane and membrane reactor technologies in the treatment of syngas streams produced from gasification processes. In *Gasification: Chemistry, Processes and Applications*, 2011; pp 139-174.

3. Tsuru, T.; Igi, R.; Kanezashi, M.; Yoshioka, T.; Fujisaki, S.; iwamoto, Y., Permeation properties of hydrogen and water vapor through porous silica membranes at high temperatures. *AIChE Journal* **2011,** *57* (3), 618-629.

4. Tsuru, T.; Lee, H. R.; Kanezashi, M., Controlling silica networks using bridged alkoxides for hydrogen separation membranes. In *The Sol-Gel Process: Uniformity, Polymers and Applications*, 2011; pp 827-834.

5. Nagano, T.; Sato, K., Degradation mechanism of an H2-permselective amorphous silica membrane. *Journal of Materials Science* **2014,** *49* (11), 4115-4120.

6. Ismail, A. F.; David, L. I. B., A review on the latest development of carbon membranes for gas separation. *Journal of Membrane Science* **2001,** *193* (1), 1-18.

7. Mahajan, R.; Koros, W. J., Factors controlling successful formation of mixed-matrix gas separation materials. *Industrial and Engineering Chemistry Research* **2000,** *39* (8), 2692-2696.

8. Lu, G. Q.; Diniz da Costa, J. C.; Duke, M.; Giessler, S.; Socolow, R.; Williams, R. H.; Kreutz, T., Inorganic membranes for hydrogen production and purification: A critical review and perspective. *Journal of Colloid and Interface Science* **2007,** *314* (2), 589-603.

9. Hong, M.; Falconer, J. L.; Noble, R. D., Modification of zeolite membranes for H 2 separation by catalytic cracking of methyldiethoxysilane. *Industrial and Engineering Chemistry Research* **2005,** *44* (11), 4035-4041.

10. McLeary, E. E.; Jansen, J. C.; Kapteijn, F., Zeolite based films, membranes and membrane reactors: Progress and prospects. *Microporous and Mesoporous Materials* **2006,** *90* (1-3 SPEC. ISS.), 198-220.

11. Lin, Y. S.; Kanezashi, M., Gas permeation and diffusion in small and intermediate pore zeolite membranes. In *Studies in Surface Science and Catalysis*, 2007; Vol. 170, pp 847-854.

12. Scholes, C. A.; Smith, K. H.; Kentish, S. E.; Stevens, G. W., CO2 capture from pre-combustion processes - Strategies for membrane gas separation. *International Journal of Greenhouse Gas Control* **2010,** *4* (5), 739-755.

13. Balachandran, U.; Lee, T. H.; Park, C. Y.; Emerson, J. E.; Picciolo, J. J.; Dorris, S. E., Dense cermet membranes for hydrogen separation. *Separation and Purification Technology* **2014,** *121*, 54-59.

14. Hung, I. M.; Chiang, Y. J.; Jang, J. S. C.; Lin, J. C.; Lee, S. W.; Chang, J. K.; Hsi, C. S., The proton conduction and hydrogen permeation characteristic of Sr(Ce0.6Zr0.4)0.85Y0.15O3-δ ceramic separation membrane. *Journal of the European Ceramic Society* **2015,** *35* (1), 163-170.

15. Polfus, J. M.; Li, Z.; Xing, W.; Sunding, M. F.; Walmsley, J. C.; Fontaine, M. L.; Henriksen, P. P.; Bredesen, R., Chemical stability and H2 flux degradation of cercer membranes based on lanthanum tungstate and lanthanum chromite. *Journal of Membrane Science* **2016,** *503*, 42-47.

16. Rosensteel, W. A.; Ricote, S.; Sullivan, N. P., Hydrogen permeation through dense BaCe0.8Y0.2O3-δ - Ce0.8Y0.2O2-δ composite-ceramic hydrogen separation membranes. *International Journal of Hydrogen Energy* **2016,** *41* (4), 2598-2606.

17. Zhu, Z.; Hou, J.; He, W.; Liu, W., High-performance Ba(Zr0.1Ce0.7Y0.2)O3-δ asymmetrical ceramic membrane with external short circuit for hydrogen separation. *Journal of Alloys and Compounds* **2016,** *660*, 231-234.

18. Zhu, Z.; Liu, B.; Shen, J.; Lou, Y.; Ji, Y., La2Ce2O7: A promising proton ceramic conductor in hydrogen economy. *Journal of Alloys and Compounds* **2016,** *659*, 232-239.

19. Higuchi, T.; Tsukamoto, T.; Sata, N.; Hattori, T.; Yamaguchi, S.; Shin, S., Electronic structure of protonic conductor SrCeO3 by soft-X-ray spectroscopy. *Solid State Ionics* **2004,** *175* (1-4), 549-552.

20. Higuchi, T.; Tsukamoto, T.; Sata, N.; Yamaguchi, S.; Shin, S.; Hattori, T., Electronic structure of proton conducting SrCeO3-SrZrO 3 thin films. *Solid State Ionics* **2005,** *176* (39-40), 2963-2966.

21. Song, S. J.; Wachsman, E. D.; Dorris, S. E.; Balachandran, U., Defect structure and n-type electrical properties of SrCe0.95Eu0.05O3-δ. *Journal of the Electrochemical Society* **2003,** *150* (11), A1484-A1490.

22. Yoon, H.; Song, S. J.; Oh, T.; Li, J.; Duncan, K. L.; Wachsman, E. D., Fabrication of thin-film SrCe0.9Eu0.1O 3-δ hydrogen separation membranes on Ni-SrCeO3 porous tubular supports. *Journal of the American Ceramic Society* **2009,** *92* (8), 1849-1852.

23. Takeuchi, K.; Loong, C. K.; Richardson Jr, J. W.; Guan, J.; Dorris, S. E.; Balachandran, U., Crystal structures and phase transitions in Y-doped BaCeO3: Their dependence on Y concentration and hydrogen doping. *Solid State Ionics* **2000,** *138* (1-2), 63-77.

24. Ma, G.; Matsumoto, H.; Iwahara, H., Ionic conduction and nonstoichiometry in non-doped BaxCeO3-α. *Solid State Ionics* **1999,** *122* (1-4), 237-247.

25. Ma, G.; Shimura, T.; Iwahara, H., Ionic conduction and nonstoichiometry in BaxCe0.90Y0.10O3 - α. *Solid State Ionics* **1998,** *110* (1-2), 103-110.

26. Wang, W. B.; Liu, J. W.; Li, Y. D.; Wang, H. T.; Zhang, F.; Ma, G. L., Microstructures and proton conduction behaviors of Dy-doped BaCeO3 ceramics at intermediate temperature. *Solid State Ionics* **2010,** *181* (15-16), 667-671.

27. Hooshyari, K.; Javanbakht, M.; Shabanikia, A.; Enhessari, M., Fabrication BaZrO3/PBI-based nanocomposite as a new proton conducting membrane for high temperature proton exchange membrane fuel cells. *Journal of Power Sources* **2015,** *276*, 62-72.

28. Sammes, N.; Phillips, R.; Smirnova, A., Proton conductivity in stoichiometric and sub-stoichiometric yittrium doped SrCeO3 ceramic electrolytes. *Journal of Power Sources* **2004,** *134* (2), 153-159.

29. a: Shima, D.; Haile, S. M., The influence of cation non-stoichiometry on the properties of undoped and gadolinia-doped barium cerate. *Solid State Ionics* **1997,** *97* (1-4), 443-455; b: Shimura T, Fujimoto S, Iwahara H., Proton conduction in non-perovskite-type oxides at elevated temperatures. *Solid State Ionics* **2001**, *143*, 117–23; c: Uno, M., Kosuga, A., Okui, M., Horisaka, K., Yamanaka, S., Photoelectrochemical study of lanthanide titanium oxides, $Ln_2Ti_2O_7$ (Ln = La, Sm, and Gd). *Journal of Alloys and Compounds* **2005**, *400* (1-2), 270-275.

30. Balachandran, U.; Lee, T. H.; Chen, L.; Song, S. J.; Dorris, S. E. In *Development of dense cermet membranes for hydrogen separation*, 2006 AIChE Spring Annual Meeting, 2006.

31. Balachandran, U.; Lee, T. H.; Chen, L.; Song, S. J.; Dorris, S. E. In *Dense cermet membranes for hydrogen separation from mixed gas streams*, 23rd Annual International Pittsburgh Coal Conference, PCC - Coal-Energy, Environment and Sustainable Development, 2006.

32. Song, S. J.; Wachsman, E. D.; Lee, T. H.; Chen, L.; Dorris, S. E.; Balachandran, U., Annealing effect of cermet membranes on hydrogen permeability. *Chemistry Letters* **2006,** *35* (12), 1378-1379.

33. Park, S. J.; Eom, T. W.; Oh, J. E.; Yang, H. K.; Kim, K. H. In *Preparation of high surface area Ni-SDC cermets using a surfactant-assisted co-precipitation method*, Materials Research Society Symposium Proceedings, 2006; pp 77-81.

34. Rebollo, E.; Mortalò, C.; Escolástico, S.; Boldrini, S.; Barison, S.; Serra, J. M.; Fabrizio, M., Exceptional hydrogen permeation of all-ceramic composite robust membranes based on BaCe0.65Zr0.20Y0.15O3-δ and Y- or Gd-doped ceria. *Energy and Environmental Science* **2015,** *8* (12), 3675-3686.

35. Zhang, Q.; Wang, H.; Fan, X.; Chen, S.; Yu, H.; Quan, X., A controlled wet-spinning and dip-coating process for preparation of high-permeable TiO2 hollow fiber membranes. *Water Science and Technology* **2016,** *73* (4), 725-733.

36. Zhang, X.; Cheng, J.; Li, S.; Wang, Y., Preparation and modification of Ba0.5Sr0.5Co0.8Fe0.2O3-δ hollow fiber membranes for oxygen permeation by wet spinning process. *Kuei Suan Jen Hsueh Pao/Journal of the Chinese Ceramic Society* **2016,** *44* (3), 392-396.

37. Dejang, N.; Limpichaipanit, A.; Watcharapasorn, A.; Wirojanupatump, S.; Niranatlumpong, P.; Jiansirisomboon, S., Fabrication and properties of plasma-sprayed Al 2O 3/ZrO 2 composite coatings. *Journal of Thermal Spray Technology* **2011,** *20* (6), 1259-1268.

38. Kassner, H.; Siegert, R.; Hathiramani, D.; Vassen, R.; Stoever, D., Application of suspension plasma spraying (SPS) for manufacture of ceramic coatings. *Journal of Thermal Spray Technology* **2008,** *17* (1), 115-123.

39. Huang, Y.; Dittmeyer, R., Preparation and characterization of composite palladium membranes on sinter-metal supports with a ceramic barrier against intermetallic diffusion. *Journal of Membrane Science* **2006,** *282* (1-2), 296-310.

40. Ruder, A.; Buchkremer, H. P.; Jansen, H.; Malléner, W.; Stöver, D., Wet powder spraying-a process for the production of coatings. *Surface and Coatings Technology* **1992,** *53* (1), 71-74.

41. Zhao, L.; Bram, M.; Buchkremer, H. P.; Stöver, D.; Li, Z., Preparation of TiO 2 composite microfiltration membranes by the wet powder spraying method. *Journal of Membrane Science* **2004,** *244* (1-2), 107-115.

42. Adhikari, S.; Fernando, S., Hydrogen membrane separation techniques. *Industrial and Engineering Chemistry Research* **2006,** *45* (3), 875-881.

43. Koros, W. J.; Fleming, G. K., Membrane-based gas separation. *Journal of Membrane Science* **1993,** *83* (1), 1-80.

44. Li, P.; Wang, Z.; Qiao, Z.; Liu, Y.; Cao, X.; Li, W.; Wang, J.; Wang, S., Recent developments in membranes for efficient hydrogen purification. *Journal of Membrane Science* **2015,** *495*, 130-168.

45. Dolan, M. D., Non-Pd BCC alloy membranes for industrial hydrogen separation. *Journal of Membrane Science* **2010,** *362* (1-2), 12-28.

46. Darby, M. I.; Read, M. N., Energy of hydrogen in b.c.c. transition metals. *Journal of The Less-Common Metals* **1983,** *91* (2), 209-215.

47. Companion, A. L.; Liu, F.; Onwood, D. P., On the location of a hydrogen atom in body-centered cubic 3d transition metal lattices. *Journal of The Less-Common Metals* **1985,** *107* (1), 131-138.

48. Latgé, A.; Ribeiro-Teixeira, R. M.; Iglesias, J. R., Binding energy of a hydrogen impurity in an f.c.c. lattice. *Solid State Communications* **1984,** *52* (2), 87-91.

49. Khan, M. A.; Parlebas, J. C.; Demangeat, C., Electronic structure and ordering of hydrogen in f.c.c. transition metals. *Journal of The Less-Common Metals* **1981,** *77* (1), P1-P8.

50. Graham, T., On the absorption and dialytic separation of gases by colloid septa. *Journal of the Franklin Institute* **1867,** *83* (1), 39-41.

51. Yukawa, H.; Nambu, T.; Matsumoto, Y.; Watanabe, N.; Zhang, G.; Morinaga, M., Alloy design of Nb-based hydrogen permeable membrane with strong resistance to hydrogen embrittlement. *Materials Transactions* **2008,** *49* (10), 2202-2207.

52. Yukawa, H.; Zhang, G. X.; Watanabe, N.; Morinaga, M.; Nambu, T.; Matsumoto, Y., Hydrogen diffusion coefficient during hydrogen permeation through Nb-based hydrogen permeable membranes. In *Defect and Diffusion Forum*, 2008; Vol. 283-286, pp 225-230.

53. Busnyuk, A. O.; Notkin, M. E.; Grigoriadi, I. P.; Alimov, V. N.; Lifshitz, A. I., Thermal degradation of a palladium coating on hydrogen-tight niobium membranes. *Technical Physics* **2010,** *55* (1), 117-124.

54. Rothenberger, K. S.; Cugini, A. V.; Howard, B. H.; Killmeyer, R. P.; Ciocco, M. V.; Morreale, B. D.; Enick, R. M.; Bustamante, F.; Mardilovich, I. P.; Ma, Y. H., High pressure hydrogen permeance of porous stainless steel coated with a thin palladium film via electroless plating. *Journal of Membrane Science* **2004,** *244* (1-2), 55-68.

55. Bosko, M. L.; Miller, J. B.; Lombardo, E. A.; Gellman, A. J.; Cornaglia, L. M., Surface characterization of Pd-Ag composite membranes after annealing at various temperatures. *Journal of Membrane Science* **2011,** *369* (1-2), 267-276.

56. Gallucci, F.; Fernandez, E.; Corengia, P.; van Sint Annaland, M., Recent advances on membranes and membrane reactors for hydrogen production. *Chemical Engineering Science* **2013,** *92*, 40-66.

57. Wise, M. L. H.; Farr, J. P. G.; Harris, I. R., X-ray studies of the α/β miscibility gaps of some palladium solid solution-hydrogen systems. *Journal of The Less-Common Metals* **1975,** *41* (1), 115-127.

58. O'Brien, C. P.; Howard, B. H.; Miller, J. B.; Morreale, B. D.; Gellman, A. J., Inhibition of hydrogen transport through Pd and Pd47Cu53 membranes by H2S at 350 °C. *Journal of Membrane Science* **2010,** *349* (1-2), 380-384.

59. Ali, J. K.; Newson, E. J.; Rippin, D. W. T., Deactivation and regeneration of PdAg membranes for dehydrogenation reactions. *Journal of Membrane Science* **1994,** *89* (1-2), 171-184.

60. (a) Ackerman, F. J.; Koskinas, G. J., Permeation of hydrogen and deuterium through palladium-silver alloys. *Journal of Chemical and Engineering Data* **1972,** *17* (1), 51-55; (b) Ackerman, F. J.; Koskinas, G. J., A model for predicting the permeation of hydrogen-deuterium-inert gas mixtures through palladium tubes. *Industrial and Engineering Chemistry Fundamentals* **1972,** *11* (3), 332-338; (c) Serra, E.; Kemali, M.; Perujo, A.; Ross, D. K., Hydrogen and deuterium in Pd-25 Pct Ag alloy: Permeation, diffusion, solubilization, and surface reaction. *Metallurgical and Materials Transactions A: Physical Metallurgy and Materials Science* **1998,** *29* (13), 1023-1028.

61. Knapton, A. G., PALLADIUM ALLOYS FOR HYDROGEN DIFFUSION MEMBRANES. *Platinum Metals Review* **1977,** *21* (2), 44-50.

62. Paglieri, S. N.; Way, J. D., Innovations in palladium membrane research. *Separation and Purification Methods* **2002,** *31* (1), 1-169.

63. Karakaya, I.; Thompson, W. T., The Ag-Pd (Silver-Palladium) system. *Bulletin of Alloy Phase Diagrams* **1988,** *9* (3), 237-243.

64. McKinley, D. L., Metal alloy for hydrogen separation and purification. *Union Carbide Corp.* **1967**.

65. McKinley, D. L., Metal alloy for hydrogen separation and purification. *US Patent* **1967,** *3*.

66. Nam, S. E.; Lee, K. H., Hydrogen separation by Pd alloy composite membranes: Introduction of diffusion barrier. *Journal of Membrane Science* **2001,** *192* (1-2), 177-185.

67. Hughes, D. T.; Harris, I. R., A comparative study of hydrogen permeabilities and solubilities in some palladium solid solution alloys. *Journal of The Less-Common Metals* **1978,** *61* (2), P9-P21.

68. Baranowski, B.; Majchrzak, S.; Flanagan, T. B., The volume increase of fcc metals and alloys due to interstitial hydrogen over a wide range of hydrogen contents. *Journal of Physics F: Metal Physics* **1971,** *1* (3), 258-261.

69. Lewis, F. A., The palladium-hydrogen system: Structures near phase transition and critical points. *International Journal of Hydrogen Energy* **1995,** *20* (7), 587-592.

70. Ward, T. L.; Dao, T., Model of hydrogen permeation behavior in palladium membranes. *Journal of Membrane Science* **1999,** *153* (2), 211-231.

71. Wert, C.; Zener, C., Interstitial atomic diffusion coefficients. *Physical Review* **1949,** *76* (8), 1169-1175.

72. Vargas, P.; Miranda, L.; Rodriguez, L.; Lagos, M.; Rogan, J., Quantum diffusion in transition metals. *Journal of The Less-Common Metals* **1991,** *172-174* (PART B), 557-571.

73. Kehr, K. W., Theory of the diffusion of hydrogen in metals. In *Hydrogen in Metals I: Basic Properties*, Alefeld, G.; Völkl, J., Eds. Springer Berlin Heidelberg: Berlin, Heidelberg, 1978; pp 197-226.

74. Fukai, Y.; Sugimoto, H., Diffusion of hydrogen in metals. *Advances in Physics* **1985,** *34* (2), 263-326.

75. Fletcher, S., THIN FILM PALLADIUM – YTTRIUM MEMBRANES FOR HYDROGEN SEPARATION. *PhD Thesis, University of Birmingham* **2010**.

76. Barlag, H.; Opara, L.; Züchner, H., Hydrogen diffusion in palladium based f.c.c. alloys. *Journal of Alloys and Compounds* **2002,** *330-332*, 434-437.
77. Holleck, G. L., Diffusion and solubility of hydrogen in palladium and palladium-silver alloys. *Journal of Physical Chemistry* **1970,** *74* (3), 503-511.

78. (a) Nishimura, C.; Komaki, M.; Hwang, S.; Amano, M., V-Ni alloy membranes for hydrogen purification. *Journal of Alloys and Compounds* **2002,** *330-332*, 902-906; (b) Phair, J. W.; Donelson, R., Developments and design of novel (non-palladium-based) metal membranes for hydrogen separation. *Industrial and Engineering Chemistry Research* **2006,** *45* (16), 5657-5674.

79. (a) Alimov, V. N.; Hatano, Y.; Busnyuk, A. O.; Livshits, D. A.; Notkin, M. E.; Livshits, A. I., Hydrogen permeation through the Pd–Nb–Pd composite membrane: Surface effects and thermal degradation. *International Journal of Hydrogen Energy* **2011,** *36* (13), 7737-7746; (b) Moss, T. S.; Peachey, N. M.; Snow, R. C.; Dye, R. C., Multilayer metal membranes for hydrogen separation. *International Journal of Hydrogen Energy* **1998,** *23* (2), 99-106; (c) Livshits, A. I.; Sube, F.; Solovyev, M. N.; Notkin, M. E.; Bacal, M., Plasma driven superpermeation of hydrogen through group Va metals. *Journal of Applied Physics* **1998,** *84* (5), 2558-2564.

80. Alimov, V. N.; Busnyuk, A. O.; Notkin, M. E.; Livshits, A. I., Pd–V–Pd composite membranes: Hydrogen transport in a wide pressure range and mechanical stability. *Journal of Membrane Science* **2014,** *457*, 103-112.

81. Yukawa, H.; Nambu, T.; Matsumoto, Y., V–W alloy membranes for hydrogen purification. *Journal of Alloys and Compounds* **2011,** *509, Supplement 2*, S881-S884.

82. (a) Adibhatla, A.; Dolan, M. D.; Chien, W. M.; Chandra, D. In *A H2-D2 exchange study on Ni-based binary-ternary amorphous and crystalline membranes for hydrogen separation*, Materials Science and Technology Conference and Exhibition 2013, MS and T 2013, 2013; pp 2146-2153; (b) El Naggar, A. M. A.; Kazak, C., Preparation and characterization of novel nano-structured porous nickel alloy composite induced by electroless deposition and its performance in the hydrogen separation. *Separation and Purification Technology* **2016,** *160*, 73-80; (c) Santucci, A.; Tosti, S.; Basile, A., Alternatives to palladium in membranes for hydrogen separation: Nickel, niobium and vanadium alloys, ceramic supports for metal alloys and porous glass membranes. In *Handbook of Membrane Reactors*, 2013; Vol. 1, pp 183-217.

83. (a) Alimov, V. N.; Busnyuk, A. O.; Notkin, M. E.; Livshits, A. I., Pd-V-Pd composite membranes: Hydrogen transport in a wide pressure range and mechanical stability. *Journal of Membrane Science* **2014,** *457*, 103-112; (b) Dolan, M. D.; Kellam, M. E.; McLennan, K. G.; Liang, D.; Song, G., Hydrogen transport properties of several vanadium-based binary alloys. *International Journal of Hydrogen Energy* **2013,** *38* (23), 9794-9799; (c) Dolan, M. D.; McLennan, K. G.; Chandra, D.; Kochanek, M. A.; Song, G., Suppression of the critical temperature in binary vanadium hydrides. *Journal of Alloys and Compounds* **2014,** *586*, 385-391; (d) Ko, W. S.; Oh, J. Y.; Shim, J. H.; Suh, J. Y.; Yoon, W. Y.; Lee, B. J., Design of sustainable V-based hydrogen separation membranes based on grain boundary segregation. *International Journal of Hydrogen Energy* **2014,** *39* (23), 12031-12044; (e) Shim, J. H.; Ko, W. S.; Kim, K. H.; Lee, H. S.; Lee, Y. S.; Suh, J. Y.; Cho, Y. W.; Lee, B. J., Prediction of hydrogen permeability in V-Al and V-Ni alloys. *Journal of Membrane Science* **2013,** *430*, 234-241; (f) Viano, D. M.; Dolan, M. D.; Weiss, F.; Adibhatla, A., Asymmetric layered vanadium membranes for hydrogen separation. *Journal of Membrane Science* **2015,** *487*, 83-89.

84. Yang, J. Y.; Nishimura, C.; Komaki, M., Preparation and characterization of Pd–Cu/V–15Ni composite membrane for hydrogen permeation. *Journal of Alloys and Compounds* **2007,** *431* (1–2), 180-184.

85. Dolan, M. D.; Song, G.; Liang, D.; Kellam, M. E.; Chandra, D.; Lamb, J. H., Hydrogen transport through V85Ni10M5 alloy membranes. *Journal of Membrane Science* **2011,** *373* (1-2), 14-19.

86. (a) Zhang, Y.; Ozaki, T.; Komaki, M.; Nishimura, C., Hydrogen permeation of Pd-Ag alloy coated V-15Ni composite membrane: Effects of overlayer composition. *Journal of Membrane Science* **2003,** *224* (1-2), 81-91; (b) Zhang, Y.; Ozaki, T.; Komaki, M.; Nishimura, C., Hydrogen permeation characteristics of V-15Ni membrane with Pd/Ag overlayer by sputtering. *Journal of Alloys and Compounds* **2003,** *356-357*, 553-556; (c) Ozaki, T.; Zhang, Y.; Komaki, M.; Nishimura, C., Hydrogen permeation characteristics of V-Ni-Al alloys. *International Journal of Hydrogen Energy* **2003,** *28* (11), 1229-1235.

87. (a) Paglieri, S. N.; Wermer, J. R.; Buxbaum, R. E.; Ciocco, M. V.; Howard, B. H.; Morreale, B. D., Development of membranes for hydrogen separation: Pd coated V-10Pd. *Energy Materials: Materials Science and Engineering for Energy Systems* **2008,** *3* (3), 169-176; (b) Alimov, V. N.; Busnyuk, A. O.; Notkin, M. E.; Peredistov, E. Y.; Livshits, A. I., Substitutional V-Pd alloys for the membranes permeable to hydrogen: Hydrogen solubility at 150-400 °C. *International Journal of Hydrogen Energy* **2014,** *39* (34), 19682-19690; (c) Alimov, V. N.; Busnyuk, A. O.; Notkin, M. E.; Peredistov, E. Y.; Livshits, A. I., Hydrogen transport through V-Pd alloy membranes: Hydrogen solution, permeation and diffusion. *Journal of Membrane Science* **2015,** *481*, 54-62.

88. (a) Hao, S.; Sholl, D. S., Using first-principles calculations to accelerate materials discovery for hydrogen purification membranes by modeling amorphous metals. *Energy and Environmental Science* **2008,** *1* (1), 175-183; (b) Kang, S. G.; Coulter, K. E.; Gade, S. K.; Way, J. D.; Sholl, D. S., Identifying metal alloys with high hydrogen permeability using high throughput theory and experimental testing. *Journal of Physical Chemistry Letters* **2011,** *2* (24), 3040-3044; (c) Kamakoti, P.; Sholl, D. S., Towards first principles-based identification of ternary alloys for hydrogen purification membranes. *Journal of Membrane Science* **2006,** *279* (1-2), 94-99; (d) Semidey-Flecha, L.; Sholl, D. S., Combining density functional theory and cluster expansion methods to predict H2 permeance through Pd-based binary alloy membranes. *Journal of Chemical Physics* **2008,** *128* (14).

89. Ockwig, N. W.; Nenoff, T. M., Membranes for hydrogen separation. *Chemical Reviews* **2007,** *107* (10), 4078-4110.

90. Pauling, L., Location of hydrogen atoms in tetragonal and monoclinic modifications of β1-V2H. *Journal of Solid State Chemistry* **1989,** *79* (1), 63-64.

91. Reilly, J. J.; Wiswall Jr, R. H., The higher hydrides of vanadium and niobium. *Inorganic Chemistry* **1970,** *9* (7), 1678-1682.

92. (a) Duś, R.; Nowicka, E.; Wolfram, Z., Surface phenomena in the process of vanadium hydride formation. *Journal of Alloys and Compounds* **1997,** *253-254*, 496-499; (b) Troev, T.; Markovski, A.; Petrova, M.; Peneva, S.; Yoshiie, T., Positron lifetime calculations of defects in vanadium containing hydrogen. *Nuclear Instruments and Methods in Physics Research, Section B: Beam Interactions with Materials and Atoms* **2006,** *248* (2), 297-304; (c) Golubkov, A. N.; Yukhimchuk, A. A., Synthesis of the dihydride phase of vanadium. *Journal of Alloys and Compounds* **2005,** *404-406* (SPEC. ISS.), 35-37.

93. Schober, T., Vanadium-deuterium: Calorimetry and phase diagram. *Scripta Metallurgica* **1978,** *12* (6), 549-554.

94. Yukawa, H.; Ito, S.; Yamashita, D.; Morinaga, M., Local electronic structures of hydrogen and phase stability of vanadium hydride, V2H. In *Advances in Quantum Chemistry*, 2003; Vol. 42, pp 263-273.

95. Dolan, M. D.; Kochanek, M. A.; Munnings, C. N.; McLennan, K. G.; Viano, D. M., Hydride phase equilibria in V–Ti–Ni alloy membranes. *Journal of Alloys and Compounds* **2015,** *622*, 276-281.

96. (a) Seo, C. Y.; Kim, J. H.; Lee, P. S.; Lee, J. Y., Hydrogen storage properties of vanadium-based b.c.c. solid solution metal hydrides. *Journal of Alloys and Compounds* **2003,** *348* (1-2), 252-257; (b) Cauceglia, D.; Hampton, M. D.; Lomness, J. K.; Slattery, D. K.; Resan, M., Hydrogen uptake characteristics of mechanically alloyed TiVNi. *Journal of Alloys and Compounds* **2006,** *417* (1–2), 159-163; (c) Yukawa, H.; Takagi, M.; Teshima, A.; Morinaga, M., Alloying effects on the stability of vanadium hydrides. *Journal of Alloys and Compounds* **2002,** *330-332*, 105-109.

97. Matumura, T.; Yukawa, H.; Morinaga, M., Alloying effects on the electronic structures of VH2 and V2H. *Journal of Alloys and Compounds* **1999,** *284* (1-2), 82-88.

98. Martin, M.; Gommel, C.; Borkhart, C.; Fromm, E., Absorption and desorption kinetics of hydrogen storage alloys. *Journal of Alloys and Compounds* **1996,** *238* (1-2), 193-201.

99. Evtimova, J.; Drioli, E.; De Luca, G., A density functional theory study of hydrogen occupation in VNiTi alloys used for dense metal membranes. *Journal of Alloys and Compounds* **2016,** *665*, 225-230.

100. Lynch, J. F.; Reilly, J. J.; Millot, F., The absorption of hydrogen by binary vanadium-chromium alloys. *Journal of Physics and Chemistry of Solids* **1978,** *39* (8), 883-890.

101. Dolan, M. D., Non-Pd BCC alloy membranes for industrial hydrogen separation. *Journal of Membrane Science* **2010,** *362* (1–2), 12-28.

102. Edlund, D. J.; McCarthy, J., The relationship between intermetallic diffusion and flux decline in composite-metal membranes: implications for achieving long membrane lifetime. *Journal of Membrane Science* **1995,** *107* (1), 147-153.

103. Zeitschrift für Physikalische Chemie. **1887**.

104. Handbook of Ternary Alloy Phase Diagrams, ASM International, Russell Township. **1995**.

105. (a) Nishimura, C.; Komaki, M.; Amano, M., Hydrogen Permeation Characteristics of Vanadium-Nickel Alloys. *Materials Transactions, JIM* **1991,** *32* (5), 501-507; (b) Dolan, M. D.; McLennan, K. G.; Way, J. D., Diffusion of Atomic Hydrogen through V–Ni Alloy Membranes under Nondilute Conditions. *The Journal of Physical Chemistry C* **2012,** *116* (1), 1512-1518.

106. (a) Mundschau, M. V., Hydrogen separation using dense composite membranes: Part 1 fundamentals. In *Inorganic Membranes for Energy and Environmental Applications*, 2009; pp 125-153; (b) Dolan, M. D.; McLennan, K. G.; Song, G.; Liang, D.; Kellam, M. E., The effect of Ti on hydrogen absorption and diffusivity in V–Ti–Al alloy membranes. *Journal of Membrane Science* **2013,** *446*, 405-409; (c) Dolan, M. D.; Song, G.; McLennan, K. G.; Kellam, M. E.; Liang, D., The effect of Ti on the microstructure, hydrogen absorption and diffusivity of V–Ni alloy membranes. *Journal of Membrane Science* **2012,** *415–416*, 320-327.

107. (a) Jiang, P.; Yu, Y.; Song, G.; Liang, D.; Kellam, M.; Dolan, M., Effect of heat treatment on microstructure, hardness and rollability of V55Ti30Ni15 alloy membranes. *Materials & Design* **2014,** *63*, 136-141; (b) Song, G.; Dolan, M. D.; Kellam, M. E.; Liang, D.; Zambelli, S., V–Ni–Ti multi-phase alloy membranes for hydrogen purification. *Journal of Alloys and Compounds* **2011,** *509* (38), 9322-9328.

108. Hashi, K.; Ishikawa, K.; Matsuda, T.; Aoki, K., Hydrogen permeation characteristics of (V, Ta)–Ti–Ni alloys. *Journal of Alloys and Compounds* **2005,** *404–406*, 273-278.

109. Adams, T. M.; Mickalonis, J., Hydrogen permeability of multiphase V–Ti–Ni metallic membranes. *Materials Letters* **2007,** *61* (3), 817-820.

110. (a) Watanabe, K.; Saito, Y.; Fukai, Y., International Symposium on the Properties and Applications of Metal Hydrides Effects of substitutional impurities on the phase diagrams of V-H and V-D systems. *Journal of the Less Common Metals* **1982,** *88* (1), 43-47; (b) Griffiths, R.; Pryde, J. A.; Righini-Brand, A., Phase diagram and thermodynamic data for the hydrogen/vanadium system. *Journal of the Chemical Society, Faraday Transactions 1: Physical Chemistry in Condensed Phases* **1972,** *68* (0), 2344-2349.

111. Jung, J.-H.; Lee, H.-H.; Yu, J.-S.; Jang, K.-J.; Lee, J.-Y., Self-discharge mechanism of vanadium-titanium metal hydride electrodesfor Ni-MH rechargeable battery. *Metals and Materials* **1997,** *3* (3), 178-182.

112. San-Martin, A.; Manchester, F. D., The H−Ti (Hydrogen-Titanium) system. *Bulletin of Alloy Phase Diagrams* **1987,** *8* (1), 30-42.

113. Jiang, P.; Yu, Y.; Song, G.; Liang, D.; Kellam, M.; Dolan, M., Effect of heat treatment on microstructure, hardness and rollability of V55Ti30Ni15 alloy membranes. *Materials and Design* **2014,** *63*, 136-141.

114. Song, G.; Dolan, M. D.; Kellam, M. E.; Liang, D.; Zambelli, S., V-Ni-Ti multi-phase alloy membranes for hydrogen purification. *Journal of Alloys and Compounds* **2011,** *509* (38), 9322-9328.

115. Adams, T. M.; Mickalonis, J., Hydrogen permeability of multiphase V-Ti-Ni metallic membranes. *Materials Letters* **2007,** *61* (3), 817-820.

116. (a) Al-Mufachi, N. A.; Nayebossadri, S.; Speight, J. D.; Bujalski, W.; Steinberger-Wilckens, R.; Book, D., Effects of thin film Pd deposition on the hydrogen permeability of Pd<inf>60</inf>Cu<inf>40</inf> wt% alloy membranes. *Journal of Membrane Science* **2015,** *493*, 580-588; (b) Fernandez, E.; Medrano, J. A.; Melendez, J.; Parco, M.; Viviente, J. L.; van Sint Annaland, M.; Gallucci, F.; Pacheco Tanaka, D. A., Preparation and characterization of metallic supported thin Pd-Ag membranes for hydrogen separation. *Chemical Engineering Journal* **2015**; (c) Haydn, M.; Ortner, K.; Franco, T.; Schafbauer, W.; Behrens, A.; Dittmar, B.; Hummel, S.; Sulik, M.; Rüttinger, M.; Venskutonis, A.; Sigl, L. S., Metal-supported palladium membranes for hydrogen separation. *Powder Metallurgy* **2015,** *58* (4), 250-253; (d) Hemra, K.; Atong, D., Characteristic of

thin palladium membrane on Al<inf>2</inf>O<inf>3</inf> and YSZ supports for hydrogen separation prepared by electroless plating technique. *Research Journal of Chemistry and Environment* **2014,** *18* (7), 28-32; (e) Lee, T. H.; Park, C. Y.; Lee, G.; Dorris, S. E.; Balu Balachandran, U., Hydrogen transport properties of palladium film prepared by colloidal spray deposition. *Journal of Membrane Science* **2012,** *415-416*, 199-204; (f) Medrano, J. A.; Fernandez, E.; Melendez, J.; Parco, M.; Tanaka, D. A. P.; van Sint Annaland, M.; Gallucci, F., Pd-based metallic supported membranes: High-temperature stability and fluidized bed reactor testing. *International Journal of Hydrogen Energy* **2015**; (g) Pereira, A. I.; Pérez, P.; Rodrigues, S. C.; Mendes, A.; Madeira, L. M.; Tavares, C. J., Deposition of Pd-Ag thin film membranes on ceramic supports for hydrogen purification/separation. *Materials Research Bulletin* **2015,** *61*, 528-533.

117. (a) Roa, F.; Douglas Way, J.; McCormick, R. L.; Paglieri, S. N., Preparation and characterization of Pd-Cu composite membranes for hydrogen separation. *Chemical Engineering Journal* **2003,** *93* (1), 11-22; (b) Sun, G. B.; Hidajat, K.; Kawi, S., Ultra thin Pd membrane on α-Al2O3 hollow fiber by electroless plating: High permeance and selectivity. *Journal of Membrane Science* **2006,** *284* (1-2), 110-119.

118. Pan, X. L.; Xiong, G. X.; Sheng, S. S.; Stroh, N.; Brunner, H., Thin dense Pd membranes supported on α-Al2O3 hollow fibers. *Chemical Communications* **2001,** (24), 2536-2537.

119. (a) Gao, H.; Lin, J. Y. S.; Li, Y.; Zhang, B., Electroless plating synthesis, characterization and permeation properties of Pd-Cu membranes supported on ZrO2 modified porous stainless steel. *Journal of Membrane Science* **2005,** *265* (1-2), 142-152; (b) Nam, S. E.; Lee, K. H., Preparation and characterization of palladium alloy composite membranes with a diffusion barrier for hydrogen separation. *Industrial and Engineering Chemistry Research* **2005,** *44* (1), 100-105.

120. Okazaki, J.; Ikeda, T.; Pacheco Tanaka, D. A.; Llosa Tanco, M. A.; Wakui, Y.; Sato, K.; Mizukami, F.; Suzuki, T. M., Importance of the support material in thin palladium composite membranes for steady hydrogen permeation at elevated temperatures. *Physical Chemistry Chemical Physics* **2009,** *11* (38), 8632-8638.

121. Anderson, D. H.; Evenson Iv, C. R.; Harkins, T. H.; Jack, D. S.; Mackay, R.; Mundschau, M. V., Hydrogen separation using dense composite membranes part 2: Process integration and scale-up for H2 production and CO2 sequestration. In *Inorganic Membranes for Energy and Environmental Applications*, 2009; pp 155-171.

122. Pinacci, P.; Basile, A., Palladium-based composite membranes for hydrogen separation in membrane reactors. In *Handbook of Membrane Reactors*, 2013; Vol. 1, pp 149-182.

3. Thin films deposition techniques

3.1. Introduction

The deposition of membranes with a thickness below 5 μm is required to meet the US Department of Energy flux targets[1], but such membranes have to be supported by adequate porous substrates. The most common layout is a thin metal layer deposited onto a porous stainless steel or a porous ceramic, mainly alumina. Porous substrates often requires the use of intermediate layers with a finer pore size (graded porosity substrates), in order to deposit a defect-free thin membrane[2] and to reduce the whole thickness of the hydrogen selective layer.

Selectivity (the hydrogen/gas leakage detector permeability ratio) is usually used to quantify the quality of the deposited metal layer. A defect-free membrane has infinite selectivity, as only hydrogen can permeate the metal layer. Macroscopic defects have the greatest effect on selectivity and even a low defects density will greatly reduce the ideal selectivity of the membrane[3,4]. Ma et al.[5] suggested that, in order to deposit a defect-free membrane, the minimum thickness required is approximately 3 times the maximum surface pore size. Studies on porous nickel[6] and porous stainless steel[7] substrates supported this general rule. Undoubtedly, the quality of a thin membrane is predominantly determined by the underlying substrate surface onto which it is deposited.

3.2. Thin films preparation

The most common processes in membrane technology for thin film deposition are electroless plating and sputtering.

3.2.1. Electroless Plating

Electroless plating is the main technique for thin membrane production, since it can prepare thin membranes of a wide range of thicknesses (from 1 μm[8] to tens of μm[7]) onto substrates with complex geometries. Electroless plating is an autocatalytic reaction, involving three

stages: surface cleaning, surface activation and film deposition. Surface cleaning consists of washing the substrate in dilute acid, alcohol or acetone and rinsing it with deionised water. After cleaning, the substrate surface must be activated. In case of a palladium deposition, tin chloride is used as sensitising agent and small clusters of metal are deposited onto the surface (substrate seeding) by activation baths[9]. These clusters act as catalysts for the plating reaction, which employs a palladium-amine complex stabilised by a sequestering agent such as Na_2EDTA. Controlled deposition of palladium is achieved via chemical reduction of Pd ions using a suitable reducing agent[9a, 10], according to the reaction:

$$2Pd(NH_3)_4^{2+} + N_2H_4 + 4OH^- \rightarrow 2Pd + N_2 + 8NH_3 + 4H_2O$$

Although electroless deposition is a well-established technique, there are several limitations:

- Films often possess significantly lower densities than the equivalent bulk material, due to voids and impurities[11];
- The deposition rate, film structure and morphology strongly depend on some variables. In general, high plating temperatures produce small closely packed crystallites. Films have a denser structure with a smaller grain size, with fewer defects and therefore greater selectivity. However, if the deposition rate is too high, voids may be formed within the film, introducing defects and reducing the selectivity[12].

Using a porous substrate as deposition substrate, the non-uniform film thickness is the most common observed drawback, making the reproducibility of the desired thickness extremely difficult. When the thickness is uncertain, hydrogen flux is often presented as permeance rather than permeability[7-8, 13]. However, one of the main drawbacks of the electroless plating technique is the difficulty on metal alloys deposition[10b, 14]. Shu et al.[14a] found that silver deposits preferentially and inhibits palladium deposition, unless the amount of palladium in the plating bath is high (> 80% Pd). A possible solution could be the sequential deposition of distinct layers followed by an appropriate annealing treatment[15, 16], but temperatures as high as 800°C have been required for effective homogenisation[15c].

3.2.2. Sputtering

In the sputtering process, a thin film is deposited onto the substrate surface when ions (produced by ionization of an inert gas, typically Argon) bombard a metal target, dislodging metal atoms from its surface. Both conducting and non-conducting substrates can be used. Xomeritakis and Lin[4b] deposited Pd-Ag membranes (100 – 500 nm) using a single Pd-Ag25 target. McCool[4a] found that using an alloy target is necessary to wait the "equilibration time[3,18]", in order to sputter the alloy components at the same ratio as the target composition. Moreover, McCool[4a] stated that the most important variables are target equilibration time and deposition power; Hoang et al.[21] investigated substrate temperature, since it has strong effects on phase microstructure and grain size of the film. Membrane can be also prepared from pure targets (co-sputtering)[19,17,20].

Sputtering has several advantages[22]:

- Deposition of ultrathin films with minimal impurity;
- Easily controllable process parameters;
- Flexibility for synthesizing alloys[4a, 17];
- Ability to generate nanostructured films[23];
- Excellent film uniformity, particularly over large areas;
- Surface smoothness, thickness control and good film/substrate adhesion.

In addition, membranes do not always require a post-deposition thermal treatment.

Thin membranes for hydrogen purification were found to be very sensitive to the substrate pore size and surface roughness[4c,25]. Jayaraman et al.[4c] found that, to deposit Pd-Ag thin membranes onto porous alumina, an optimum coating temperature is 400°C, which gave them the best gas-tightness performance.

One of the main drawbacks of sputtering deposition is the typical columnar growth of the film: if the columnar microstructure is not compact the thin film loses the required selectivity. Pereira et al.[24] found that the use of low working pressures and heating to 200°C control the columnar growth and enhance the membrane selectivity.

Since sputtering process is the technique used in the thesis, the following sections are dedicated to a more rigorous description of the traditional sputtering process; moreover, the HiPIMS technique (High Power Impulse Magnetron Sputtering), will be introduced, a tech-

nique employed in this thesis for the first time to prepare membranes for hydrogen separation.

3.3. The sputter deposition

Sputter deposition[3,26] is a physical vapour deposition (PVD) process involving the removal of atoms from solid targets by bombarding them with positive and energetic ions (Fig. 3.1), generated by ionization of an inert gas (generally Ar). Sputtering has a mechanical nature, so refractory materials can be easily deposited at temperatures well below their melting point. The sputtering yield, Y, defined as the ratio of number of ejected particles to the number of bombarding ions, is influenced by the energy and incident angle of bombarding ions and by the crystal structure and chemical composition of the target materials. Depending on the kinetic energy E_k of the incident ions, four different regimes can be found[27]:

1. Low energy regime ($0 < E_k < 20\text{-}50$ eV): the incident ion has not sufficient energy to eject a target atom;
2. Moderate energy regime (50 eV $< E_k <$ 1000 eV): this is the typical energy range of PVD techniques;
3. High energy regime (1 keV $< E_k <$ 50 keV): the incident particles has enough energy to break the bonds between atoms in a region close to the impact site thus causing the formation of a dense cascade of secondary particles;
4. Very high energy regime ($E_k >$ 50 keV): the incident ion penetrates into the target material (ion implantation), with the emission of very few atoms.

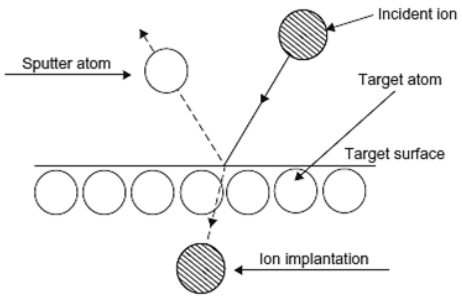

Fig. 3.1: sputter deposition process[28].

3.3.1. DC diode sputtering

In a diode plasma system (Fig. 3.2), the cathode is the source of the sputtered atoms, while the substrate is placed over the anode. It is characterized by a flux of ions that strikes the cathode and by a flux of electrons that move toward the anode. The working gas pressure values are between 1 and 100 Pa. An advantage of the diode sputtering is the efficient use of the target material, since the electric field between the electrodes is quite uniform, so the ion flux is nearly constant over the target. One of the main drawbacks of DC diode plasma is the low ion currents to the cathode, due to the low cross section for electron-gas particle ionization collisions. Another problem occurs when a reactive gas (oxygen in particular) is added to the gas mixture: the cathode becomes rapidly oxidized and the net DC current drops. In diode sputter sources the bombardment of energetic electrons causes a significant increase of substrate temperature. In order to enhance the ionization of gas, the triode source was developed: it consists of a heated filament added to a diode source, to provide electrons to sustain glow discharge. The discharge is able to operate at lower pressures and lower targets voltage. Higher deposition rates (several thousand Å per minute) can be achieved with planar diodes.

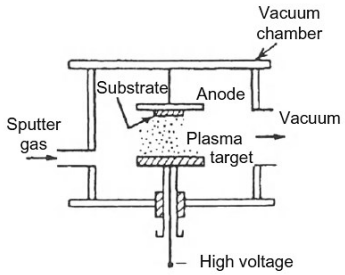

Fig. 3.2: DC diode sputtering system[28].

3.3.2. Radio frequency (RF) sputtering

The RF sputtering system is similar to the DC diode system (Fig. 3.3), except for the addition of an impedance matching network (matchbox) between power supply and electrodes. The matchbox optimises the impedance of the plasma, maximizes the amount of power that can be delivered to the plasma and matches the net impedance of the plasma side of the circuit to the load capacitor. The RF powered electrode oscillates between positive and negative.

Thanks to the higher mobility of the electrons it picks up a much greater electron current than ion current in one cycle and, consequently, the electrode accumulates a negative charge. A capacitor placed in the impedance network blocks this DC potential from the power supply. On each successive RF cycle the electrode is charging more negatively: the ion collection time in each cycle will consequently increase while the electron collection time decreases. After several cycle a negative DC potential sets up on the electrode at a value that is approximately close to one half of the applied RF peak to peak voltage. Only for a very short time of each RF cycle the electrode is positive and collects electron, while for the rest of the cycle it is negative and collects ions: since there is no net current flow there is no charging at the insulating surface of the target. The RF power increases the ion current and the deposition rates compared to the DC case: the rapid change of the voltage polarity traps the electrons (both plasma and secondary electrons) within the plasma, enhancing the ionization rates and the plasma density.

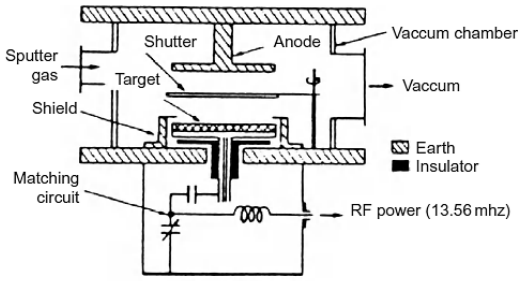

Fig. 3.3: RF diode sputtering system[28].

3.3.3. Magnetron sputtering

In the magnetron sputtering system a magnetic field (from 50 to 500 Gauss) helps in increasing the deposition rate[29], operating at low pressures (10^{-2} Pa order) and low voltages (e.g. 350 V). The current density has the highest value where the magnetic field lines are tangent to the surface of the cathode, but this causes a not uniform erosion of the target (only 20-30% of the cathode material is used), because the ion bombardment is localized directly under the **E** x **B** closed path. The magnetic field does not directly affect the ion motion; however, because of electrostatic attraction, the ions move with the electrons, keeping the plasma neutral. Substrate bombardment can be significantly increased with the unbalanced

magnetron configuration, in which the flux from the north pole is unequal to that entering the south pole. There are two types of unbalanced magnetron configuration[30]:

- Type I: the flux from the central magnet is larger than that of the outer magnet. It gives low ion and electron currents at the substrate and low self-bias voltages;
- Type II: the central flux is less than the outer flux. It gives large ion currents (3 to 10 mA/cm^2[2,30]) and large electron currents (about 100 times larger than the case of type I sources) to the substrate, and high self-bias voltages (20 - 30 V).

The most common magnetron configuration has the target material backed by a permanent magnet, providing a magnetic field with field lines forming a close tunnel on the target surface (Fig. 3.4). The electric field is normal to the surface of the target and in combination with the magnetic field traps the secondary electrons in the region close to the cathode, increasing the number of collisions between the electrons with the gas atoms. The ions experience the same force as the electrons but, due to the much higher mass, their motion is not confined and the sputter bombardment proceeds as in a normal diode. Typical magnetron characteristics are:

- Cathode current density: 20 mA/cm^2;
- Discharge voltage: from 250 to 800 V;
- Minimum pressure: $1.33 \cdot 10^{-1}$ Pa;
- Target to substrate distance: from few cm to 20 cm;
- Deposition rates: several thousand Å/min with metals; 100-2000 Å/min with dielectrics.

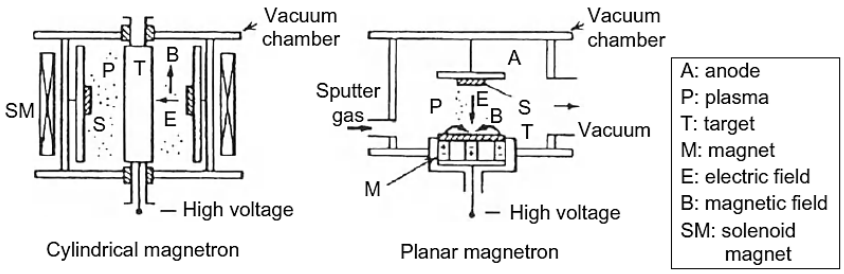

Fig. 3.4: cylindrical and planar magnetron sputtering configurations[28].

3.3.4. Bias sputtering

In bias sputtering the electric field near the substrate is altered, in order to vary the flux and energy of the incident charged particles. This is achieved by applying either a negative DC or RF bias to the substrate holder. Bias voltages from -50 to -300 V are generally used. The bias sputtering is useful to change many properties of the growing films: hardness, residual stresses, morphology (from columnar microstructure to compact fine-grained structure) and adhesion[27].

3.4. Film structure

In sputtering operation, pressure is a key parameter since it influences the atoms transport to the substrate, the mobility of adatoms and so the film microstructure. It usually ranges from 10 mPa to 10 Pa. At low pressure (10 mPa or less), the sputtered atoms reach the substrate after very few or no collisions, maintaining their original kinetic energy. Films deposited in this regime are generally small-grained, dense, with a good adhesion to the substrate and have compressive stress. At larger pressure, atoms lose their kinetic energy in collisions with the gas atoms and thermalize before reaching the substrate. The resulting films show larger grain size, lower defects density, worst adhesion to the substrate and a tensile character. Another important parameter is the deposition temperature. In order to find possible correspondences between the microstructure of metallic thin films and the parameters affecting the mobility of adatoms (pressure and temperature), structure zone diagrams (SZD) have been developed. They are a convenient way of illustrating common features of relatively thick (>100 nm) polycrystalline films, by reducing several deposition parameters to as few as possible. They are not models, but representations of expected film microstructure trends versus deposition parameters. They were first introduced by Movchan and Demchishin[31] in 1969. In their SZD the only reduced parameter was the homologous temperature, T_h, defined as the film growth temperature (substrate temperature) normalized by the melting temperature of the deposited material. With the introduction of magnetron sputtering, the SZD were modified to accommodate the process pressure. Thornton divided the microstructure of sputtered films in four zones[32] (Fig. 3.5):

- Zone 1 structure, consisting of tapered columns and significant voids between columns. It is prevalent when T_h is less than 0.3. The adatom mobility is negligible and most of the sputtered flux is deposited on the high points of the film. Zone 1 structures are associated with rough surfaces, poor stability and properties that are far from those of the bulk material[33].
- Zone 2 structure, usually found in the range $0.3 < T_h < 0.5$. It is associated with significant adatom mobility on grain surfaces. Zone 2 structures show columnar, platelet or whisker grains separated by dense intercrystalline boundaries.
- Zone 3 structure, occurring at relative high temperatures ($T_h > 0.5$), when diffusion within the grains is a significant mechanism of film growth. Zone 3 is associated with equiaxied grains and epitaxial growth on the substrate.
- Zone T (transition) structure, results from bombardment-induced surface mobility. Films expected to be Zone 1 structures according to T_h, can be grown with a very smooth surface and high density by bombarding the growing film with energetic ions or neutrals during film growth[32b, 34]. The latter species originate from the target as positive ions neutralized and reflected from the target surface[35], or as sputtered negative ions that are accelerated and then neutralized in the gas[36]. Film material is moved into the spaces between grains by forward sputtering[32a, 37] and by energy deposited locally by the bombarding particles, leading to tightly packed fibrous grains.

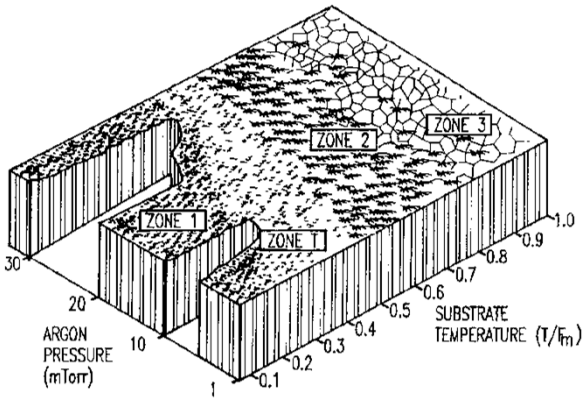

Fig. 3.5: Thornton model of thin films.

Surface mobility and, consequently, Zone T structures, can be promoted by control of positive ions bombardment[38]. The ion energies can be increased by applying a negative bias to

the substrate and bombardment effects can be also influenced by the pressure, angle of incidence, magnetic field configuration, discharge current and working gas species[39].

In order to develop a more universal SZD, one possible solution is to modify the Thornton model generalizing its meaning. The changes[40] proposed are (Fig. 3.6):

- Replacement of the T_h axis with a generalized temperature T*, with contributes from the homologous temperature and a temperature shift caused by the potential energy of particles impinging onto the surface;
- Replacement of the linear pressure axis with a logarithmic axis for a normalized energy E*, describing displacement and heating effect caused by the kinetic energy of bombarding particles;
- Introduction of a z-axis with a net film thickness t*, in order to keep the familiar qualitative illustration of film structure while indicating thickness reduction by densification and sputtering.

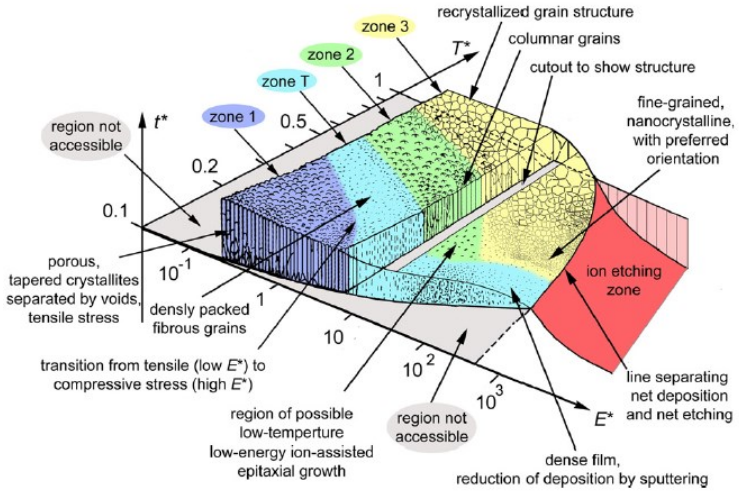

Fig. 3.6: structure zone diagram applicable to energetic deposition (from [40]).

3.5. HiPIMS (High Power Impulse Magnetron Sputtering)

In the common magnetron sputtering, the degree of ionization of the plasma particles is relatively low[41] and the ionized sputtered species are typically less than 1%[41,42]. Their increase has been the goal of many research works during the recent decades, because a high fraction of ionized sputtered species improves the film density, the surface (smoother) and

the adhesion, decreasing the substrate temperature and reducing the defects density. Layers produced with HiPIMS show superior properties compared to standard magnetron sputter deposited layers (Fig. 3.7). Several approaches, such as inductively coupled plasma superimposed on a magnetron plasma[43], hollow cathode magnetron[43] and an external ion source[44] have been proposed in the past decades, until Bugaev[45] and Fetisov[46] demonstrated, in the mid-90s, that a conventional sputtering source in a pulse mode (pulse duration ranging from 1 µs to 1 s, Fig. 3.8) allowed pulsed target currents two orders of magnitude higher than the average target currents in a conventional sputtering technique[45,46] with formation of ultra-dense plasmas (electron densities in the order of 10^{18} m^{-3} [45,46], much higher than the values of 10^{14}-10^{16} m^{-3} for DC magnetron sputtering). The consequence is a much higher ionization of the sputtered species, typically more than 50%.

The peak power is typically of the order of $kWcm^{-2}$. The pulse is then repeated with such a frequency that the average power is kept low. A common way to define the strength of the pulse is the pulse energy (a typical value of the pulse energy is 50 mJ cm^{-2}). Some power supplies also have the possibility to detect and suppress a transition to an arc discharge: by measuring the voltage or the current on the output, they open the switch and stop the discharge if it deviates too much from the normal operation.

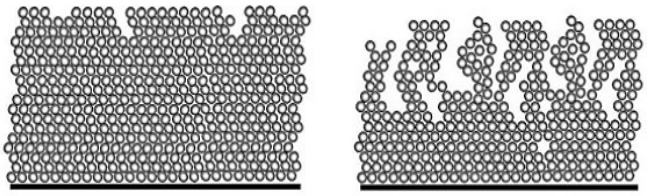

Fig. 3.7: comparison between film growth in HiPIMS (left) and magnetron sputtering (right) (from [47]).

HiPIMS power supplies consist of three different modules[49]:

- A continuous DC power supply, providing continuous power to charge the storage unit with a charging voltage of several hundreds of V up to several kV.
- A storage and pulse unit, which holds back the stored energy and delivers it in short HiPIMS pulses of defined width (from 5 to 3000 µs) and frequency (from 10 Hz to 10 kHz). The peak target current density may reach values of up to several A/cm^2, which are up to 3 order of magnitude higher than the current densities in DC magnetron sputtering[43];

- A pulse shaping (matching) unit, shaping the output current pulse in order to match the requirements of the different cathodes. It is used also to eliminate any plasma oscillations.

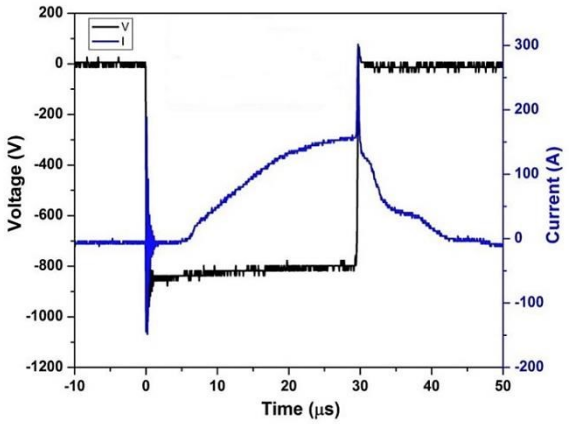

Fig. 3.8: a typical voltage-current plot on a HiPIMS discharge (adapted from [48]).

In the principal setup, the target of the magnetron is connected to the high, negative voltage pulse output, which ignites the plasma, accelerating the Ar^+ ions towards the target. An additional negative bias voltage can be supplied, to accelerate the sputtered ions towards the substrate and to deposit in complex geometries. To get high ionization levels in the plasma, we need long pulses of 100 μs or longer and a current of 1 A/cm^2 or higher.

HIPIMS is currently taking the first steps towards industrial applications. The unique features of the discharge should be well suited for a number of application areas:

- **Densification and smoothening of metallic and compound films:** the high fraction of ionized sputtered material has been used to tailor and improve the properties of the growing films, both metals and ceramics[50,51,52,53], especially in the field of hard coatings;
- **Deposition onto complex shaped substrates:** deposition on complex-shaped substrates (cutting inserts, drills, …) is of high importance in many high tech applications[50].
- **Phase tailoring:** an important example concerns Ta. Tantalum in its bulk form has a bcc-structure, but as a thin film it has almost always a tetragonal structure (β-structure). By using the highly ionized sputtered material present in HiPIMS, it was possi-

ble to obtain a deposition window for the β-Ta on Si (with native oxide present)[54]. This phenomenon is largely attributed to the fact that a large fraction of the bombarding species consists of ions of the film material itself, which ensures an efficient momentum transfer from the plasma ions to the film surface.

- **Electrical and optical properties modification by HiPIMS:** the effect of HiPIMS on the electrical properties of thin metallic films was investigated in a number of works[51,54]. Sarakinos et al.[51] reported that the electrical resistivity of ultra-thin Ag films was determined by the film density and the topographic characteristics of the film surface. Davis et al.[55] studied the growth and the properties of TiO_2 films deposited by HiPIMS and DCMS from a metallic Ti target. Glocker et al.[56] deposited ZrO_2 and Ta_2O_5 films both by HiPIMS and mid-frequency pulsed magnetron sputtering (MFPMS).
- **Adhesion enhancement:** in order to optimize conditions for a good adhesion, cleaning of the substrate surface (by ion etching) prior to the deposition is a common practice. However, this is in many cases inefficient, due to the incorporation of a high concentration of Ar gas in the interface. HiPIMS plasma contains a mixture of single and double-charged metal and Ar ions[57] and it was used to pre-treat the surface of stainless substrates using different ion energies and pre-treatment durations[58,59].

There are two main drawbacks with HiPIMS: reduction of deposition rate and arc discharge. The deposition rate for the HIPIMS discharge is expected to be in the range 30-80% compared to a conventional magnetron discharge with the same average power[45,60,61]. One explanation for the reduction in deposition rate is that some of the material that is ionized is attracted back to the cathode and that ions can sputter also the coating during depositions. The other problem with HIPIMS is the tendency to form arcs on the cathode surface. There are mainly two types of arcs, heavy arcs and light arcs. The light arc (a little spark on the target surface) is minor problem, since it does not produce large number of microdroplets, as the heavy arc does. The heavy arc can be a serious problem and they can sometimes be observed as extended plasma columns going from the cathode into the bulk plasma. The arc locally heats the target, ejecting microdroplets. Materials with relatively high melting point, such as Ti, Ta, and Cr has a very low tendency to arc, while materials with relatively low melting point, like Cu and Al, have a higher tendency to arc. Choosing a modest power level

or a shorter pulse length can reduce the arcing frequency. Even arc suppressors[62] can be used to reduce arcing problems.

Table 3.1 reports the main differences between HiPIMS and DC magnetron sputtering:

Parameter	HIPIMS	DC Magnetron
Working Pressure	0.001 – 0.1 mbar	0.001 – 0.1 mbar
Cathode Current Density	$J_{MAX} \leq 10$ A/cm^2	$J_{MAX} \leq 0.1$ A/cm^2
Discharge Voltage	0.5 – 1.5 kV	0.3 – 0.6 kV
Plasma Density	$\leq 10^{13}$ cm^{-3}	$\leq 10^{11}$ cm^{-3}
Cathode Power Density	1 – 3 kW/cm^2	< 0.1 kW/cm^2
Ionization Fraction	30% – 90%	< 1%

Tab. 3.1: main differences between HiPIMS and DC magnetron sputtering [48].

The typical applications of HiPIMS is in the deposition of hard coatings on metals, e.g. for cutting tools, by exploiting the important advantages of good coating adhesion and high density. Very few works have been published so far on the use of HiPIMS on non-conducting and porous substrates and no papers were published on the study of this technique for the deposition of gas selective membranes. The unique work were HiPIMS is used to prepare a selective layer is the work of Ortiz-Medina et al.[63], who used HiPIMS to prepare ultrathin, flexible and highly water permeable nanostructure carbon - based membranes on porous polymer substrates in order to fabricate carbon-based membranes for water desalination.

References

1. Dolan, M. D., Non-Pd BCC alloy membranes for industrial hydrogen separation. *Journal of Membrane Science* **2010,** *362* (1-2), 12-28.

2. Tong, J.; Matsumura, Y.; Suda, H.; Haraya, K., Thin and dense Pd/CeO2/MPSS composite membrane for hydrogen separation and steam reforming of methane. *Separation and Purification Technology* **2005,** *46* (1-2), 1-10.

3. Jayaraman, V.; Lin, Y. S., Synthesis and hydrogen permeation properties of ultrathin palladium-silver alloy membranes. *Journal of Membrane Science* **1995,** *104* (3), 251-262.

4. (a) McCool, B.; Xomeritakis, G.; Lin, Y. S., Composition control and hydrogen permeation characteristics of sputter deposited palladium-silver membranes. *Journal of Membrane Science* **1999,** *161* (1-2), 67-76; (b) Xomeritakis, G.; Lin, Y. S., Fabrication of thin metallic membranes by MOCVD and sputtering. *Journal of Membrane Science* **1997,** *133* (2), 217-230; (c) Jayaraman, V.; Lin, Y. S.; Pakala, M.; Lin, R. Y., Fabrication of ultrathin metallic membranes on ceramic supports by sputter deposition. *Journal of Membrane Science* **1995,** *99* (1), 89-100; (d) Zhao, H. B.; Xiong, G. X.; Baron, G. V., Preparation and characterization of palladium-based composite membranes by electroless plating and magnetron sputtering. *Catalysis Today* **2000,** *56* (1-3), 89-96.

5. Ma, Y. H.; Mardilovich, I. P.; Mardilovich, P. P., Effects of the porosity and pore size distribution of the porous stainless steel on the thickness and hydrogen flux of palladium membranes. *American Chemical Society, Division of Petroleum Chemistry, Preprints* **2001,** *46* (2), 154-156.

6. (a) Ryi, S. K.; Park, J. S.; Kim, S. H.; Hong, S. C.; Kim, D. W., Development of porous nickel membrane made by uniaxial pressing for hydrogen separation. *Desalination* **2006,** *200* (1-3), 213-215; (b) Ryi, S. K.; Park, J. S.; Kim, S. H.; Hong, S. C.; Kim, D. W., The study of a new porous nickel support for palladium-based alloy membrane. *Desalination* **2006,** *200* (1-3), 216-218.

7. Mardilovich, I. P.; Engwall, E.; Ma, Y. H., Dependence of hydrogen flux on the pore size and plating surface topology of asymmetric Pd-porous stainless steel membranes. *Desalination* **2002,** *144* (1-3), 85-89.

8. Keuler, J. N.; Lorenzen, L.; Miachon, S., Preparing and testing Pd films of thickness 1-2 micrometer with high selectivity and high hydrogen permeance. *Separation Science and Technology* **2002,** *37* (2), 379-401.

9. (a) Sun, G. B.; Hidajat, K.; Kawi, S., Ultra thin Pd membrane on α-Al2O3 hollow fiber by electroless plating: High permeance and selectivity. *Journal of Membrane Science* **2006,** *284* (1-2), 110-119; (b) Keuler, J. N.; Lorenzen, L.; Sanderson, R. N.; Linkov, V., Optimizing Palladium Conversion in Electroless Palladium Plating of Alumina Membranes. *Plating and Surface Finishing* **1997,** *84* (8), 34-40.

10. (a) Shi, Z.; Wu, S.; Szpunar, J. A.; Roshd, M., An observation of palladium membrane formation on a porous stainless steel substrate by electroless deposition. *Journal of Membrane Science* **2006,** *280* (1-2), 705-711; (b) Huang, T. C.; Wei, M. C.; Chen, H. I., Preparation of hydrogen-permselective palladium-silver alloy composite membranes by electroless co-deposition. *Separation and Purification Technology* **2003,** *32* (1-3), 239-245.

11. Roa, F.; Way, J. D., The effect of air exposure on palladium-copper composite membranes. *Applied Surface Science* **2005,** *240* (1-4), 85-104.

12. Honma, H.; Kanemitsu, K., ELECTROLESS NICKEL PLATING ON ALUMINA CERAMICS. *Plating and Surface Finishing* **1987,** *74* (9), 62-67.

13. Tong, J.; Shirai, R.; Kashima, Y.; Matsumura, Y., Preparation of a pinhole-free Pd-Ag membrane on a porous metal support for pure hydrogen separation. *Journal of Membrane Science* **2005,** *260* (1-2), 84-89.

14. (a) Shu, J.; Grandjean, B. P. A.; Ghali, E.; Kaliaguine, S., Simultaneous deposition of Pd and Ag on porous stainless steel by electroless plating. *Journal of Membrane Science* **1993,** *77* (2-3), 181-195; (b) Okazaki, J.; Tanaka, D. A. P.; Tanco, M. A. L.; Wakui, Y.; Mizukami, F.; Suzuki, T. M., Hydrogen permeability study of the thin Pd-Ag alloy membranes in the temperature range across the α-β phase transition. *Journal of Membrane Science* **2006,** *282* (1-2), 370-374.

15. (a) Keuler, J. N.; Lorenzen, L., Developing a heating procedure to optimise hydrogen permeance through Pd-Ag membranes of thickness less than 2.2 µm. *Journal of Membrane Science* **2002,** *195* (2), 203-213; (b) Bosko, M. L.; Yepes, D.; Irusta, S.; Eloy, P.; Ruiz, P.; Lombardo, E. A.; Cornaglia, L. M., Characterization of Pd-Ag membranes after exposure to hydrogen flux at high temperatures. *Journal of Membrane Science* **2007,** *306* (1-2), 56-65; (c) Uemiya, S.; Matsuda, T.; Kikuchi, E., Hydrogen permeable palladium-silver alloy membrane supported on porous ceramics. *Journal of Membrane Science* **1991,** *56* (3), 315-325; (d) Yepes, D.; Cornaglia, L. M.; Irusta, S.; Lombardo, E. A., Different oxides used as diffusion barriers in composite hydrogen permeable membranes. *Journal of Membrane Science* **2006,** *274* (1-2), 92-101; (e) Thoen, P. M.; Roa, F.; Way, J. D., High flux palladium-copper composite membranes for hydrogen separations. *Desalination* **2006,** *193* (1-3), 224-229; (f) Roa, F.; Douglas Way, J.; McCormick, R. L.; Paglieri, S. N., Preparation and characterization of Pd-Cu composite membranes for hydrogen separation. *Chemical Engineering Journal* **2003,** *93* (1), 11-22.

16. Ma, Y. H.; Akis, B. C.; Ayturk, M. E.; Guazzone, F.; Engwall, E. E.; Mardilovich, I. P., Characterization of intermetallic diffusion barrier and alloy formation for Pd/Cu and Pd/Ag porous stainless steel composite membranes. *Industrial and Engineering Chemistry Research* **2004,** *43* (12), 2936-2945.

17. Yang, J. Y.; Nishimura, C.; Komaki, M., Preparation and characterization of Pd-Cu/V-15Ni composite membrane for hydrogen permeation. *Journal of Alloys and Compounds* **2007,** *431* (1-2), 180-184.

18. Mejdell, A. L.; Klette, H.; Ramachandran, A.; Borg, A.; Bredesen, R., Hydrogen permeation of thin, free-standing Pd/Ag23% membranes before and after heat treatment in air. *Journal of Membrane Science* **2008,** *307* (1), 96-104.

19. (a) Zhang, Y.; Ozaki, T.; Komaki, M.; Nishimura, C., Hydrogen permeation of Pd-Ag alloy coated V-15Ni composite membrane: Effects of overlayer composition. *Journal of Membrane Science* **2003,** *224* (1-2), 81-91; (b) Zhang, Y.; Maeda, R.; Komaki, M.; Nishimura, C., Hydrogen permeation and diffusion of metallic composite membranes. *Journal of Membrane Science* **2006,** *269* (1-2), 60-65.

20. Ryi, S. K.; Park, J. S.; Kim, S. H.; Cho, S. H.; Kim, D. W.; Um, K. Y., Characterization of Pd-Cu-Ni ternary alloy membrane prepared by magnetron sputtering and Cu-reflow on porous nickel support for hydrogen separation. *Separation and Purification Technology* **2006,** *50* (1), 82-91.

21. Hoang, H. T.; Tong, H. D.; Gielens, F. C.; Jansen, H. V.; Elwenspoek, M. C., Fabrication and characterization of dual sputtered Pd-Cu alloy films for hydrogen separation membranes. *Materials Letters* **2004,** *58* (3-4), 525-528.

22. Tong, H. D.; Vanden Berg, A. H. J.; Gardeniers, J. G. E.; Jansen, H. V.; Gielens, F. C.; Elwenspoek, M. C., Preparation of palladium - Silver alloy films by a dual-sputtering technique and its application in hydrogen separation membrane. *Thin Solid Films* **2005,** *479* (1-2), 89-94.

23. (a) Bryden, K. J.; Ying, J. Y., Nanostructured palladium membrane synthesis by magnetron sputtering. *Materials Science and Engineering A* **1995,** *204* (1-2), 140-145; (b) Ying, J. Y., Structure and morphology of nanostructured oxides synthesized by thermal vaporization/magnetron sputtering and gas condensation. *Journal of Aerosol Science* **1993,** *24* (3), 315-338.

24. Pereira, A. I.; Pérez, P.; Rodrigues, S. C.; Mendes, A.; Madeira, L. M.; Tavares, C. J., Deposition of Pd-Ag thin film membranes on ceramic supports for hydrogen purification/separation. *Materials Research Bulletin* **2015,** *61*, 528-533.

25. O'Brien, J.; Hughes, R.; Hisek, J., Pd/Ag membranes on porous alumina substrates by unbalanced magnetron sputtering. *Surface and Coatings Technology* **2001,** *142-144*, 253-259.

26. Checchetto, R.; Bazzanella, N.; Patton, B.; Miotello, A., Palladium membranes prepared by r.f. magnetron sputtering for hydrogen purification. *Surface and Coatings Technology* **2004,** *177-178*, 73-79.

27. Mattox, D. M., Particle bombardment effects on thin-film deposition: A review. *Journal of Vacuum Science & Technology A* **1989,** *7* (3), 1105-1114.

28. k., W., Handbook of Sputter Deposition Technology, 2nd Edition, Elsevier. **2012**.

29. (a) Thornton, J. A., MAGNETRON SPUTTERING: BASIC PHYSICS AND APPLICATION TO CYLINDRICAL MAGNETRONS. *J Vac Sci Technol* **1978,** *15* (2), 171-177; (b) Waits, R. K., PLANAR MAGNETRON SPUTTERING. *J Vac Sci Technol* **1978,** *15* (2), 179-187; (c) Thornton, J. A., RECENT DEVELOPMENTS IN SPUTTERING - MAGNETRON SPUTTERING. *Met Finish* **1979,** *77* (5), 83-87.

30. Window, B.; Savvides, N., Charged particle fluxes from planar magnetron sputtering sources. *Journal of Vacuum Science and Technology A: Vacuum, Surfaces and Films* **1986,** *4* (2), 196-202.

31. Movchan, B. A.; Demchishin, A. V., STUDY OF THE STRUCTURE AND PROPERTIES OF THICK VACUUM CONDENSATES OF NICKEL, TITANIUM, TUNGSTEN, ALUMINUM OXIDE AND ZIRCONIUM DIOXIDE. *Fiz Metallov i Metalloved* **1969,** *28* (4), 653-660.

32. (a) Thornton, J. A., HIGH RATE THICK FILM GROWTH. *Annual Review of Materials Science* **1977,** *7*, 239-260; (b) Thornton, J. A., INFLUENCE OF APPARATUS GEOMETRY AND DEPOSITION CONDITIONS ON THE STRUCTURE AND TOPOGRAPHY OF THICK SPUTTERED COATINGS. *J Vac Sci Technol* **1974,** *11* (4), 666-670.

33. Dirks, A. G.; Leamy, H. J., Columnar microstructure in vapor-deposited thin films. *Thin Solid Films* **1977,** *47* (3), 219-233.

34. (a) Bland, R. D.; Kominiak, G. J.; Mattox, D. M., EFFECT OF ION BOMBARDMENT DURING DEPOSITION ON THICK METAL AND CERAMIC DEPOSITS. *J Vac Sci Technol* **1974,** *11* (4), 671-674; (b) Mattox, D. M.; Kominiak, G. J., PHYSICAL PROPERTIES OF THICK SPUTTER-DEPOSITED GLASS FILMS. *Journal of the Electrochemical Society* **1973,** *120* (11), 1535-1539.

35. Hoffman, D. W.; Thornton, J. A., The compressive stress transition in Al, V, Zr, Nb and W metal films sputtered at low working pressures. *Thin Solid Films* **1977,** *45* (2), 387-396.

36. Tominaga, K.; Iwamura, S.; Shintani, Y.; Tada, O., ENERGY ANALYSIS OF HIGH-ENERGY NEUTRAL ATOMS IN THE SPUTTERING OF ZNO AND BATIO//3. *Jpn J Appl Phys Part 1* **1982,** *V 21* (N 5), 688-692.

37. Thornton, J. A., The influence of bias sputter parameters on thick copper coatings deposited using a hollow cathode. *Thin Solid Films* **1977,** *40* (C), 335-344.

38. (a) Hoffman, D. W.; Thornton, J. A., INTERNAL STRESSES IN Cr, Mo, Ta, AND Pt FILMS DEPOSITED BY SPUTTERING FROM A PLANAR MAGNETRON SOURCE. *Journal of vacuum science & technology* **1981,** *20* (3), 355-358; (b) Sun, R. C.; Tisone, T. C.; Cruzan, P. D., The origin of internal stress in low-voltage sputtered tungsten films. *Journal of Applied Physics* **1975,** *46* (1), 112-117.

39. Hoffman, D. W.; Thornton, J. A., EFFECTS OF SUBSTRATE ORIENTATION AND ROTATION ON INTERNAL STRESSES IN SPUTTERED METAL FILMS. *J Vac Sci Technol* **1979,** *16* (2), 134-137.

40. Anders, A., A structure zone diagram including plasma-based deposition and ion etching. *Thin Solid Films* **2010,** *518* (15), 4087-4090.

41. Christou, C.; Barber, Z. H., Ionization of sputtered material in a planar magnetron discharge. *Journal of Vacuum Science and Technology A: Vacuum, Surfaces and Films* **2000,** *18* (6), 2897-2907.

42. (a) Ricard, A.; Nouvellon, C.; Konstantinidis, S.; Dauchot, J. P.; Wautelet, M.; Hecq, M., Density and temperature in an inductively amplified magnetron discharge for titanium deposition. *Journal of Vacuum Science and Technology A: Vacuum, Surfaces and Films* **2002,** *20* (4), 1488-1491; (b) Konstantinidis, S.; Ricard, A.; Ganciu, M.; Dauchot, J. P.; Ranea, C.; Hecq, M., Measurement of ionic and neutral densities in amplified magnetron discharges by pulsed absorption spectroscopy. *Journal of Applied Physics* **2004,** *95* (5), 2900-2905.

43. Helmersson, U.; Lattemann, M.; Bohlmark, J.; Ehiasarian, A. P.; Gudmundsson, J. T., Ionized physical vapor deposition (IPVD): A review of technology and applications. *Thin Solid Films* **2006,** *513* (1-2), 1-24.

44. Kaufman, H. R., TECHNOLOGY OF ION BEAM SOURCES USED IN SPUTTERING. *J Vac Sci Technol* **1978,** *15* (2), 272-276.

45. Bugaev, S. P.; Koval, N. N.; Sochugov, N. S.; Zakharov, A. N. In *Investigation of a high-current pulsed magnetron discharge initiated in the low-pressure diffuse arc plasma*, International Symposium on Discharges and Electrical Insulation in Vacuum, ISDEIV, 1996; pp 1074-1076.

46. Fetisov, I. K.; Filippov, A. A.; Khodachenko, G. V.; Mozgrin, D. V.; Pisarev, A. A., Impulse irradiation plasma technology for film deposition. *Vacuum* **1999,** *53* (1-2), 133-136.

47. Ochs, D., HIPIMS Power for Improved Thin Film Coatings. *Vakuum in Forschung und Praxis* **2008,** *20* (4), 34-38.
48. www.lesker.com/newweb/blog/post.cfm/high-power-impulse-magnetron-sputtering-hipims.

49. Sarakinos, K.; Alami, J.; Konstantinidis, S., High power pulsed magnetron sputtering: A review on scientific and engineering state of the art. *Surface and Coatings Technology* **2010,** *204* (11), 1661-1684.
50. Alami, J.; Persson, P. O. Å.; Music, D.; Gudmundsson, J. T.; Bohlmark, J.; Helmersson, U., Ion-assisted physical vapor deposition for enhanced film properties on nonflat surfaces. *Journal of Vacuum Science and Technology A: Vacuum, Surfaces and Films* **2005,** *23* (2), 278-280.

51. Sarakinos, K.; Alami, J.; Wuttig, M., Process characteristics and film properties upon growth of TiOx films by high power pulsed magnetron sputtering. *Journal of Physics D: Applied Physics* **2007,** *40* (7), 2108-2114.

52. Sarakinos, K.; Alami, J.; Klever, C.; Wuttig, M., Growth of TiOx films by high power pulsed magnetron sputtering from a compound TiO1.8 target. *Reviews on Advanced Materials Science* **2007,** *15* (1), 44-48.

53. Konstantinidis, S.; Hemberg, A.; Dauchot, J. P.; Hecq, M., Deposition of zinc oxide layers by high-power impulse magnetron sputtering. *Journal of Vacuum Science and Technology B: Microelectronics and Nanometer Structures* **2007,** *25* (3), 19-21.

54. Alami, J.; Eklund, P.; Andersson, J. M.; Lattemann, M.; Wallin, E.; Bohlmark, J.; Persson, P.; Helmersson, U., Phase tailoring of Ta thin films by highly ionized pulsed magnetron sputtering. *Thin Solid Films* **2007,** *515* (7-8), 3434-3438.

55. 47th Annual Technical Conference Proceedings of the Society of Vacuum Coaters. **2004**, 215.

56. 47th Annual Technical Conference Proceedings of the Society of Vacuum Coaters. **2004**.

57. Vlček, J.; Pajdarová, A. D.; Musil, J., Pulsed dc magnetron discharges and their utilization in plasma surface engineering. *Contributions to Plasma Physics* **2004,** *44* (5-6), 426-436.

58. Lattemann, M.; Ehiasarian, A. P.; Bohlmark, J.; Persson, P. Å. O.; Helmersson, U., Investigation of high power impulse magnetron sputtering pretreated interfaces for adhesion enhancement of hard coatings on steel. *Surface and Coatings Technology* **2006,** *200* (22-23 SPEC. ISS.), 6495-6499.

59. Ehiasarian, A. P.; Wen, J. G.; Petrov, I., Interface microstructure engineering by high power impulse magnetron sputtering for the enhancement of adhesion. *Journal of Applied Physics* **2007,** *101* (5).

60. Proceedings of the 47th Annual Technical Conference Proceedings of the Society of Vacuum Coaters. **2004**.

61. Christie, D. J., Target material pathways model for high power pulsed magnetron sputtering. *Journal of Vacuum Science and Technology A: Vacuum, Surfaces and Films* **2005,** *23* (2), 330-335.

62. Christie, D. J.; Tomasel, F.; Sproul, W. D.; Carter, D. C., Power supply with arc handling for high peak power magnetron sputtering. *Journal of Vacuum Science and Technology A: Vacuum, Surfaces and Films* **2004,** *22* (4), 1415-1419.

63. Ortiz-Medina, J.; Kitano, H.; Morelos-Gomez, A.; Wang, Z.; Araki, T.; Kang, C. S.; Hayashi, T.; Takeuchi, K.; Kawaguchi, T.; Tanioka, A.; Cruz-Silva, R.; Terrones, M.; Endo, M., Nanostructured carbon-based membranes: Nitrogen doping effects on reverse osmosis performance. *NPG Asia Materials* **2016,** *8*.

4. Porous substrates for hydrogen separation membranes

4.1. Introduction

According to IUPAC, porous materials are classified in macroporous (pore diameter d > 50 nm), mesoporous (50 nm > d > 2 nm) and microporous (d < 2 nm) and are used typically for filtration and separation of fluids. Porous materials have been used to support thin membranes, to provide adequate mechanical strength. However, several other requirements must be fulfilled:

- Chemical compatibility with the hydrogen selective layer and high temperature stability;
- Good selective layer/substrate adhesion;
- Resistance to possible contamination within the feed gas stream;
- Low production cost and ease of sealing in the gas separation module;
- Low resistance to hydrogen diffusion.

The most common materials are alumina[1], titania[2], zirconia[3], porous glass[4] and porous metals including stainless steel[5] and Inconel[6]. Alternative substrates are porous nickel[7], porous silicon[8], mixed ceramics[9] and lithographically deposited dense nickel strips[10].
Currently, no single substrate material meets all the aforementioned requirements, but, among them, ceramics, particularly alumina[11], are widely used, thanks to the pore size tunability and the good chemical stability at high temperature. Moreover, it is the best option in terms of ease of workability, costs and chemical compatibility. Ceramic substrates can be prepared with very fine pore sizes, reducing the minimum thickness required to deposit a defect-free membrane. However, reducing the pore size can decrease the flux through the substrate (pressure drop), thus limiting the advantage of the reduced membrane thickness. Hydrogen flux can be increased using an asymmetric substrate, coupling layers with different pore sizes or depositing one single mesoporous layer (usually, a layer of γ-Al_2O_3[1c,12]) on the

top of a macroporous substrate. However, even though this approach is relatively simple, it employs high purity starting reagents and some steps to prepare the final mesoporous layer, increasing the cost of the ceramic substrate. Commonly, a relatively thin (1 µm) micro- or mesoporous layer is supported by a thick (1 mm) macroporous layer, usually with at least one intermediate mesoporous layer made of titania, zirconia and γ-alumina[13]. In order to avoid the deposition of the mesoporous layer, graded-porosity substrates can be prepared: they are usually prepared by raw ceramic/pore former powder mixtures layers with different amounts of pore former pressed together. However, even if the preparation of such substrates is very fast and easy, the main drawback is a strong deformation of the material during sintering, due to the different layer shrinkage.

In general, the major drawback of ceramic substrates is the relatively weak adhesion of the metallic layer, which can cause delamination[14], due to the different thermal expansion coefficient. Moreover, ceramic substrates are rather brittle and sealing problems can arise[15]. However, they can be a good alternative to porous stainless steel.

Porous metallic substrates are not brittle and have very similar thermal expansion coefficients to the metal hydrogen selective layer. They are fabricated by sintering milled or atomised metal powders, with various grades of stainless steel, Inconel, aluminium and titanium. Porous stainless steel (PSS) substrates are widely used thanks to low cost, ease of sealing, low mass transfer resistance, lack of thermal expansion issues and excellent film adhesion. However, they typically have a wide pore size distribution and intermetallic diffusion between substrate and film is a very common problem. Many authors tried to solve these issues by modifying the substrate surface with the deposition of a barrier made of oxides or ceramics[3,16], but they create additional interfaces affecting membrane adhesion and the overall flow resistance.

4.2. Ceramic porous substrates preparation

Partial sintering, pore formers, replica templates and direct foaming are the most common methods to prepare porous ceramic substrates.

4.2.1. Partial sintering

Partial sintering[17] of powder compacts is the most conventional and frequently employed method to prepare porous ceramics. The grade of sintering is a balance between the desired porosity and the final mechanical properties required. The size of the starting powder controls the final pore size and the degree of partial sintering controls the final porosity of the material, a property depending even on compact forming pressure, sintering temperature and time. Other processing factors (type and amount of additives, green density and sintering conditions) greatly affect the microstructure of porous ceramics[18]. The mechanical properties of a partial sintered material depend largely on neck growth between grains, as well as porosity and pore size. The final porosity is usually below 50%. In industry, this method has been used for the production of gas bubble generators in wastewater treatment plants[19] and water purification membranes. The drawback of this method is usually a low mechanical strength that often is overtaken by the use of pore formers.

4.2.2. The sintering process

The sintering process[20] produces a density-controlled material by the application of thermal energy to a powder compact. It can be divided in solid state sintering (a solid state densification of powder compact) and liquid phase sintering (presence of a liquid phase in the powder compact during sintering). Liquid phase sintering allows easy control of microstructure and reduction in processing cost, but reduces mechanical properties.
The driving force of sintering is the reduction of the total interfacial energy, γA:

$$\Delta(\gamma A) = \Delta\gamma A + \gamma\Delta A$$

where γ is the specific surface (interface) energy, A is the total surface (interface) area of the compact (depending on grain coarsening), Δγ is the variation in interfacial energy (depending on densification). In solid state sintering, Δγ is related to the replacement of solid/air by solid/solid interfaces. The variables determining the sinterability and the sintered microstructure of a powder compact can be divided in material and process variables. The former include chemical composition of powder compact, powder size, shape and size distribution, degree of powder agglomeration etc. These variables influence the powder compressibility and sinterability (both densification and grain growth). The other variables are mainly ther-

modynamic variables, involved in the sintering process: temperature, time, atmosphere, pressure, heating and cooling rate, affecting the final microstructure of the sintered material.

4.2.3. Pore former agents

Pore formers leave voids after their evaporation or burning during sintering. The most common pore formers include polymer beads, starch, cellulose, cotton and graphite. They are commonly used when a homogenous porosity (size and shape) is desired, or to improve mechanical strength. The choice of the pore former is very important, since the final porosity of the sintered material is controlled by the amount of pore former introduced and by its shape and size. Pore formers allow the preparation of high open porosity materials but they require an adequate mixing with the ceramic powder for a uniform and regular distribution of pores. Organic materials are usually removed by burning, but it can require long-term heat treatments, with the release of harmful by-products. Polymethylmethacrylate (PMMA) beads and microbeads have been frequently employed[21], thanks to the ease of powder mixture preparation, low burning temperature and well-interconnected final porosity; the polymer can be reticulated by choosing appropriate solvents. Long fibres are often used for obtaining porous ceramics with a channel-like porosity, while short fibres, or whiskers, combine the advantages of partially sintered porous ceramic with unidirectional pores. Liquid phases, such as water and oil, are evaporated or sublimated. The freeze-drying[22] of water, or liquid-based slurry, has become quite common in recent years to produce ceramics of unique structure. This method has several advantages, including simple sintering process (no materials to burn out), a wide range of porosity (30-99%) controlled by the slurry concentration, applicability to various types of ceramics and no emission of harmful products. In order to improve the connection among the pores, the use of pore former agents can be coupled with partial sintering, with the aim to avoid a full sintering of the ceramic matrix.

4.2.4. Replica templates

Replica technique[23] allows the preparation of porous substrates with well interconnected large pores. It starts with the impregnation of a porous or cellular structure (synthetic or natural) with a ceramic suspension, precursor solution, etc. The most frequently used syn-

thetic templates are porous polymeric sponges such as polyurethane, soaked into the ceramic slurry or the precursor solution to form uniform ceramic layers over the sponge walls, draining and removing the excess of slurry. Pyrolysis decomposes the impregnated sponges and then the ceramic layers are sintered at higher temperatures. Porosity higher than 90% can be obtained, with cell sizes ranging from a few hundred micrometres to several millimetres. The open cells are well interconnected but the mechanical properties are generally poor[24]. Natural materials (woods, sea sponge, etc.) can be also use as replica templates by infiltration of oxides and non-oxides species.

4.2.5. Direct foaming

In direct foaming technique[25] a ceramic suspension is foamed (by incorporating air or gas), stabilised, dried and finally sintered to obtained solid structures. The main advantages of this technique are a low-cost and an easy production of highly porous ceramic materials (porosity > 95%). Porous ceramics with unidirectional channels can be developed by using continuous bubble formation in ceramic slurry[26]. However, due to thermodynamic instability, the gas bubbles are likely to coalesce, resulting in large pores in the final porous bodies. The stabilization of the air or gas bubble in the ceramic suspension is very important, and it is reached with the use of surfactants, which reduce the interfacial energy of the gas-liquid boundaries. The pore size of the porous body ranges from below 50 µm up to the mm scale, depending on how effectively and rapidly the surfactants work.

4.3. Types of porous ceramic substrate

4.3.1. Tubular

Tubular ceramic substrates are a very common geometry in membranes manufacturing and are generally prepared by extrusion of ceramic powders mixed with waxes, organics and plastifiers. Standard dimensions are 100-250 mm diameter (limited by extruder tool) and 1-2 m length (limited by sintering furnace). After the extrusion, tubes are gently dried, to remove the water, and then burned in a sintering furnace. One of the most common materials is pure α-Al_2O_3, and tubes prepared from it are sintered in a hanging position to avoid deformation. Other materials can be used, such as TiO_2 or mixtures of α-Al_2O_3 with TiO_2 and ZrO_2,

and they are sintered at temperatures around 1300-1400°C. Tubular substrates have enough mechanical stability to withstand high trans-membrane pressures. To test their strength they are filled with a liquid simulating the bursting pressure inside the tube. Depending on the geometry, limiting pressures between 50 and over 100 bar can be measured; a safety pressure is usually included between 40 and 80 bar. Among the advantages of tubular membranes are high surface available for hydrogen permeation, the scalability, the ease of sealing inside the permeation apparatus and the possibility to pack a lot of tubular membranes in the same permeation facility.

4.3.2. Planar

Planar substrates are industrially prepared mainly from tape casting and dry powder pressing. The tape casting process employs a mixture of ceramic powders, solvents and organic binders to produce a stable suspension of defined viscosity. The resulting tape is flexible, thanks to the high organic amount, and its thickness is limited by the viscosity of the casting solution. The sintering temperatures are similar to those for tubular substrates and before sintering a careful organic burning step, up to 500°C, is necessary to eliminate the high contents of organics without damaging the ceramic structure.

In the dry powder pressing process, ceramic powders can be mixed with solvents and organics, such as liquefiers and binders, to help the green in maintaining its integrity, or can be pressed. The binders prevent disaggregation of the pressed powder after removal from the mould. Some pore formers, such as starch, can help the consolidation of the green during pressing. Powder pressing can be uniaxial or isostatic. With the dry pressing technique low thicknesses can be achieved (below half a mm), but a careful sintering procedure is necessary to avoid the deformation of sintered pellets.

References

1. (a) Sun, G. B.; Hidajat, K.; Kawi, S., Ultra thin Pd membrane on α-Al2O3 hollow fiber by electroless plating: High permeance and selectivity. *Journal of Membrane Science* **2006,** *284* (1-2), 110-119; (b) Roa, F.; Douglas Way, J.; McCormick, R. L.; Paglieri, S. N., Preparation and characterization of Pd-Cu composite membranes for hydrogen separation. *Chemical Engineering Journal* **2003,** *93* (1), 11-22; (c) Jayaraman, V.; Lin, Y. S.; Pakala, M.; Lin, R. Y., Fabrication of ultrathin metallic membranes on ceramic supports by sputter deposition. *Journal of Membrane Science* **1995,** *99* (1), 89-100; (d) Li, A.; Xiong, G.; Hughes, R., Repair of Pd/α-Al2O3 composite membrane with defects. *Science in China, Series B: Chemistry* **1999,** *42* (6), 612-616.

2. (a) Wu, L. Q.; Xu, N.; Shi, J., Preparation of a palladium composite membrane by an improved electroless plating technique. *Industrial and Engineering Chemistry Research* **2000,** *39* (2), 342-348; (b) Li, X.; Fan, Y.; Jin, W.; Huang, Y.; Xu, N., Improved photocatalytic deposition of palladium membranes. *Journal of Membrane Science* **2006,** *282* (1-2), 1-6.

3. Gao, H.; Lin, J. Y. S.; Li, Y.; Zhang, B., Electroless plating synthesis, characterization and permeation properties of Pd-Cu membranes supported on ZrO2 modified porous stainless steel. *Journal of Membrane Science* **2005,** *265* (1-2), 142-152.

4. Uemiya, S.; Sato, N.; Ando, H.; Kude, Y.; Matsuda, T.; Kikuchi, E., Separation of hydrogen through palladium thin film supported on a porous glass tube. *Journal of Membrane Science* **1991,** *56* (3), 303-313.

5. (a) Mardilovich, P. P.; She, Y.; Ma, Y. H.; Rei, M. H., Defect-Free Palladium Membranes on Porous Stainless-Steel Support. *AIChE Journal* **1998,** *44* (2), 310-322; (b) Mardilovich, I. P.; Engwall, E.; Ma, Y. H., Dependence of hydrogen flux on the pore size and plating surface topology of asymmetric Pd-porous stainless steel membranes. *Desalination* **2002,** *144* (1-3), 85-89; (c) Tong, J.; Matsumura, Y.; Suda, H.; Haraya, K., Thin and dense Pd/CeO2/MPSS composite membrane for hydrogen separation and steam reforming of methane. *Separation and Purification Technology* **2005,** *46* (1-2), 1-10.

6. Jarosch, K.; De Lasa, H. I., Novel riser simulator for methane reforming using high temperature membranes. *Chemical Engineering Science* **1999,** *54* (10), 1455-1460.

7. (a) Ryi, S. K.; Park, J. S.; Kim, S. H.; Hong, S. C.; Kim, D. W., Development of porous nickel membrane made by uniaxial pressing for hydrogen separation. *Desalination* **2006,** *200* (1-3), 213-215; (b) Ryi, S. K.; Park, J. S.; Choi, S. H.; Cho, S. H.; Kim, S. H., Fabrication and characterization of metal porous membrane made of Ni powder for hydrogen separation. *Separation and Purification Technology* **2006,** *47* (3), 148-155.

8. Starkov, V.; Vyatkin, A.; Volkov, V.; Presting, H.; Konle, J.; Konig, U. In *Highly efficient to hydrogen permeability palladium membranes supported in porous silicon*, Physica Status Solidi C: Conferences, 2005; pp 3457-3460.

9. Gryaznov, V. M.; Serebryannikova, O. S.; Serov, Y. M.; Ermilova, M. M.; Karavanov, A. N.; Mischenko, A. P.; Orekhova, N. V., Preparation and catalysis over palladium composite membranes. *Journal of Membrane Science* **1993,** *77* (2-3), 284.

10. (a) Zhang, Y.; Gwak, J.; Murakoshi, Y.; Ikehara, T.; Maeda, R.; Nishimura, C., Hydrogen permeation characteristics of thin Pd membrane prepared by microfabrication technology. *Journal of Membrane Science* **2006,** *277* (1-2), 203-209; (b) Zhang, Y.; Lu, J.; Ikehara, T.; Maeda, R.; Nishimura, C., Characterization and permeation of microfabricated palladium membrane. *Materials Transactions* **2006,** *47* (2), 255-258.

11. (a) Hou, K.; Hughes, R., The effect of external mass transfer, competitive adsorption and coking on hydrogen permeation through thin Pd/Ag membranes. *Journal of Membrane Science* **2002,** *206* (1-2), 119-130; (b) Hou, K.; Hughes, R., Preparation of thin and highly stable Pd/Ag composite membranes and simulative analysis of transfer resistance for hydrogen separation. *Journal of Membrane Science* **2003,** *214* (1), 43-55; (c) Uemiya, S.; Matsuda, T.; Kikuchi, E., Hydrogen permeable palladium-silver alloy membrane supported on porous ceramics. *Journal of Membrane Science* **1991,** *56* (3), 315-325.

12. (a) McCool, B.; Xomeritakis, G.; Lin, Y. S., Composition control and hydrogen permeation characteristics of sputter deposited palladium-silver membranes. *Journal of Membrane Science* **1999,** *161* (1-2), 67-76; (b) Pereira, A. I.; Pérez, P.; Rodrigues, S. C.; Mendes, A.; Madeira, L. M.; Tavares, C. J., Deposition of Pd-Ag thin film membranes on ceramic supports for hydrogen purification/separation. *Materials Research Bulletin* **2015,** *61*, 528-533; (c) Jayaraman, V.; Lin, Y. S., Synthesis and hydrogen permeation properties of ultrathin palladium-silver alloy membranes. *Journal of Membrane Science* **1995,** *104* (3), 251-262.

13. Burggraaf, A. J., Chapter 9 Transport and separation properties of membranes with gases and vapours. In *Membrane Science and Technology*, 1996; Vol. 4, pp 331-433.

14. Tosti, S.; Bettinali, L.; Castelli, S.; Sarto, F.; Scaglione, S.; Violante, V., Sputtered, electroless, and rolled palladium-ceramic membranes. *Journal of Membrane Science* **2002,** *196* (2), 241-249.

15. Paglieri, S. N.; Way, J. D., Innovations in palladium membrane research. *Separation and Purification Methods* **2002,** *31* (1), 1-169.

16. Huang, Y.; Dittmeyer, R., Preparation and characterization of composite palladium membranes on sinter-metal supports with a ceramic barrier against intermetallic diffusion. *Journal of Membrane Science* **2006,** *282* (1-2), 296-310.

17. (a) Deng, Z. Y.; Yang, J. F.; Beppu, Y.; Ando, M.; Ohji, T., Effect of agglomeration on mechanical properties of porous zirconia fabricated by partial sintering. *Journal of the American Ceramic Society* **2002,** *85* (8), 1961-1965; (b) Jean, G.; Sciamanna, V.; Demuynck, M.; Cambier, F.; Gonon, M., Macroporous ceramics: Novel route using partial sintering of alumina-powder agglomerates obtained by spray-drying. *Ceramics International* **2014,** *40* (7 PART A), 10197-10203; (c) Kalemtas, A.; Topates, G.; Özcoban, H.; Mandal, H.; Kara, F.; Janssen, R., Mechanical characterization of highly porous β-Si3N4 ceramics fabricated via partial sintering & starch addition. *Journal of the European Ceramic Society* **2013,** *33* (9), 1507-1515.

18. Fukushima, M.; Zhou, Y.; Miyazaki, H.; Yoshizawa, Y. I.; Hirao, K.; Iwamoto, Y.; Yamazaki, S.; Nagano, T., Microstructural characterization of porous silicon carbide membrane support with and without alumina additive. *Journal of the American Ceramic Society* **2006,** *89* (5), 1523-1529.

19. Scheffler, M.; Colombo, P., *Cellular Ceramics: Structure, Manufacturing, Properties and Applications*. 2006; p 1-645.

20. Kang , S., Sintering, densification, grain growth and microstructure, Elsevier, **2004**.

21. (a) Colombo, P., Engineering porosity in polymer-derived ceramics. *Journal of the European Ceramic Society* **2008,** *28* (7), 1389-1395; (b) Descamps, M.; Richart, O.; Hardouin, P.; Hornez, J. C.; Leriche, A., Synthesis of macroporous β-tricalcium phosphate with controlled porous architectural. *Ceramics International* **2008,** *34* (5), 1131-1137; (c) Kamitani, K.; Hyodo, T.; Shimizu, Y.; Egashira, M., Fabrication of porous alumina ceramics having cell windows with controlled size by PMMA template method. *Journal of Materials Science* **2010,** *45* (13), 3602-3609.

22. (a) Liu, B. T.; Luo, B.; Xu, Z. Z.; Liu, G. S., The preparation of porous alumina ceramics with directional pore channels structure by a camphene-based freeze-casting. *Gongneng Cailiao/Journal of Functional Materials* **2011,** *42* (SUPPL. 1), 163-167; (b) Liu, L.; Geng, G., Preparing β-Si3N4 crystals by freeze-drying and using 10 wt% Ba0.75Sr0.25Al2Si2O8 as flux. *Materials Letters* **2016,** *167*, 109-111; (c) Marrero-Jerez, J.; Larrondo, S.; Rodríguez-Castellón, E.; Núñez, P., TPR, XRD and XPS characterisation of ceria-based materials synthesized by freeze-drying precursor method. *Ceramics International* **2014,** *40* (5), 6807-6814; (d) Villanueva, R.; Gõmez, A.; Vie, D.; Martínez, E.; Beltrán, A.; Sapiña, F.; Vila, J., Nanostructured solids from freeze-dried precursors: Multigram scale synthesis of TiO2-based powders. *Journal of the American Ceramic Society* **2013,** *96* (4), 1324-1331.

23. (a) Bucharsky, E. C.; Schell, K. G.; Oberacker, R.; Hoffmann, M. J., Preparation of transparent glass sponges via replica method using high-purity silica. *Journal of the American Ceramic Society* **2010,** *93* (1), 111-114; (b) Lee, Y. J.; Kim, S. R.; Kim, Y. H.; Shin, D. G.; Won, J. Y.; Kwon, W. T., Characterization of microstructure on porous silicon carbide prepared by polymer replica template method. *Journal of the Korean Ceramic Society* **2014,** *51* (6), 539-543.

24. Brown, D. D.; Green, D. J., Investigation of strut crack formation in open cell alumina ceramics. *Journal of the American Ceramic Society* **1994,** *77* (6), 1467-1472.

25. (a) Barg, S.; Soltmann, C.; Andrade, M.; Koch, D.; Grathwohl, G., Cellular ceramics by direct foaming of emulsified ceramic powder suspensions. *Journal of the American Ceramic Society* **2008,** *91* (9), 2823-2829; (b) Zhang, L. Y.; Zhou, D. L.; Chen, Y.; Liang, B.; Zhou, J. B., Preparation of high open porosity ceramic foams via direct foaming molded and dried at room temperature. *Journal of the European Ceramic Society* **2014,** *34* (10), 2443-2452.

26. (a) Banno, T.; Yamada, Y.; Nagae, H., Fabrication of porous alumina ceramics by simultaneous thermal gas generating and thermal slurry solidification. *Nippon Seramikkusu Kyokai Gakujutsu Ronbunshi/Journal of the Ceramic Society of Japan* **2009,** *117* (1365), 713-716; (b) Song, H. Y.; Islam, S.; Lee, B. T., A novel method to fabricate unidirectional porous hydroxyapatite body using ethanol bubbles in a viscous slurry. *Journal of the American Ceramic Society* **2008,** *91* (9), 3125-3127.

5. Hydrogen permeation in metallic membranes

5.1. Introduction

The H_2 permeation through dense metallic membranes involves a series of steps which can be summarized in: 1) dissociation of H_2 to H atoms at the surface of the membrane, 2) diffusion of the H atoms across the membrane and 3) recombination of H atoms into H_2 at the opposite surface. At low temperatures the associative desorption of H_2 is the rate-limiting step for H_2 permeation, but at temperature higher than 150°C[1], when both absorption/desorption processes are at the thermodynamic equilibrium, the rate limiting step is the H diffusion through the bulk. However, if the membrane is very thin, the diffusion of H atoms is very fast and the new rate-limiting step is the H_2 desorption, even though both absorption/desorption are at the thermodynamic equilibrium. Ward and Dao[2] proved that the desorption of H_2 is the rate limiting step at low temperatures and that absorption is the rate-limiting step only at very low H_2 partial pressures (<< 1 bar) or in case of severe surface contamination.

When the diffusion of H atoms through the bulk is the rate limiting step, Fick's first law is assumed and the H_2 flux through the membrane is proportional to the difference in the amount of H dissolved at the high pressure side of the membrane and the amount of H dissolved at the low pressure side of the membrane. In order to determine the concentration of dissolved H, a relation between H_2 pressure in the gas phase and the H dissolved in the bulk needs to be used. At very low H_2 pressures, this relation is given by the equation of Sieverts:

$$P_{H_2}^{0.5} = K(T) \cdot c(H)$$

where P_{H_2} is the H_2 pressure, $K(T)$ is the Sieverts constant and c(H) is the H concentration in the metal bulk. Sieverts equation is only valid at low pressures, so deviations (exponent ≠ 0.5) are expected at high H_2 pressures[3]. Other causes of deviations from Sieverts' law also occur when the membrane is defective and when the surface has low activity for the dissoci-

ation of H_2, which happens when contaminants are adsorbed onto the surface (poisoning of the membrane).

5.2. Hydrogen permeation in metal membranes

Hydrogen permeability (Φ) is used to quantify the permeation rate of hydrogen through a membrane[2,4]. When the diffusion of H atoms through the membrane bulk is the rate limiting step, the diffusion flux, J_H (mol m^{-2} s^{-1}), is described by Fick's 1st law:

$$J_H = -D\frac{\Delta c_H}{x}$$

where D is the diffusion coefficient (m^2 s^{-1}), c_H is the atomic concentration of hydrogen (mol m^{-3}) and x is the membrane thickness (m).

The application of Sieverts' law gives the atomic concentration of hydrogen (c_H) as a function of the partial pressure:

$$c_H = P_{H_2}^{0.5} / K(T)$$

where K_s is the Sieverts' constant and P_{H_2} is the pressure of molecular hydrogen. Combining J_H and c_H equations and integrating through the membrane thickness (l), we get the equation of hydrogen flux (J) in terms of the partial pressure of hydrogen at both the high (P1) and low (P2) pressure sides of the membrane:

$$J_{H_2} = \Phi\,\frac{\left(P1_{H_2}^{0.5} - P2_{H_2}^{0.5}\right)}{l}$$

Φ is the hydrogen permeability (mol m^{-1} s^{-1} $Pa^{-0.5}$) of the membrane and it is the product of diffusivity and solubility (equal to $1/K_s$):

$$\phi = D_H S_H$$

The H_2 permeability is temperature dependent via the H_2 diffusion coefficient D_H and the solubility S_H, both following an Arrhenius-type equation:

$$D_H(T) = D_0 \cdot \exp\left(-\frac{E_{diff}}{RT}\right) \qquad S_H(T) = S_0 \cdot \exp\left(-\frac{\Delta_r H}{RT}\right)$$

where E_{diff} is the activation energy for H diffusion (J mol^{-1}), R the universal gas constant (J mol^{-1} K^{-1}), T the absolute temperature (K), $\Delta_r H$ is the enthalpy of absorption of H_2 (J mol^{-1}). Combining the above equations we obtain:

$$J_{H_2} = \frac{\Phi_0}{l} e^{-\frac{E_p}{RT}} \cdot (P1^{0.5} - P2^{0.5})$$

with:

$$\Phi_0 = D_0 \cdot S_0 \qquad E_p = E_{diff} + \Delta_r H$$

where E_p is the activation energy of H_2 permeation (J mol^{-1}). The H_2 flux can be further written in terms of H_2 permeability, Φ(T), as shown in the equation below:

$$J_{H_2} = \frac{\Phi(T)}{l} \cdot (P1^{0.5} - P2^{0.5})$$

The H_2 permeance is defined as Φ(T)/l. This equation accurately describes the diffusion-limited hydrogen flux through dense metal membranes in the majority of cases. However, bulk diffusion is not the unique rate determining step of the hydrogen diffusion through membranes[2]. If hydrogen dissociation at the membrane surface is the unique rate-limiting step, the partial pressure exponent increases from 0.5 to 1; when both surface effects and bulk diffusion contribute to the overall permeation, the pressure exponent will range between 0.5 and 1.

A more general form of the hydrogen flux equation, valid for the various rate determining steps can therefore be given as:

$$J_{H_2} = \frac{\Phi_0}{l} e^{-\frac{E_p}{RT}} \cdot (P1^{n} - P2^{n})$$

where the value of n varies between 0.5 and 1. Other factors that can increase the value of n are Knudsen diffusion of molecular hydrogen along defects and grain boundaries, surface contamination, changes in structure and internal stresses[5]. In case of palladium and palladium alloys the predominant reason for change in n value is surface poisoning by CO[5b, 6] and H_2S[7], due to the extremely active surfaces for hydrogen dissociation.

We have seen that the hydrogen flux through a membrane is inversely proportional to the membrane thickness (l) and is directly proportional to both the permeability (Φ) and the par-

tial pressure gradient across the membrane. It is clear that the maximum potential flux can be increased by reducing the thickness and/or increasing the permeability.

5.2.1. H_2 permeation through composite membranes

Hydrogen flux is inversely proportional to membrane thickness[8] for relatively thick membranes, where the hydrogen flux is controlled by diffusion. If we reduce the thickness of the membrane, until the diffusion through the membrane is so fast that surface reactions are expected to limit the flux, the relation is no longer valid. There is wide disagreement concerning the value of a critical thickness below which permeation is surface-controlled. According to Ward[2], at high temperatures (> 300°C) and in the absence of external mass transfer resistance, diffusion-limited permeation is expected for clean Pd at thicknesses down to 1 µm. This has been experimentally confirmed by Mejdell[9] and Gade[10] for free-standing membranes down to just 1.3 µm. However, the presence of a porous substrate adds more degrees of complexity, since H_2 also needs to flow through the porous media.

In order to describe hydrogen flux through a composite membrane and try to find all the contributions to flux, Huang et al.[11] estimated the performance of composite membrane employing the resistance model, first proposed by Henis and Tripodi[12] (Fig. 5.1). According to this model, the permeation behaviour of gas through the composite membrane is analogous to the flow of electricity through an array of resistors. A schematic diagram for gas permeation through a composite membrane is constituted by a circuit formed by three component resistances: the transport resistance of hydrogen flow through the alumina substrate (R_S), the transport resistance of hydrogen flow through the pores or defects in the metal layer (R_P) and the transport resistance of hydrogen flow through the bulk Pd-based alloy film in the layer (R_{Pd}). The resistances reported in the model are the inverse of the related permeabilities.

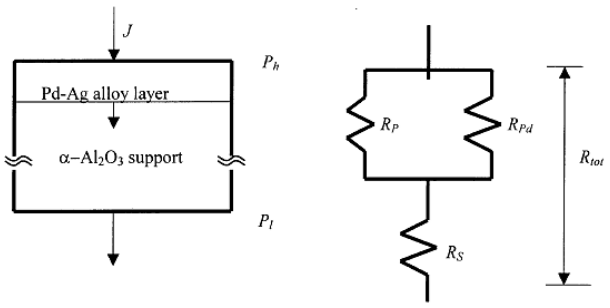

Fig. 5.1: the resistance model[11].

The overall resistance (and permeability) can be determined by summing each contribution:

$$\frac{1}{\mathrm{R_{tot,H_2}}} = \frac{1}{\mathrm{R_{PS,H_2}}} + \frac{1}{\mathrm{R_{Pmet,H_2}}} + \frac{1}{\mathrm{R_{met}}} = \Phi_{\mathrm{PS,H_2}} + \Phi_{\mathrm{Pmet,H_2}} + \Phi_{\mathrm{met}}$$

where $\mathrm{R_{PS,H_2}}$ is the transport resistance of hydrogen through the pores of the ceramic substrate, $\mathrm{R_{Pmet,H_2}}$ is the transport resistance of hydrogen through the pores of the metallic layer, $\mathrm{R_{met}}$ is the transport resistance through metal layer, $\Phi_{\mathrm{PS,H_2}}$, $\Phi_{\mathrm{Pmet,H_2}}$ and Φ_{met} are respectively the hydrogen permeabilities through the pores of the ceramic substrate, through the pores of the metallic layer and the permeability of the bulk metallic layer. In order to determine the effective resistance of each layer, the relevant hydrogen transport mechanism must be fully understood.

5.2.2. Permeation through porous substrate

Molecular gas transport through porous solids may take place via four different mechanisms: viscous (Poiseuille flow), slip flow, Knudsen diffusion and continuum diffusion[13,14]. The main parameters defining the dominant transport mechanism are pore size distribution, temperature and pressure. In many cases, several transport mechanisms act simultaneously and it has been shown that flow and diffusion are completely independent and are therefore additive[15]. The most widely used models to describe the gas transport through porous solids are the dusty gas model[16], phenomenological approaches based on Maxwell-Stefan equations[17], Darcy's law[18] and modified kinetic gas theory[19]. One feature in common of these models is the combination of Poiseuille flow, slip flow, Knudsen diffusion and continuum diffusion. For pure gases continuum diffusion can be ignored, as it describes the transport of

mixed gas species. Additionally, the pore size regimes of most porous substrates used in composite membranes are sufficiently small so that the Poiseuille flow is laminar.

As flow and diffusion are independent of each other, the transport of hydrogen through a porous media can be described as the sum of the Poiseuille flow and the Knudsen diffusion. The flow of gas according to Knudsen mechanism can be described by the equation[11]:

$$J_K = \frac{2}{3}\frac{\varepsilon r}{\tau}\frac{1}{lRT}\left(\frac{8RT}{\pi M}\right)^{0.5}\Delta P$$

Where M is the molecular mass of the gas, ε the porosity, τ the tortuosity, R the gas constant, T the temperature, r the pore radius and l the thickness of the membrane. It is clear that the flux due to Knudsen diffusion is proportional to the average pore radius r and inversely proportional to the square root of the molecular mass M.

Gas can flow also as laminar Poiseuille flow; the flux (J_v) can be described by[11]:

$$J_V = \frac{\varepsilon r^2}{8\tau\mu lRT}\,Pave\,\Delta P$$

Where μ is the viscosity of the gas and P_{ave} the average pressure between high pressure and low pressure sides. For pores with an average radius greater than 1.5 nm there will be a combined contribution to flux[20]. As Knudsen diffusion and Poiseuille flow are additive, the total hydrogen flux through the porous substrate can be expressed by

$$J_{total} = \left[\frac{2}{3}\frac{\varepsilon r}{\tau}\frac{1}{lRT}\left(\frac{8RT}{\pi M}\right)^{0.5}\right] + \left[\left(\frac{1}{8}\frac{\varepsilon}{\tau\mu}\frac{r^2}{RTl}\right)P_{ave}\right]\Delta P$$

This equation is usually simplified to give the linear expression

$$J_{total} = [\alpha_k + (\beta_V\ P_{av})]\,\Delta P$$

where α_K and β_V are the Knudsen and Poiseuille permeation coefficients, respectively. Assuming a linear pressure drop across the substrate, the values of α_K and β_V can be determined by plotting J_{Total} / ΔP against P_{av}, where α_K is the intercept and β_V the slope of the linear regression. Using the experimentally derived values for α_K and β_V, the unknown geometrical factors in J_{total} equation can be calculated. However, it is difficult to isolate either the porosity or the tortuosity uniquely, as a result they are usually reported as the ratio ε/τ .

The main observations which can be drawn from J_{total} equation are the dependence of the flux on both average pore size and temperature. The consequence is a complication on thin membranes preparation, since by reducing the surface pore size we can deposit thinner membranes, but the reduction of pore size involve a decrease of the effective permeability[21]. So, whilst enabling the deposition of thinner selective layers, smaller pore sizes add considerable resistance to permeation, causing a not negligible pressure drop in the substrate. It is also clear that flows decrease with increasing temperature. Assuming that the geometric factors ε, τ and r do not vary with temperature, the α_K and β_V permeation coefficients can be used to predict the hydrogen flux through the substrate under any conditions of pressure and temperature.

5.2.3. The leak model

If the metallic layer is not dense, but defects, such as pinholes, are present, hydrogen diffuses through the metal by solution-diffusion mechanism, but also Knudsen diffusion and viscous flow contribute to the overall flux, leading to an overestimation of the H_2 that permeates through the membrane and so to an incorrect estimation of real permeability (Fig. 5.2).

The total H_2 flux permeating through the metal foil is equal to the sum of the H_2 permeating according to the "solution-diffusion" mechanism and the H_2 permeating along the defects. The model is based on the following assumptions[22]:

- The H_2 flux permeating according to the "solution diffusion" mechanism is independent on the selectivity value;
- The H_2 flux permeating through the metal membrane follows Sieverts' law;
- Molecular H_2 diffuses through the defects according to a mixed Knudsen viscous mechanism. The amount of H_2 flowing through defects can be estimated using a leak gas diffusing through the defects[13].

The α and β coefficients, determined for the porous substrate, can turn out to be useful in order to calculate specific parameters related to the dense metallic film.

The total H_2 flux (the sum of the H_2 flowing through defects and the H_2 flowing through the metal lattice) can be described by the following equation[22] :

$$J_{H_2} = \frac{Q(T)}{l}\left(P1^{0.5} - P2^{0.5}\right) + \left[\alpha \cdot \sqrt{\frac{M_{leak\,gas}}{M_{H_2}}} + \beta \cdot \frac{\eta_{leak\,gas}}{\eta_{H_2}} P_{ave}\right](\Delta P)$$

where the H_2 flux is the sum of a solution-diffusion term, a Knudsen term (α) and viscous term (β). M are the molar masses of the hydrogen and of the gas used to measure leaks (He or N_2) and η is the viscosity of the gas. All pressures are H_2 partial pressures.

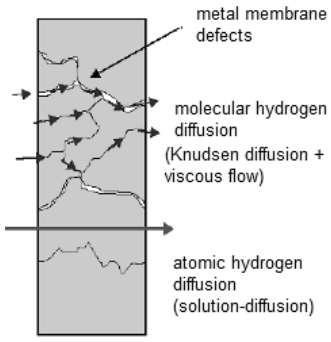

Fig. 5.2: in case of defects inside the membrane, the overall flux is non determined only by solution-diffusion but even Knudsen diffusion and viscos flow contribute (adapted from [22]).

In composite membranes having large leaks the pressure exponent n will be higher than 0.5. Mass transfer within the porous substrate adds another resistance to the overall H_2 permeation mechanism. Moreover, if the thickness of the membrane is thin enough and the porous substrate does not have a high inert gas permeance, which is the case in substrates having a low porosity, the pressure drop within the porous substrate is high and the H_2 diffusion within the porous media becomes the rate-limiting step for the H_2 permeation. If H_2 diffusion through the porous media is the rate-limiting step, the pressure exponent n is higher than 0.5 and the activation energy for H_2 permeation decreases.

References

1. Ragaini, V.; Giannantonio, R.; Magni, P.; Lucarelli, L.; Leofanti, G., Dispersion measurement by the single introduction method coupled with the back-sorption procedure: A chemisorption and TPD study of the different chemisorbed hydrogen species. II. Pd on Alumina. *Journal of Catalysis* **1994,** *146* (1), 116-125.

2. Ward, T. L.; Dao, T., Model of hydrogen permeation behavior in palladium membranes. *Journal of Membrane Science* **1999,** *153* (2), 211-231.

3. Gillespie, L. J.; Galstaun, L. S., The palladium-hydrogen equilibrium and new palladium hydrides. *Journal of the American Chemical Society* **1936,** *58* (12), 2565-2573.

4. Buxbaum, R. E.; Marker, T. L., Hydrogen transport through non-porous membranes of palladium-coated niobium, tantalum and vanadium. *Journal of Membrane Science* **1993,** *85* (1), 29-38.

5. (a) Paglieri, S. N.; Way, J. D., Innovations in palladium membrane research. *Separation and Purification Methods* **2002,** *31* (1), 1-169; (b) Li, A.; Liang, W.; Hughes, R., The effect of carbon monoxide and steam on the hydrogen permeability of a Pd/stainless steel membrane. *Journal of Membrane Science* **2000,** *165* (1), 135-141; (c) Nam, S. E.; Lee, K. H., A study on the palladium/nickel composite membrane by vacuum electrodeposition. *Journal of Membrane Science* **2000,** *170* (1), 91-99.

6. Gielens, F. C.; Knibbeler, R. J. J.; Duysinx, P. F. J.; Tong, H. D.; Vorstman, M. A. G.; Keurentjes, J. T. F., Influence of steam and carbon dioxide on the hydrogen flux through thin Pd/Ag and Pd membranes. *Journal of Membrane Science* **2006,** *279* (1-2), 176-185.

7. (a) Morreale, B. D.; Ciocco, M. V.; Howard, B. H.; Killmeyer, R. P.; Cugini, A. V.; Enick, R. M., Effect of hydrogen-sulfide on the hydrogen permeance of palladium-copper alloys at elevated temperatures. *Journal of Membrane Science* **2004,** *241* (2), 219-224; (b) Iyoha, O.; Enick, R.; Killmeyer, R.; Morreale, B., The influence of hydrogen sulfide-to-hydrogen partial pressure ratio on the sulfidization of Pd and 70 mol% Pd-Cu membranes. *Journal of Membrane Science* **2007,** *305* (1-2), 77-92.

8. (a) Mardilovich, I. P.; Engwall, E.; Ma, Y. H., Dependence of hydrogen flux on the pore size and plating surface topology of asymmetric Pd-porous stainless steel membranes. *Desalination* **2002,** *144* (1-3), 85-89; (b) Balachandran, U.; Lee, T. H.; Chen, L.; Song, S. J.; Picciolo, J. J.; Dorris, S. E., Hydrogen separation by dense cermet membranes. *Fuel* **2006,** *85* (2), 150-155.

9. Mejdell, A. L.; Klette, H.; Ramachandran, A.; Borg, A.; Bredesen, R., Hydrogen permeation of thin, free-standing Pd/Ag23% membranes before and after heat treatment in air. *Journal of Membrane Science* **2008,** *307* (1), 96-104.

10. Gade, S. K.; Thoen, P. M.; Way, J. D., Unsupported palladium alloy foil membranes fabricated by electroless plating. *Journal of Membrane Science* **2008,** *316* (1-2), 112-118.

11. Huang, T. C.; Wei, M. C.; Chen, H. I., Preparation of palladium-silver alloy composite membranes for hydrogen permeation. *Chemical Engineering Communications* **2002,** *189* (9), 1262-1282.

12. Henis, J. M. S.; Tripodi, M. K., Composite hollow fiber membranes for gas separation: the resistance model approach. *Journal of Membrane Science* **1981,** *8* (3), 233-246.

13. Mardilovich, P. P.; She, Y.; Ma, Y. H.; Rei, M. H., Defect-Free Palladium Membranes on Porous Stainless-Steel Support. *AIChE Journal* **1998,** *44* (2), 310-322.

14. Beuscher, U.; H. Gooding, C., The permeation of binary gas mixtures through support structures of composite membranes. *Journal of Membrane Science* **1998,** *150* (1), 57-73.

15. Mason, E. A.; Malinauskas, A. P.; Evans Iii, R. B., Flow and diffusion of gases in porous media. *The Journal of Chemical Physics* **1967,** *46* (8), 3199-3216.

16. Veldsink, J. W.; van Damme, R. M. J.; Versteeg, G. F.; van Swaaij, W. P. M., The use of the dusty-gas model for the description of mass transport with chemical reaction in porous media. *The Chemical Engineering Journal and The Biochemical Engineering Journal* **1995,** *57* (2), 115-125.

17. Burggraaf, A. J., Single gas permeation of thin zeolite (MFI) membranes: Theory and analysis of experimental observations. *Journal of Membrane Science* **1999,** *155* (1), 45-65.

18. Gabitto, J.; Tsouris, C., Hydrogen transport in composite inorganic membranes. *Journal of Membrane Science* **2008,** *312* (1-2), 132-142.

19. Shapiro, A. A.; Wesselingh, J. A., Gas transport in tight porous media. Gas kinetic approach. *Chemical Engineering Journal* **2008,** *142* (1), 14-22.

20. Uhlhorn, R. J. R.; Keizer, K.; Burggraaf, A. J., Gas and surface diffusion in modified γ-alumina systems. *Journal of Membrane Science* **1989,** *46* (2-3), 225-241.

21. Lin, Y. S.; Burggraaf, A. J., Experimental studies on pore size change of porous ceramic membranes after modification. *Journal of Membrane Science* **1993,** *79* (1), 65-82.

22. Guazzone, F., Engineering of Substrate Surface for the Synthesis of Ultra-Thin Composite Pd and Pd-Cu Membranes for H2 Separation, PhD Thesis. **2005**.

6. Zeolite membrane for gas separation

6.1. Zeolites

Zeolites[1] are three dimensional, microporous crystalline solids with well-defined structures containing aluminium, silicon and oxygen in their framework, made of regular channels of discrete size, accessible through pores of well-defined dimensions. Silicon and aluminium form tetrahedra, connected to each other through shared oxygen atoms. The Si/Al ratio varies considerably: from the 1:1 ratio (for zeolite X) to near infinity (in silicalite), modulating the ionicity of the material, which increases with decreasing Si/Al ratio. The SiO_4 group carries a formal charge of -4, but in a solid having an O/T (O = octahedral sites, T = tetrahedral sites) ratio of 2 (as found for all zeolite structures) this unit is neutral, because each oxygen atom is part of a bridge between two T atoms. AlO_4 tetrahedra have a -1 charge, so the overall zeolite framework is negatively charged. These negative charges can be compensated with pentavalent T-atoms (P^{5+} in aluminophosphates) or with cations or protons. Zeolites can be classified into small, medium, large and ultra-large pore materials. Small pore structures have pore openings with six, eight or nine tetrahedra, medium pore frameworks have 10-membered rings, large pore zeolites have 12-membered rings and ultra-large structures have 14-, 18- or 20- membered rings. Many zeolites are thermally stable to over 500°C and are stable in alkaline and acidic environments. They have a strong resistance in harsh environment and tolerate high pressure drops.

The main drawbacks are brittleness and difficulty in scaling-up to industrial production. Zeolites are employed as size-selective reactors (thanks to the uniform pore dimensions), ion exchange applications and in tuning acidity or basicity. Zeolites can be used in gas separation processes[1b,2], but, a great size difference between the molecules to separate is required for high selectivity. Many types of zeolite membrane have been studied (e.g. Mordenite Framework Inverted – MFI, Linde Type A - LTA, mordenite - MOR, faujasite - FAU) and the first commercial application is that of LTA zeolite membranes[3]. No industrial applications are reported for zeolite membranes in the gas separation field[4], due to poor reproducibility. A H_2/N_2 selectivity of 24 was reported for the small-pore zeolite A[5], but no higher values were

reported, due to the presence of intercrystalline spaces in the zeolite layer. Furthermore, the separation of hydrogen from other gases, e.g. CO_2, is difficult due to similar kinetic diameters (Tab. 6.1). As to estimated costs zeolite membrane modules, can be expected that, once in mass use and production, costs will reduce significantly to less than \$1,000/m^2 [6].

Among the several zeolites available, hydroxy-sodalite can be a promising choice for the development of zeolite membranes for hydrogen separation. Hydroxy-sodalite has a six-membered ring aperture with a pore size of 2.8-3 Å, with a Si/Al ratio of 1 ($Na_8[AlSiO_4]_6(OH)_2 \cdot nH_2O$, $0 < n \leq 4$). Only small molecules, such as helium, hydrogen and water, etc., can enter the pores of hydroxy-sodalite. Despite the potential of hydroxy-sodalite, only a limited amount of literature currently exists dealing with the synthesis of hydroxy-sodalite membranes[7,8,9].

Molecule	Kinetic diameter (Å)	Molecule	Kinetic diameter (Å)
H_2O	2.65	CH_4	3.76
H_2	2.89	C_2H_4	4.16
CO_2	3.30	C_2H_6	4.44
O_2	3.47	n-C_4H_{10}	4.69
N_2	3.64	i-C_4H_{10}	5.28
CO	3.69	SF_6	5.50

Tab. 6.1: kinetic diameters for some molecules.

6.2. Preparation of zeolite membranes

Zeolite membranes can be self-standing or grown on suitable substrates. Different methods for the preparation of supported zeolite membranes have been established[4a]. Basically, they can be distinguished into one-step methods (in situ) and in secondary growth (seeding techniques) methods. In situ synthesis was the first to be used; the main advantage is the minimal number of preparation steps, but membrane shows substrate coverage dishomogeneitis and thickness discontinuity. The seeding technique (depositions of seeds – 50-1000 nm – before the crystal growth), separating zeolite nucleation from crystal growth, allows optimizing the conditions of each step independently, reducing or suppressing any secondary nucleation[10]. Many methods are employed to deposit zeolite seeds: dip-coating, filtration, rubbing, electrostatic and chemical deposition. Seeding is a very complex step, since it requires a reliable seeds step preparation and the seeds distribution has to be homogenous. A

membrane grown by secondary growth shows high flux and the possibility to orient the seed crystals[11], but the main drawback is the ease of formation of defects, which do not allow the selectivity required for a gas separation membrane.

A typical one-step synthesis mixture contains the silica source (colloidal silica, fumed silica, sodium silicate, tetraethyl orthosilicate, etc.), the alumina source (aluminium hydroxide, sodium aluminate, aluminium salts, aluminium powder), a structure-directing agent (SDA), if present (amines, tetralkylammonium salts, crown-ethers, etc.), a base (alkali and/or organic bases) and water as solvent. After homogenization, the as prepared gel is poured into an autoclave containing the porous substrate. Zeolite membranes are usually grown on rigid inorganic substrates, with a high stability in hydrothermal and alkaline synthesis conditions, low gas diffusion resistance, a smooth surface without defects and affinity with the membrane layer material. Ceramics materials (α-alumina, titania, silica) or stainless steel are the most common substrates. Since zeolites usually have negative thermal expansion coefficients (they contract upon heating[12]), the choice of the right substrate is very important[13]. Recently, some efforts have been done to prepare high quality zeolite films on relatively cheap and macroporous tubular substrates[14,15]. The use of cheap porous substrate is an active part of zeolite membrane research, since the substrate may constitute up to 70% of the total membrane cost.

6.2.1. Hydrothermal synthesis

Hydrothermal synthesis[1c, 16] was identified as an important technology for materials synthesis in the 20th century. Generally, hydrothermal synthesis employs single or heterogeneous phase reactions in aqueous media, at elevated temperature and pressure, to prepare crystalline ceramic materials directly from solution. In most cases, syntheses are performed at autogenous pressure. Hydrothermal synthesis allows the control of rate and uniformity of nucleation, growth and aging, improving the control on size and morphology of crystallites and reducing aggregation, with a better microstructure control. Another important advantage is the purity of synthesized materials, since hydrothermal crystallization is a self-purifying process, characterized by the rejection of impurities present in the growth environment during crystals/crystallites growing. Hydrothermal processing can take place in a wide variety of combinations of aqueous and solvent mixture-based systems. Liquids accelerate

diffusion, adsorption, reaction rate and crystallization and one of the most employed liquid is water. It has many advantages: it is environmentally friendly and it is cheaper than other solvents and by simply tuning the temperature and pressure process it can act as a catalyst. Moreover, it can be easily removed from the reaction products. Hydrothermal synthesis can be hybridized with other processes like microwave, electrochemistry, ultrasounds, mechano-chemistry, optical radiation and hot pressing.

Crystal growth under hydrothermal conditions requires a reaction vessel (autoclave). The autoclave must be capable to resist the chemical aggression at high temperature and pressure for long time. The most resistant materials are high strength alloys, such as 316 series stainless steel, iron, nickel, cobalt based super alloys and titanium and its alloys. To avoid corrosion of the autoclave material, a non-reactive material coating, such as Teflon, is used.

6.3. Permeation of gas through a zeolite membrane

The transport of gas through a zeolite membrane, as a function of temperature, is described by Fig. 6.1[17]:

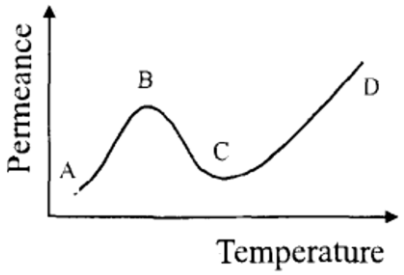

Fig. 6.1: diagram showing the dependence of single gas permeance with temperature (from [17]).

Initially (A→B), the permeance increases since the increase in temperature enhances the mobility of adsorbed species, even though the amount of physically adsorbed material starts to decrease. Eventually, point B is reached, and from this temperature the decline in occupancy prevails, giving rise to a decrease in permeance (B→C). At a sufficiently high temperature (C) the effect of adsorption becomes negligible, and the permeance is controlled by activated transport through micropores, increasing with temperature (C→D). The transport of gases in zeolite has been described by the superposition of Stefan Maxwell approach at low

temperatures, which takes into account only adsorption[18], and activated Knudsen diffusion at higher temperatures[19].

The first step of gas permeation is the adsorption of the molecules onto the zeolite surface. Up to 100-200°C, depending on zeolite structure and polarity, the more strongly adsorbed component of a gas mixture reduces or blocks permeation of other components (adsorption selectivity). The strength of the molecule/zeolite surface interaction is determined by the polarization of the molecule and by its dipole/quadrupole moments. Polarity is one of the most important parameters, which in turns relies on the chemical composition (relation between Al content and polarity) and, in general, more polar is the zeolite framework, stronger is the adsorption of gas molecules. Permeation of gases at moderate temperature is controlled by surface diffusion. It can be conveniently described by a hopping of molecules from one adsorption site to another[20]. At higher temperature, the transport of non-adsorbing and adsorbing molecules is defined by activated gaseous diffusion[21]. Excluding flow through defects, the overall flux through the zeolite membrane is a combination of surface and gaseous diffusion. The concentration of the gas in the zeolite framework reaches saturation at a certain pressure and at this point the surface diffusion flux does not further increase by increasing pressure. An increase in temperature, at constant pressure, leads to a lower concentration of adsorbed component and to a lower driving force, while the flux increases. The contribution of surface diffusion may increase, decrease or have a maximum as a function of temperature, depending on activation energy and adsorption enthalpy[22].

The main separation mechanisms by high quality zeolite membranes are:

- Adsorption selectivity: it takes place when adsorption of one component is much stronger than that of another component. It is the dominant separation mechanism at low temperatures;
- Diffusion selectivity: it takes place when molecules of one component are smaller and their diffusivity is faster than that of larger component. It increases with temperature;
- Size exclusion (molecular sieving): it is an extreme case of diffusion selectivity, when one component can scarcely or not at all permeate through zeolite pores.

If zeolite membranes have defects Knudsen diffusion, molecular diffusion and even viscous flow can become the dominant diffusion mechanisms[23].

References

1. (a) Caro, J.; Noack, M., Zeolite membranes - Recent developments and progress. *Microporous and Mesoporous Materials* **2008,** *115* (3), 215-233; (b) Caro, J.; Noack, M.; Kölsch, P.; Schäfer, R., Zeolite membranes - state of their development and perspective. *Microporous and Mesoporous Materials* **2000,** *38* (1), 3-24; (c) Cundy, C. S.; Cox, P. A., The hydrothermal synthesis of zeolites: Precursors, intermediates and reaction mechanism. *Microporous and Mesoporous Materials* **2005,** *82* (1-2), 1-78; (d) Davis, M. E.; Lobo, R. F., Zeolite and molecular sieve synthesis. *Chemistry of Materials* **1992,** *4* (4), 756-768.

2. Yang, M.; Crittenden, B. D.; Perera, S. P.; Moueddeb, H.; Dalmon, J. A., The hindering effect of adsorbed components on the permeation of a non-adsorbing component through a microporous silicalite membrane: The potential barrier theory. *Journal of Membrane Science* **1999,** *156* (1), 1-9.

3. Morigami, Y.; Kondo, M.; Abe, J.; Kita, H.; Okamoto, K., The first large-scale pervaporation plant using tubular-type module with zeolite NaA membrane. *Separation and Purification Technology* **2001,** *25* (1-3), 251-260.

4. (a) Caro, J.; Noack, M.; Kölsch, P., Zeolite membranes: From the laboratory scale to technical applications. *Adsorption* **2005,** *11* (3-4), 215-227; (b) McLeary, E. E.; Jansen, J. C.; Kapteijn, F., Zeolite based films, membranes and membrane reactors: Progress and prospects. *Microporous and Mesoporous Materials* **2006,** *90* (1-3 SPEC. ISS.), 198-220.

5. Xu, X.; Yang, W.; Liu, J.; Chen, X.; Lin, L.; Stroh, N.; Brunner, H., Synthesis and gas permeation properties of an NaA zeolite membrane. *Chemical Communications* **2000,** (7), 603-604.

6. Ockwig, N. W.; Nenoff, T. M., Membranes for hydrogen separation. *Chemical Reviews* **2007,** *107* (10), 4078-4110.

7. Nabavi, M. S.; Mohammadi, T.; Kazemimoghadam, M., Hydrothermal synthesis of hydroxy sodalite zeolite membrane: Separation of H2/CH4. *Ceramics International* **2014,** *40* (4), 5889-5896.

8. Xu, X.; Bao, Y.; Song, C.; Yang, W.; Liu, J.; Lin, L., Microwave-assisted hydrothermal synthesis of hydroxy-sodalite zeolite membrane. *Microporous and Mesoporous Materials* **2004,** *75* (3), 173-181.

9. Julbe, A.; Motuzas, J.; Cazevielle, F.; Volle, G.; Guizard, C., Synthesis of sodalite/αAl2O3 composite membranes by microwave heating. *Separation and Purification Technology* **2003,** *32* (1–3), 139-149.

10. Lovallo, M. C.; Gouzinis, A.; Tsapatsis, M., Synthesis and characterization of oriented MFI membranes prepared by secondary growth. *AIChE Journal* **1998,** *44* (8), 1903-1913.

11. Lai, Z.; Bonilla, G.; Diaz, I.; Nery, J. G.; Sujaoti, K.; Amat, M. A.; Kokkoli, E.; Terasaki, O.; Thompson, R. W.; Tsapatsis, M.; Vlachos, D. G., Microstructural optimization of a zeolite membrane for organic vapor separation. *Science* **2003,** *300* (5618), 456-460.

12. Lightfoot, P.; Woodcock, D. A.; Maple, M. J.; Villaescusa, L. A.; Wright, P. A., The widespread occurrence of negative thermal expansion in zeolites. *Journal of Materials Chemistry* **2001,** *11* (1), 212-216.

13. (a) Den Exter, M. J.; Van Bekkum, H.; Rijn, C. J. M.; Kapteijn, F.; Moulijn, J. A.; Schellevis, H.; Beenakker, C. I. N., Stability of oriented silicalite-1 films in view of zeolite membrane preparation. *Zeolites* **1997,** *19* (1), 13-20; (b) Dong, J.; Lin, Y. S.; Hu, M. Z. C.; Peascoe, R. A.; Payzant, E. A., Template-removal-associated microstructural development of porous-ceramic-supported MFI zeolite membranes. *Microporous and Mesoporous Materials* **2000,** *34* (3), 241-253.

14. (a) Wang, Z.; Ge, Q.; Gao, J.; Shao, J.; Liu, C.; Yan, Y., High-Performance Zeolite Membranes on Inexpensive Large-Pore Supports: Highly Reproducible Synthesis using a Seed Paste. *ChemSusChem* **2011,** *4* (11), 1570-1573; (b) Ma, J.; Shao, J.; Wang, Z.; Yan, Y., Preparation of Zeolite NaA Membranes on Macroporous Alumina Supports by Secondary Growth of Gel Layers. *Industrial & Engineering Chemistry Research* **2014,** *53* (14), 6121-6130.

15. (a) Peng, Y.; Zhan, Z.; Shan, L.; Li, X.; Wang, Z.; Yan, Y., Preparation of zeolite MFI membranes on defective macroporous alumina supports by a novel wetting–rubbing seeding method: Role of wetting agent. *Journal of Membrane Science* **2013,** *444*, 60-69; (b) Peng, Y.; Lu, H.; Wang, Z.; Yan, Y., Microstructural optimization of MFI-type zeolite membranes for ethanol-water separation. *Journal of Materials Chemistry A* **2014,** *2* (38), 16093-16100.

16. Cundy, C. S.; Cox, P. A., The hydrothermal synthesis of zeolites: History and development from the earliest days to the present time. *Chemical Reviews* **2003,** *103* (3), 663-701.

17. Coronas, J.; Santamaría, J., Separations using zeolite membranes. *Separation and Purification Methods* **1999,** *28* (2), 127-177.

18. (a) Krishna, R.; van den Broeke, L. J. P., The Maxwell-Stefan description of mass transport across zeolite membranes. *The Chemical Engineering Journal and The Biochemical Engineering Journal* **1995,** *57* (2), 155-162; (b) Krishna, R.; Baur, R., Modelling issues in zeolite based separation processes. *Separation and Purification Technology* **2003,** *33* (3), 213-254.

19. (a) Bakker, W. J. W.; Van Den Broeke, L. J. P.; Kapteijn, F.; Moulijn, J. A., Temperature Dependence of One-Component Permeation through a Silicalite-1 Membrane. *AIChE Journal* **1997,** *43* (9), 2203-2214; (b) Burggraaf, A. J., Single gas permeation of thin zeolite (MFI) membranes: Theory and analysis of experimental observations. *Journal of Membrane Science* **1999,** *155* (1), 45-65.

20. (a) Shelekhin, A. B.; Dixon, A. G.; Ma, Y. H., Theory of gas diffusion and permeation in inorganic molecular-sieve membranes. *AIChE Journal* **1995,** *41* (1), 58-67; (b) Yoshioka, T.; Nakanishi, E.; Tsuru, T.; Asaeda, M., Experimental studies of gas permeation through microporous silica membranes. *AIChE Journal* **2001,** *47* (9), 2052-2063.

21. (a) Xiao, J.; Wei, J., Diffusion mechanism of hydrocarbons in zeolites-I. Theory. *Chemical Engineering Science* **1992,** *47* (5), 1123-1141; (b) Gan, F.; Zhang, Z.; Zhu, J.; Liu, H.; He, Z.; Tian, H., Activated gaseous diffusion and support layer resistance of MFI zeolite membrane in separation of n-butane and i-butane. *Shiyou Huagong/Petrochemical Technology* **2009,** *38* (3), 284-289; (c) Gan, F.; Zhang, Z.; Zhu, J.; Liu, H.; Li, Y.; Shao, Q.; He, Z.; Tian, H., Roles of activated gaseous diffusion and support resistance in MFI zeolite membrane separation. *Beijing Huagong Daxue Xuebao (Ziran Kexueban)/Journal of Beijing University of Chemical Technology (Natural Science Edition)* **2008,** *35* (6), 6-11.

22. Kapteijn, F.; Van De Graaf, J. M.; Moulijn, J. A., One-component permeation maximum diagnostic tool for silicate-1 membrane. *AIChE Journal* **2000,** *46* (5), 1096-1100.

23. Jareman, F.; Hedlund, J.; Creaser, D.; Sterte, J., Modelling of single gas permeation in real MFI membranes. *Journal of Membrane Science* **2004,** *236* (1-2), 81-89.

7. Experimental part

7.1. Metallic membranes preparation

The research activity deals with the preparation of alloys for hydrogen separation and purification (Pd-Ag and vanadium based alloys), comparing results obtained with two PVD deposition processes, DCMS and the new thin film deposition technique HiPIMS, described in chapter 3. With the use of this new technology we wanted to deposit very thin membranes of alloy to prepare hydrogen separation membrane directly onto porous ceramic substrates. This is the first work with HiPIMS technique employed to prepare membrane for hydrogen separation, and it represents an evolution compared to common magnetron sputtering and other thin film deposition techniques that can simplify the preparation of those membranes, in view of a scale-up.

7.1.1. Deposition details

All the metallic membranes were prepared employing PVD technologies: magnetron sputtering and HiPIMS. We studied several parameters in order to prepare dense and defect-free membranes:

- Deposition temperature and time;
- Inert gas pressure in the vacuum chamber;
- DC Power or Pulsed Power;
- Bias voltage.

In Tab. 7.1 are shown the parameters studied:

	DCMS	HiPIMS
Deposition temperature	RT – 200°C – 300°C	RT – 350°C
Deposition duration	30 ÷ 60 min	20 ÷ 360 min
Inert gas pressure	$3.1 \cdot 10^{-3} \div 1.1 \cdot 10^{-2}$ mbar	$1.0 \cdot 10^{-2}$ mbar
Bias applied	-50/-100/-150/-200/-250 V	-25/-75/-150 V + alternating

Tab. 7.1: parameters studied for the thin membrane alloy depositions.

The parameters that mostly influence the film structure/morphology in a PVD process are pressure and substrate temperature, since they have strong effects on the mobility of adatoms, modifying the morphology and the microstructure of the growing films. Thornton model can help on suggesting some parameters but the model is based on a metallic and dense substrates. Bias can help in obtaining denser and well-adherent films; in DCMS it was exploited in order to improve the microstructure of the film and its adherence to the substrate, while in the case of HiPIMS bias it is a very important deposition parameter, because it drives the ions produced in the sputtering process directly on the specimen to coat, changing drastically the morphology and the microstructure of the grown film.
Below are reported the technical details of the PVD machineries used in the activity:

- **Magnetron Sputtering:**

Fig. 7.1: magnetron sputtering machine. The chamber used for the depositions is the one on the left.

General chamber features	Con-focal geometry, 3 magnetron cathodes (size: 2'')
Heating system	3 light bulbs (450 W), T_{max} 400°C
Power supply	DC power supply: Pinnacle 6 kW (Advanced Energy) RF power supply: Dressler 1310 (Cesar) Bias unit: Sorensen DCR 600-4,5 B (maximum voltage 600 V)
Vacuum line	Pre-vacuum pump: rotary pump Adixen Pascal 2015 I High- vacuum pump: TPU 170 Pfeiffer
Base vacuum	$< 10^{-6}$ mbar
Sputter gas	Argon
Targets/substrate distance	6 cm
Sample rotation	2 RPM
Cooling system	Green Box model MEC 35 WVP

Tab. 7.2: technical details of magnetron sputtering machine.

- **HiPIMS:**

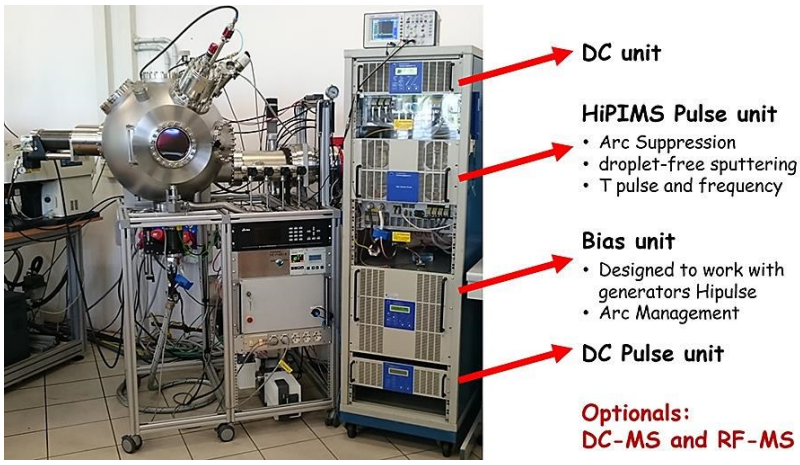

Fig. 7.2: HiPIMS machine.

General features	Spherical chamber with three cathodes (2 magnetrons size 4'' and 1 magnetron size 2'')
Heating system	8 light bulbs (1200 W), T_{max} 800°C
Power supply	True Plasma HighPulse DC unit - 1 kW (Huttinger Elektronic) Trueplasma HighPulse 4002 - 10 kW (Huttinger Elektronic) Trueplasma DC 4001 (Huttinger Elektronic) Bias unit: Trueplasma Bias 3018 - Maximum voltage 1200 V – (Huttinger Elektronic)
Vacuum line	Pre-vacuum pump: Adixen Pascal 2021 C1 High vacuum pump: Pfeiffer HiPACE 700 DN 160 CF-F, 3P
Base vacuum	$< 10^{-7}$ mbar
Sputter gas	Argon
Targets/substrate distance	Pd-Ag alloy: Pd (HiPIMS) 120 mm - Ag (DC pulsed) 150 mm V-Pd alloy: V (HiPIMS) 120 mm - Pd (DC pulsed) 200 mm
Pulse	22-25-50 µs
HiPIMS target	Palladium (Pd-Ag alloy) Vanadium (V-Pd alloy)
DC pulsed target	Silver (Pd-Ag alloy) Palladium (V-Pd alloy)
Sample rotation	5 RPM
Cooling system	Green Box model MEC 35 WVP/PHP SP

Tab. 7.3: technical details of HiPIMS machine.

7.2. Zeolite membrane preparation

The aim was the preparation of a zeolite membrane, supported onto a porous ceramic substrate, prepared by only one hydrothermal synthesis step. Hydroxy-sodalite membranes are

already available in scientific papers[1], but we investigated a simplification of the preparation step by modifying the synthesis parameters (hydrogel ageing and hydrothermal synthesis).

We started from very basic reagents:

- NaOH (pellets);
- Aluminium powder (Alfa Aesar, 325 mesh, 99.97%);
- Colloidal silica (Sigma Aldrich, 30 wt% suspension in water).

We prepared the hydrogel according to one of the most common hydroxy-sodalite stoichiometry $5SiO_2 : 1Al_2O_3 : 50NaOH : 1000H_2O$. Sodium silicalite and sodium aluminate solutions were prepared by adding aluminium powder and colloidal silica in distinct NaOH solutions, pre-heated at 50°C. At the end, both solutions were let to rest for one hour, until the solutions become completely transparent. Then, we added dropwise the sodium aluminate solution into the sodium silicate solution, under vigorous stirring. We studied different ageing temperatures and times of the mixture:

- Ageing temperature: 50°C / 60°C;
- Ageing time: 30 min, 2h / 12h / 24h.

After ageing the hydrogel was placed inside a Teflon liner in the autoclave (Parr autoclave, Series 4760, Parr Instruments Company), together with the porous alumina substrates described in chapter 4. The substrates were placed slightly tilted in the middle of the hydrogel, employing a Teflon home-made sample holder. The hydrothermal synthesis was carried for different times (from 2h to 4h), at different temperatures (from 90°C to 150°C), autogenous pressures. After the hydrothermal synthesis, the pellets were rinsed in deionized water, to reduce the pH of the membranes (due to NaOH residues) and were dried at room temperature.

7.3. Ceramic porous substrates

We prepared the ceramic porous substrates by mixing α-Al_2O_3 (Alfa Aesar, 99.9%, < 1.0 Micron APS powder) and pore former:

- Pore formers: starch (Sigma Aldrich), polymethilmethacrylate (PMMA, Soken);

- Powders ratio (α-Al_2O_3/pore former vol%): 80/20 – 70/30 – 60/40 – 50/50 – 35/65.

We weighted α-Al_2O_3 and pore former according to the chosen ratio and the mixtures were ball milled in milling jars (ZrO_2, 45 mL capacity). 12 milling balls (ZrO_2) of 1 cm diameter and 25 milling balls (ZrO_2) of 0.5 cm diameter were used. To assure a good powder homogenization anhydrous ethanol was used as dispersing agent. The ball milling process (Planetary Miller Pulverisette 7, Fritsch) was divided in steps of 20 min of milling at 350 RPM and 15 min of pause, for a total of 2 hours of milling. After drying ethanol, powders were sifted (100 mesh sieve). We prepared disk-shaped pellets, 2.5 cm diameter, by uniaxial dry pressing (Mignon SS-EA, Ceramic Instruments) at 141 MPa and de-aeration time 30 sec. The pellets prepared were sintered in a muffle (HT 04/17, Nabertherm) at atmospheric conditions and then measured and weighted to determine the geometric density and the porosity. A sintering procedure was developed to achieve planar and mechanically stable pellets. After various tests and according to TGA analyses the optimal procedure was identified:

PMMA:

- RT – 385°C at 180°C/h;
- 385°C 1h to allow the complete burning of pore former;
- 385°C – 1000°C at 300°C/h, very fast rate since no specific events are present;
- 1000°C – 1500°C at 30°C/h, very slow heating rate to avoid pellets deformation;
- 1500°C – RT free cooling.

Starch:

- RT - 300°C at 60°C/h;
- 300°C 1h to allow a complete burning of the majority of starch;
- 300°C – 400°C at 60°C/h;
- 400°C 1h to complete the burning of all the starch;
- 400°C – 800°C at 60°C/h;
- 800°C 1h, intermediate isotherm to prevent pellets deformation;
- 800°C – 1500°C at 120°C/h;
- 1500°C 1h;
- 1500°C – 800°C at 120°C/h, to avoid internal stresses;

- 800°C – RT free cooling.

In order to remove surface sintering defects they were polished with SiC sandpapers and then sonicated for ten minutes in deionized water to remove polishing debris.
The mean porosity of the pellets was calculated by the equation:

$$\text{Mean porosity } (\%) = \left(1 - \frac{\text{geometrical pellet density}}{\text{alumina density}}\right) \text{x } 100$$

The geometrical density was calculated measuring the mean diameter thickness and weighting the pellet; the value of 3.98 g/cm^3 was considered for alumina density.

7.4. Characterization techniques

7.4.1. SEM/EDS

SEM is used when is necessary to gather information about the surface or near-surface region of a specimen. SEMs consist of an electron gun (primary electrons generation), an electron optical column (electrons focusing and scanning on the sample surface), a vacuum system, electronics and software. Three types of electron sources exist, and the most important parameter is the brightness, which determines resolution, contrast and signal-to-noise capabilities of the imaging system:

- **Tungsten filament:** it is a very stable source of electrons, but offers lower brightness and has limited lifetimes.
- **Lanthanum hexaboride:** it can provide brightness up to ten times the tungsten filament and has longer lifetimes, but it requires higher vacuum levels.
- **Field emission guns (FEG):** they are the most expensive electron source and provide the highest imaging and analytical performance. The higher brightness and greater current density allow a better spatial resolution and a more precise X-ray analysis.

The electron beam is focused on the sample by electromagnetic lenses, whose power is changed by changing the current passing through the coils of the lens. The electronic beam

is scanned in a rectangular raster, and the interaction between electron beam and sample produces a series of events:

- Absorption or scattering of electron by the sample. Absorption causes amplitude contrast in the image, while scattering causes phase contrast. In crystalline samples, electrons are scattered in distinct directions that are function of the crystal structure, producing diffraction contrast in the image.
- Primary electrons can be deflected at large angles or reflected by sample nuclei, becoming “backscattered electrons”. They have energies higher than 50 eV and carry information about the atomic number of the interaction zone (few μm), the topography and the crystal structure of the sample. Primary electrons can also knock electrons from sample atoms producing “secondary electrons”. They have lower energies than backscattered ones and are emitted from the first atomic layers, bringing topographic information.
- The electron beam causes sample atoms to emit characteristic X-rays, very useful for microanalysis, or photons (cathodoluminescence).

X-rays emission is exploited in the energy-dispersive X-ray spectroscopy (EDS). The amount of X-rays emitted by each element is correlated to the concentration of that element. An EDS system typically consists of a semiconductor detector housed with a field-effect transistor (FET) preamplifier, cooled to a sub-ambient temperature and a main amplifier that provides further amplification and a fast pulse inspection function. All elements, except hydrogen and helium, produce characteristic X-rays; even lithium is excluded due to practical restrictions concerning a minimum energy level. Low energy X-ray emission is strongly affected by the geometry of the sample: rough or fractured surfaces can deviate the direction of the X-rays from the ideal linear path, causing a high variability in the results. EDS allows qualitative and quantitative analyses. The most basic approach is qualitative analysis, the identification of elements inside the sample by matching each peak to an element list. The minimum detectability limit varies according to the elements involved. Transition metals tend to have high count rates, with well-defined isolated peaks superimposed to a low background, allowing the system to detect low concentrations. Non-metallic elements generate much lower count rates, making it difficult to detect them at low concentrations. Despite these differences,

EDS can usually detect an element present in a sample at concentrations in the range 1000/5000 ppm. EDS allows also 2D mapping.

SEM was used to characterize all the materials (porous pellets, metallic alloys and zeolite membranes), in order to study the variation of morphology and microstructure by changing the experimental parameters. EDS spectroscopy was used as a first characterization technique to identify and quantify the elements present in the metallic alloys. The microscope is a FEG-SEM Sigma Zeiss. It has a high quality "in lens" detector, coaxial and integrated inside the lens, where the secondary electron are accelerated to high energies by a magnetic and electrostatic lens (Gemini technology). The system is completed by an EDS (Oxford X-MAX).

7.4.2. X-ray diffraction – XRD

X-ray diffraction (XRD) was used to verify the crystallinity grade of samples and to gather information about the relative abundance of phases and the lattice parameters by Rietveld refinement. X-ray diffraction is an analytical technique based on the constructive interference between a monochromatic beam of X-rays and a crystalline sample. X-ray powder diffraction is most widely used for the identification of unknown crystalline materials. The main applications are:

- characterization of crystalline materials;
- identification of fine-grained minerals that are difficult to determine optically;
- determination of unit cell dimensions;
- measurement of sample purity.

XRD can be used to:

- Determine crystal structures using Rietveld refinement;
- Determine the amounts of phases in the sample (quantitative analysis);
- Make textural measurements, such as the orientation of grains, in a polycrystalline sample.

Constructive interference comes out when Bragg law is satisfied ($n\lambda = 2d\,\mathrm{sen}\theta$), where λ is the wave length of the monochromatic X-ray beam, θ is the diffraction angle and d is the lattice spacing of the sample.

X-ray diffractometers consist of three basic elements: an X-ray tube, a sample holder and an X-ray detector. X-rays are generated in a cathode ray tube by heating a filament to produce electrons, accelerating the electrons toward a target by applying a voltage, and bombarding the target material with electrons. When electrons have sufficient energy to remove inner shell electrons of the target material (Cu, Fe, Mo, Cr), characteristic X-ray spectra are produced. Copper is the most common target material for single-crystal diffraction, with CuK_α radiation = 1.5418Å. These X-rays are collimated and directed onto the sample. During XRD analysis, the sample rotates in the path of the collimated X-ray beam at an angle θ while the X-ray detector is mounted on an arm to collect the diffracted X-rays and rotates at an angle of 2θ.

The diffractometer used in the work is a Philips X'PERT PW3710, equipped with a Philips PW 1830 generator and a Philips PW 3020 vertical goniometer. The tube with a copper anode emits CuK_α radiation in the experimental condition 40 kV and 30 mA. The sample holder is provided with a spinning system, employed in case of powders, which can rotate at 1 RPS. X rays are detected by a Xenon gas PW3011 detector. Normal operating condition are 5°-90°, with 0.02°step and a measurement time of 2 sec for step.

7.4.2.1. Rietveld refinement

Rietveld method is an iterative procedure of minimization, based on a function that includes many structural and microstructural parameters of the system. The method has been developed in the 1960s and at the beginning it was concerned to analyse the atomic position of neutron diffraction patterns. The method is based on the intensity y_{ci} of every 2θ angle of diffraction pattern and it considers the entire diffraction pattern, including the background. Working with single intensities is very useful because, especially in the case of diffraction from powders, it avoids the problems related to systematic overlap (in case of cubic or trigonal symmetries) and accidental (due to lack of resolution). The Rietveld method can extract various information from a diffraction pattern: lattice parameters, crystalline domain size, microstrain, qualitative and quantitive analyses. The single intensities can be calculated according to the function:

$$y_{ci} = s \sum_{\bar{H}} L_{\bar{H}} \, |F_{\bar{H}}|^2 \phi(\theta_i - \theta_{\bar{H}}) O_{\bar{H}} \, A + y_{bi}$$

where:

- s is the scale factor, which depends on various parameters, such as the intensity of the incident beam and the amount of specimen interacting with it;
- $\overline{H}$ is a vector of the reciprocal space belonging to the H^{th} Bragg reflection;
- $L_{\overline{H}}$ includes the Lorents factor, depending on the simmetry of the crystalline structure;
- $\phi(\theta_i - \theta_{\overline{H}})$ is the value of the function showing the reflection profile at the angular position θ;
- $O_{\overline{H}}$is the preferential orientation factor;
- A is the absorption factor;
- $F_{\overline{H}}$ is a structural factor given by:

$$F_{\overline{H}} = \sum_{j=1,\dots,n} N_j f_j \exp\left[2\pi i \overline{H} \cdot \overline{X}^j\right] \exp\left[-B_j \sin^2 \frac{\theta}{\lambda^2}\right]$$

Where:

- j are the atoms in the asymmetric unit;
- $\overline{X}^j$ is the vector of the real space showing the position of the j^{th} atom;
- f_j is the atomic form factor of the j^{th} atom, indicating how the electrons react to an electromagnetic field;
- B_j is the Debye-Waller factor;
- Nj occupancy number of every crystallographic site.

By the use of the data coming from a diffraction pattern it is possible to calculate the S quantity which should be minimized during the refinement:

$$S = \sum_i w_i \, (y_{0i} - y_{ci})^2$$

Where y_{0i} is the step intensity, y_{ci} is the value calculated from the previous equation and w_i is the weight of every point. Bigger the numbers of known parameters, more reliable are the results. Moreover, the starting parameters have to be close to the final values, in order to

perform the fit with small changes of the parameters to refine. The Goodness of Fit (GoF) is defined as the ratio R_{wp}/R_{exp}:

$$R_{wp} = \left\{ \sum_i w_i \, [y_i(obs) - y_i(calc)]^2 \, / \sum_i w_i \, [y_i(obs)]^2 \right\}^{\frac{1}{2}}$$

In which the denominator is the value minimized during the refinement. Ideally, R_{wp} should tend to the statistical value R_{exp}:

$$R_{exp} = \left[(N - P) \, / \sum_i^N w_i y_i(obs)^2 \right]^{\frac{1}{2}}$$

Where N is the number of experimental point and P is the number of parameters. R_{exp} reflects the quality of data. Reliable analyses have GoF < 2. MAUD software was used to perform the Rietvield analyses reported in the thesis; phases were identified by Match! software.

7.4.3. Thermal analyses

Thermal analyses were used mainly for the characterization of ceramic porous pellets, in order to optimize the sintering step. Two techniques were employed:

- Dilatometric analysis;
- Thermogravimetry/differential scanning calorimetry (TGA-DSC).

Dilatometric analysis quantifies the volume variations of solids, powders and liquids when are subjected to a specific temperature/time programme. We studied the shrinkage behaviour of alumina pellets prepared with different amounts of PMMA, employed as pore former. Our aim was to understand if pellets with a different amount of PMMA had comparable shrinkages in order to prepare graded porosity supports.

The dilatometer used in the work (Netzcsh, DIL 402 PC) can perform dilatometric analysis with dimensional variations up to 5000 micron, with a resolution of 8 nm/digit. It is possible to study specimens with various dimensions, up to 50 mm length and 20 mm diameter. The

temperature range is RT-1600°C, and several heating rates and temperature segments (heating, cooling, isotherms) can be programmed.

TGA-DSC analyses were performed on pore formers (PMMA and starch) to identify their exact burning temperatures. Thermogravimetric analyses were performed using TA Instruments SDTQ600, which can measure in the same time both the weight variation (TGA) and heat flux (DSC), up to 1500°C. Analyses can be performed in controlled atmosphere (dry air, wet air, N_2, CO_2, Ar and He), controlling the flux by digital mass flow controllers. A single analysis requires from 3 to 20 mg of material. TGA-DSC can be coupled with a residual gas analyser (RGA) Hiden-HPR20 QIC. The quadrupole mass analyser HAL 7 (interval 1/300 a.m.u.) can gather information about the gas species generated during the thermogravimetric analysis.

7.4.4. Adhesion properties

Scratch tests were used to evaluate metal/ceramic substrate adhesion, in order to find the adhesion force required to remove a film from its substrate. Various parameters are involved: film brittleness, adhesion to the substrate, adhesion to the pin, pin geometry, Young moduli of thin metal layer and substrate.

In these tests, a pin scratches the surface until the upper layer is removed from the substrate (Fig. 7.3). By microscopy observation (optical or electron microscopy) is possible to see the exact point were the pin removes the deposited layer, and the coefficient of friction (COF) can be evaluated from the data collected.

The applied load (expressed in Newton) is progressively increased until the separation of film from the substrate is achieved; the registration of acoustic emission (AE) signal can be useful to find the exact point of thin layer adhesion loss.

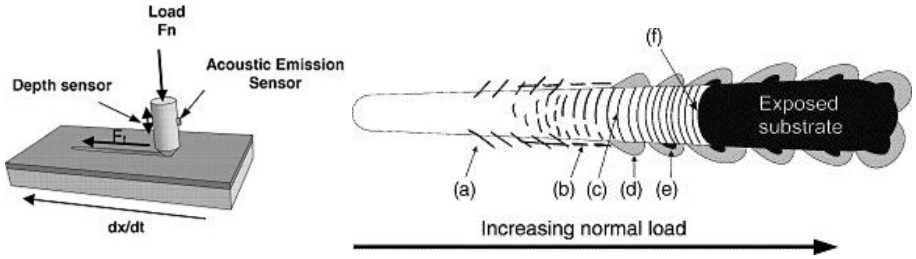

Fig. 7.3: left, scheme of a scratch test. Right, thin layer damage mechanisms during a scratch test: a) Chevron cracks, b) parallel cracks, c) hertzian cracks, d) film spalling, e) film shoulders, f) substrate exposure.

Scratch tests were performed with the CETR UMT-2 tribometer, which can work in several configurations: ball-on-disk and pin-on-disk (rotary motion of sample), or ball-on-flat and pin-on-flat (linear motion of sample). Applied force and friction can be determined with load cells, while a piezoelectric transducer reveals an amplified acoustic emission. Penetration depth is determined by an encoder connected to the load engine.

Scratch tests are carried out in the on-flat configuration, using a Rockwell C standard pin (apex angle 120°).

7.4.5. Permeation apparatus

Single gas permeation tests (hydrogen, nitrogen) were performed in a permeation test station entirely developed at CNR-ICMATE. Membranes were clamped and sealed in a stainless steel module (Fig. 7.4) using graphite gaskets, with the metallic layer facing the feed side. The module is made of two parts (feed side and permeate side), connected to each other by a small channel (Ø 0.923 ± 0.025 cm, the permeated area) closed by the membrane to test. The module was placed in a temperature controlled electric furnace (Nabertherm N11/HR). The membrane housing temperature was monitored by a K thermocouple put directly inside the module test. The pressure at the feed side is set gas flow (MKS mass flow controllers 1179B). Hydrogen is produced by electolyzer Perkin Elmer PGX Plus H_2 160. Fig. 7.5 shows a scheme of the entire station.

For permeability tests, upstream pressure was varied during the permeation tests setting a pressure from 100 kPa to 400 kPa, while the downstream pressure was fixed at atmospheric pressure (permeated hydrogen was collected by a N_2 sweep gas, 50 sccm). The analysis consisted in setting the upstream pressure (increasing the gas flux by mass flow controllers), in the feed side, at a specific value, and measuring the gas flow necessary to maintain the pressure difference desired. Flux was measured only when the system reached stationary conditions (it required a variable time, quantifiable from 5 to 10 min according to the pressure set). Once the pressure set was achieved, we waited 5 min for the pressure stabilization before to proceed with the measurement. In case of pressure oscillations, we measured the flux when those oscillations were below the 2% of the set point. The flux value had an error within the 0.5% of the reading + 0.2% of full-scale; the resolution of the flux measurements was 0.1% of full-scale. The accuracy of the pressure measurement was in the order of the

mbar. Before the permeation test, correction factor of the specific gas used must be inserted in the mass flow controller settings (Multi gas controller 647C). Flux is controlled by PID (proportional – integral – derivative controller). To control and monitor the tests a Labview interface was developed (Fig. 7.6).

A complete set of permeation data required almost a week. Prior the collection of the final permeation data, used for permeance calculations, preliminary tests were performed in order to identify permeation variations with time. Reported data were collected after flux stabilization, repeating the test at the same temperature and at the same pressure within 24h, in order to reach full membrane performance and gather permeation data in reproducible conditions.

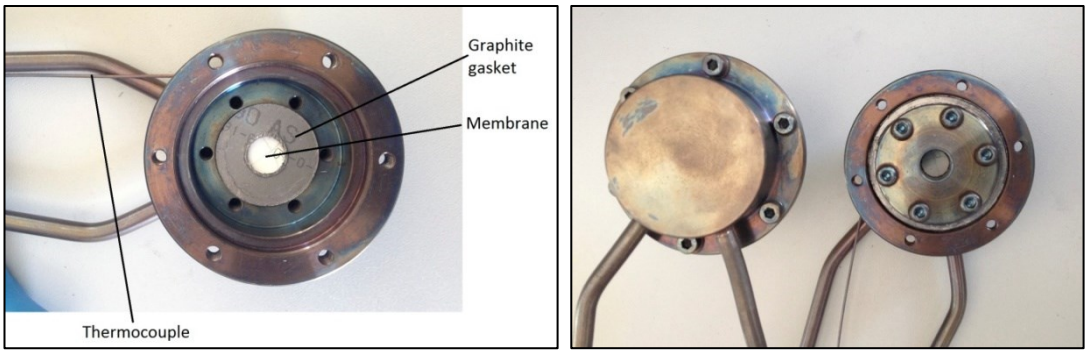

Fig. 7.4: permeation test module.

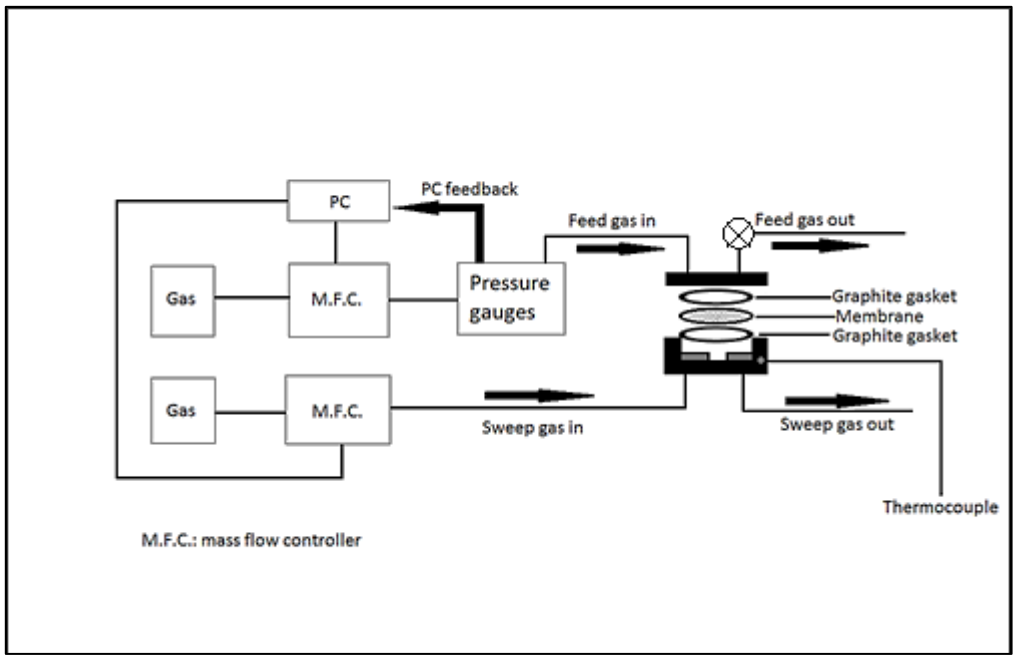

Fig. 7.5: scheme of the entire permeation test station.

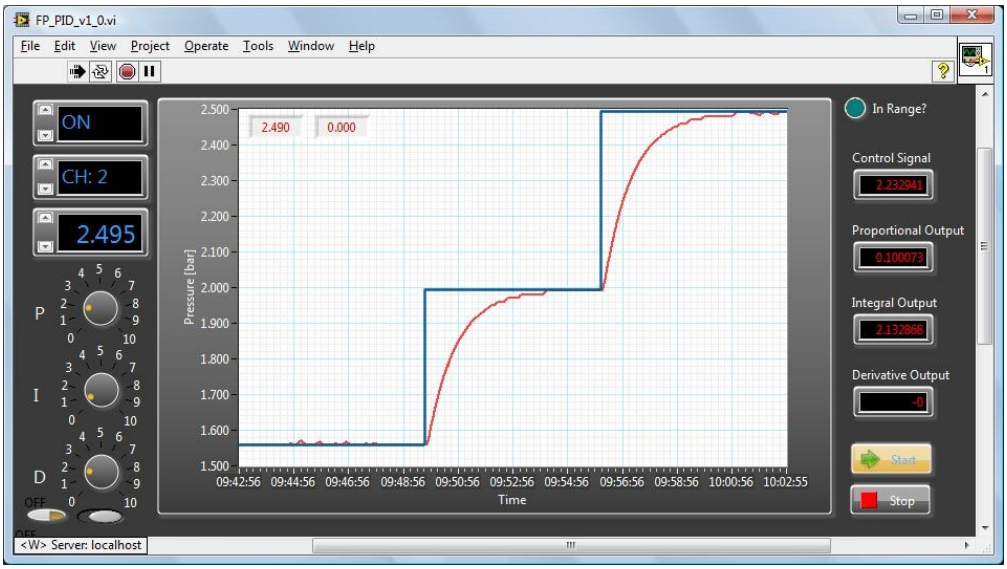

Fig. 7.6: screenshot of the Labview interface.

References

1. (a) Khajavi, S.; Sartipi, S.; Gascon, J.; Jansen, J. C.; Kapteijn, F., Thermostability of hydroxy sodalite in view of membrane applications. *Microporous and Mesoporous Materials* **2010,** *132* (3), 510-517; (b) Nabavi, M. S.; Mohammadi, T.; Kazemimoghadam, M., Hydrothermal synthesis of hydroxy sodalite zeolite membrane: Separation of H2/CH4. *Ceramics International* **2014,** *40* (4), 5889-5896; (c) Xu, X.; Bao, Y.; Song, C.; Yang, W.; Liu, J.; Lin, L., Microwave-assisted hydrothermal synthesis of hydroxy-sodalite zeolite membrane. *Microporous and Mesoporous Materials* **2004,** *75* (3), 173-181.

Discussion

8. Porous ceramic substrates preparation

In chapter 4 the main qualities of a good porous substrate were mentioned:

- Pore interconnection;
- High bulk porosity for a fast gas flow rate (porosity > 35%);
- A fine surface porosity to deposit a selective layer without defects, but sufficiently open to let the gas to flow in;
- Thermal and mechanical stabilities in operating conditions.

8.1. Alpha alumina partial sintering

We firstly approached the development of porous substrates by partial sintering of pure alpha alumina, studying various sintering temperatures (1100 – 1200 – 1300 – 1500°C). Alumina powder was simply sifted (100 mesh sieve) before pellets preparation (disk-like pellets, 2.5 cm diameter, uniaxial dry pressing at 141 MPa). The sintering route was very simple:

- From room temperature to sintering temperature at 300°C/h;
- 1h isotherm at sintering temperature;
- From sintering temperature to room temperature free cooling.

Fig. 8.1 shows the cross sections of pellets prepared:

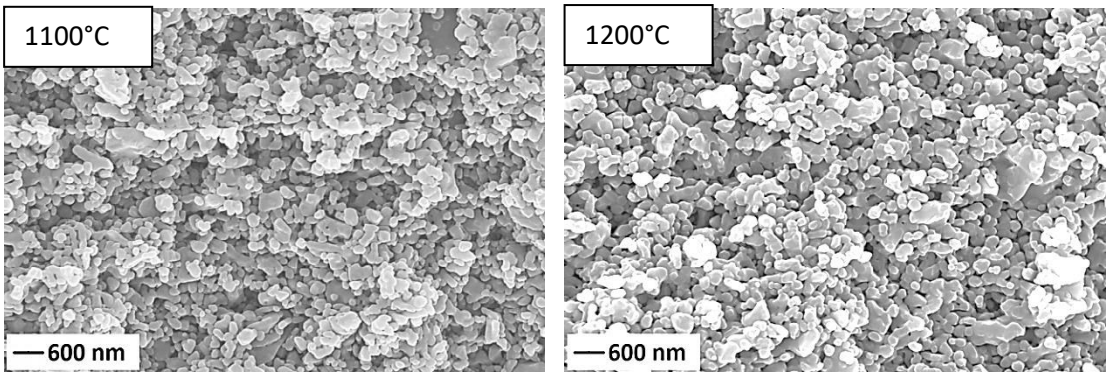

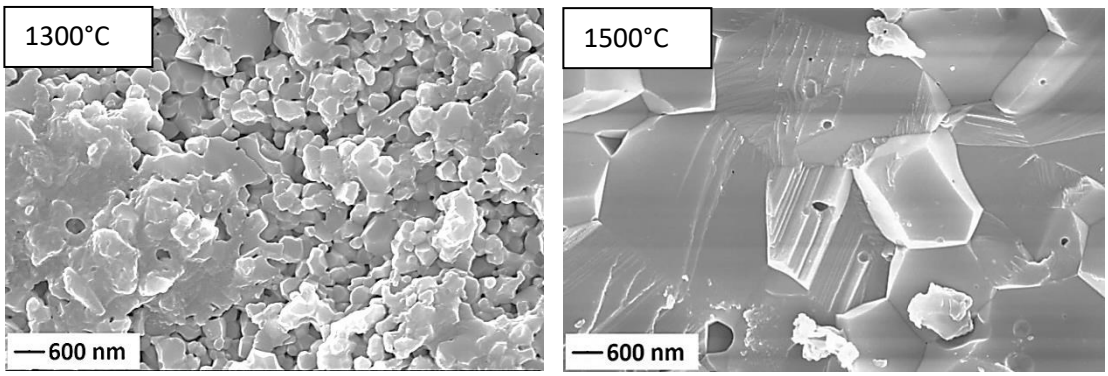

Fig. 8.1: cross sections of pure alumina pellets sintered at different temperatures.

As one could expect, higher temperatures reduced the porosity of pellets and increased the density. The 1500°C-sintered specimen was an almost full-dense material, useless for gas permeation. On the other hand, the porosity of 1100°C-sintered specimen was quite high, but the pellets easily broke if tested by applying a load. The porosity and the diameter shrinkage of pellets after the sintering step are reported in Fig. 8.2.

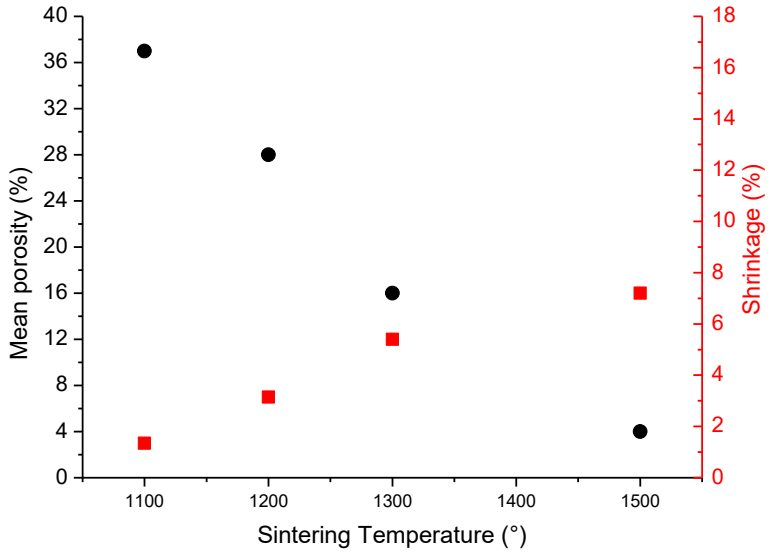

Fig. 8.2: porosity/shrinkages of pellets prepared from pure alumina powder.

Considering the lack of a proper sintering procedure to achieve both porous and stable specimens, some pore formers were investigated in order to increase sintering temperature by achieving at the same time a homogenous porosity.

8.2. PMMA

We prepared the porous ceramic substrates mixing alumina powder with poly methyl methacrylate (PMMA), available in three different mean particle sizes (7 µm, 3 µm and 1.5 µm). We studied several powder mixtures with specific volumetric ratios of Al_2O_3 and PMMA, and the preliminary results obtained pointed out the difficulty to prepare planar and thin pellets, with the desired porosity. In order to avoid pellet deformation during sintering, thermal analyses (TGA-DSC, Fig. 8.3, and dilatometry, Fig. 8.4) were performed to find the burning temperature of the pore former and the right heating rates. Dilatometric analyses were performed after a series of preliminary tests in muffle, intended to evaluate the behaviour of different powder mixtures regarding final porosity and deformation of pellets during thermal treatment, with the aim of optimizing the sintering step.

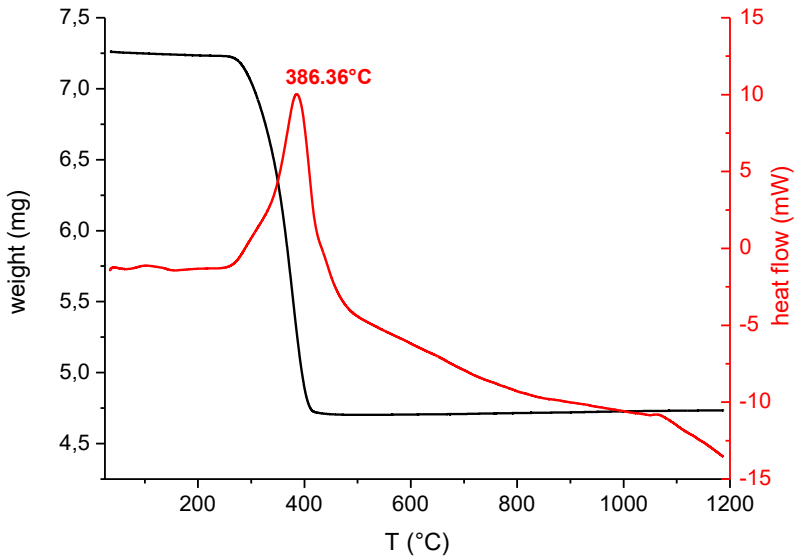

Fig. 8.3: TGA-DSC analysis performed on a sample of α-Al_2O_3/PMMA powder.

TGA-DSC analysis (RT - 1200°C at 10°C/min, free cooling, thermal treatment in air, air flux 100 mL/min) showed the main exothermic event at 386°C, so we set a specific sintering treatment having some isotherms close to this temperature to slowly burn the pore former of the powder mixture.

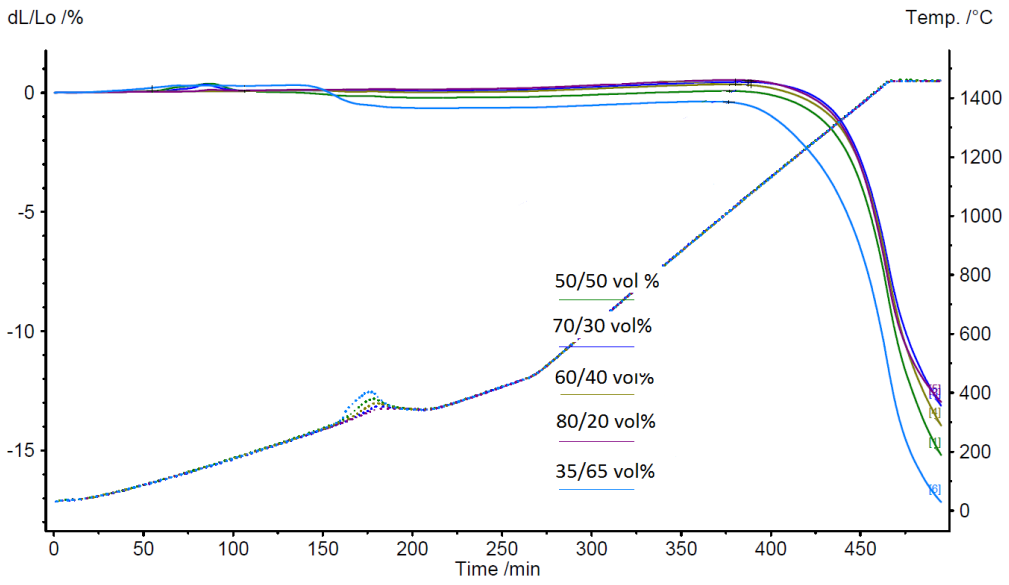

Fig. 8.4: dilatometric analyses performed on different mixtures of α-Al_2O_3/PMMA (vol%).

The dilatometric analyses (RT – 1500°C at 5°C/min, in air) showed common features:

- Before the pore former burning the size variation is within 1% and pellets do not show specific events;
- At the burning temperature of the pore former (around 400°C), the effect of exothermic pore former burning was observed;
- At T > 1000°C pellets started to shrink. The shrinkage is higher for higher amount of pore former;
- The final shrinkage varied between 13 and 17% and it seems not complete at 1500°C, thus suggesting the need for slower ramp, especially at temperatures around pore former burning.

To sum up, in the first part of the thermal analysis (from RT to ≈ 1000°C), the unique important event is the burning of the pore former, which needs an isothermal step for complete burning. After 1000°C, heating rate has to be slowed down to avoid deformation and defects formation in pellets, until the final temperature is achieved.

The results gathered from these thermal analyses were combined in the following sintering route:

- Room temperature – 385°C at 180°C/h;
- 385°C for 1h, to allow the complete burning of pore former;

- 385°C – 1000°C at 300°C/h, very fast heating rate;
- 1000°C – 1500°C at 30°C/h, very slow heating rate to avoid pellets deformation;
- 1500°C – room temperature free cooling.

8.2.1. PMMA / alpha alumina powder mixtures

Several powder mixtures alumina/PMMA were prepared (volumetric ratio: 80/20 – 70/30 – 60/40 – 50/50 – 35/65) and various PMMA powders having different size were tested, especially 7 and 1.5 µm. Fig. 8.5 reports SEM pictures of powder mixtures prepared with different amounts of PMMA 7 µm:

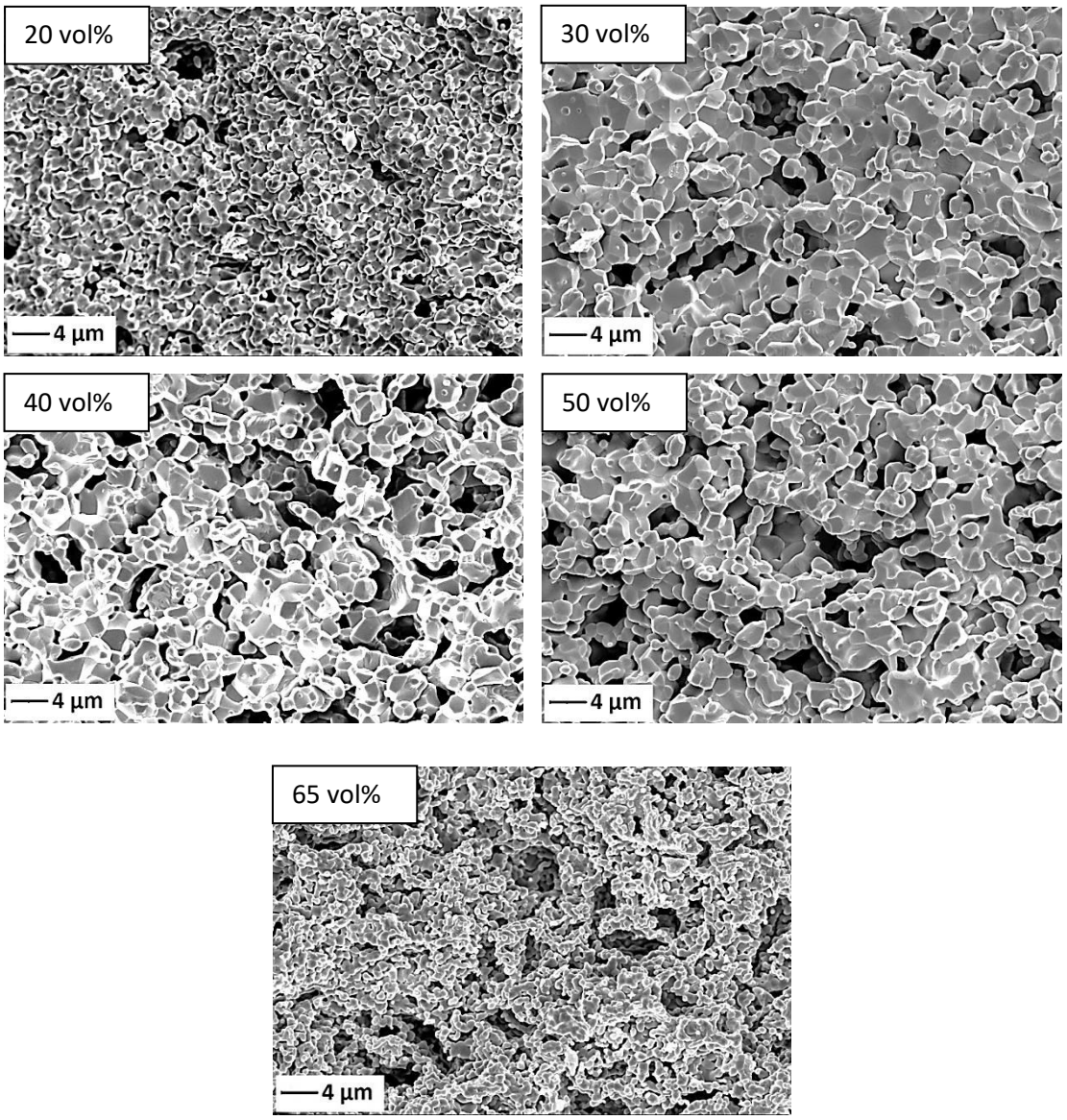

Fig. 8.5: cross section of pellets prepared with different amounts of PMMA 7 µm.

We can clearly see the large voids (> 4 µm) left after the thermal treatment. Pellets prepared with 50 vol% and 65 vol% of PMMA have a high porosity (Tab. 8.1) but those voids can be detrimental for the compactness of sputtered membranes. Improvements in microstructure are required, to prepare pellets with high and more homogenous porosity, with a good pore interconnection.

We tried to modify the powder mixtures adding 3 wt% polyvinyl butyral (PVB) as ceramic powder binder. Fig. 8.6 reports SEM picture of the cross section of a pellet prepared adding PVB to a 50/50 vol% alumina/pore former powder mixture:

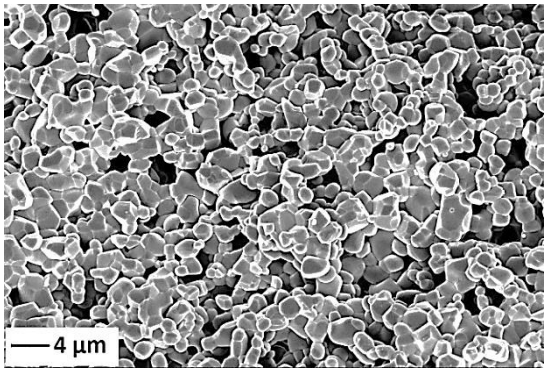

Fig. 8.6: cross section of pellet prepared with 50/50 vol% (alumina/PMMA 7 µm) + PVB.

No significant differences were detected, except for a strong deformation of the pellets after the thermal treatment.

To improve microstructure, PMMA with smaller powder size was tested (Figs 8.7-8.8):

- PMMA 3 µm 20 vol% (a), 50 vol% (b):

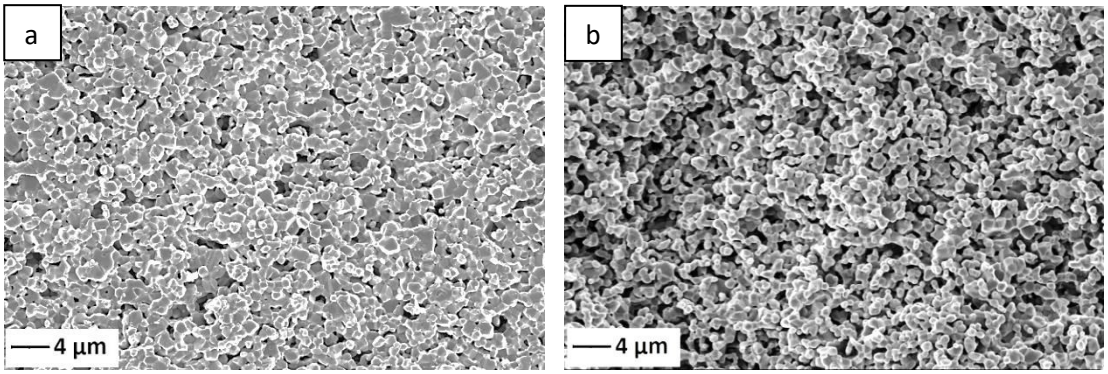

Fig. 8.7: a, cross section of pellet prepared with 20 vol% PMMA 3 µm; b, with 50 vol% PMMA 3 µm.

- PMMA 1.5 µm 20 vol% (a), 50 vol% (b):

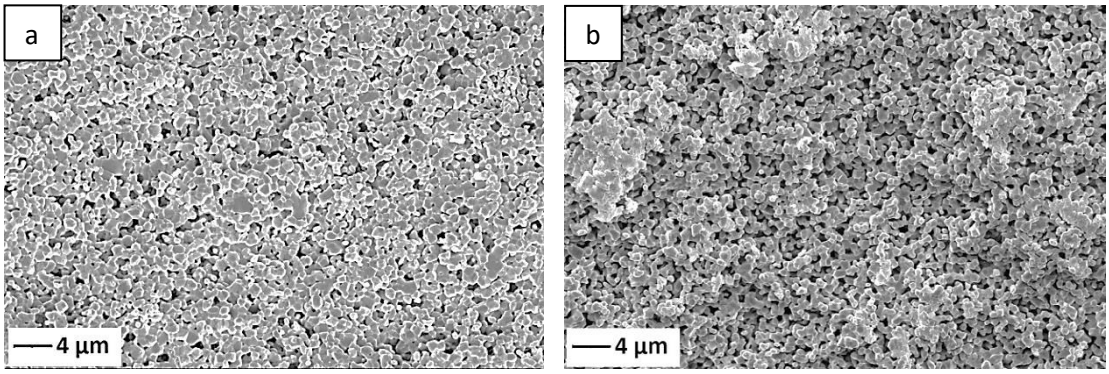

Fig. 8.8: a, cross section of pellet prepared 20 vol% PMMA 1.5 µm; b, with 50 vol% PMMA 1.5 µm.

Smaller PMMA powders help in shrinking the final pore size (< 1 µm); the final pore size distribution is more homogenous. PMMA is a very good pore former, since changing the amount introduced in the powder mixture we could easily control the final porosity, and changing the size of PMMA we could easily modify the microstructure of pellets. Pellets prepared with PMMA 3 µm show a broad pore size distribution (from 500 nm to > 1 µm), so we finally focused on PMMA 1.5 µm. A porosity of 31% (Tab. 8.1), however, is still under target, so we increased the PMMA amount to 65 vol% obtaining a final porous substrate with a porosity > 35%. The SEM pictures of Fig. 8.9 shows the cross sections of the 65 vol% PMMA pellet.

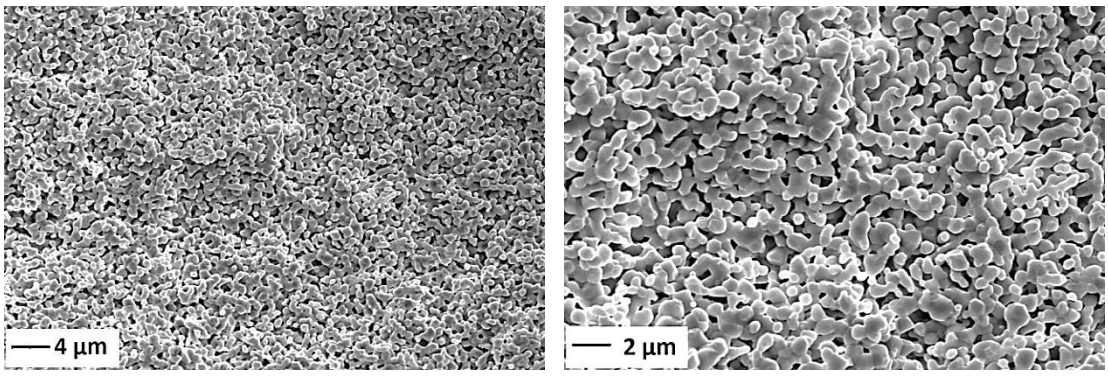

Fig. 8.9: cross section of the pellet prepared with 65 vol% of PMMA 1.5 µm.

Pellets obtained from a powder mixture with a 65 vol% of PMMA 1.5 µm were chosen as the definitive substrate for metallic membranes deposition and zeolite membranes growth. The maximum pore size of the pellet is around 500-600 nm. This value is slightly higher than the pore size of ceramic substrates commonly used for membrane growing by PVD process; ac-

cording to some works, the most common ceramic substrates have pore size around 200 nm[1,2] but in some cases higher porosity were reported[3]. In many works, the surface roughness is reduced by polishing and the surface porosity is further reduced by a layer of γ-Al_2O_3 deposited by sol-gel[4 5]. However, since this final step is time consuming (sol-gel deposition + calcination, repeated for all the γ-Al_2O_3 layers required), we only polished the surfaces of pellets.

Pellets surfaces, before and after the polishing, were characterized by 3D surface profile mapping (mechanical profiler Tencor P10, Figs 8.10-8.11). SPIP software was used to analyse the 3D surface mapping.

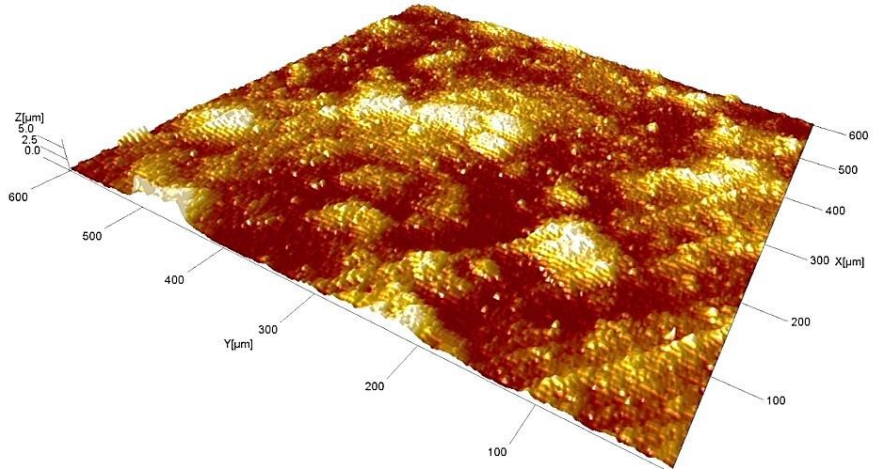

Fig. 8.10: 3D surface mapping of pellet before surface finishing.

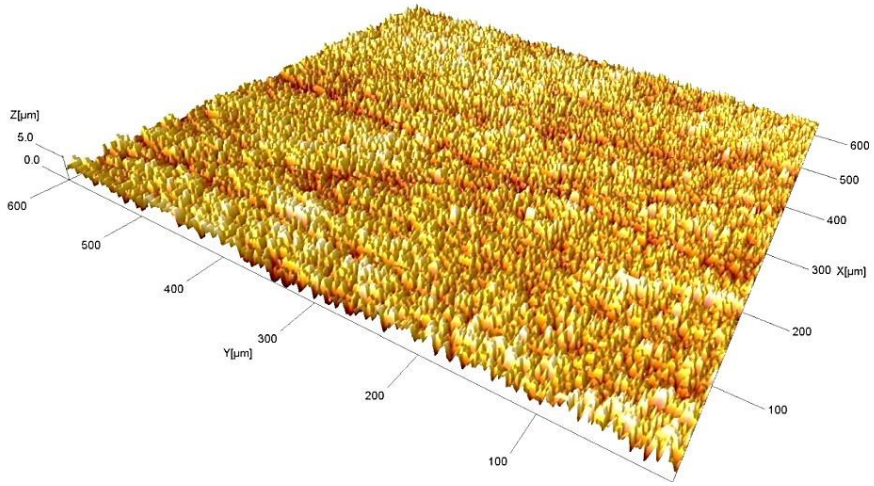

Fig. 8.11: 3D surface mapping after surface finishing.

If we compare 2D profiles (Figs 8.12-8.13) we can clearly see that the overall roughness of the polished pellet is lower than the roughness of the as sintered pellet:

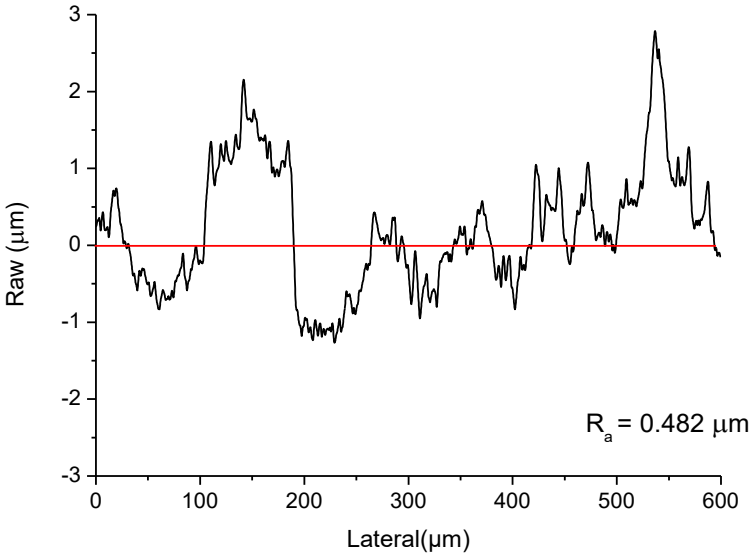

Fig. 8.12: surface roughness of pellet before surface finishing.

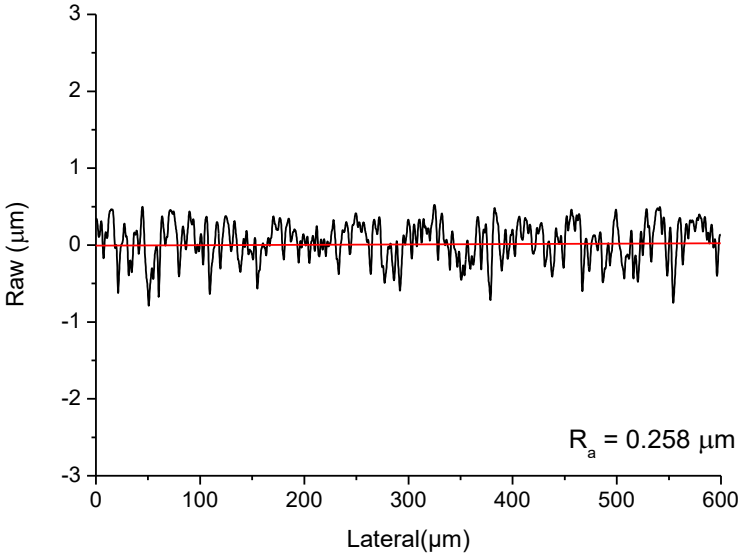

Fig. 8.13: surface roughness of pellet after surface finishing.

Surface finishing reduces surface mean roughness from 0.48 to 0.26 µm and makes the pellet surface more suitable to the next step of membrane deposition/growing.

Tab. 8.1 reports porosities and shrinkages for all the series of pellets:

Pore former	Porosity (%) / shrinkage (%) 20 vol% PMMA	Porosity (%) / shrinkage (%) 30 vol% PMMA	Porosity (%) / shrinkage (%) 40 vol% PMMA	Porosity (%) / shrinkage (%) 50 vol% PMMA	Porosity (%) / Shrinkage (%) 65 vol% PMMA
PMMA 7 µm	≈ 14.5 / ≈ 8.5	≈ 23 / ≈ 20	≈ 26 / ≈ 22	≈ 32 / ≈ 23	≈ 40 / ≈ 24.5
PMMA 3 µm	≈ 12 / ≈ 20	-	-	≈ 34 / ≈ 21	-
PMMA 1.5 µm	≈ 16.5 / ≈ 20	-	-	≈ 31 / ≈ 23	>35 / ≈ 27

Tab. 8.1: porosities and shrinkages of the series of pellets studied. The number of pellets prepared varied from 3/4 to 16 (approved substrate) within the same thermal treatment.

8.2.2. Graded porosity

A method to increase bulk porosity (and thus gas permeation) but maintaining a low surface porosity is the preparation of pellets with graded porosity. To this end, some pellets were prepared co-pressing two powder layers containing different amounts of pore former. The results were not satisfying, due to two main drawbacks:

- The difference in PMMA average size and the change in pellets shrinkage did not allow a significant change in porosity among different layers;
- After the sintering step, pellets showed a strong bending.

Figs 8.14-8.15 report few examples of graded pellets (mm refer to power load thickness in the press mould):

- 5 mm 50/50 vol% + 2 mm 70-30 vol% (PMMA 7 µm) – porosity 23%:

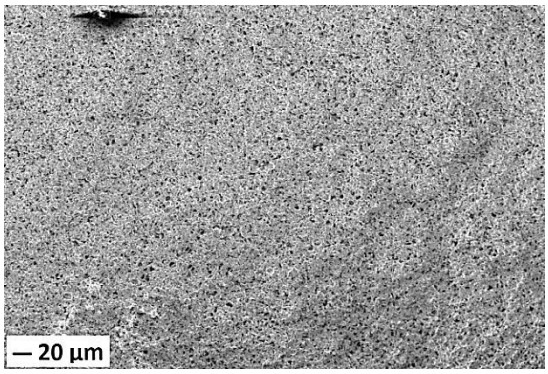

Fig. 8.14: pellet prepared by stacking 50/50 vol% and 70/30 vol % powder mixtures.

- 5 mm 50/50 vol% + 2 mm 60/40 vol% (PMMA 7 µm) – porosity 26%:

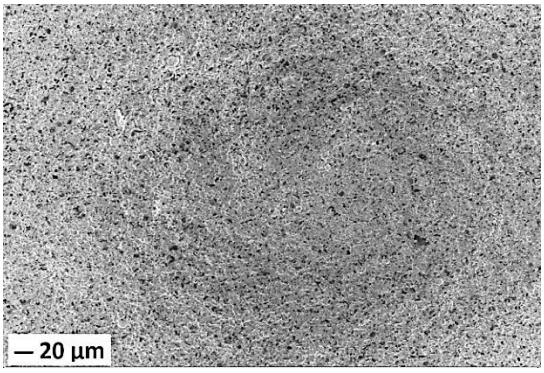

Fig. 8.15: pellet prepared by stacking 50/50 vol% and 60/40 vol % powder mixtures.

A graded porosity was observed only if layers with PMMA with different average size were used (Figs 8.16-8.17), but pellets deformation persisted:

- 2 mm PMMA 3 µm + 4 mm PMMA 7 µm (both 80/20 vol%) – porosity 25%:

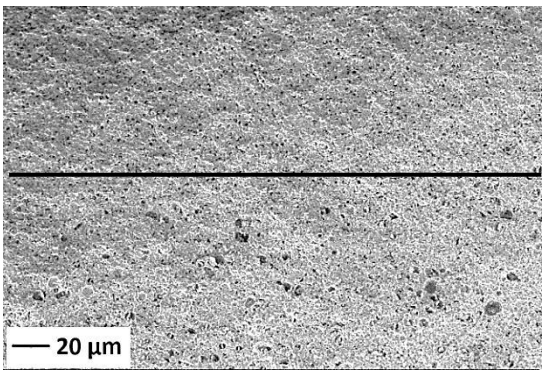

Fig. 8.16: pellet prepared by stacking 80/20 vol% powder mixtures (up, PMMA 3 µm, down PMMA 7 µm).

- 2 mm PMMA 3 µm + 4 mm PMMA 7 µm (both 50/50 vol%) – porosity 28%:

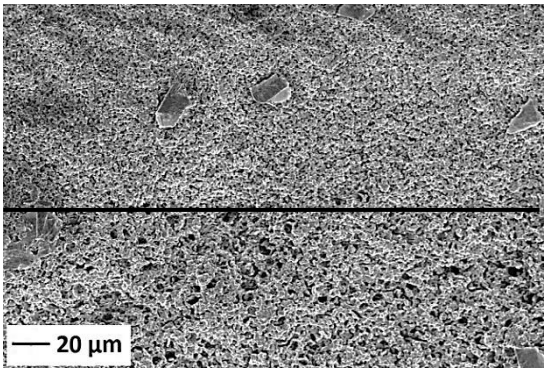

Fig. 8.17: pellet prepared by stacking 50/50 vol% powder mixtures (up, PMMA 3 µm, down PMMA 7 µm).

We also combined layers with different thicknesses to limit the deformation of pellets during the thermal treatment, but no satisfying results were obtained, so we abandoned the preparation of this kind of pellets.

Tab. 8.2 reports the mean porosity of the graded porosity pellets prepared:

Co-pressed powder mixtures *	Porosity (%) / shrinkage (%)
Alumina/PMMA 7 µm 50/50 + Alumina/PMMA 7 µm 35/65	≈ 43 / ≈ 25
Alumina/PMMA 7 µm 50/50 + Alumina/PMMA 7 µm 70/30	≈ 42 / ≈ 22.5
Alumina/PMMA 7 µm 60/40 + Alumina/PMMA 7 µm 70/30	≈ 35 / ≈ 22
Alumina/PMMA 7 µm 50/50 + Alumina/PMMA 7 µm 60/40	≈ 22 / ≈ 22
Alumina/PMMA 3 µm 80/20 + Alumina/PMMA 7 µm 80/20	≈ 25 / ≈ 18
Alumina/PMMA 3 µm 50/50 + Alumina/PMMA 7 µm 50/50	≈ 28 / ≈ 22

Tab. 8.2: porosities and shrinkages) of graded pellets tested. Data were gathered from series of pellets prepared in 3/4 samples (* = volumetric ratios).

8.3. Starch

8.3.1. Characterization

We characterized the starch by TGA-DSC to find the most suitable burning temperature. Fig. 8.18 reports the result of the thermal analysis (RT - 1200°C at 10°C/min, free cooling, thermal treatment in air, air flow 100 mL/min):

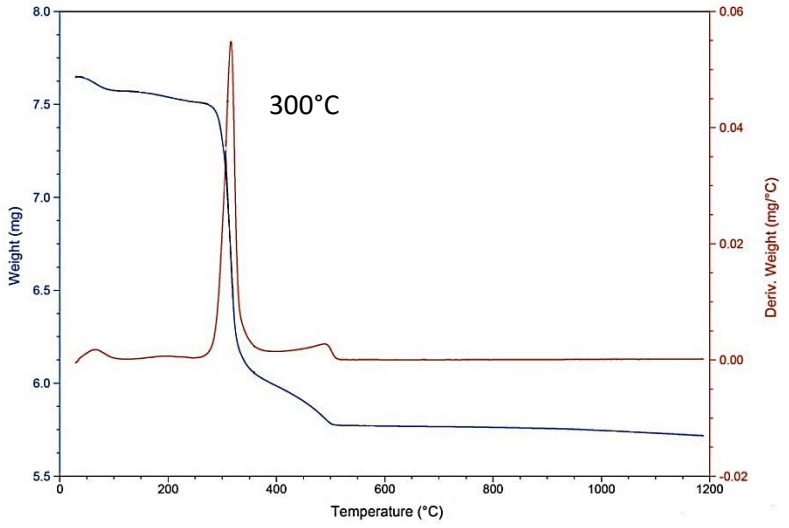

Fig. 8.18: TGA-DSC analysis performed on a powder mixture having starch as pore former.

The analysis shows that the main exothermic event is around 300°C, so we set a sintering treatment having an isotherm at this temperature. After some sintering tests, we came up

with the following thermal treatment route, having several steps because the preliminary study highlighted a strong deformation issue:

- Room temperature - 300°C at 60°C/h;
- 300°C for 1h to allow the burning of most of starch;
- 300°C – 400°C at 60°C/h, slow step to end the starch burning process;
- 400°C for 1h to complete the burning of all the starch;
- 400°C – 800°C at 60°C/h;
- 800°C for 1h, intermediate isotherm that resulted fundamental to prevent pellets deformation;
- 800°C – 1500°C at 120°C/h;
- 1500°C for 1h;
- 1500°C – 800°C at 120°C/h;
- 800°C – room temperature free cooling.

8.3.2. Alumina / starch powder mixtures

Fig. 8.19 reports some examples concerning pellets prepared from alumina/starch powder mixture. The SEM pictures refer to powder mixtures with very different starch amount, to best highlight the effect of starch:

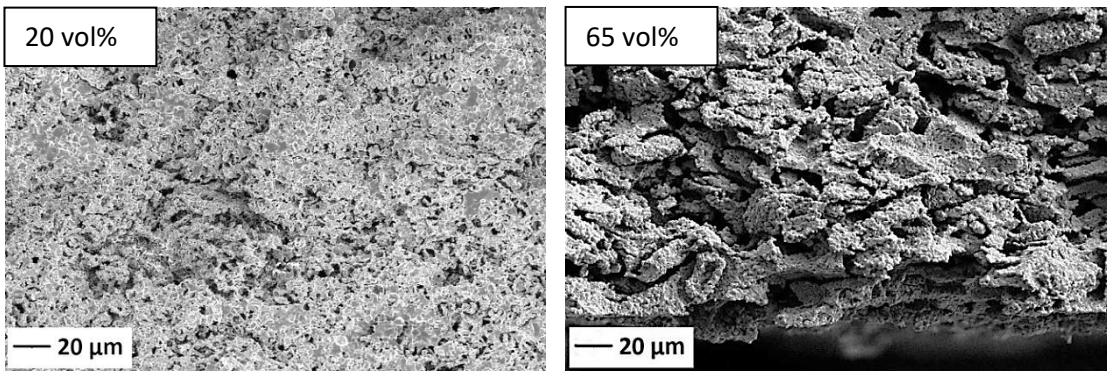

Fig. 8.19: cross section of pellets prepared with different amounts of starch.

Both pellets share some common features:

- Very big voids in the bulk (≈ 10/15 µm in the 80/20 pellet, > 20 µm in the 35/65 pellet), that reduce the mechanical strength (pellets were brittle). Probably, starch forms aggregates forming the pores in the bulk of the pellets;
- Pellets do not have a homogenous pore distribution as in PMMA pellets.

Therefore, very high porosity (Tab. 8.3), low quality mechanical properties and broad pore size distribution were identified. Moreover, despite the slow heating rates applied in the sintering step, pellets still showed deformation.

Alumina / starch powder mixture	Porosity (%) / shrinkage (%)
90/10 wt%	1400°C: ≈ 45 / ≈ 10
80/20 wt%	1400°C: ≈ 50 / ≈ 9.5 1500°C: ≈ 39 / ≈ 10
75/25 wt%	1400°C: ≈ 50 / ≈13 1500°C: ≈ 40 / ≈16
35/65 vol%	1500°C: > 50 / ≈23

Tab. 8.3: porosities and shrinkages of pellets prepared with different alumina/starch powder mixtures. Data were gathered from series of pellets prepared in 3/4 samples.

8.3.3. Graded porosity

Figs 8.20-8.21 report only few examples of tests of graded porosity (mm refers to thickness of power load in the mould; pellets were so deformed that it was impossible to measure geometrical parameters):

- 2 mm 80/20 wt% + 2 mm 95/5 wt%:

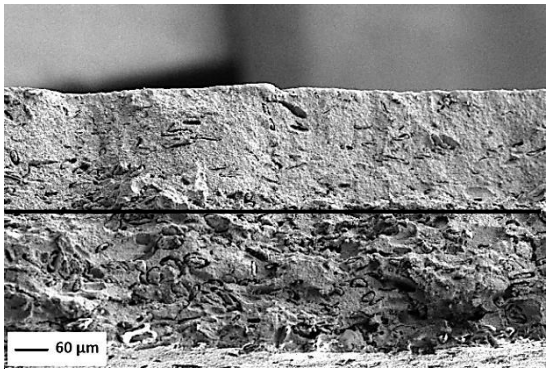

Fig. 8.20: pellets prepared by stacking 80/20 vol% and 95/5 vol% powder mixtures.

- 2 mm 80/20 wt% + 2 mm 90/10 wt%:

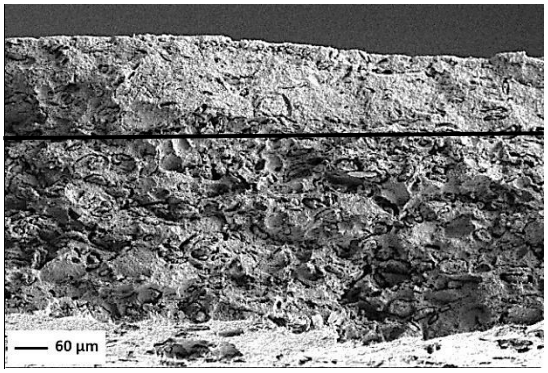

Fig. 8.21: pellets prepared by stacking 80/20 vol% and 90/10 vol % powder mixtures.

References:

[1] Pereira, A.I., Perez, P., Rodrigues S.C., Mendes, A., Madeira L.M., Tavares, C.J., Deposition of Pd–Ag thin film membranes on ceramic supports for hydrogen purification/separation. *Materials Research Bulletin* **2015** 61, 528–533.

[2] Xomeritakis, G., Lin, Y.S., Fabrication of a thin palladium membrane supported in a porous ceramic substrate by chemical vapour deposition. *Journal of Membrane Science* **1996** 120, 261-272.

[3] O'Brien, J., Hughes, R., Hisek, J., Pd-Ag membranes on porous alumina substrates by unbalanced magnetron sputtering. *Surface and Coatings Technology* **2001** 142-144, 253-259.

[4] Jayaraman, V., Lin, Y.S., Pakala, M., Lin, R.Y., Fabrication of ultrathin metallic membranes on ceramic supports by sputter deposition. *Journal of Membrane Science* **1995** 99, 89-100.

[5] McCool, B. A., Lin, Y. S., Nanostructured thin palladium-silver membranes: Effects of grain size on gas permeation properties. *Journal of Material Science* **2001** 36, 3221-3227.

9. Pd-Ag(23 wt%)

9.1. DC magnetron sputtering - DCMS

9.1.1. Targets calibration

The magnetron sputtering process needed some preliminary steps prior to the depositions. A calibration of sputtering rates is first of all necessary, especially when preparing a co-deposition of an alloy with a specific composition from pure metal targets. To this end, some depositions where performed from single targets on flat substrates (typically glass, Fig. 9.1), covering a small part of the glass with kapton tape; the sputtering yield was estimated by measuring off-line the thickness of the coatings by stylus mechanical profiler (KLA Tencor P10). The depositions were performed at room temperature and starting from the argon pressure typically used for this kind of depositions (1-1.2·10^{-2} mbar). Various depositions at different powers were then performed (Tab. 9.1). The substrates were rotated during the deposition (2 RPM) and the thickness homogeneity was also estimated by mechanical profiler.

Palladium Target			Silver Target		
Power (W)	Rate (nm/min)	Rate variation (%)	Power (W)	Rate (nm/min)	Rate variation (%)
50	23	18	20	14	8
75	35	3	30	24	6
100	48	4	50	32	20

Tab. 9.1: thicknesses and thickness variation of palladium and silver depositions used to calibrate the targets.

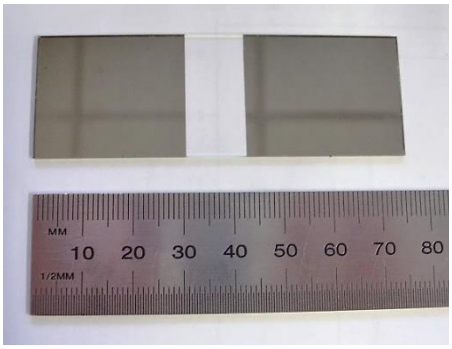

Fig. 9.1: sample used to evaluate the thickness of the deposited metal.

Once the calibration was completed, the power ratio between Pd and Ag targets was set up and then checked and slightly adjusted by measuring the thickness and the alloy composition after the deposition onto alumina.

9.1.2. Influence of temperature and substrate on alloy morphology

Pd-Ag alloy was deposited onto the porous alumina substrates, and Fig. 9.2 shows the size of our samples:

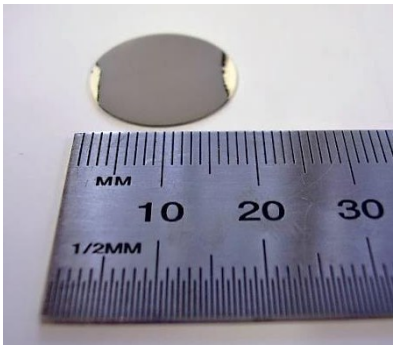

Fig. 9.2: size of samples prepared during the sputtering tests.

In order to achieve a good surface coverage of the substrate and a dense membrane, various deposition temperatures were tested and different alumina porous substrates (prepared with PMMA powder mixture and having different porosities) were used. Fig. 9.3 reports the preliminary results obtained using a porous substrate prepared with 50 vol% of PMMA having a 7 µm particles size (Pd 100 W, Ag 24 W, 30 min, $1.1 \cdot 10^{-2}$ mbar, no bias voltage) at different temperatures:

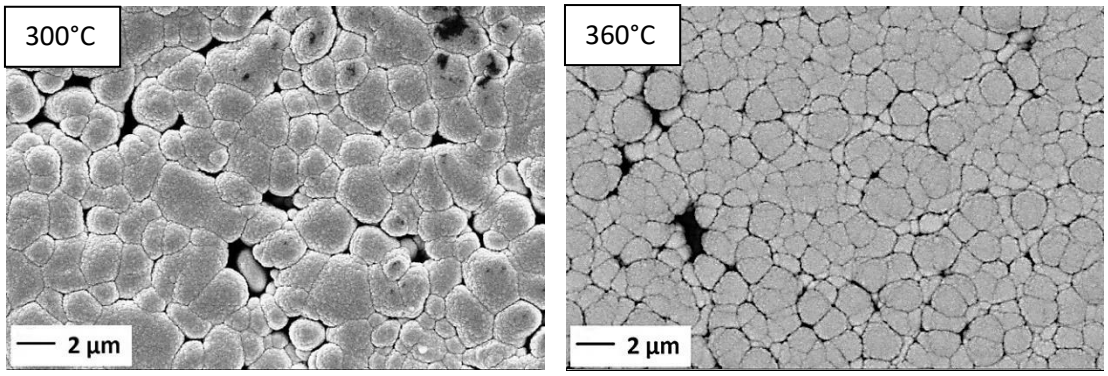

Fig. 9.3: Pd-Ag alloy deposited at 300 and 360°C.

The two depositions reported show some similar features, such as big voids (≈ 2 µm) clearly visible in all SEM pictures. Since the sputtered alloy morphologies are very similar to each other, we adopted a deposition temperature of 300°C. High temperatures favour the crystallization of the alloy in isolated columns and not into a continuous compact layer, and the columnar growth was probably enhanced by the porous surface of the ceramic substrate, which can seriously prevent the formation of a continuous thin layer. We performed some tests even at a lower temperature (200°C), but the results were not satisfactory, as can be seen in the SEM pictures reported (Fig. 9.4, pressure $1.1 \cdot 10^{-2}$ mbar, 30 min, same Pd and Ag targets power of the previous depositions) regarding depositions on pellets with 50 vol% of PMMA with different particles sizes:

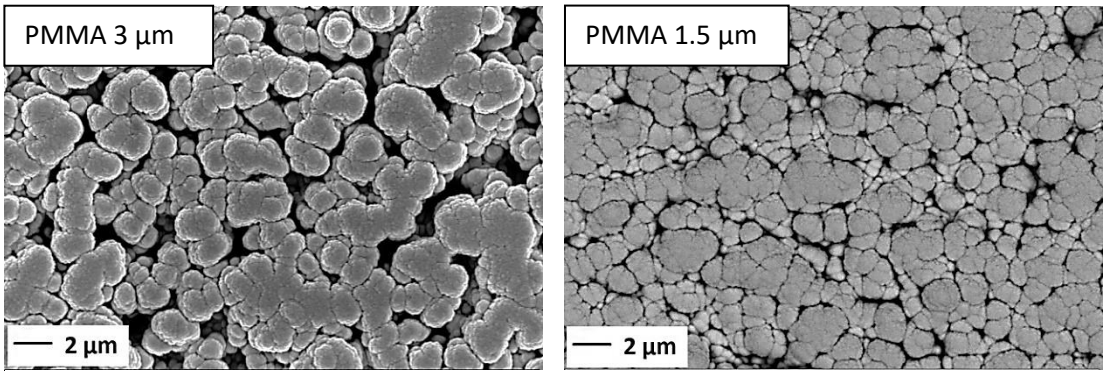

Fig. 9.4: Pd-Ag alloy deposited at 200°C.

Once identified the most suitable ceramic substrate features for this aim, other deposition parameters were tested. Fig. 9.5 reports the surface and the cross section pictures of the alloy deposited at 300°C (Pd 100 W, Ag 24 W, 30 min, no bias voltage applied, $1.1 \cdot 10^{-2}$ mbar).

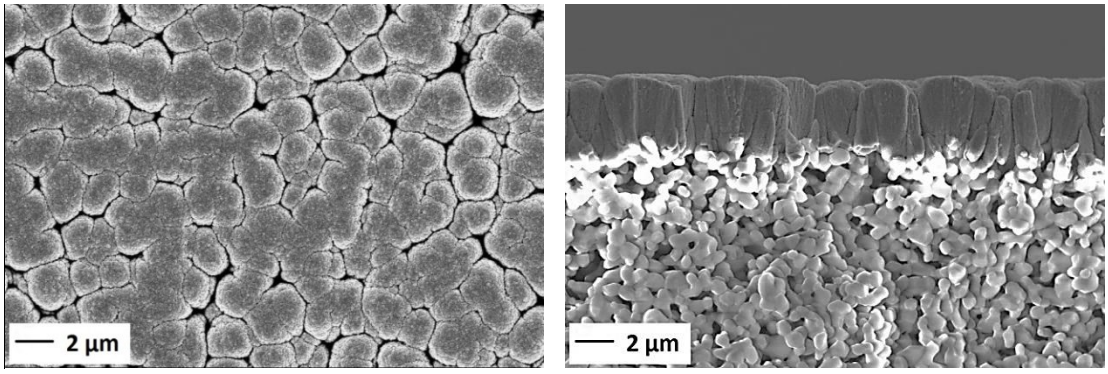

Fig. 9.5: top view and cross section of Pd-Ag alloy deposited onto the substrate prepared using the 35/65 vol% powder mixture (alumina/PMMA 1.5 µm).

SEM pictures show a good metal/ceramic adhesion and the typical columnar growth of sputtered thin layers, that causes the formation of surface voids; moreover we can clearly see how the substrate surface roughness drives the growth. Cross section pictures show columns that are not broken or damaged, indicating that they are apparently isolated from each other. The cross-section pictures seem indicating the presence of pores in the metal layer where a gas can pass through. Fig. 9.5 clearly shows how the temperature can help in depositing denser metal layers, considering that at 200°C the alloy showed a lot of voids and pores, even though the substrates were less porous with respect to Fig. 9.3. Furthermore, even if the deposition conditions were not suitable to achieve more compact layers, it is clear from the top view SEM pictures that smaller pore former particles bring to denser metal layers with fewer defects.

In order to evaluate the adhesion, we performed scratch tests on the sample reported in Fig 9.6:

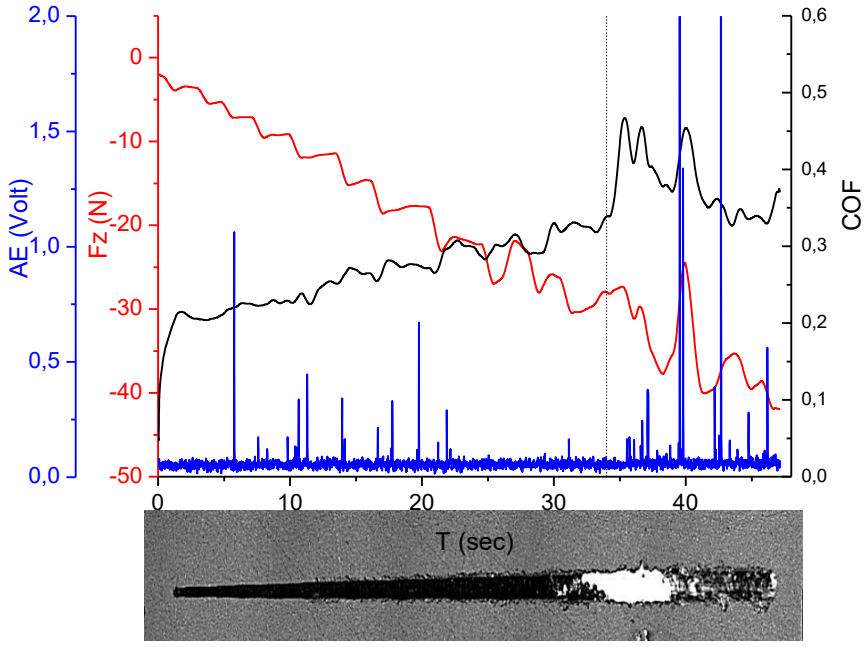

Fig. 9.6: scratch test performed to evaluate the adhesion of the metal layer onto alumina substrate.

In Fig. 9.6 COF stands for coefficient of friction, Fz is the force applied along the z axis and AE is the acoustic emission. The test reveals a discontinuity in the COF parameter (indicated by

the dotted vertical line), but we cannot associate it to the real COF of the metal layer. A closer look of the track (Fig. 9.7) points out that the white zone of the track photograph below the graph is not the separation of the metal from the ceramic, but it is the damage of the ceramic substrate caused by the applied load. A weak point caused the failure of the substrate, removing the metal deposited above.

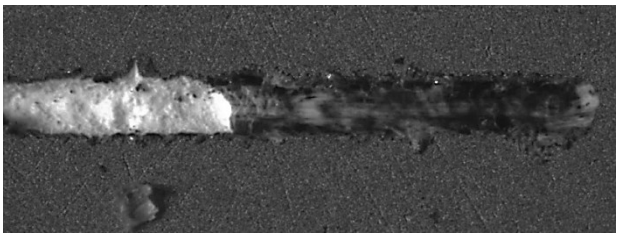

Fig. 9.7: high magnification of the track showing the alumina damage.

This happens whenever a soft and ductile material (Pd-Ag alloy in this case) is coupled with a hard and brittle material (the alumina substrate): the ductile material compensates for the applied load and the substrate breaks when a critical load is achieved for the specific point of load application. Scratch tests show different behaviours from one track to another (Fig. 9.8), thus preventing any valuable evaluation of adhesion and COF.

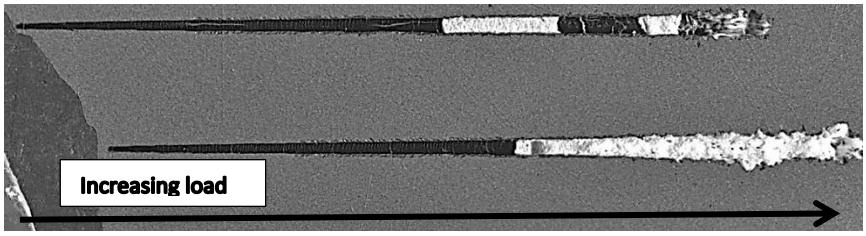

Fig. 9.8: scratch tracks showing different behaviours.

9.1.3. Influence of bias voltage and pressure on alloy morphology

Other parameters were tested in order to improve the compactness of the alloy: bias voltage and deposition pressure. Ceramic samples were prepared for bias deposition by a short PVD deposition (in the same vacuum chamber) without bias, to cover the surface with a very thin metal layer to assure electrical contact. After that, bias was applied at the desired value. We modified the pre-sputtering process by depositing a very thin palladium layer on both surfaces of the ceramic substrates. After that, the coated substrates were fixed to the sample

holder by conductive Kapton tape, but no improvements were noticed. SEM pictures reported in Fig. 9.9 show the results obtained keeping the same pressure ($1.1 \cdot 10^{-2}$ mbar), temperature (300°C) and targets power (Pd = 100 W, Ag = 24 W, 30 min) of the previous depositions but applying different bias voltages:

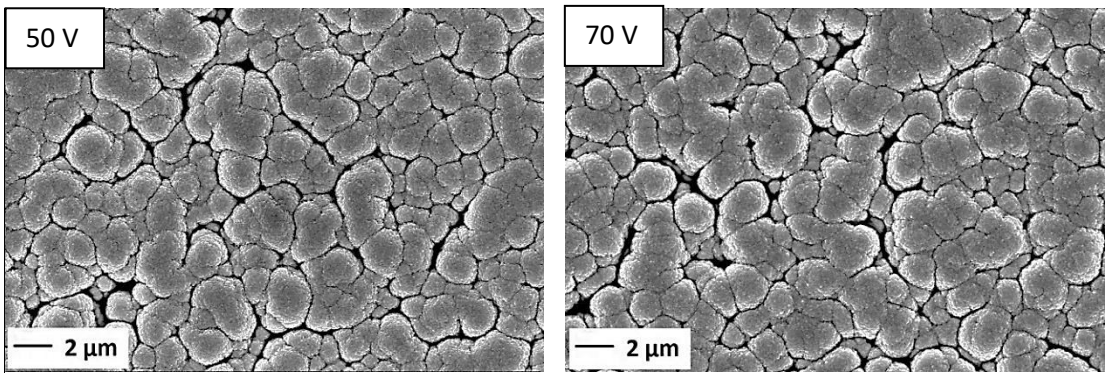

Fig. 9.9: top view of Pd-Ag alloy deposited by applying different bias voltages.

No improvements were achieved and a similar difference in bias voltages did not influenced the compactness of alloy. Various bias voltages were tested (100/200 V, Fig. 9.10), but the morphology of the alloy was unchanged, probably as a consequence of the insulating nature of the substrate that hindered a proper charging of substrate.

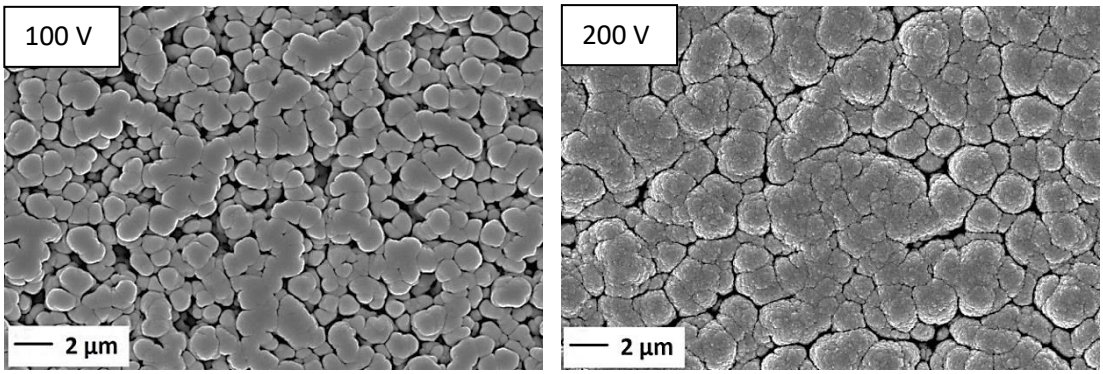

Fig. 9.10: Pd-Ag alloy sputtered applying 100 V and 200 V bias voltages.

Also various argon pressures were tested:

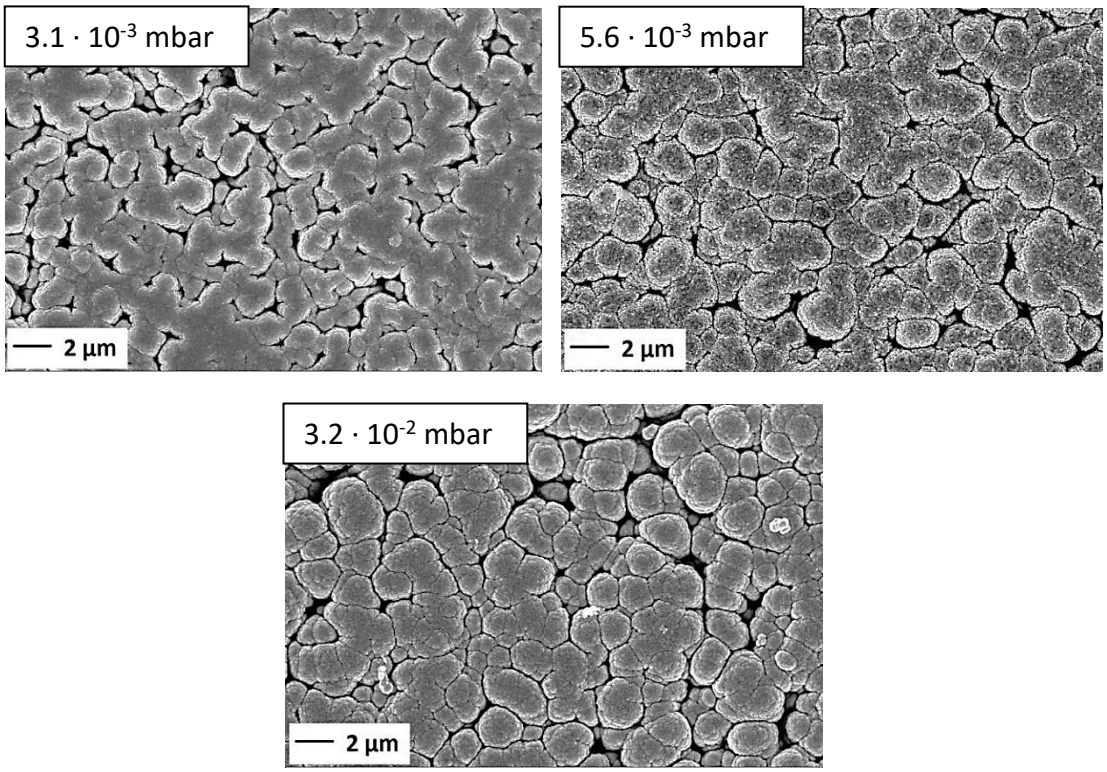

Fig. 9.11: Pd-Ag alloy sputtered at different argon pressures.

Low pressures are associated to energetic sputtered particles, thanks to the low number of collisions in the plasma. Such species have more mobility and can diffuse faster on the substrate to coat, improving coating qualities such as compactness. However, in case of insulating and porous substrates, the pressure resulted ineffective in significantly influencing the final density. The use of lower or higher deposition pressures is not possible in this apparatus configuration due to plasma ignition problems or plasma stability.

All tests showed difficulties in preparing compact thin membranes for hydrogen separation. However, the depositions pointed out the important role of temperature, the parameter having clear and visible effects on the final morphology.

9.1.4. EDS/XRD

The alloy was characterized by EDS and XRD analyses. EDS analyses confirmed the right alloy composition within the EDS uncertainty.

XRD analyses confirmed the alloy formation during the sputtering process, as we can see in the diffraction pattern (Fig. 9.12) of the sample prepared at 300°C, 1.1 ·10^{-2} mbar (Pd 100 W, Ag 24 W, no bias):

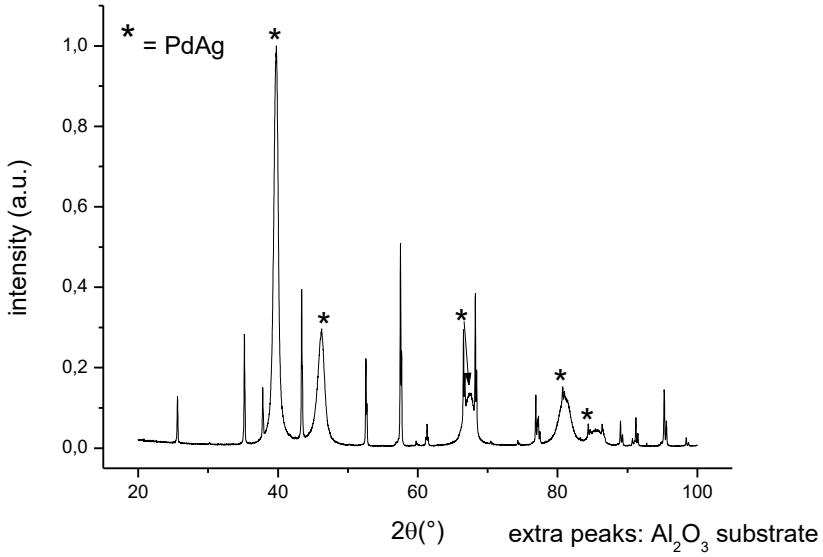

Fig. 9.12: XRD pattern of Pd-Ag alloy onto porous alumina substrate.

The diffraction pattern[1] does not show diffraction peaks belonging to other metallic phases (the extra peaks belong to the alumina substrate), confirming the alloying of metals and identifying 300°C a good deposition temperature. According to Rietvield refinement (Tab. 9.2) no specific palladium or silver diffraction peaks are recognizable.

Crystal structure Pd-Ag alloy	Cubic
Space group	Fm-3m
Parameter of the cell	3.937 Å
Crystallite size (nm)	20

Tab. 9.2: Rietvield analysis on Pd-Ag alloy sputtered by DC magnetron sputtering.

9.1.5. Thermal treatment

To promote alloy crystallization and grain coarsening, and thus the densification, some post-annealing treatments were tested. The treatments were performed in argon atmosphere to protect the metal surface from oxidation (Fig. 9.13 refers to samples prepared at $1.1 \cdot 10^{-2}$ mbar, Pd 100 W, Ag 24 W, no bias voltage applied):

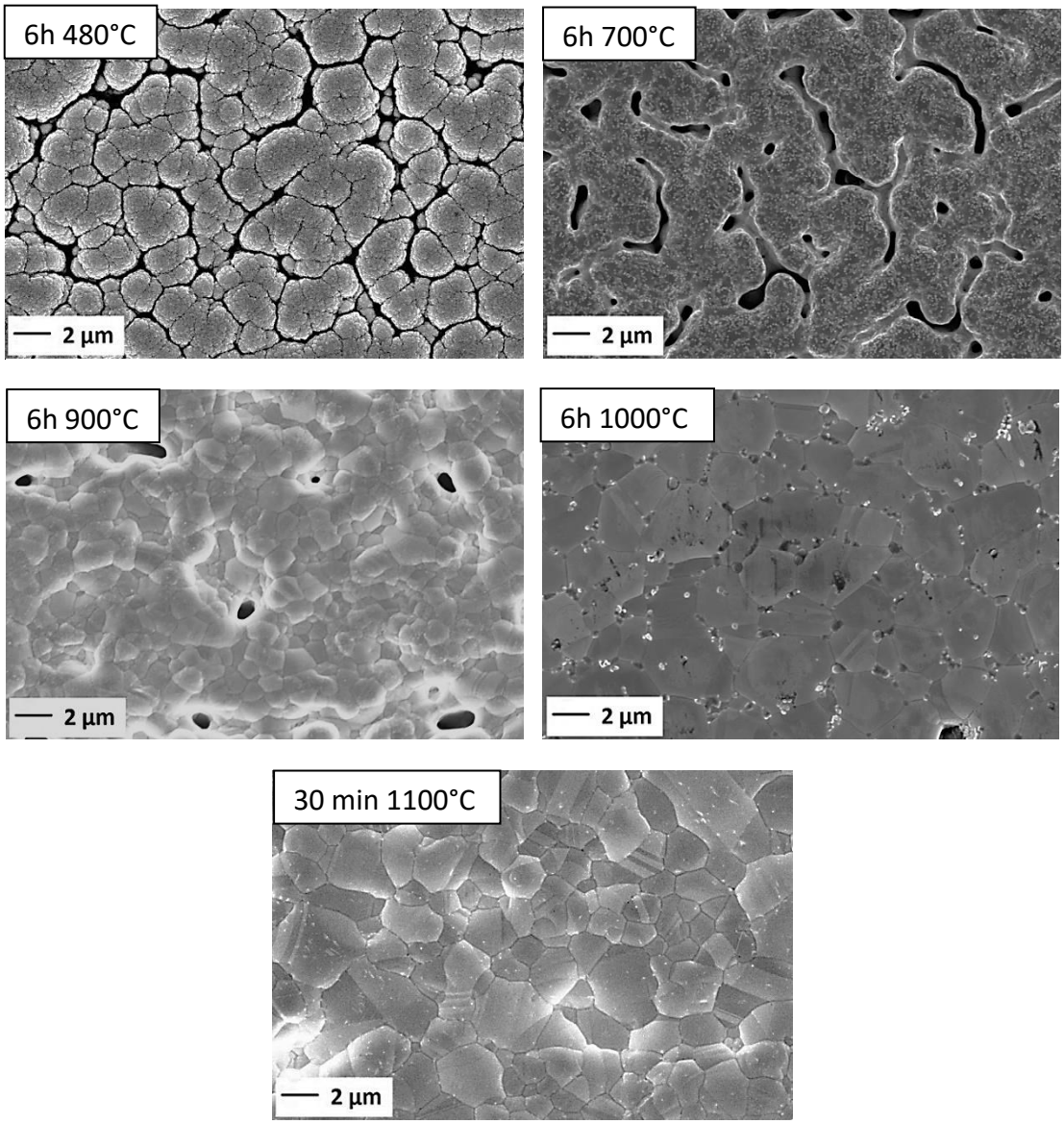

Fig. 9.13: Pd-Ag alloy after the thermal annealings.

A clear grain coarsening was observed. At higher temperatures quite dense metal layers were achieved, but a loss in metal/ceramic adhesion was also observed, probably due to a low wettability of the alloy when the metal softening takes place.

In order to improve density and adhesion, HiPIMS was tested for the first time for this kind of application.

9.2. HiPIMS

9.2.1. Influence of deposition parameters on alloy morphology

Considering the change of the sputtering apparatus, vacuum chamber and power supplies, the calibration was repeated, especially because with HiPIMS very high power for very short impulses is used. However, in this configuration the sputtering yield of a target is influenced by the other targets. Therefore, the calibration was achieved by performing various depositions of the alloy and by gradually adjusting the power supplies according to compositions detected by EDS.

Both configurations were tested, with palladium or silver targets working with high power impulses and the other in pulsed DC, but the configuration with palladium in HiPIMS was chosen, since palladium is the main component of the alloy.

Preliminary depositions were performed at room temperature, Ar pressure $1.04 \cdot 10^{-2}$ mbar, 75 V bias voltage, Pd 800 W and Ag 330 W (Fig. 9.14).

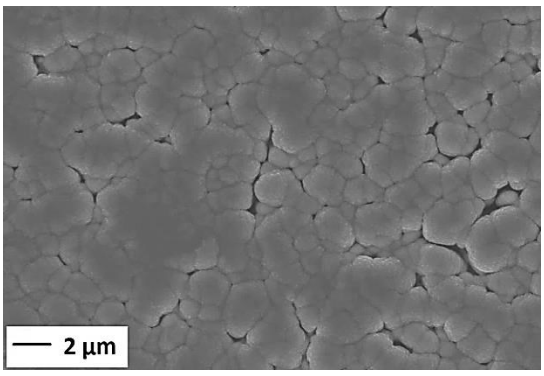

Fig. 9.14: top view of Pd-Ag alloy deposited at room temperature ($1.04 \cdot 10^{-2}$ mbar, bias voltage 75 V).

SEM picture reported in Fig. 9.14 shows that pores and voids of the alloy are drastically reduced with respect to DC magnetron sputtering; the metal layer is more compact even if it still does not allow hydrogen selectivity.

Also at higher temperature compact membranes were not achieved and that, as already observed in DC magnetron sputtering, was attributed to the insulating nature of substrates. Therefore, a sample holder was designed (Fig. 9.15) to improve the electrical contact between the sample holder and the substrate surface to coat.

Fig. 9.15: stainless steel HiPIMS sample holder with a sample after the sputtering process. Screws fasten the sample and guarantee electrical contact.

Moreover, prior to the membrane deposition, we deposited by HiPIMS a very thin layer of palladium alloy (room temperature, from 3 to 5 min, bias voltage 75 V, same targets power) onto the insulating ceramic substrates, to guarantee electrical contact with sample holder. The layer thus deposited is porous and it can be helpful also to decouple the thermal expansion mismatch between the ceramic substrate and the main metal layer, lowering the risks of peeling.

Figs 9.16-9.17 report two samples prepared with the double sputtering process:

- room temperature deposition (20 min sputtering time):

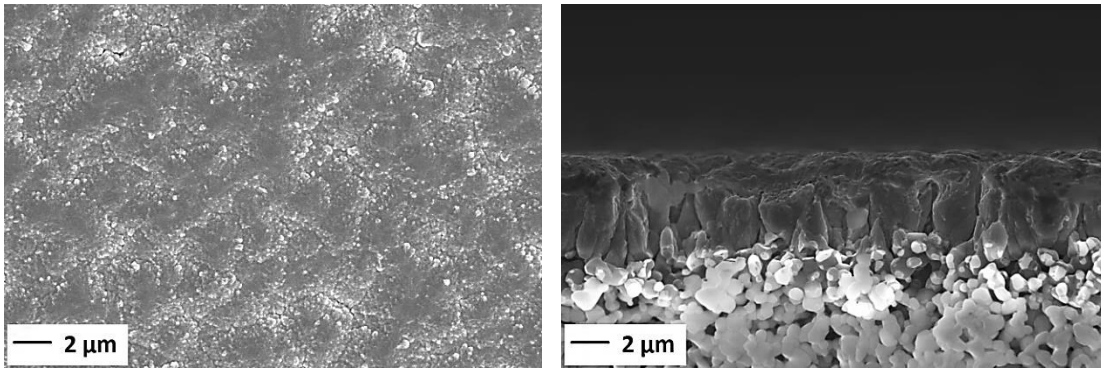

Fig. 9.16: top view and cross section of Pd-Ag alloy deposited at room temperature (20 min).

- 350°C deposition (25 min sputtering time):

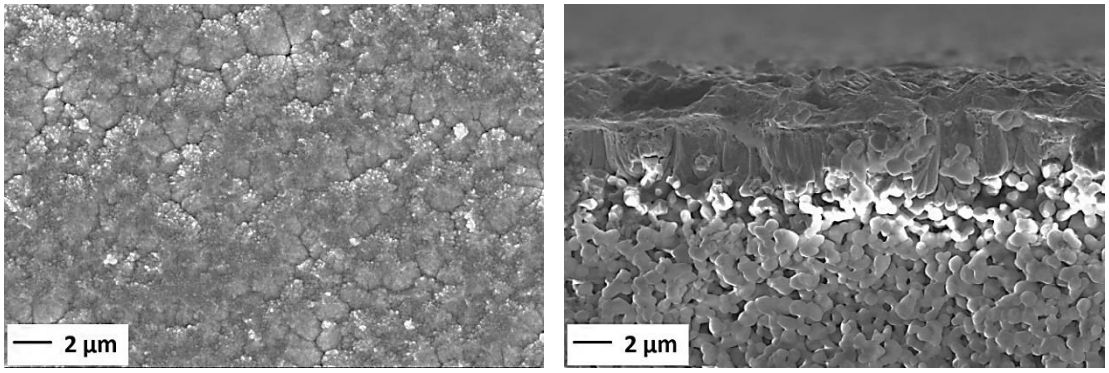

Fig. 9.17: top view and cross section of Pd-Ag alloy deposited at 350°C (25 min).

The electrical contact guaranteed a bias voltage on the surface, thus strongly increasing metal layer density and homogeneity. High temperature further increased the alloy crystallization (Fig. 9.17). Extending the duration of the sputtering process the final quality strongly improved (Figs 9.18-9.19, depositions of 35 and 45 min, all the other sputtering parameters constant):

- 35 min:

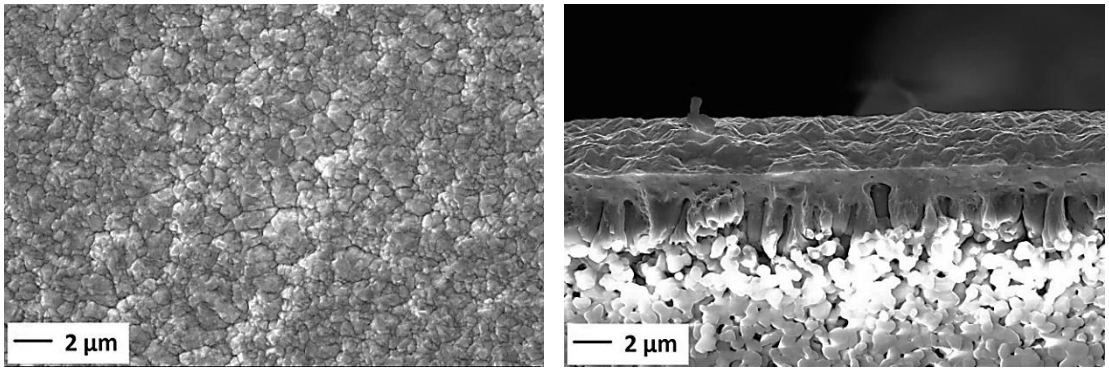

Fig. 9.18: top view and cross section of Pd-Ag alloy deposited at 350°C (35 min).

- 45 min:

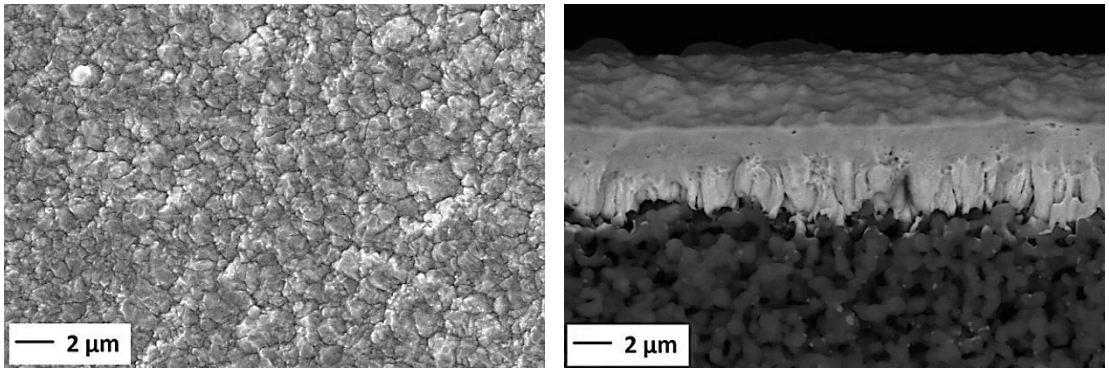

Fig. 9.19: top view and cross section of Pd-Ag alloy deposited at 350°C (45 min).

Samples are compact and no defects are visible. The total thickness is less than 5 µm for 45 min of deposition, and the dense layer is typically between 2-3 µm, a value compatible with the thickness desired to have high hydrogen fluxes and a low cost membrane.

Comparing HiPIMS samples with DC magnetron sputtering samples, we can see that HiPIMS allows the preparation of more crystalline selective layers directly onto porous substrates. This is the main achievement of the work: thanks to the high percentage of ionized species produced by HiPIMS, the preparation of a dense and compact layer of Pd-Ag alloy, directly onto a porous substrate, without involving graded porosity steps or other surface modifications, is possible, reducing the time required for membrane preparation and preparing a very simple membrane layout.

Other parameters were also studied in order to improve the quality of the membranes and potentially still reduce the alloy thickness. We studied combinations of high temperature and alternating bias voltages (25/75 V and 75/150 V, Figs 9.20 – 9.21), repeating the cycle 5 min low bias + 5 min high bias for the overall deposition time, to study the influence of the bias and reduce the stress induced by high bias voltages.

- 25/75 V:

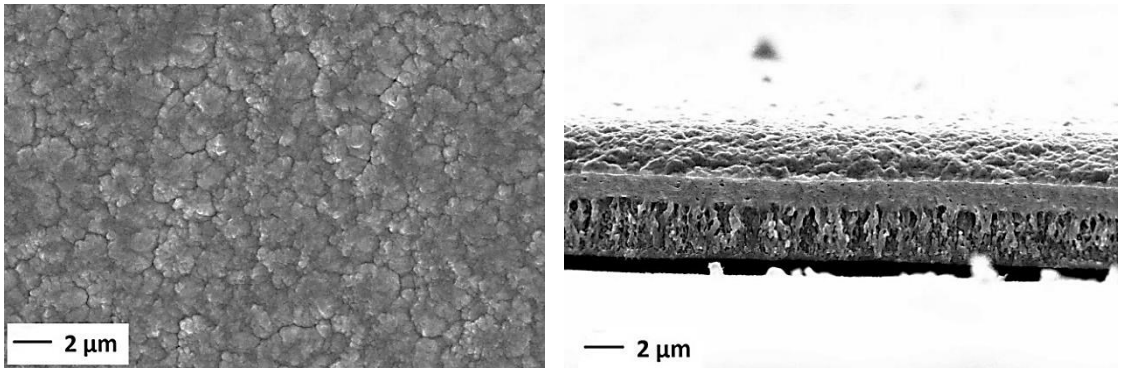

Fig. 9.20: top view and cross section of Pd-Ag alloy deposited at 350°C with alternating bias voltages 25/75 V (cross section of sample sputtered onto silicon wafer).

- 75/150 V:

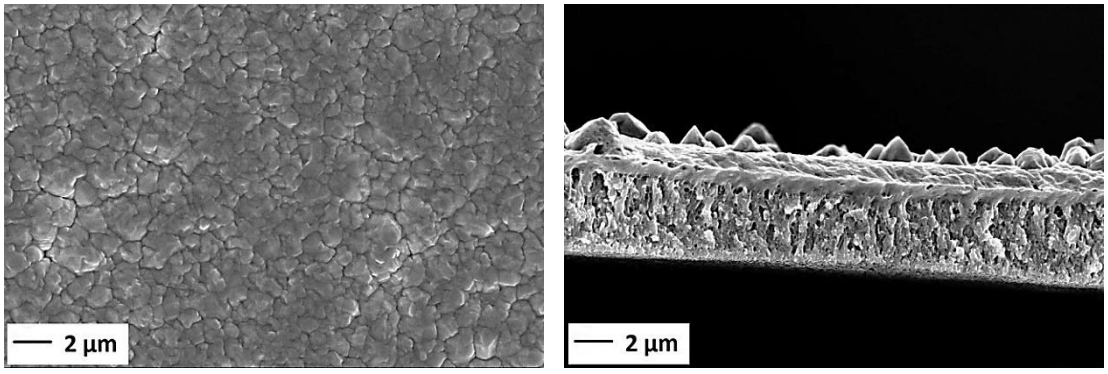

Fig. 9.21: top view and cross section of Pd-Ag alloy deposited at 350°C with alternating bias voltages 75/150 V (cross section of sample sputtered onto silicon wafer).

Both samples show very good substrate coverage, with almost no defects (small pores of submicron size) and have very similar morphologies. The dense layer of the Pd-Ag alloy is thicker in the case of the 25/75 V (≈ 2 µm) deposition, while it is thinner in the 75/150 V deposition (≈ 1 µm). Probably, this is due to the high bias voltage, causing a more intense ion bombardment with a higher material removal. Moreover, higher bias seems to improve the crystallization of the alloy. However, comparing the alternating bias depositions with the simple deposition at 75 V, no significant improvement in morphology and microstructure were identified, so we discarded the alternating bias approach.

The work done with this new technology has demonstrated that with HiPIMS composite membranes for hydrogen separation and purification can be prepared in very few steps, directly onto porous substrates.

9.2.2. EDS/XRD

EDS analyses confirmed the stoichiometry of the alloy. Fig. 9.22 reports the EDS spectrum performed on sample deposited at 350°C (bias 75 V, 35 min, Pd 800 W, Ag 330 W, $1.03 \cdot 10^{-2}$ mbar); Tab. 9.3 reports the analysis result.

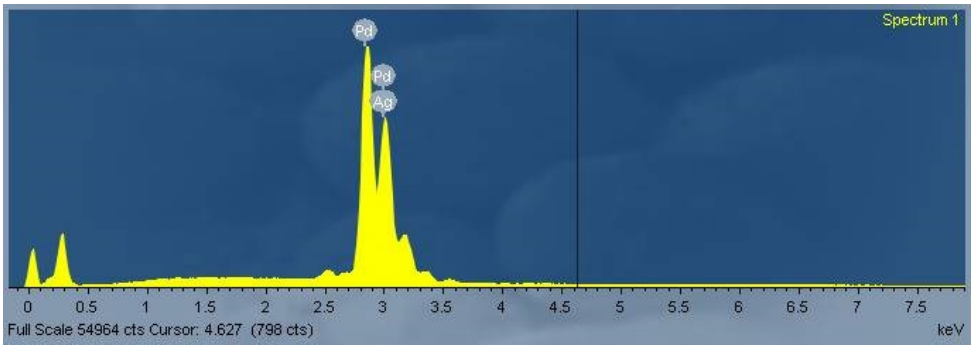

Fig. 9.22: Pd-Ag EDS spectrum.

Element	Weight %
Pd	≈ 78
Ag	≈ 22

Tab. 9.3: Pd-Ag alloy composition; EDS analysis values are intended within the EDS error range.

Tab. 9.4 reports EDS analyses of other samples deposited in different conditions:

Sputtering parameters	Pd	Ag
RT, 20 min; Pd 800 W; Ag 330 W; Bias 75 V; $1.01 \cdot 10^{-2}$ mbar	≈ 77 wt%	≈23 wt%
350°C, 25 min; Pd 800 W; Ag 350 W; Bias 75 V; $1.02 \cdot 10^{-2}$ mbar	≈77 wt%	≈23 wt%
350°C, 35 min; Pd 800 W; Ag 350 W; Bias 75 V; $1.03 \cdot 10^{-2}$ mbar	≈79 wt%	≈21 wt%
350°C, 35 min; Pd 800 W; Ag 350 W; Bias 25/75 V alternated; $1.03 \cdot 10^{-2}$ mbar	≈79 wt%	≈ 21 wt%

Tab. 9.4: EDS analysis on different samples.

Some samples show small deviations from the desired stoichiometry, but they are within the EDS error range.

X-ray diffraction patterns (Fig. 9.23) completed the characterization of the membranes. Conversely to what observed in Pd-Ag alloy sputtered by DC magnetron sputtering, all the as sputtered samples presented a mix of Pd-Ag alloy and pure palladium peaks. HiPIMS sputtering process need a further step to complete the alloy formation. Thermally treating the as

prepared samples (6/12h at 520°C, argon atmosphere), we obtained a complete conversion into the final alloy. Rietveld analyses suggested that the less intense diffraction peaks belong to an early stage Pd-Ag alloy. Analysing the XRD patterns with a pure silver reference instead of the Pd-Ag reference, we did not find a perfect match with the peaks positions of our patterns. Moreover, in case of pure silver reflections, pure metals diffraction peaks should be clearly distinct from each other, as reported in Folletto et al.[2] and Engin Ayturk et al.[3]. Instead of previous thermal treatment at 520°C, membranes where left in the cell for permeability tests at 450°C in nitrogen atmosphere for 24 hours prior to tests and the permeability was checked with time to control the attainment of the alloy and thus of a stable hydrogen permeance.

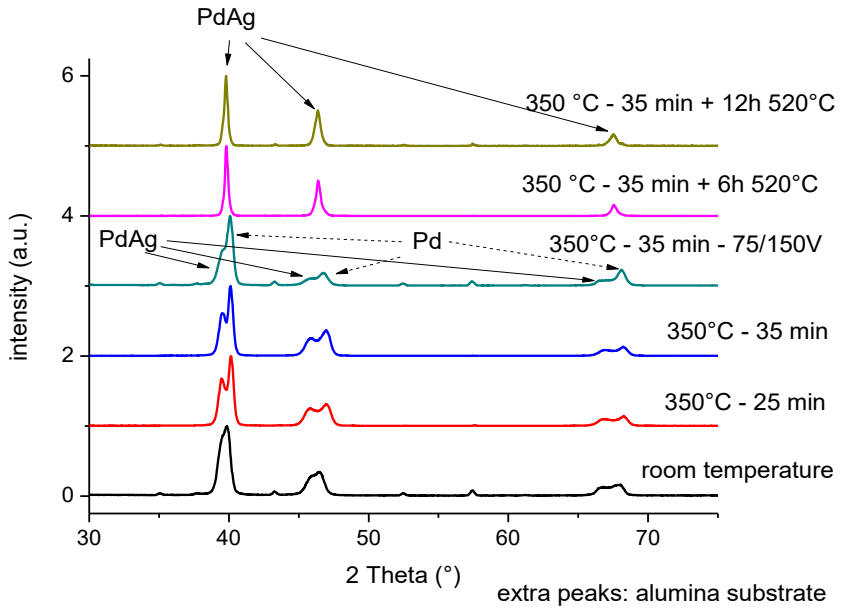

Fig. 9.23: XRD patterns (common parameters: pressure 1.02 · 10^{-2} mbar, Pd 800 W, Ag 350 W).

Tab. 9.5 summarizes some Rietveld analyses of different HiPIMS depositions (first column specifies the sputtering parameter/treatment specific of the membrane; common sputtering condition: Pd 800 W, Ag 330 W, 1.03 · 10^{-2} mbar). Palladium and palladium silver alloy are cubic, space group Fm-3m.

	Palladium	Pd-Ag alloy
Room temperature	Cell parameter = 3.910 Å Crystallite size ≈ 65 nm	Cell parameter = 3.958 Å Crystallite size ≈ 48 nm
Alternating bias voltage 75/150 V (*)	Cell parameter = 3.895 Å Crystallite size ≈ 130 nm	Cell parameter = 3.953 Å Crystallite size ≈ 45 nm
35' 350°C (*)	Cell parameter = 3.888 Å Crystallite size ≈ 250 nm	Cell parameter = 3.949 Å Crystallite size ≈ 85 nm
35' 350°C + 6h 520°C	< 4 wt%	Cell parameter = 3.920 Å Crystallite size ≈ 155 nm
35' 350°C + 12h 520°C	< 1.5 wt%	Cell parameter = 3.924 Å Crystallite size ≈ 270 nm

* = Goodness of Fit between 7-9 (all the other analyses had GoF between 2.5 – 4.5)

Tab. 9.5: Rietvield refinement of some HiPIMS samples.

References

1. Jayaraman, V.; Lin, Y. S., Synthesis and hydrogen permeation properties of ultrathin palladium-silver alloy membranes. *Journal of Membrane Science* **1995,** *104* (3), 251-262.

2. Folletto, E. L.; Wirbitzi da Silvera, J. V.; Jahn, S. L., Preparation of palladium-silver alloy membranes for hydrogen separation. *Latin American Applied Research* **2008**, *38*, 79-84.

3. Engin Ayturk, M.; Mardilovich, I. P.; Engwall E. E.; Ma, Y. H., Synthesis of composite Pd-porous stainless steel (PSS) membranes with a Pd/Ag intermetallic diffusion barrier. *Journal of Membrane Science* **2006**, *285*, 385-394.

10.Vanadium based alloys

Vanadium has high hydrogen permeability and diffusivity, but it is known to be affected by hydrogen embrittlement and, for this reason, has always been investigated only as bulk material due to embrittlement of thin membranes. Since a reduction of the membrane thickness can strongly enhance the hydrogen permeation, this work was aimed at identifying a vanadium alloy suitable for PVD deposition, resistant to hydrogen embrittlement.

10.1. $V_{90}Pd_{10}$

We firstly studied the feasibility of the deposition of $V_{90}Pd_{10}$ using DC magnetron sputtering, but the results were unsatisfying. Prior to the sputtering depositions, calibration of vanadium and palladium targets was necessary (Tab. 10.1), to calculate the target powers required to deposit the desired alloy.

Power V (W)	Rate (nm/min)	Rate variation (%)	Power Pd (W)	Rate (nm/min)	Rate variation (%)
50	15	4	**50**	10	14
70	16	7	**75**	15	8
100	28	5	**100**	24	4
130	36	5.5			

Tab. 10.1: vanadium calibration (DC power unit) and palladium calibration (RF power unit).

Fig. 10.1 reports the alloy sputtered by DC magnetron sputtering (300°C, Ar $1.1 \cdot 10^{-2}$ mbar, Pd 20 W, V 100 W, no bias) onto porous alumina substrate, but several defects were recognizable.

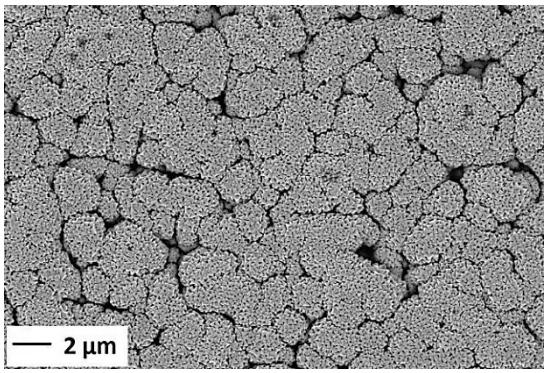

Fig.10.1: top view pictures of V-Pd alloy sputtered by DC magnetron sputtering.

Therefore, we investigated the possibility to deposit this alloy by HiPIMS. Preliminary HiPIMS depositions were performed to calibrate the target powers and to find the correct substrate/target distance (120 mm for vanadium, 200 mm for palladium) to deposit the alloy in right composition. When all these parameters were found, we deposited the alloy at room temperature (Pd 10 W, V 700 W, $1 \cdot 10^{-2}$ mbar, 75 V bias, 60 min, 2 RPM sample rotation, Figs 10.2):

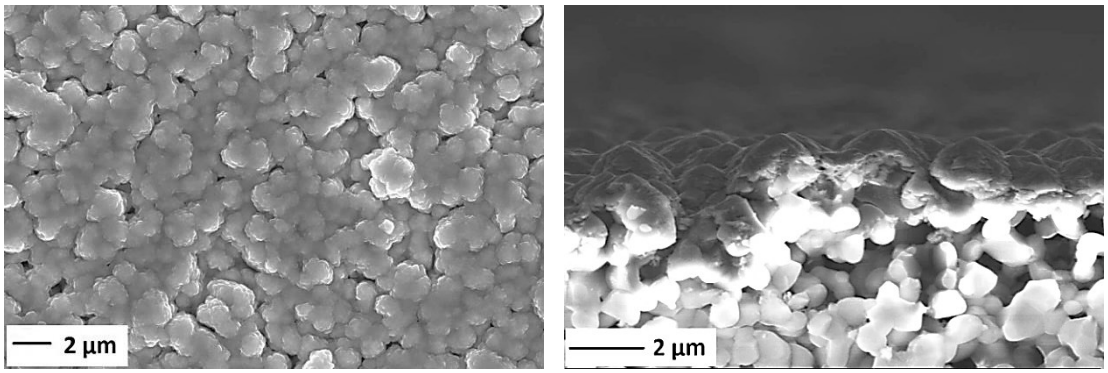

Fig. 10.2: top view (left) and cross section (right) pictures of V-Pd alloy sputtered by HiPIMS (room temperature deposition).

As expected, HiPIMS deposition showed sample morphology strongly different compared to DC magnetron sputtering deposition: the alloy is smoother and the sharp structures disappeared, thanks to the higher ion-bombarding effect typical of HiPIMS. However, many defects were clearly visible, probably due to the limited thickness.

In order to improve the surface coverage of the porous substrate, we extended the deposition up to 3 hours ($1 \cdot 10^{-2}$ mbar, 350°C, other parameters constant), and to guarantee the right electrical contact between sample holder and substrate, before the V-Pd deposition we sputtered a thin Pd layer at room temperature:

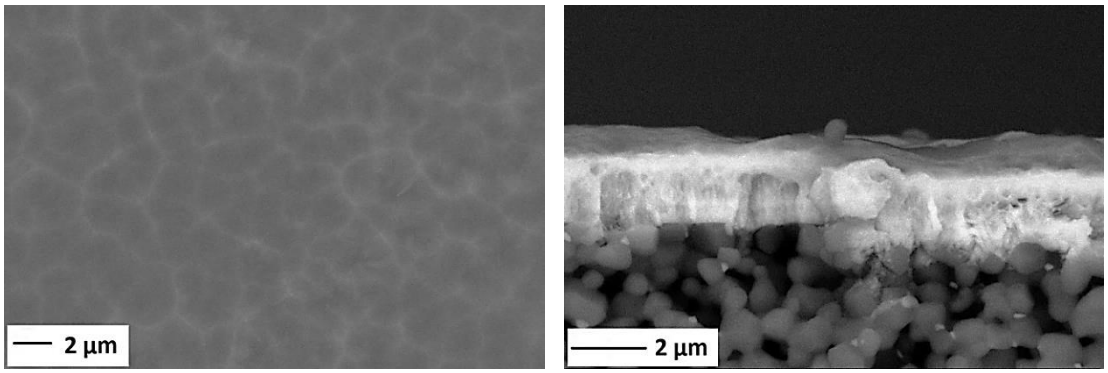

Fig. 10.3: top view (left) and cross section (right) of V-Pd alloy sputtered by HiPIMS (350°C).

Fig 10.3 shows a very good metal layer, with no defects and with a very smooth surface. The final thickness was below 2 µm.

EDS analyses confirmed the stoichiometry of the alloy (average values V ≈ 93 at%, Pd ≈ 7 at%, within the error range of the analysis); Fig. 10.4 reports an EDS spectrum as example:

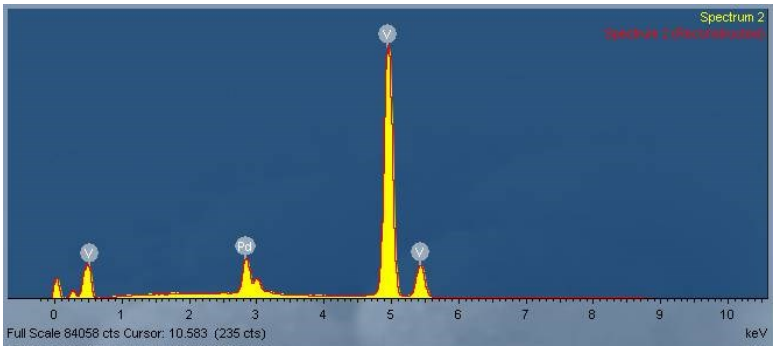

Fig. 10.4: EDS spectrum of V-Pd alloy.

Fig. 10.5 reports the XRD pattern of V-Pd alloy sputtered at 350°C (180 min, $1 \cdot 10^{-2}$ mbar):

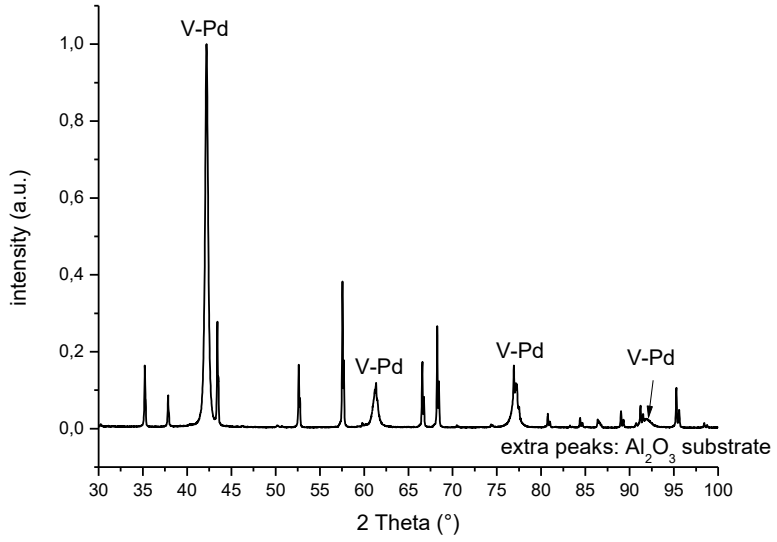

Fig. 10.5: XRD pattern of V-Pd alloy.

The X-ray diffraction peaks were identified by comparing our diffraction pattern with a pattern found in literature[1] and by Rietvield analysis, that identified peaks belonging to pure vanadium phase (actually a vanadium solid solution with palladium). No peaks belonging to pure palladium were detected. The V-Pd solid solution (Im-3m space group) has a cell parameter of 3.034 Å and crystallites size of ≈ 90 nm (GoF ≈ 5).

Since vanadium is prone to oxidation, two thin layers of palladium (around 200 nm each) at both sides of the V-Pd film were deposited.

10.2. Ternary Alloy $V_{84.2}Ni_{5.3}Ti_{10.5}$

10.2.1. Stainless steel substrate

Considering the complexity of a co-deposition of a ternary alloy from three targets (DC magnetron sputtering), we approached the study of this new alloy by preliminary depositions onto dense stainless steel foils (Fig. 10.6), to discover possible criticalities and to proceed with the sputtering onto the ceramic substrate only if satisfactory results were achieved.

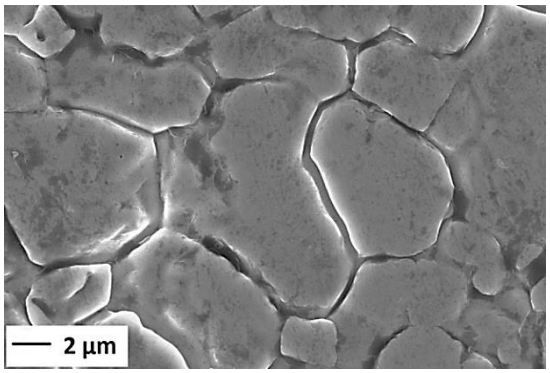

Fig. 10.6: SEM picture of the stainless steel substrate.

Prior to the sputtering depositions, calibration of titanium and nickel targets was necessary (Tab. 10.2), to calculate the target powers required to deposit the desired alloy (for vanadium calibration see Tab. 10.1).

Power Ti (W)	Rate (nm/min)	Rate variation (%)	Power Ni (W)	Rate (nm/min)	Rate variation (%)
150	37	11	**100**	8	12
200	54	4	**150**	15	9
250	57	4	**200**	20	12

Tab. 10.2: titanium calibration (DC power unit) and nickel calibration (RF power unit).

Fig. 10.7 shows the stainless steel substrate before (left) and after (right) PVD deposition.

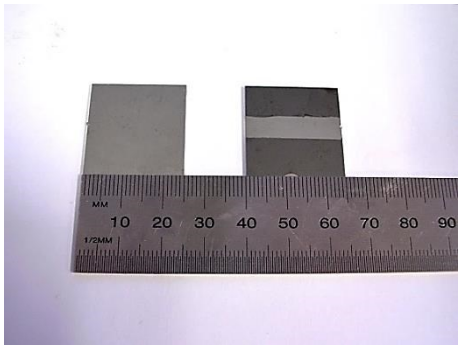

Fig. 10.7: stainless steel substrate before (left) and after (right) the PVD deposition.

Preliminary depositions (30 min) were performed at room temperature, with no bias voltage applied and at $1.1 \cdot 10^{-2}$ mbar. After the targets calibration, the depositions were performed with the following target powers: vanadium 173 W, titanium 25 W and nickel 21 W. Fig. 10.8 reports the SEM pictures of the top view of the sample:

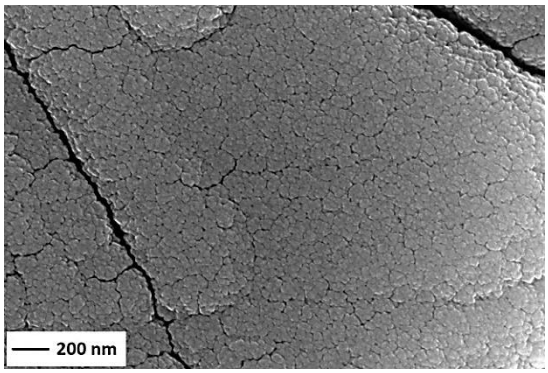

Fig. 10.8: PVD deposition at room temperature and 1.1 · 10^{-2} mbar.

The sample showed the typical columnar structure of DC magnetron sputtering. To avoid these structures, higher temperatures and bias voltage were attempted. Fig. 10.9 reports the sample deposited at 200°C:

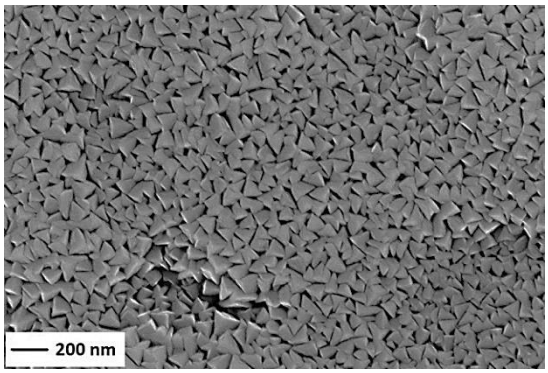

Fig. 10.9: PVD deposition at 200°C and 1.1 · 10^{-2} mbar.

As expected, high temperature helped the crystallization, but large pyramidal crystals formed with no compact layer. Therefore, various bias voltages were systematically studied in order to increase the ion bombarding effect.

Fig. 10.10 shows samples prepared applying 50 V and 100 V bias voltage (common sputtering conditions: room temperature, 1.1 · 10^{-2} mbar):

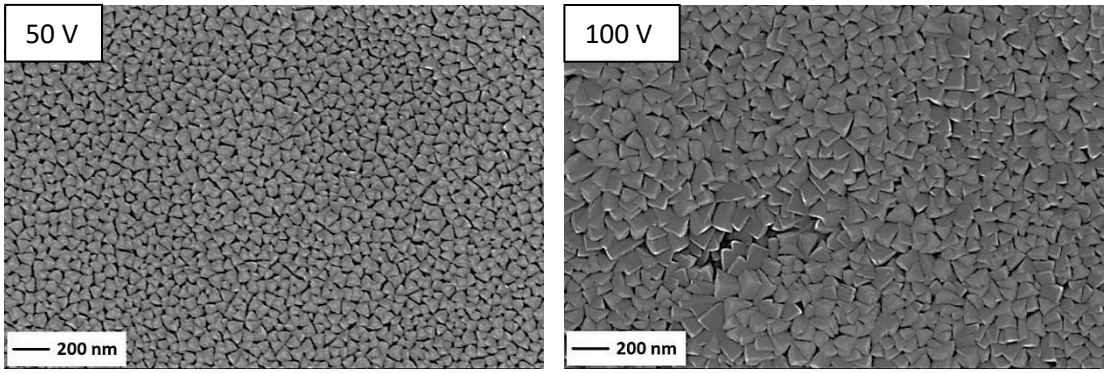

Fig. 10.10: PVD depositions at room temperature, $1.1 \cdot 10^{-2}$ mbar, bias voltages 50 V (left) and 100 V (right).

Bias voltages turn out to be useless and the high ion energy induced a crystallization of the alloy. Samples morphology is very similar to a 200°C sputtering deposition (bias voltage of 50 V and a pressure of $1.1 \cdot 10^{-2}$ mbar, Fig. 10.11):

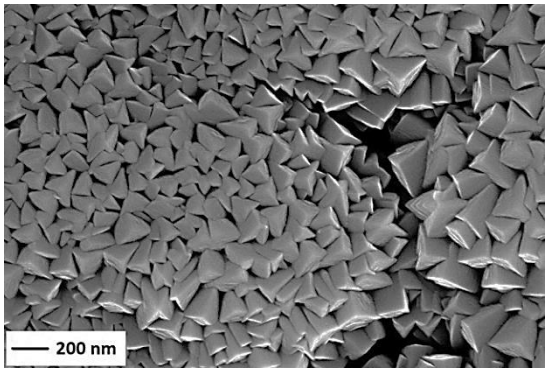

Fig. 10.11: PVD deposition at 200°C, $1.1 \cdot 10^{-2}$ mbar, bias voltage 50 V.

It is clear that higher temperatures and higher bias voltages favoured the crystallization and do not help the deposition of a continuous and compact metal layer, so we focused our attention on the sputtering pressure. Lowering the pressure, higher energetic atoms can reach the substrate, thus reducing the crystallization and increasing surface diffusion. Therefore, the pressure inside the chamber was reduced to $3.3 \cdot 10^{-3}$ mbar, a value near to lower ignition plasma limit but sufficient to allow a deposition with a stable argon plasma. Fig. 10.12 reports SEM pictures of samples sputtered at low pressure, applying a bias of 50 V and changing the deposition temperature:

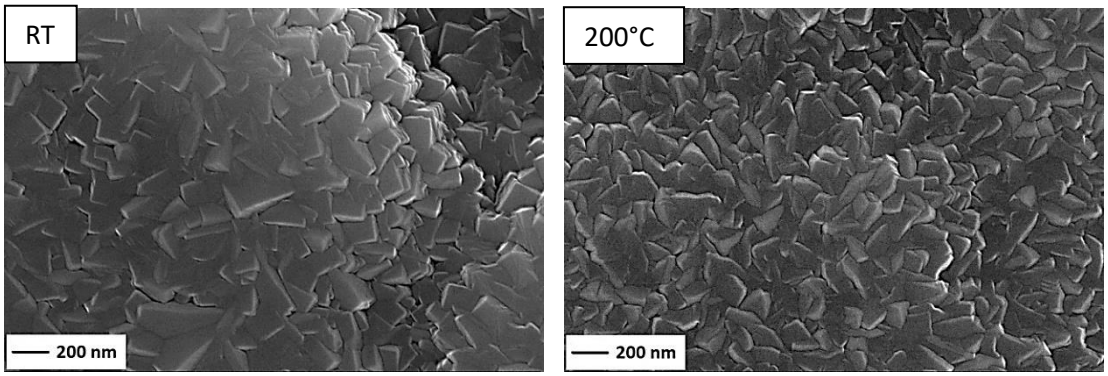

Fig. 10.12: PVD deposition at room temperature (left) and 200°C (right) – argon pressure 3.3 · 10^{-3} mbar.

The lower pressure inside the chamber promoted the growth of dense and compact coatings. As expected, the higher temperature deposition enhances crystallization. After these promising preliminary results, we proceeded with the sputtering onto the porous alumina substrate.

10.2.2. Porous alumina substrate

Before the ternary alloy deposition, both alumina pellets sides were covered by a very thin palladium layer (10 nm), to guarantee the electrical contact between ceramic pellet and sample holder. Porous substrates were fixed to the sample holder with conductive Kapton tape.

Preliminary depositions onto the alumina substrate (Fig. 10.13) were performed at 200°C, 3.3 · 10^{-3} mbar, 50 V bias voltage and 60 min; target powers were tuned in the following ranges to achieve the correct stoichiometry: vanadium 160-173 W, titanium 24-30 W, nickel 21-35 W.

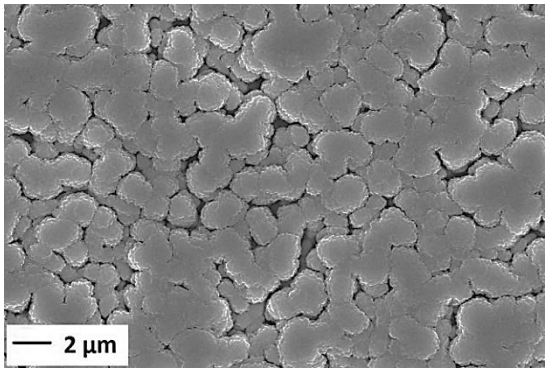

Fig. 10.13: PVD deposition at 200°C, 50 V and argon pressure 3.3 · 10^{-3} mbar.

Due to the surface roughness of the pellet, metal layers were not compact. We tried to combine two sputtering depositions dividing the process into two steps:

- I part: room temperature, $3.3 \cdot 10^{-3}$ mbar, no bias, 30 min;
- II part: 200°C, $3.3 \cdot 10^{-3}$ mbar, 50 V, 30 min.

However, Fig. 10.14 shows a result similar to previous deposition:

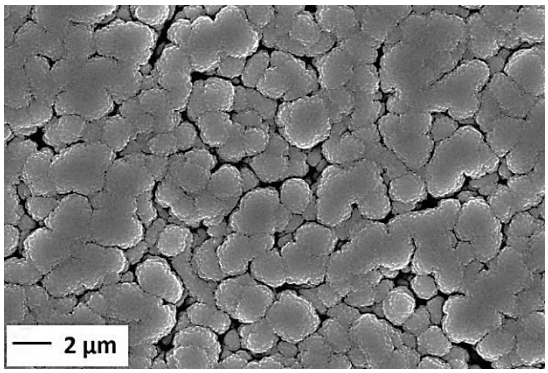

Fig. 10.14: combination of two sequential PVD depositions. I: RT, $3.3 \cdot 10^{-3}$ mbar, no bias, 30 min; II: 200°C, $3.3 \cdot 10^{-3}$ mbar, 50 V, 30 min.

In order to deposit a dense layer, various bias voltages were tested. Fig. 10.15 shows samples deposited at 200°C and $3.3 \cdot 10^{-3}$ mbar (60 min deposition) varying the applied bias:

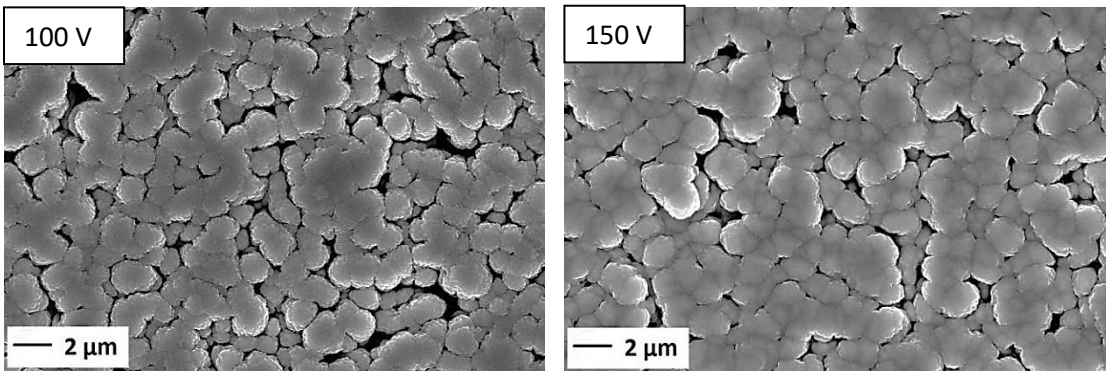

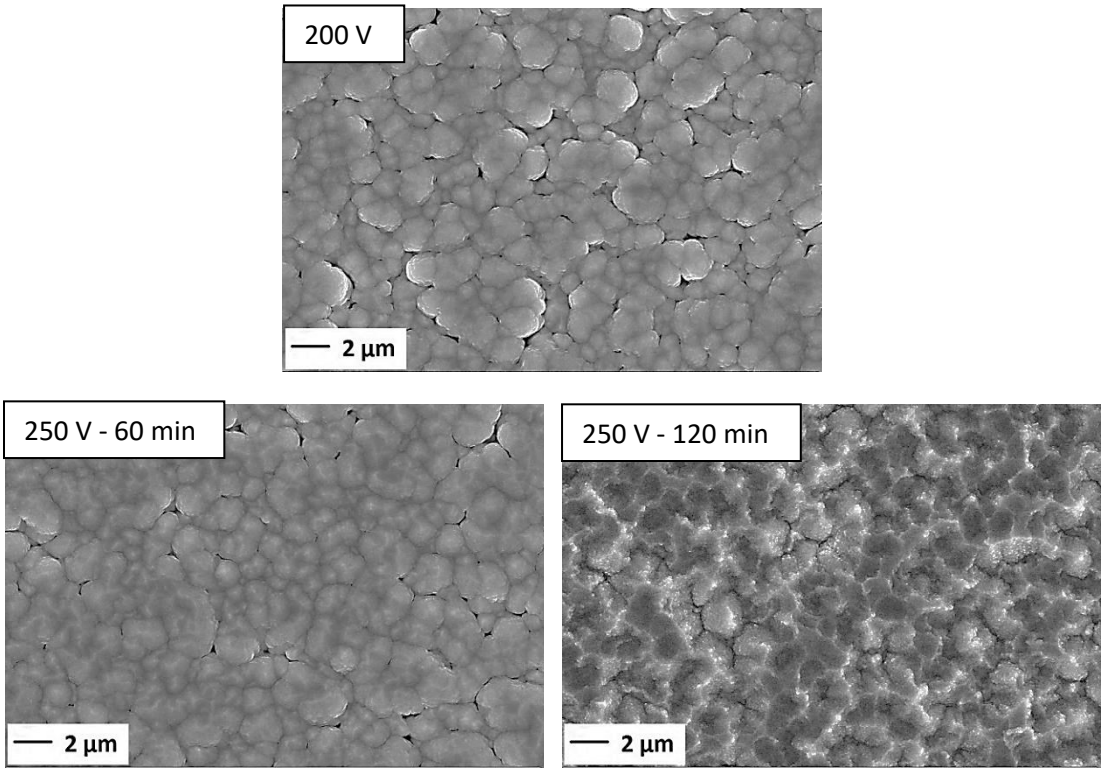

Fig. 10.15: PVD depositions at 200°C, 3.3 · 10^{-3} mbar, at various bias voltages.

We can clearly see that higher bias voltages improved the surface coverage of the alumina pellets, and samples become progressively more compact and denser. The 250 V bias deposition showed some submicrometric holes only in the 60 min sample; the 120 min sample is compact and dense. However, although a high bias voltage is useful for the preparation of a dense and compact vanadium based layers, it could induce stresses inside the metal layer, eventually leading to peeling risks.

In order to reduce the bias voltage, higher temperatures were tested (Fig. 10.16), common sputtering parameters 150 V and 3.3 · 10^{-3} mbar), but no significant results were obtained:

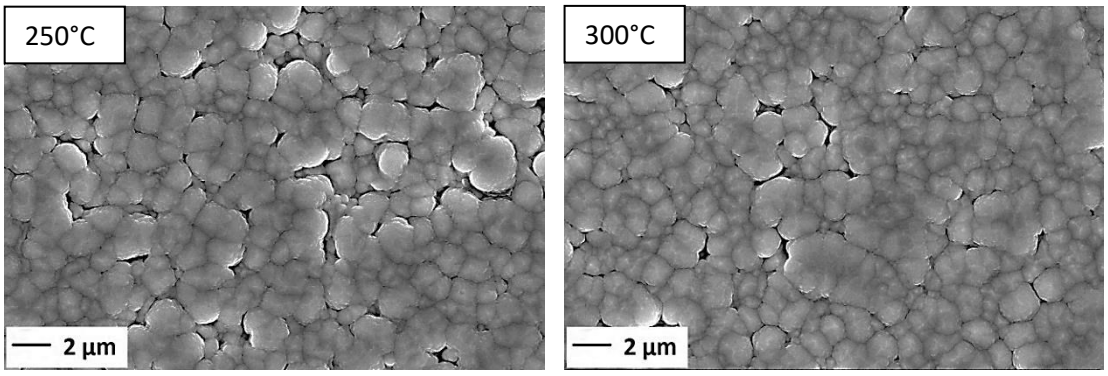

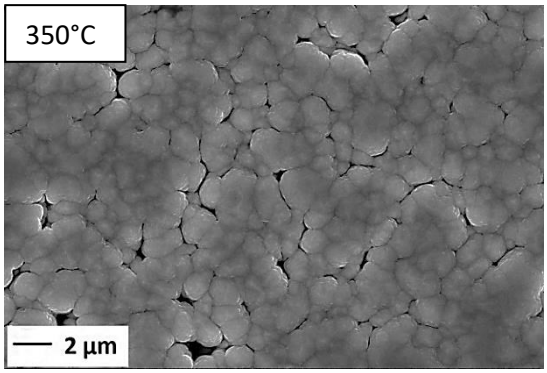

Fig. 10.16: PVD depositions at 200 – 250 - 300°C, 3.3 · 10^{-3} mbar and 150 V bias voltage.

In order to prepare metal layers with a good surface coverage and lower residual stresses, we decided to reduce the bias voltage applied and to extend the sputtering deposition to 4 hours. As shown by Fig. 10.17, after only one hour of deposition the metal layer is too thin (≈ 1.5 µm) and a good surface coverage was not achieved; increasing the sputtering time up to 4 hours we obtained a promising sample (thickness around 5 µm).

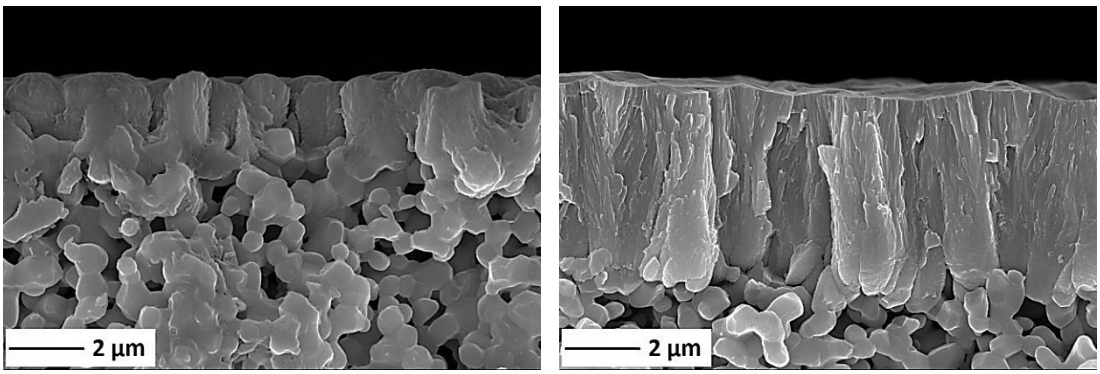

Fig. 10.17: thickness comparison between 1h deposition (left) and 4h deposition (right).

With DC magnetron sputtering a dense selective layer (Fig. 10.18) was achieved, suitable for gas separation.

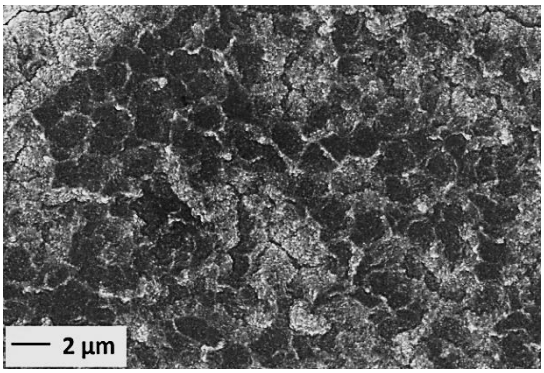

Fig. 10.18: top view of PVD deposition onto porous alumina at 200°C, 3.3 · 10^{-3} mbar and 150 V bias voltage (4h deposition).

10.2.3. EDS/XRD

Each change of deposition parameters can alter the alloy composition. Therefore, after each deposition the stoichiometry was checked out by EDS analyses and the target powers adjusted consequently. In fact, the bias voltage can particularly modify the stoichiometry of the alloy (Tab. 10.3, common sputtering parameters: 3.3 · 10^{-3} mbar, 200°C). Fig. 10.19 reports an EDS spectrum of ternary alloy.

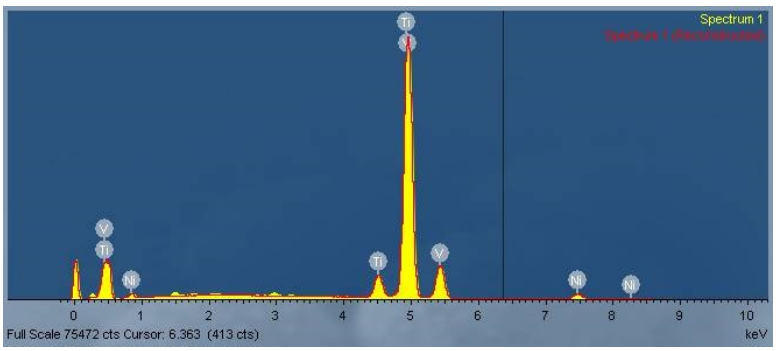

Fig. 10.19: V-Ni-Ti EDS analysis.

Target powers* (W)	Bias (V)	Elemental analysis
V = 173 - Ni = 21 - Ti = 25	-50	V ≈ 87 at% - Ni ≈ 3 at% - Ti ≈ 10 at%
V = 172 - Ni = 26 - Ti = 24	-100	V ≈ 85 at% - Ni ≈ 5 at% - Ti ≈ 10 at%
V = 172 - Ni = 26 - Ti = 24	-150	V ≈ 87 at% - Ni ≈ 4 at% - Ti ≈ 9 at%
V = 170 - Ni = 27 - Ti = 24	-200	V ≈ 88 at% - Ni ≈ 4 at% - Ti ≈ 8 at%
V = 170 - Ni = 27 - Ti = 24	-250	V ≈ 91 at% - Ni ≈ 3 at% - Ti ≈ 6 at%

* vanadium and titanium sputtered by DC power units, nickel sputtered by a RF power unit.

Tab. 10.3: EDS analyses of samples sputtered with different bias voltages

Tab. 10.2 shows the influence of bias voltage on the alloy composition: the increase of bias increases the amount of vanadium and reduces the amount of nickel and titanium. Bias voltage, causing an ion bombardment of the film surface, is responsible for the resputtering of the surface atoms. This effect is more marked for lighter atoms (e.g. for titanium with respect to vanadium) or for elements having high sputter yield (as for nickel, as already reported in NiTi depositions[2]). The total effect is a reduction of titanium and nickel in the sputtered alloy, and the necessary adjustment of targets powers is required.

Samples were further analysed by X-ray diffraction. Fig. 10.20 reports the as-sputtered alloy (200°C, 3.3 · 10^{-3} mbar, -150 V bias voltage, V = 172 W, Ti = 24 W, Ni =26 W) and the pure vanadium and alumina substrate as reference.

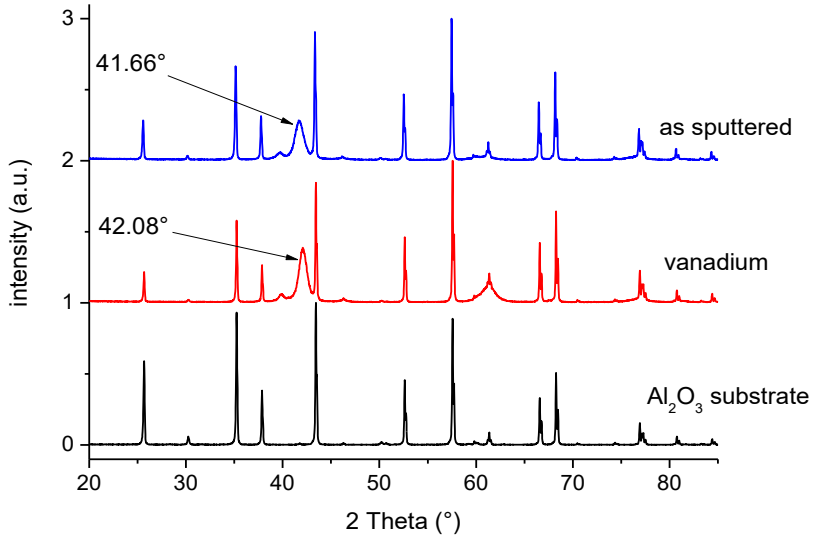

Fig. 10.20: XRD patterns of V-Ni-Ti and pure vanadium. Alumina substrate pattern is reported to identify extra peaks.

Considering the most intense pure vanadium reflection (41.66°, cubic – Im-3m, 3.037 Å cell parameter) we observed a shift of this peak towards smaller diffraction angles, since the introduction of nickel and titanium metals caused the formation of vanadium solid solution with an enlargement of the vanadium unit cell. No other phases were identified by Rietvield analysis. A research of possible Ni-Ti compounds was performed, but no evidences were found. These patterns are very different from what was found in literature[3]; all the works concerning this ternary alloy dealt with an arc melting preparation and no works were found about a PVD preparation of the alloy, so no clear references are available.

Since the preliminary study of the ternary alloy involved tests with different bias voltages, in Fig. 10.21 are collected some XRD diffraction patterns performed on ternary alloys prepared by varying the bias voltage applied.

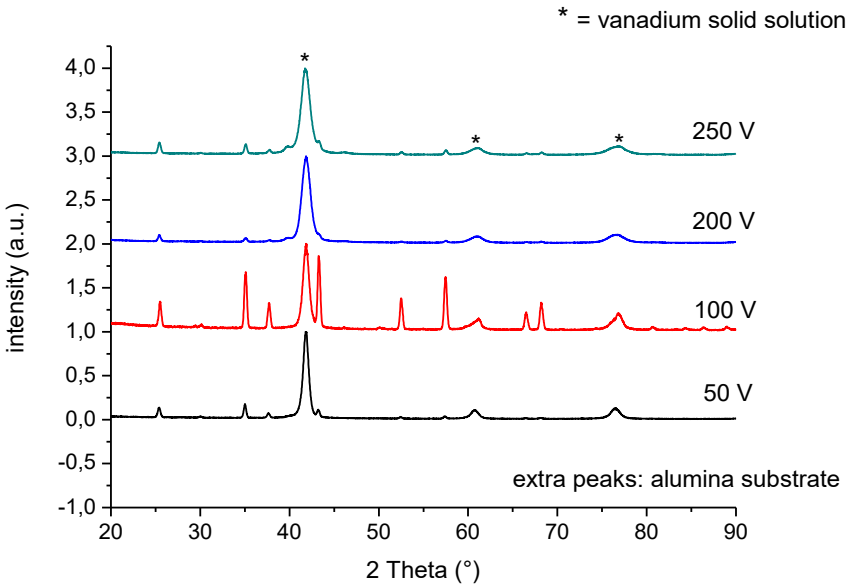

Fig. 10.21: XRD diffraction patterns of ternary alloy deposited applying different bias voltages (grazing incidence).

X-ray diffraction patterns show a clear alloy microstrain, recognizable by the broadening of the peaks, especially at high angles. Microstrain is typical for solid solutions, and it is related to the defectivity of the unit cell. It is reasonable that an increase of bias voltage promotes the formation of defects inside the alloy, due to the increasing energy of ions impinging on the coated surface. Rietveld analyses have detected only peaks compatible with vanadium (cubic, Im-3m space group, actually a vanadium solid solution as explained above), with no peaks belonging to V-Ti, V-Ni and Ni-Ti compounds, as reported in literature. The cell parameter is included in the range 3.048 – 3.037 Å (from 50 V to 250 V bias voltage applied, GoFs between 1.9 and 2.4), with crystallites size from ≈ 30 nm to ≈ 300 nm.

References

1. Paglieri, S. N.; Wermer, J. R.; Buxbaum, R. E.; Ciocco, M. V.; Howard, B. H.; Morreale, B. D., Development of membranes for hydrogen separation: Pd coated V-10Pd. *Energy Materials: Materials Science and Engineering for Energy Systems* **2008,** *3* (3), 169-176.

2. Martins, R. M. S.; Schell, N.; Reuther, H.; Pereira, L.; Mahesh, K. K.; Silva, R. J. C.; Fernandes, F. M. B., Texture development, microstructure and phase transformation characteristics of sputtered Ni–Ti Shape Memory Alloy films grown on TiN<111&gt. *Thin Solid Films* **2010,** *519* (1), 122-128.

3. Jiang, P., Yu, Y., Song, G., Liang, D., Kellam, M., Dolan, M., Effect of heat treatment on microstructure, hardness and rollability of $V_{55}Ti_{30}Ni_{15}$ alloy membrane. *Materials and Design* **2014**, 63, 136-141.

11.Zeolite membrane for hydrogen separation

11.1. Powder

Aim of this work was the growth of a zeolite membrane directly onto the ceramic substrate in a one-step process, but, before membranes, a preliminary study about zeolite powders and their synthetic approach was performed.

To prepare pure LTA (Linde Type A) zeolite, before the hydrothermal synthesis (2h 90°C), the hydrogel (combination of silicate and aluminate solutions) was aged for 24h at 60°C, to improve the reticulation of the alumino-silicate framework. In the first hours of the ageing the hydrogel was clear, but after 24h the solution become opaque and a very thin layer of material covered the inner surface of the reaction flask. We poured in the autoclave only the liquid part of the hydrogel.

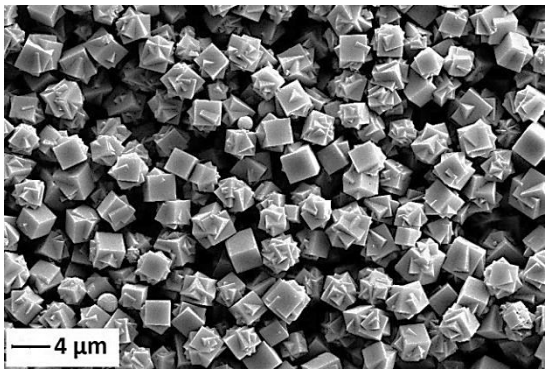

Fig. 11.1: sample prepared with an ageing step of 24h at 60°C, followed by a hydrothermal synthesis at 90°C for 2h.

We obtained a sample of pure LTA zeolite (Fig. 11.1). SEM pictures show the typical LTA cubic morphology, with a narrow size distribution of cubes of ≈ 3 µm.

XRD diffraction pattern (Fig. 11.2) confirmed the synthesis of LTA zeolite.

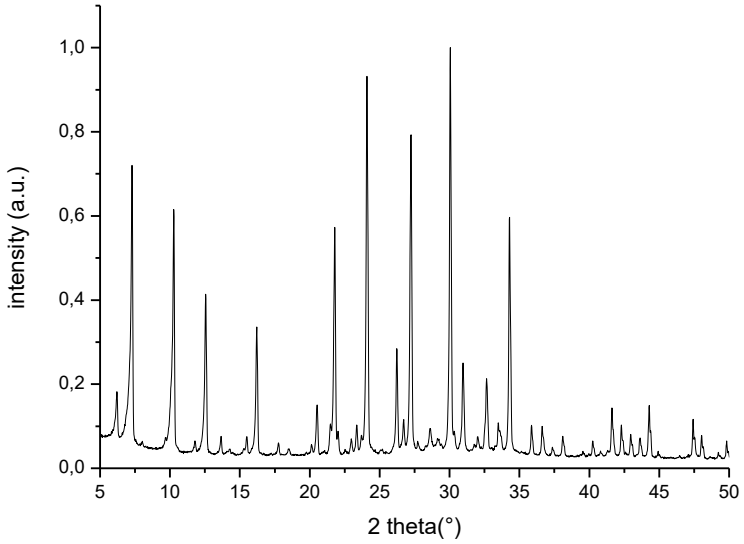

Fig. 11.2: diffraction pattern of LTA zeolite sample.

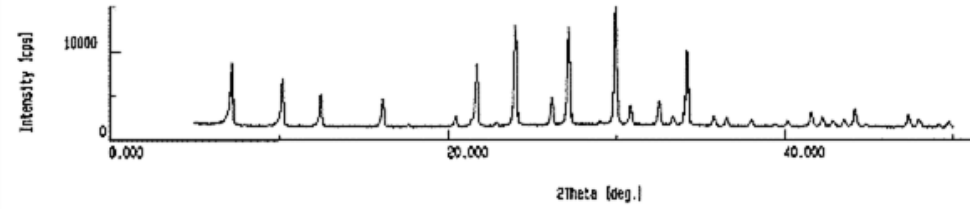

Fig. 11.3: reference diffraction pattern for LTA zeolite[1].

As confirmed by Rietvield analysis and by literature (Fig. 11.3), the main peaks belong to LTA zeolite; traces of NaOH (< 1 wt%), belonging to the reaction batch reagent, were detected. TGA-DSC analysis (RT-450°C, 10°C/min, thermal treatment in air, air flux 100 mL/min, Fig. 11.4) was useful to find the temperature stability range of the zeolite:

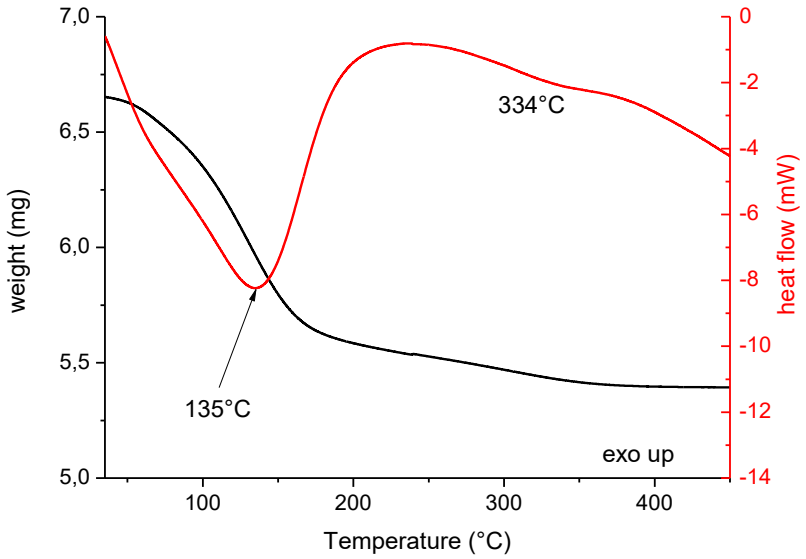

Fig. 11.4: TGA-DSC analysis on LTA zeolite sample.

Comparing with literature[2] we can identify the major weight losses and the corresponding heat flows:

- endothermic minimum at 135°C: desorption of physically absorbed water;
- exothermic peak (200-400°C): desorption of the remaining zeolite water in the zeolitic matrix.

However, since LTA channels are of about 0.40 – 0.41 nm, to prepare membranes for hydrogen separation with high selectivity we investigated the synthesis of hydroxy-sodalite (HS) zeolite, which has smaller channels, even though the temperature stability range of this zeolite in the synthesis is low and, as a consequence, the synthesis of pure HS is complicated. To this end, we changed the hydrothermal treatment (keeping the same ageing step, Fig. 11.5) increasing the temperature, since many literature works obtained HS zeolite at higher temperature (common hydrogel ageing step 24h 60°C, the hydrothermal treatment is reported in the box):

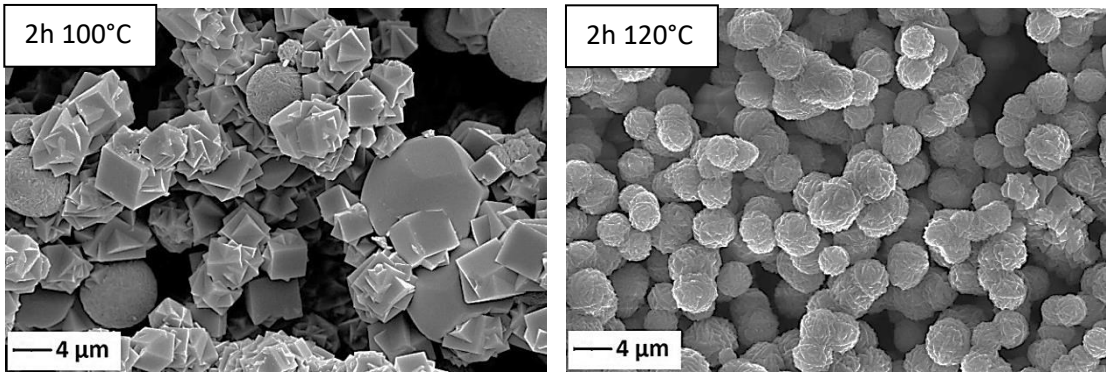

Fig. 11.5: samples prepared with an ageing step of 24h at 60°C, followed by a hydrothermal synthesis at 100°C for 2h (left) and 2h 120°C (right).

In the 2h 100°C treatment there are only traces of HS zeolite (easily recognizable morphology, thread-ball like), and LTA zeolite is still the main phase. By increasing the hydrothermal synthesis temperature up to 120°C, we found the right temperature to prepare the HS phase with our experimental setup: HS zeolite is the unique phase present in the sample; its typical morphology is evident and the particles show a size distribution between 2 and 4 µm (as single particles, since they are assembled in clusters). XRD analyses confirmed the HS zeolite synthesis (Fig. 11.6), similar to literature (Fig. 11.7).

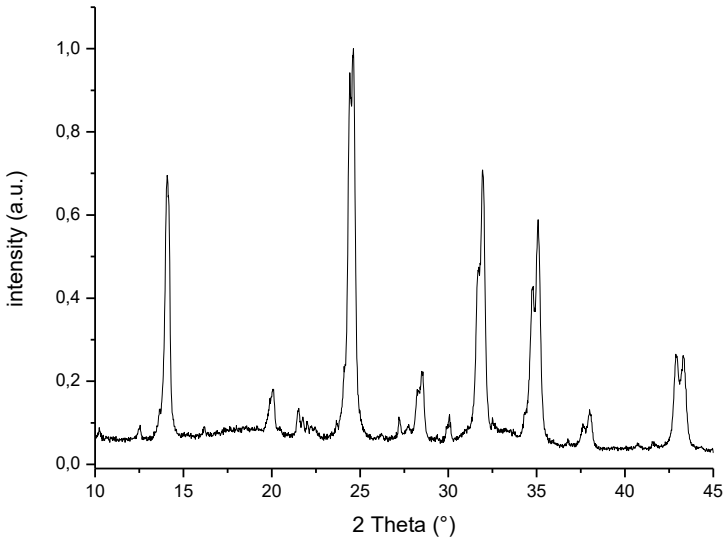

Fig. 11.6: diffraction pattern of HS zeolite sample.

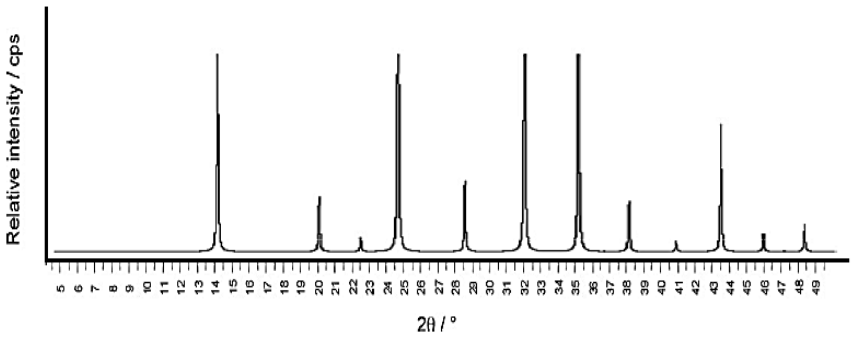

Fig. 11.7: reference diffraction pattern for HS zeolite[3].

Main XRD peaks belong to hydroxy-sodalite phase (confirmed by Rietvield analysis); traces of NaOH (< 1%) were detected.

HS analysis was completed by TGA-DSC analysis (RT-450°C, 10°C/min, thermal treatment in air, air flux 100 mL/min, Fig. 11.8), to find the temperature stability range of this zeolite in view of future applications as membrane for hydrogen separation.

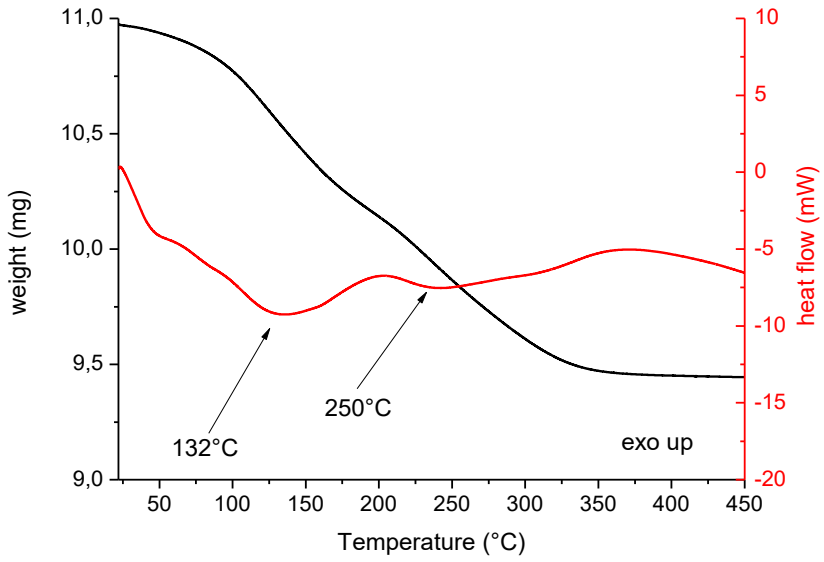

Fig. 11.8: TGA-DSC analysis of HS zeolite sample.

Comparing our thermal analysis with a literature reference[4], the weight variation in the range RT-450°C is due to the loss of water from the channels (a total weight loss of 14% from RT to 450°C was measured), and the water is lost in two events, around 150°C and 250°C. No morphological changes are present within this temperature range. Since HS zeolite is a hy-

drophilic zeolite, the most important task is the removal of water from the channels, to allow the sieving of hydrogen from the gas mixture.

11.2. Membranes

In order to deposit the HS zeolite membrane, a specific sample holder (Fig. 11.9) was designed to keep the substrates in the correct position during the hydrothermal synthesis. Alumina substrates were hold by a Teflon disk, with three housing for the ceramic substrate and three holes to allow the free flow of solution during the hydrothermal synthesis. The height from the base was regulated by a stainless steel threaded pole. Membrane grown in the lower side of the ceramic substrate was more homogenous than the membrane grown in the upper side.

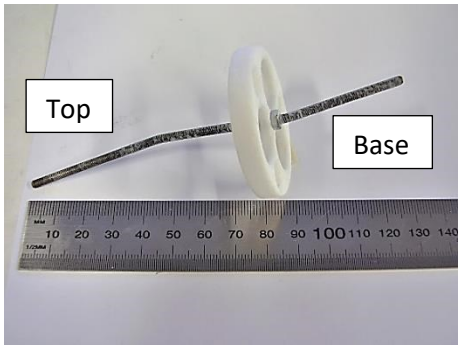

Fig. 11.9: sample holder designed to grow zeolite membranes onto porous alumina substrates.

First of all, we used the parameters for the HS powder synthesis (hydrogel ageing 24h 60°C + hydrothermal synthesis 2h 120°C), but a mixture of LTA and HS zeolites was obtained (Fig. 11.10).

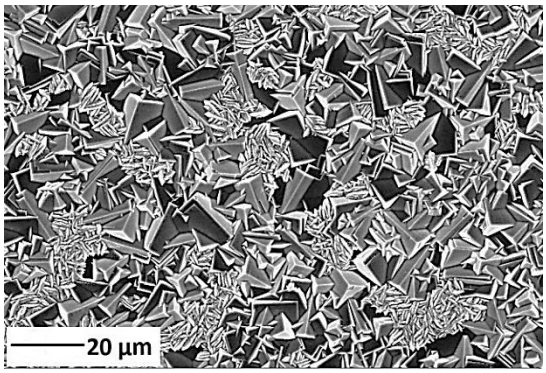

Fig. 11.10: membrane prepared with an ageing step of 24h at 60°C, followed by a hydrothermal synthesis at 120°C for 2h.

We had to find new experimental conditions to prepare pure HS zeolite membranes, so we extended the hydrothermal synthesis up to 4h, keeping the same ageing step (Fig. 11.11).

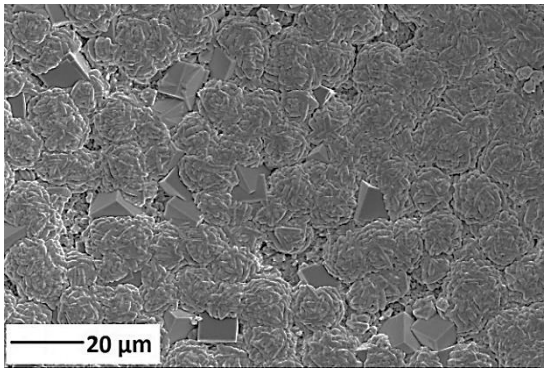

Fig. 11.11: membrane prepared with an ageing step of 24h at 60°C, followed by a hydrothermal synthesis at 120°C for 4h.

Synthesis was not satisfying, with a bad substrate coverage. We decided to modify the experimental process changing the ageing step, keeping 60°C but reducing the ageing time from 24h to 12h, to avoid an excessive hydrogel depletion (formation of tiny crystals onto the inner surface of the reaction flask), pouring into the autoclave a more concentrated hydrogel (Fig. 11.12).

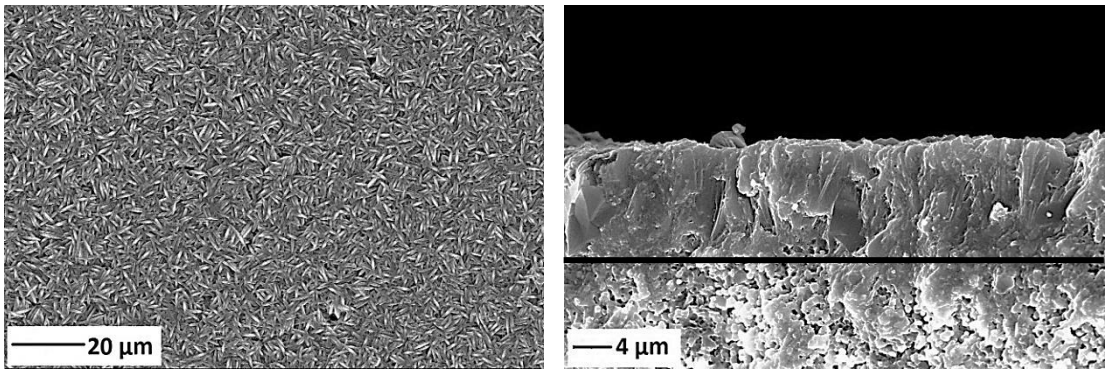

Fig. 11.12: membrane prepared with an ageing step of 12h at 60°C, followed by a hydrothermal synthesis at 120°C for 2h.

Applying the new experimental conditions we succeeded in preparing a pure HS zeolite supported membrane having mean thickness of about 10 µm. HS zeolite was confirmed by X-ray diffraction analysis (Fig. 11.13). However, from the top view SEM pictures, some dishomogeneitis are recognizable, and probably these defects are due to the presence of LTA cubes (indicated by the arrow in Fig. 11.14).

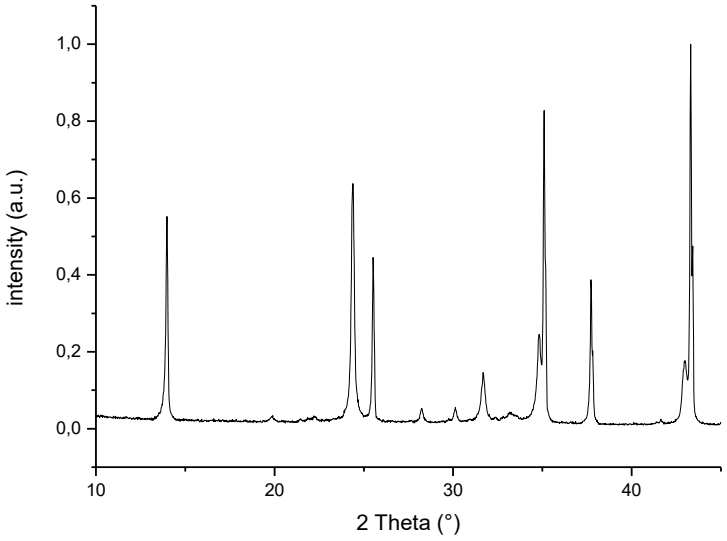

Fig. 11.13: XRD diffraction pattern of HS zeolite membrane.

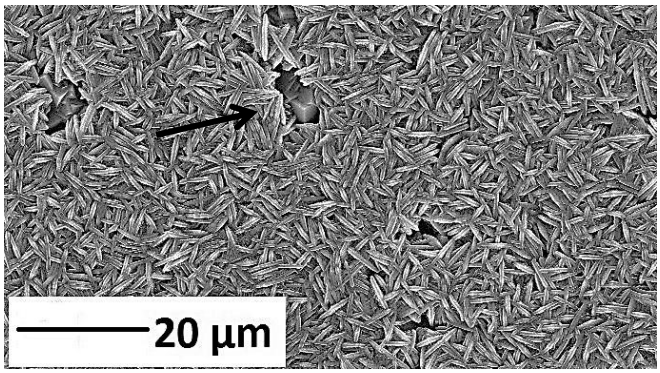

Fig. 11.14: LTA cubes inside the HS zeolite membrane.

The LTA amount increased when we prolonged the hydrothermal synthesis up to 4h (Fig. 11.15), keeping all the other synthesis conditions constant.

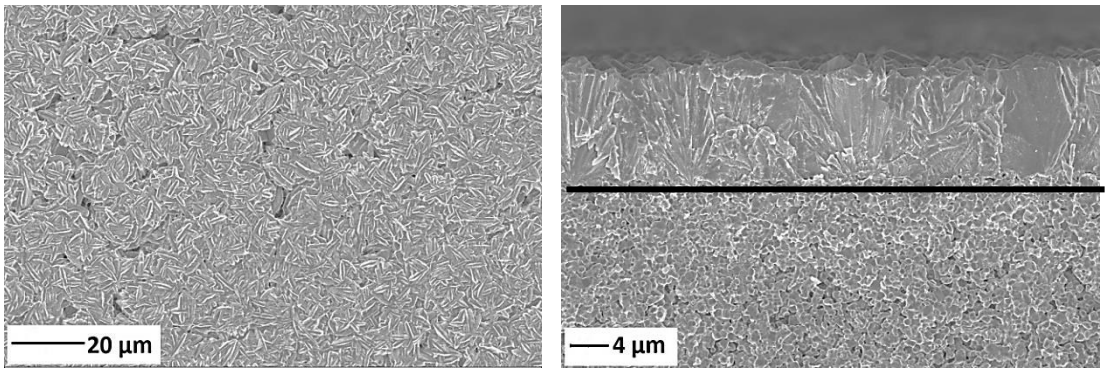

Fig. 11.15: membrane prepared with an ageing step of 12h at 60°C, followed by a hydrothermal synthesis at 120°C for 4h.

As expected, membrane is thicker than the 2h sample, but, as in the previous synthesis, LTA cubes (≈ 2 µm) had formed (Fig. 11.16).

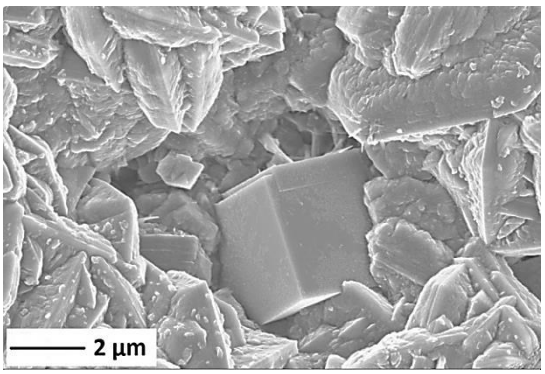

Fig. 11.16: LTA cube inside the HS zeolite membrane.

Other strategies were tested to prepare a pure HS membrane:

- Pouring the hydrogel into the pre-heated autoclave;
- Heating very quickly the hydrogel before to pour it in the autoclave;
- Increasing the hydrothermal temperature (130°C-150°C);
- Changing the ageing step (as to duration and temperature).

We had no success in preparing a pure HS membrane without defects; Fig. 11.17 shows few examples of SEM picture of zeolite membranes prepared increasing the hydrothermal synthesis temperature, but the pure HS membrane was not prepared.

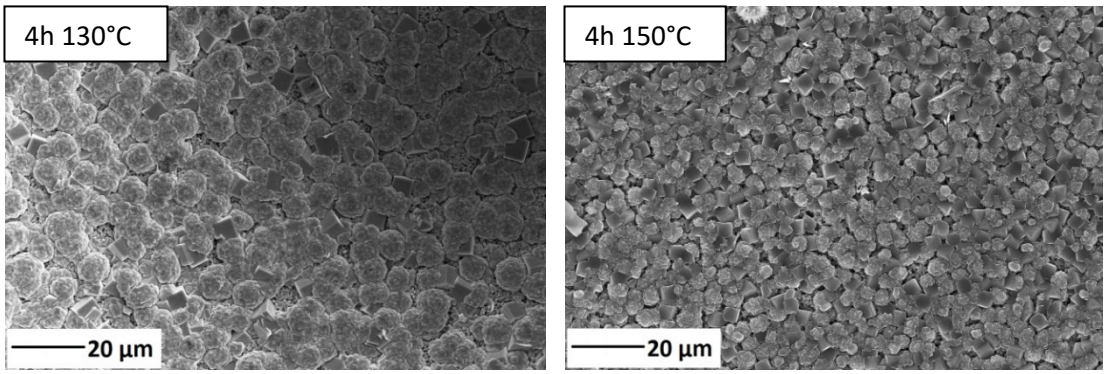

Fig. 11.17: membranes prepared with an ageing step of 12h at 60°C, followed by a hydrothermal synthesis at 130°C for 4h (left) and 4h 150°C (right).

Considering the thickness of membranes and the high percentage of HS that can lead to neglect to effect of few LTA cubes in membrane selectivity, the activity was focused on achieving membranes with good substrate coverage, the most important parameter in view of a gastight membrane. A membrane with LTA and HS mixture but with compact and promising gastight properties was already shown in Fig. 11.10. Therefore, those synthesis parameters were adopted and slightly adjusted to prepare some samples for gas permeation measurements.

Fig. 11.18 reports the top views and cross section of a membrane prepared from a hydrogel aged at 60°C for 12 h, followed by a hydrothermal synthesis at 100°C for 4h.

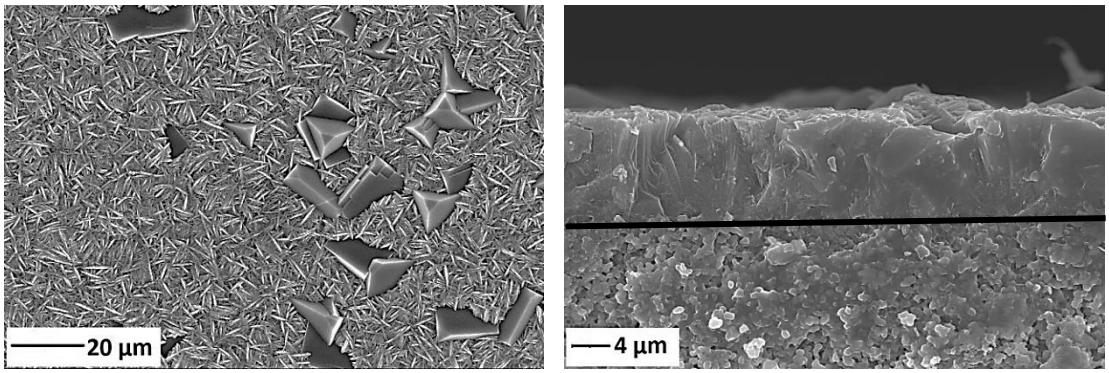

Fig. 11.18: membrane prepared with an ageing step of 12h at 60°C, followed by a hydrothermal synthesis at 100°C for 4h.

We can see that zeolite membrane was compact and had a homogenous thickness (≈ 10 µm); it was well adherent onto the ceramic substrate.

Other synthesis parameters were tested (H.A. = hydrogel ageing, H.S. = hydrothermal synthesis), Fig. 11.19.

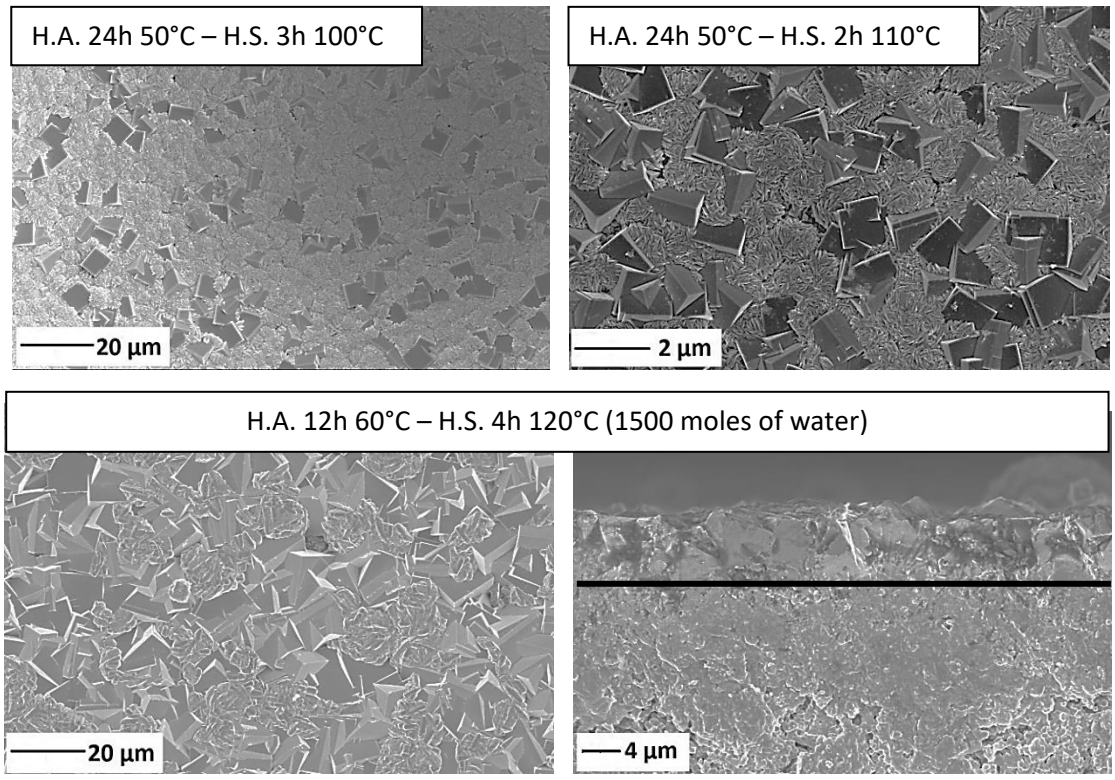

Fig. 11.19: LTA/HS membranes prepared the synthesis parameters (ageing step, hydrothermal synthesis, water content).

References

1. Sathupunya, M.; Gulari, E.; Wongkasemjit, S., Na-A (LTA) zeolite synthesis directly from alumatrane and silatrane by sol-gel microwave techniques. *Journal of the European Ceramic Society* **2003,** *23* (8), 1293-1303.

2. Kim, Y. M.; Kim, I. J., Synthesis and Morphological Transformation of NaA Zeolite Crystals at High Temperature. *Journal of the Korean Ceramic Society* **2006,** *43* (1), 1-3.

3. van Niekerk, A.; Zah, J.; Breytenbach, J. C.; Krieg, H. M., Direct crystallisation of a hydroxy sodalite membrane without seeding using a conventional oven. *Journal of Membrane Science* **2007,** *300* (1-2), 156-164.

4. Khajavi, S.; Sartipi, S.; Gascon, J.; Jansen, J. C.; Kapteijn, F., Thermostability of hydroxy sodalite in view of membrane applications. *Microporous and Mesoporous Materials* **2010,** *132* (3), 510-517.

12.Hydrogen permeation tests

12.1. Permeation through porous ceramic substrate

Before the permeation tests of membranes, we tested the porous alumina substrates (thickness 0.6 µm, powder mixture 35/65 vol% alumina/PMMA 1.5 µm).

A general equation[1a] used for gas flux (J) through a porous medium is:

$$J = F_P (P_h - P_l) \quad (1)$$

where F_P is the permeance value of the material and P_h and P_l are the partial pressures of gas in the high pressure side (P_h) and low pressure side (P_l) of the membrane, respectively.

Figs. 12.1 report the N_2 flux at room temperature and 400°C.

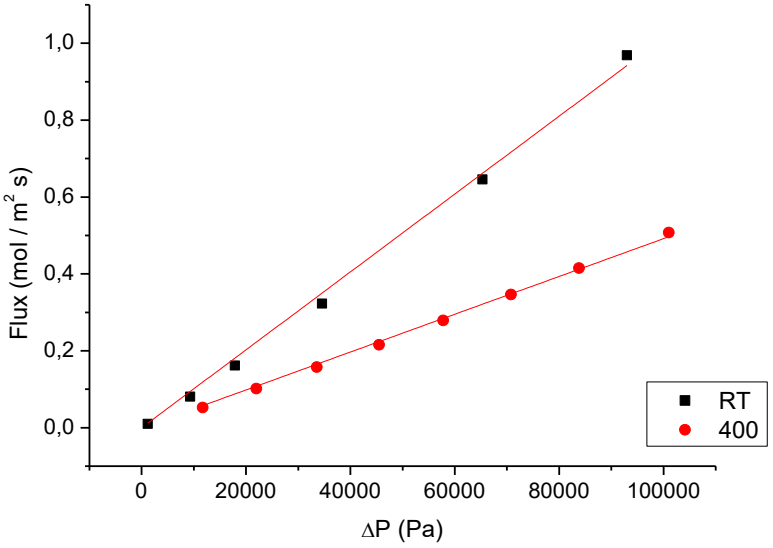

Fig. 12.1: N_2 permeation tests of porous ceramic substrate.

Total permeance can be split into two contributions[5]: Knudsen (F_{PK}) and viscous contributions (F_{PV}) (Eq. 2).

$$F_p = F_{PK} + F_{PV} P_{AVE} \quad (2)$$

$$F_{PK} = \left(\frac{2\varepsilon r}{3\tau LRT}\right)\left(\frac{8RT}{\pi M}\right)^{0.5} \quad (3)$$

$$F_{PV} = \frac{\varepsilon r^2}{8\tau\mu LRT} \quad (4)$$

where:

- P_{ave} = average pressure between high pressure side and low pressure side (Pa);
- ε = mean porosity;
- r = mean pore size of ceramic material (m);
- τ = tortuosity factor of pores;
- L = mean thickness of the porous material (m);
- R = gas constant (8.314 J mol^{-1} K^{-1});
- T = temperature (K);
- M = molecular weight (Kg mol^{-1}).

Combining Eq. 1 and 2 we get Eq. 5, useful to determine the Knudsen and viscous contributions (F_{PK} and F_{PV}), plotting data in the ($J / P_h - P_l$) vs P_{AVE} form (Fig. 12.2).

$$J = (F_{PK} + F_{PV}P_{ave})(P_h - P_l) \quad (5)$$

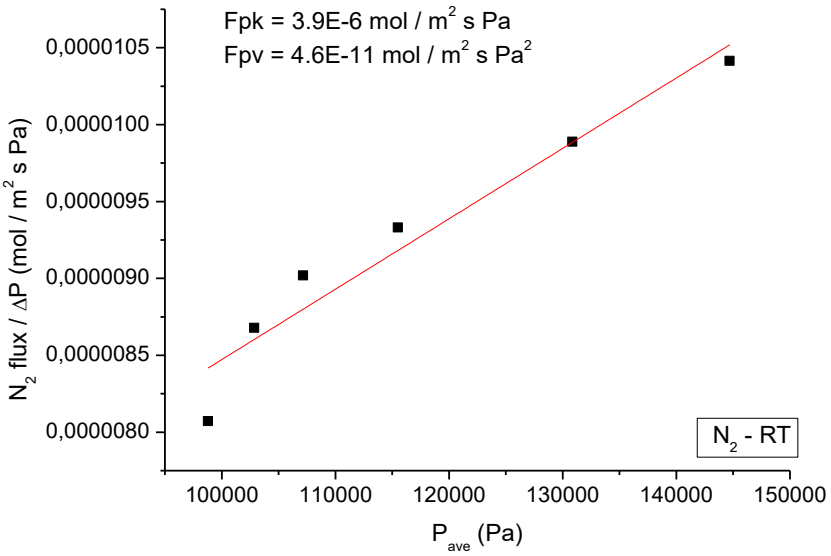

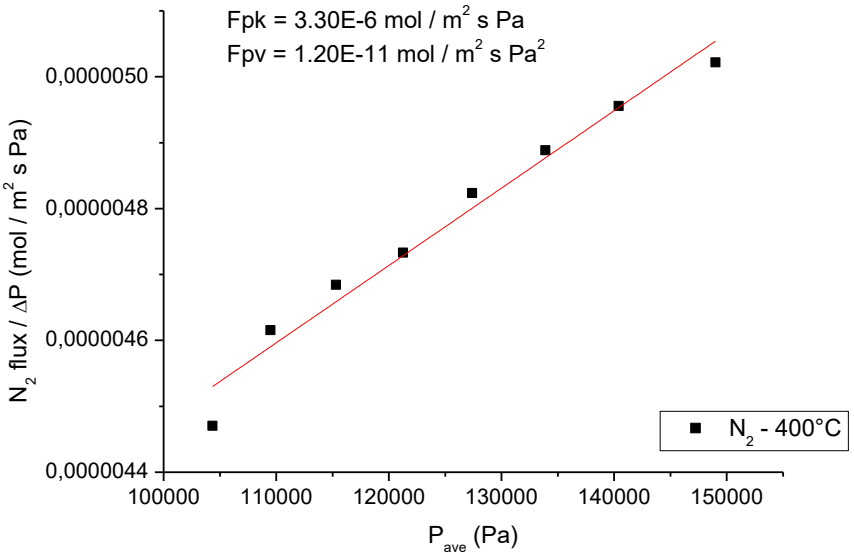

Fig. 12.2: determination of the Knudsen and viscous N_2 permeance contributions at RT and 400°C.

Knudsen diffusion is the main diffusion mechanism inside the porous ceramic substrate. One could expect that the porosity of the pellet would favour the viscous flow mechanism, but analysis do not validated the hypothesis. This fact could be due to high tortuosity paths inside the pellet, causing a lot of scattering phenomena of permeating gas.

Combining equations (3) and (4) we estimated the average pore size, r:

$$r = \frac{F_{PV}}{F_{PK}} \cdot \frac{16}{3}\mu \cdot \left(\frac{8RT}{\pi M}\right)^{0.5} \quad (6)$$

where μ is the gas viscosity at temperature T (expressed in Poiseuille, Pl). Considering the value of $1.76 \cdot 10^{-5}$ Pl for N_2 viscosity at room temperature, we estimated a mean pore size of the porous substrate: ≈ 520 nm, a value compatible with the pore size shown by SEM pictures.

12.2. Permeation tests of Pd-Ag(23wt%) membranes

Prior the permeation tests in pure hydrogen, membranes were thermal treated at 450°C for 24h to complete alloy conversion, as suggested by XRD analyses reported in Pd-Ag(23 wt%) alloy characterization section.

Fig. 12.3 reports the permeation analyses of the Pd-Ag(23 wt%) alloy (4.8 µm thick), collecting flux measurements in the temperature range 300-400°C, at various pressures (from 100 kPa to 400 KPa); values are plotted according to the n exponent (0.5) of the Sieverts' law.

$$J_{H_2} = \phi \left(P_{high}^{0.5} - P_{low}^{0.5}\right)$$

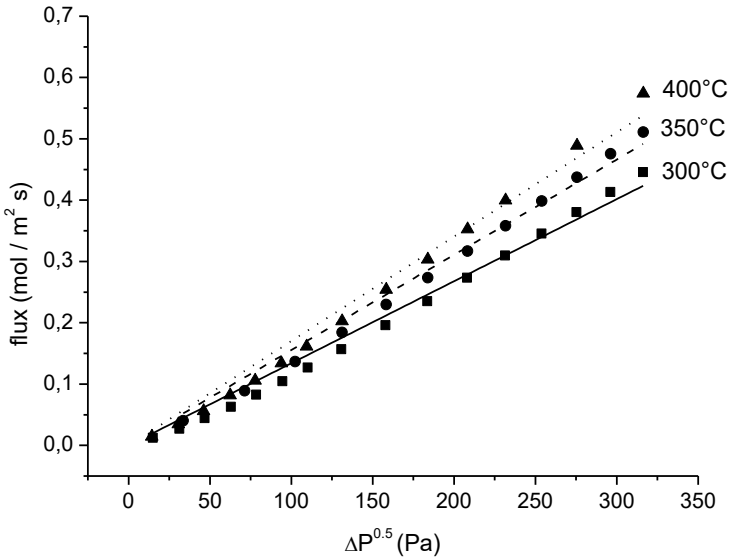

Fig. 12.3: flux data plotted according n exponent = 0.5.

All the data reported in Fig. 12.3 show a deviation from the pure Sieverts behaviour (n exponent = 0.5). The linear fit, superimposed to the flux data to guide the eye, cannot be used to correctly fit the permeation data. All the palladium alloy membranes prepared show this behaviour. Deviations from 0.5 exponent can be attributed to several factors: defects in the metal layer, surface contamination, transport resistance of the substrate material, gas leakage[1b 1c]. Jun et al. [1d] observed a strong deviation from linearity plotted with n = 0.5 and they attributed it to hysteresis behaviour: they proposed that an atomic molecular diffusion mechanism is responsible for the hydrogen permeation hysteresis. The dissolved atomic hydrogen is suggested to recombine as a molecular-hydrogen species in defects within the membrane. The lattice dilatation around the defects caused by the formation of molecular hydrogen can be responsible for the hysteresis and the higher pressure power dependence of the permeability. Flanagan et al.[1e] suggested that deviation from Sieverts' law could be attributed to hydrogen segregation in dislocation and vacancies. If they observation is right,

the membrane fabrication method is the key parameter to determine membrane micro- and nanostructures, as well as the homogeneity and the purity of the alloy composition. In this respect, sputtering/evaporation, HiPIMS, arc melting-cold rolling and wet chemical techniques are very different. Many investigations find n-values between 0.5 and 1, indicating that the transport mechanism is more complicated [1f, 1g]. In general[1c], an exponent of unity suggests that permeation through the bulk of the membrane is fast and this behaviour is usually shown by thin membranes (usually less than 5-6 µm), but n-values of 0.5-0.8 have been reported even for thin (< 5 µm) palladium membranes[2,3]. In case of thick (> 5 µm) membranes, n-values greater than 0.5 can be attributed to defects or pin-holes through which a substantial portion of the hydrogen permeates[4,5]. According to several works (Tab. 12.1), the general trend suggests that, in case of membranes having thicknesses below 10 µm, permeance can be calculated with a n-value close to 1, and in case of membranes thinner than 7 µm (as our membranes), with a n-value equal to 1.

Membrane	Preparation method	Metal thickness	n-value	Ref
Pd/Al_2O_3	Electroless deposition	8.5 µm	0.778	6
Pd/Al_2O_3	Electroless deposition	11.4 µm	0.58	7
Pd/Al_2O_3	Electroless deposition	4.5 µm	1	8
Pd/Al_2O_3	Electroless deposition	5 µm	1	9
Pd/Al_2O_3	Electroless deposition	7 µm	0.54	10
$Pd/\gamma\text{-}Al_2O_3$ with $Pd/\gamma\text{-}Al_2O_3$	Electroless deposition	6 µm	1	11
$Pd/\gamma\text{-}Al_2O_3$	CVD	1 µm	1	12
$Pd/\gamma\text{-}Al_2O_3$ with Pd	Electroless deposition	1 µm	1	13
$PdAg/Al_2O_3$	Sputtering	0.73-1.41 µm	1	14
$Pd_{75}Ag_{25}/\gamma\text{-}Al_2O_3$	Sputtering	< 1 µm	1	15
$Pd_{77}Ag_{23}$	Electroless deposition	12 µm	0.5	16
$Pd_{70}Ag_{30}$	Electroless deposition	13 µm	0.5	17a
Pd	Electroless plating	11.4 µm	0.6	17b
Pd	CVD	3-5 µm	1	17c
Pd-Ag	Spray pirolysis	1.5-2 µm	1	17d
Pd-Ag	Sputtering	350 nm	1	17e
Pd-Ag	Sputtering	50 nm	1	17f

Tab. 12.1: reference values showing membrane thicknesses and n-value used to fit the permeation data.

Fig. 12.4 shows the usual range of n, which can be distinguished as a function of metal layer thickness (temperature range 350-500°C).

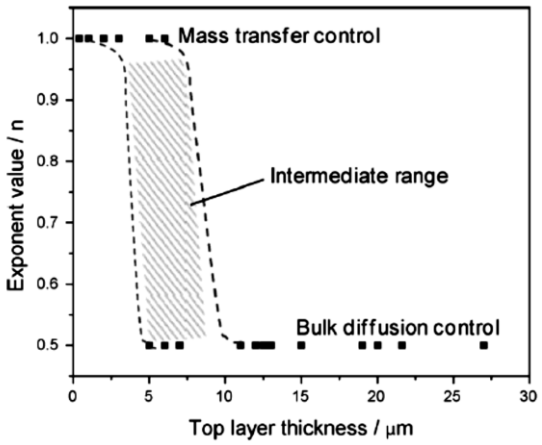

Fig. 12.4: n-exponent values vs membrane thickness [18].

Fig. 12.5 show our gas permeation data plotted with n = 1 and Tab. 12.2 collects the permeance estimates.

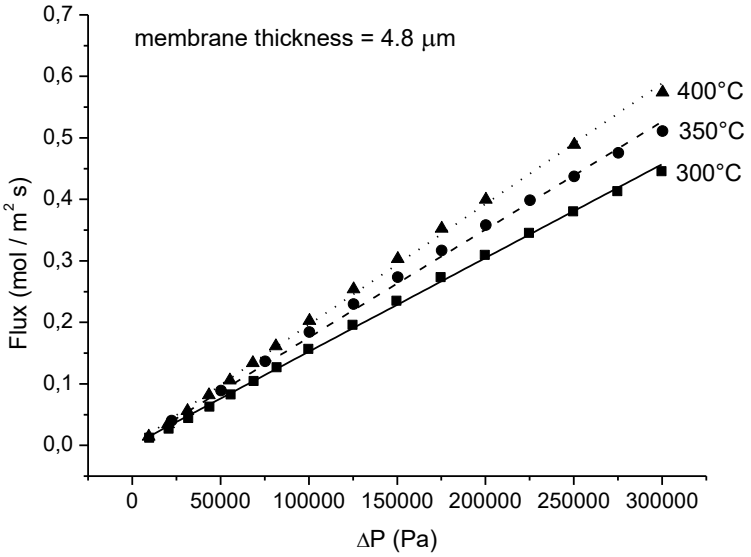

Fig. 12.5: permeation analysis of membrane sputtered for 45 min.

Temperature (°)	Permeance (10^{-6} mol / m^2 s Pa)	R-value fit	Activation energy (KJ/mol)
300	≈ 1.50	0.9995	8.5
350	≈ 1.75	0.9994	
400	≈ 1.95	0.9994	

Tab. 12.2: permeance of membrane sputtered for 45 min.

Permeation estimates of a thinner membrane, calculated in the same way of the model membrane, are reported in Tab. 12.3. The thickness of this membrane is slightly below 5 µm (shorter sputtering time).

Sputtering time (min)	Temperature (°C)	Permeance (10^{-6} mol / m^2 s Pa)	Activation Energy (KJ/mol)
35	300	≈ 1.35	7.4
	350	≈ 1.50	
	400	≈ 1.70	

Tab. 12.3: permeance estimates of a membrane having a thickness slightly below 5 µm.

Permeance estimates are compared to literature references, all regarding palladium/palladium alloy membranes prepared by sputtering deposition onto ceramic substrates (Tab. 12.4).

Hydrogen Permeance (10^{-6} mol / m^2 s Pa) - selectivity	Experimental conditions	Ref
0.71 - **H_2/N_2 = 10**	ΔP = 300 kPa - Room temperature $Pd_{82}Ag_{18}$ (wt%) Membrane thickness < 1 µm	19
Range: 0.03 – 0.1 - **H_2/He = 4-4000**	T range: 150-300°C Target: $Pd_{75}Ag_{25}$ Membrane thickness: 164 nm - 525 nm.	20
Range: 0.1 – 0.2 - **H_2/He = 80**	ΔP = 1 kPa - T = 300°C Sputtering from target $Pd_{75}Ag_{25}$ (at%) Membrane thickness: 0.1 – 1.5 µm	21
0.5 - **H_2/N_2 = 5**	ΔP = 1-20 kPa -T = 100°C Pure Pd membrane Membrane thickness: 5 µm	22

Tab. 12.4: literature references of palladium/palladium alloys sputtered onto ceramic substrates.

Reference membranes have different thicknesses and were tested in a wide range of operating conditions but our membranes have higher hydrogen permeance values than the thinner membranes reported. However, H_2/N_2 selectivity, the H_2/N_2 permeance ratio, is relatively low and ranges from 15 to 23 in the temperature range 350°C-400°C. Probably, membranes are not completely hydrogen selective (gas leakage), even if our selectivities are higher than the selectivity reported in Tab. 12.4. The activation energies are compatible to

the membranes prepared by Melendez et al.[22b] for analogous membranes. Nitrogen fluxes are reported in Fig. 12.6.

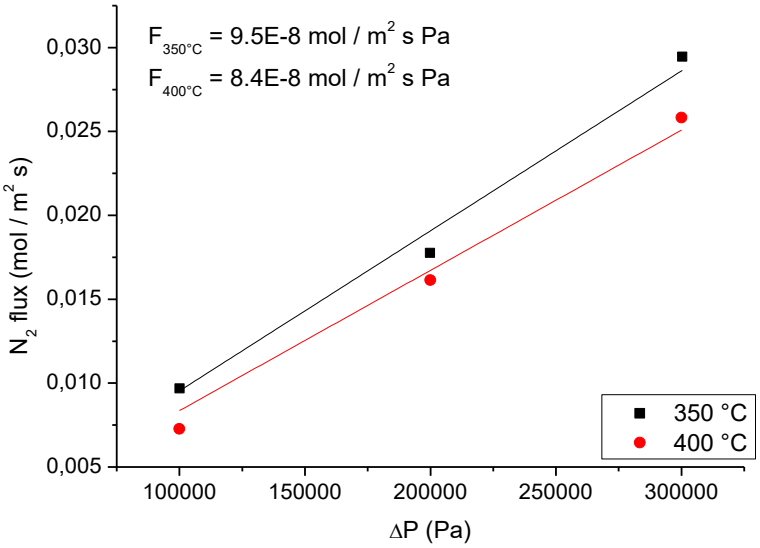

Fig. 12.6: N_2 fluxes at 350°C and 400°C.

The high permeability and low selectivity can suggest the presence of holes/defects and the need of thicker films.

12.2.1. Post permeability characterization

After the permeation tests, membranes were characterized by SEM and XRD analysis. Fig. 12.7 shows the top views and cross section of membrane after permeation tests:

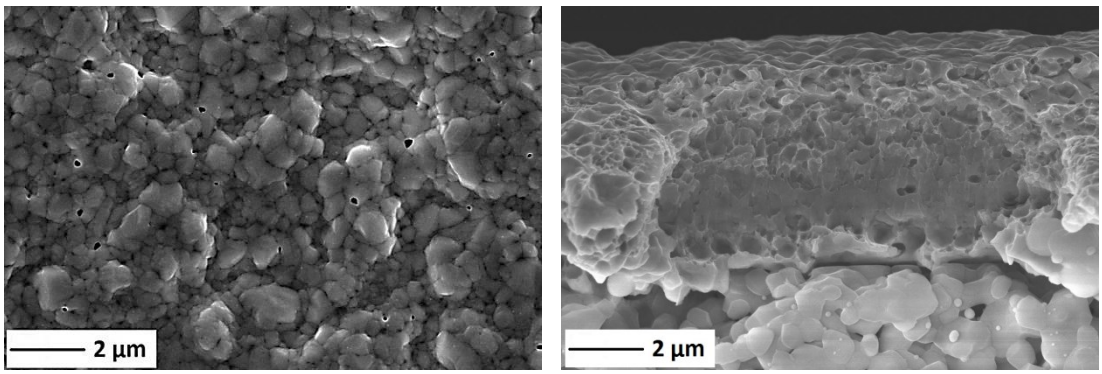

Fig. 12.7: top view and cross section of membrane after permeation test.

From the top views picture we can recognize small pinholes localized at the surface of the membrane. Apparently, they do not go through the bulk of the membrane, as cross section shows. Cross sections picture showed that the former porous layer (deposited by the very short HiPIMS sputtering process before the dense layer) rearranged in a denser layer during the permeation test, while the original dense layer does not show any defects (voids, cracks...). The membrane still maintained a very good adhesion to the ceramic substrate; no peeling of the film was observed. HiPIMS technique allowed the deposition of a high quality membrane, as to adhesion to the substrate and compactness of sputtered layer, qualities still maintained after the permeation tests.

Fig. 12.8 reports the XRD pattern of the membrane after the permeation tests:

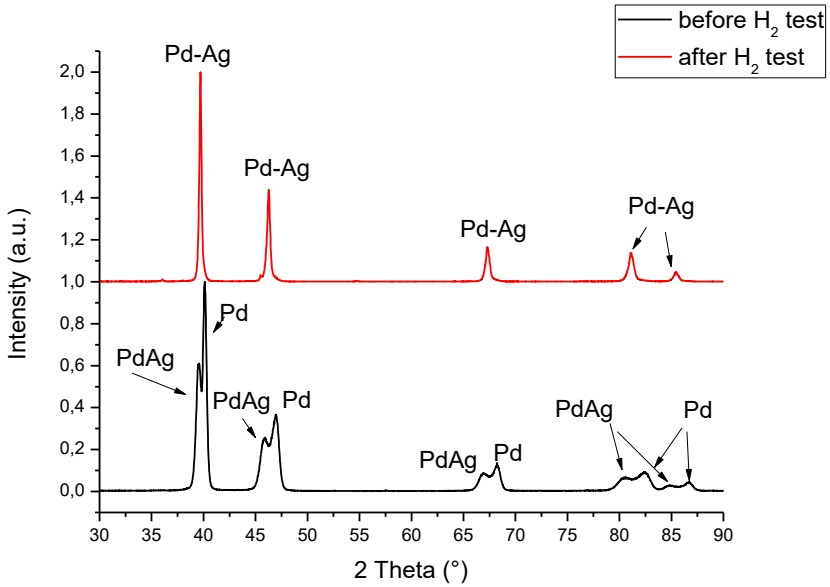

Fig. 12.8: XRD patterns before and after H_2 permeation test.

After the permeation test, the XRD pattern shows peaks belonging to Pd-Ag alloy (Rietvield analysis: a = 3.935 Å, crystallite size 100 nm – GoF ≈ 4). No H-loaded phases were detected by Rietvield analyses; a small amount (< 5 wt%) of pure palladium was detected.

12.3. Permeation tests of vanadium based membranes

Permeation data of V-Pd alloy (sputtering time 6h, 75 V bias applied, V = 700 W, Pd = 10 W, 350°C, thickness ≈ 4 µm) are shown in Fig. 12.9 (A - data plotted according to n = 0.5; B – n = 1)). No temperatures higher than 400°C were tested, as suggested by Alimov et al.[23].

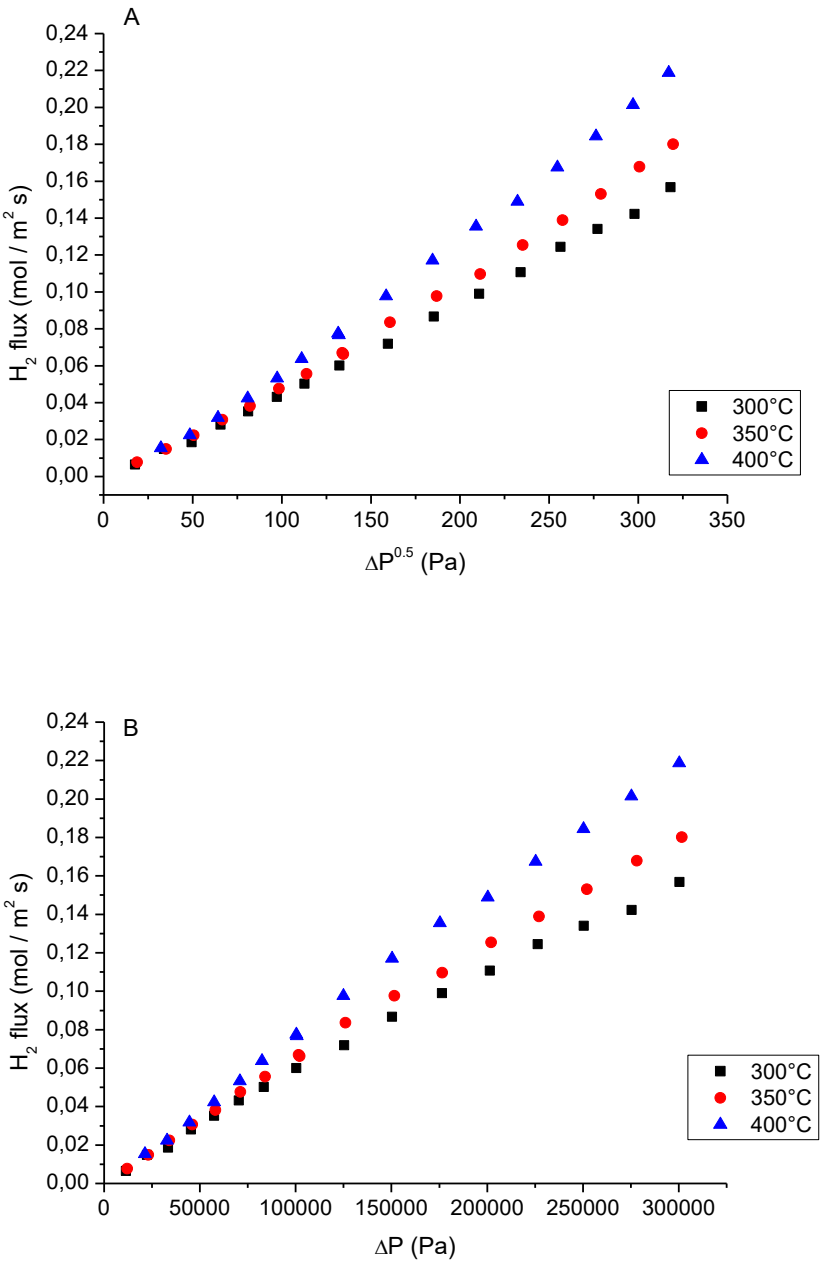

Fig. 12.9: permeation data at different temperatures of the V-Pd alloy: A) n = 0.5, B) n = 1.

Considering the curvature of the curves for n = 0.5, also for this alloy the permeance values were calculated according to n = 1 and are reported in Tab. 12.5.

Temperature (°C)	H_2 permeance (10^{-7} mol / m^2 s Pa)	n value	Activation energy (KJ/mol)
300	≈ 5.4	0.997	10
350	≈ 6.2	0.998	
400	≈ 7.4	0.999	

Tab. 12.5: permeance values of V-Pd alloy.

Permeance values increase with increasing temperature, a trend confirmed by Paglieri et al.[23b] for a thicker Pd/V-10Pd/Pd membrane.

This membrane is a composite membrane, with thin layers of palladium at both sides of the vanadium core, to assure protection against oxidation and catalytic properties, so the overall membrane behaviour is a combination of palladium and vanadium alloy properties. Permeance values are higher than the Pd-Ag alloy, confirming the properties of the vanadium based membrane as a good alternative to palladium based membranes. The H_2/N_2 selectivity at 400°C is 45; N_2 flux is shown in Fig. 12.10.

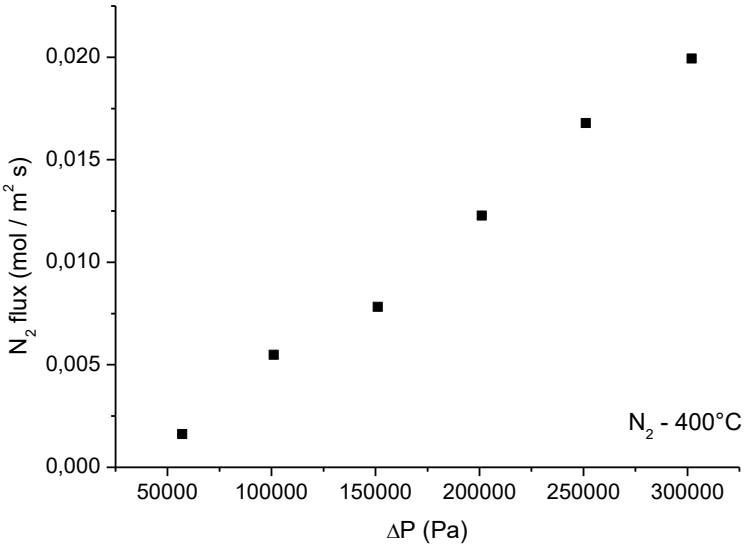

Fig. 12.10: N_2 flux at 400°C.

Moreover, V-Pd membrane did not fail during tests (hydrogen loading, heating and cooling cycles), showing a very good behaviour in testing conditions and confirming V-Pd alloy a really good candidate for the preparation of hydrogen purification membranes.

As to the V-Ni-Ti alloy, no permeation data were collected, since all the membranes tested cracked (Fig. 12.11) at the beginning of the tests, even if we set very low hydrogen

pressures. Probably, there are two main reasons: the stress induced by sputtering conditions (low pressures and high bias voltage) and the lack of NiTi phase (not revealed by XRD) that did not help the mechanical stability of the alloy. Prior to completely discard this alloy, alternative preparation routes should be tried, in order to understand if the failure of the permeation test is correlated to the PVD process or if the predicted properties of this alloy do not find an experimental validation.

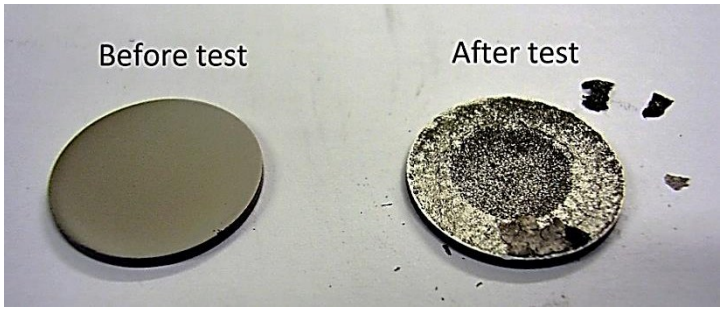

Fig. 12.11: V-Ni-Ti membrane before and after the hydrogen permeation test.

12.3.1. V-Pd post permeability characterization

Fig. 12.12 shows the top view and the cross section of the membrane after the permeation test:

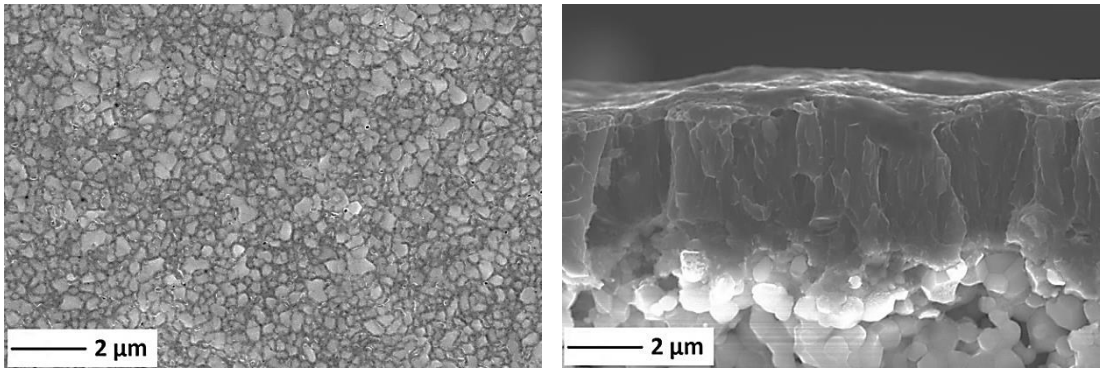

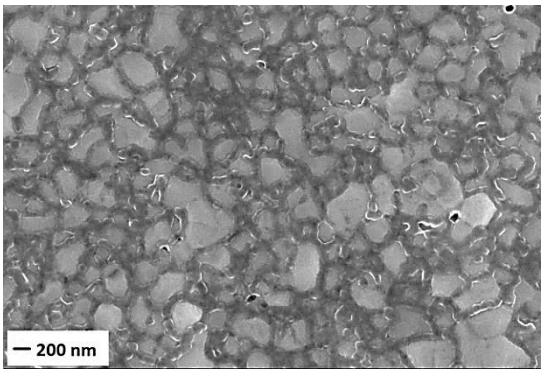

Fig. 12.12: top view and cross section of V-Pd alloy after the permeation test.

The top view SEM picture shows small defects (pinholes), appeared after the permeation test; they are clearly visible in a higher magnification image. Backscattered SEM picture shows that the protective palladium layers are still present after the permeation test (Fig. 12.13, the lighter layers).

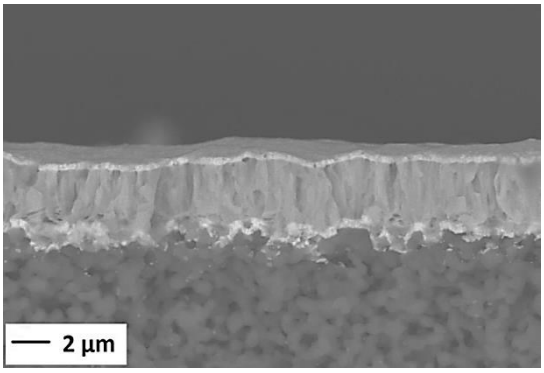

Fig. 12.13: backscattered electrons SEM picture of the V-Pd alloy cross section.

The V-Pd alloy shows the same superficial defects of the Pd-Ag alloy: these defects seem to be confined only in the upper layer of the membrane and no defects are detectable in the bulk of the membrane. Membrane still showed a good adhesion to the substrate after the permeation test.

Fig. 12.14 reports the XRD after the permeation tests (XRD analyses were performed on a composite membrane with a vanadium alloy core and palladium layers, so intense peaks of pure palladium were detected).

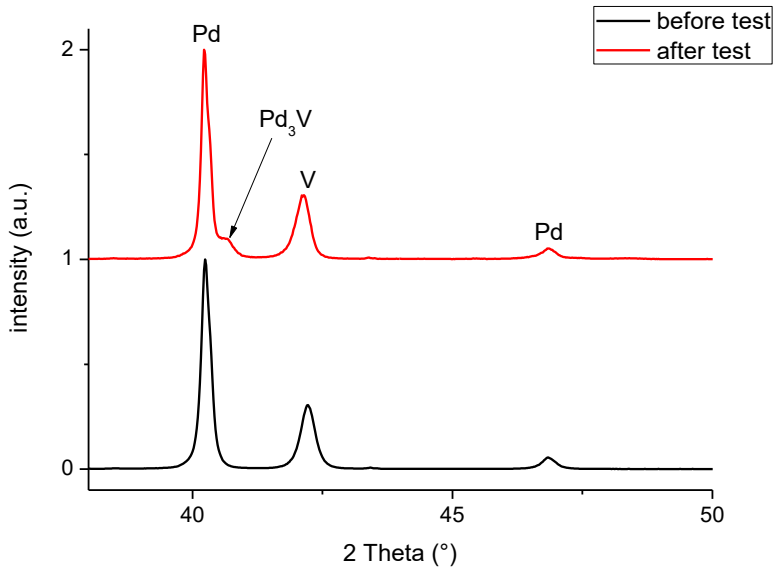

Fig. 12.14: XRD analysis of V-Pd composite membrane after the hydrogen permeation test.

X-ray diffraction shows that after the permeation test a strong palladium signal is still detected. The protective layers were not damaged during the test, assuring catalytic properties and protection to the vanadium core.

SEM and XRD analyses revealed that for all the duration of the permeation test the composite membrane maintained its properties and structural integrity; moreover, the maximum testing temperature of 400°C limited the palladium-vanadium interdiffusion phenomena, assuring a quite long-life to the membrane.

12.4. Permeation tests of zeolite membrane

When dealing with zeolite membranes, the unique method to evaluate the compactness of the zeolite layer is by permeation test, which can easily identify defects in the zeolite layer (mainly non zeolitic pores) that cause an incorrect measurement of permeance.

Fig. 12.16 reports the flux/ΔP plot of zeolite membrane (mixture of LTA and HS zeolites) prepared with an ageing step of 24h at 60°C followed by a hydrothermal synthesis of 2h at 120°C. The membrane tested was ≈ 12 µm thick (Fig. 12.15).

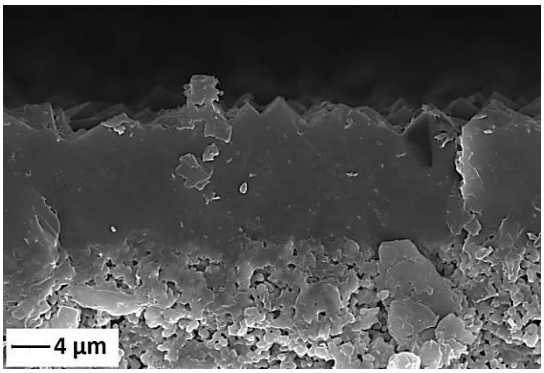

Fig. 12.15: cross section of the zeolite membrane.

The permeation tests were performed heating the membrane at the desired testing temperature and then measuring the permeance value with hydrogen and nitrogen gases. We did not heat the membrane to remove the water inside the channels, because preliminary permeation tests revealed that this thermal treatment (very slow heating up to 200°C[24]) was detrimental for the compactness of the zeolite membrane (cracking of the membrane, revealed by very high hydrogen and nitrogen fluxes).

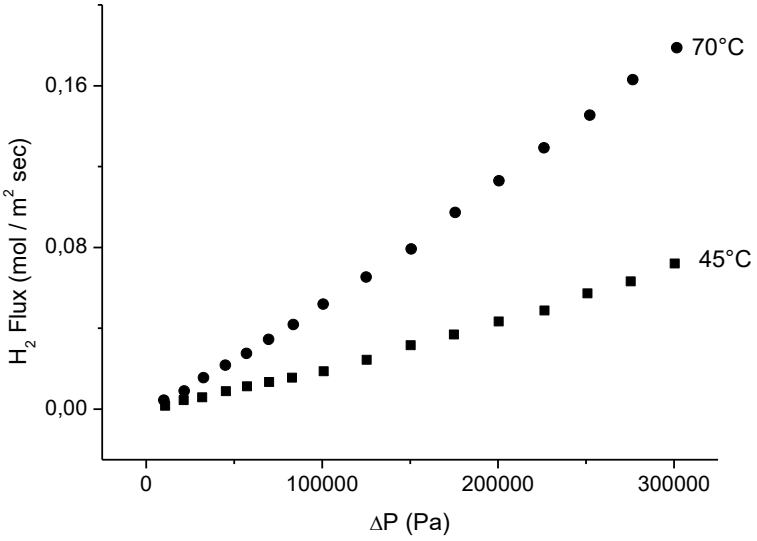

Fig. 12.16: plot of hydrogen permeation flux vs pressure difference.

Fitting the data with the equation

$$J_{H_2} = F(P_h - P_l)$$

where

- F = permeance value of the membrane (mol / m^2 s Pa);
- P_h = pressure of the high pressure side (feed side);
- P_l = pressure of the low pressure side (permeate side).

We found the permeance estimates of the membrane (45°C – 70°C, ΔP up to 0.3 MPa, Tab. 12.6).

Temperature (°C)	H_2 permeance (10^{-7} mol/m^2 s Pa)	N_2 permeance (10^{-7} mol/m^2 s Pa)	H_2/N_2 selectivity
45	≈ 2.20	≈ 0.70	3.14
70	≈ 5.70	≈ 1.40	4.07

Tab. 12.6: permeance values and selectivities of zeolite membrane.

Zeolite membranes can be affected by defects as non-zeolitic pores (with an incorrect estimation of permeance value); selectivity is a useful parameter to evaluate the separation process and the quality of membranes.

Tab. 12.7 reports some reference permeance values, regarding both HS and LTA zeolites:

Zeolite	Gas permeance (10^{-7} mol / m^2 s Pa)	Experimental conditions	Ref
HS	H_2: 1.14	ΔP = 0.1 MPa – RT	[25]
HS	H_2: 0.388	ΔP = 0.2 MPa – 50°C (four layers)	[24]
HS	He: 0.8	ΔP = 0.05 MPa – RT (direct synthesis)	[26]
LTA	H_2: 2.86	ΔP = 0.1 MPa – 25°C	[27]
LTA	H_2: 2.7	ΔP = 0.2 MPa – 50°C	[28]
LTA	H_2: 4.8 – 6.5	ΔP = 0.1 MPa – 23/107°C	[29]

Tab. 12.7: LTA and HS reference values.

Reference zeolite membranes were tested in different conditions and various permeance values were reported; reference selectivity values are in general low (< 10, Tab. 12.7 works and references therein). We tested our membrane in a wider pressure range than the most common ΔP reported in literature, and the permeance estimates found are quite similar to literature works. The comparison cannot be done by simply comparing our membrane to reference membrane, since 1) the zeolite reported are pure zeolite membranes and 2) the thicknesses are different. Even if there is a mixture of LTA and HS phases, selectivity values are comparable to literature references, which means that the surface coverage is good.

References

1. a: Mason, E. A.; Malinauskas, A. P.; Evans Iii, R. B., Flow and diffusion of gases in porous media. *The Journal of Chemical Physics* **1967**, *46* (8), 3199-3216; b: Guazzone, F., PhD Thesis: " Engineering of Substrate Surface for the Synthesis of Ultra-Thin Composite Pd and Pd-Cu Membranes for H2 Separation", Worcester Polytechnic Institute, **2005**; c: Yun, S., Ted Oyama S., Correlations in palladium membranes for hydrogen separation: A review. *Journal of Membrane Science* **2011**, 375, 28-45; d: Shu, J., Grandjean B. P.A., Kaliaguine, S., Giroir-Fendler A., Dalmond, J.A., Hysteresis in hydrogen permeation through palladium membranes. *Journal of the Chemical Society, Faraday Transactions* **1996,** *92 (15)*, 2745-2751; e: Flanagan, T.B., Balasubramaniar, R., Kirchheim, R., Exploring lattice defects in palladium and its alloys using dissolved hydrogen. Part I: hydrogen solubility and its segregation to dislocations and vacancies. *Platinum Metals Review* **2001,** *45(3)*, 114-121; f: Vicinanza, N., Svenum, I.H., Naess, L.N., Peters, T. A., Bredsen R., Borg, A., Venvik, H., Thickness dependent effects of solubility and surface phenomena on the hydrogen transport properties of sputtered Pd77%Ag23% thin film membrane. *Journal of Membrane Science* **2015**, *476*, 602-608; g: Dittmeyer, R., Hollein, V., Daub, K., Membrane reactors for hydrogenation and dehydrogenation processes based on supported palladium. *Journal of Molecular Catalysis A: Chemical* **2001**, *173 (1-2)* 135-184; h: Uemiya, S., State of the art of supported metal membranes for gas separation. *Separation and Purification Methods* **1999**, *28*, 51-85.

2. Cheng, Y. S.; Yeung, K. L., Palladium–silver composite membranes by electroless plating technique. *Journal of Membrane Science* **1999,** *158* (1–2), 127-141.

3. Souleimanova, R. S.; Mukasyan, A. S.; Varma, A., Pd membranes formed by electroless plating with osmosis: H2 permeation studies. *AIChE Journal* **2002,** *48* (2), 262-268.

4. Gade, S. K.; Thoen, P. M.; Way, J. D., Unsupported palladium alloy foil membranes fabricated by electroless plating. *Journal of Membrane Science* **2008,** *316* (1–2), 112-118.

5. a: Guazzone, F.; Engwall, E. E.; Ma, Y. H., Effects of surface activity, defects and mass transfer on hydrogen permeance and n-value in composite palladium-porous stainless steel membranes. *Catalysis Today* **2006**, *118* (1–2), 24-31; b: Guazzone, F., PhD Thesis: " Engineering of Substrate Surface for the Synthesis of Ultra-Thin Composite Pd and Pd-Cu Membranes for H2 Separation", Worcester Polytechnic Institute, **2005**; c: Huang, T.-C., Wei, M.-C., Chen, H.-I., Preparation of Palladium-silver alloy composite membrane for hydrogen separation. *Chemical Engineering Communications* **2002**, 189, 1262-1282.

6. Ilias, S.; Su, N.; Udo-Aka, U. I.; King, F. G., Application of electroless deposited thin-film palladium composite membrane in hydrogen separation. *Separation Science and Technology* **1997,** *32* (1-4), 487-504.

7. Collins, J. P.; Way, J. D., Preparation and characterization of a composite palladium-ceramic membrane. *Industrial and Engineering Chemistry Research* **1993,** *32* (12), 3006-3013.

8. Chen, H. I.; Chu, C. Y.; Huang, T. C., Comprehensive Characterization and Permeation Analysis of Thin Pd/Al2O3 Composite Membranes Prepared by Suction-Assisted Electroless Deposition. *Separation Science and Technology* **2005,** *39* (7), 1461-1483.

9. Zhang, X.; Xiong, G.; Yang, W., A modified electroless plating technique for thin dense palladium composite membranes with enhanced stability. *Journal of Membrane Science* **2008,** *314* (1–2), 226-237.

10. Liguori, S.; Iulianelli, A.; Dalena, F.; Pinacci, P.; Drago, F.; Broglia, M.; Huang, Y.; Basile, A., Performance and long-term stability of Pd/PSS and Pd/Al2O3 membranes for hydrogen separation. *Membranes* **2014,** *4* (1), 143-162.

11. Zhang, X.; Xiong, G.; Yang, W., A modified electroless plating technique for thin dense palladium composite membranes with enhanced stability. *Journal of Membrane Science* **2008,** *314* (1-2), 226-237.

12. Xomeritakis, G.; Lin, Y. S., CVD Synthesis and Gas Permeation Properties of Thin Palladium/Alumina Membranes. *AIChE Journal* **1998,** *44* (1), 174-183.

13. Zhao, H. B.; Pflanz, K.; Gu, J. H.; Li, A. W.; Stroh, N.; Brunner, H.; Xiong, G. X., Preparation of palladium composite membranes by modified electroless plating procedure. *Journal of Membrane Science* **1998,** *142* (2), 147-157.

14. Pereira, A. I.; Pérez, P.; Rodrigues, S. C.; Mendes, A.; Madeira, L. M.; Tavares, C. J., Deposition of Pd–Ag thin film membranes on ceramic supports for hydrogen purification/separation. *Materials Research Bulletin* **2015,** *61*, 528-533.

15. McCool, B.; Xomeritakis, G.; Lin, Y. S., Composition control and hydrogen permeation characteristics of sputter deposited palladium–silver membranes. *Journal of Membrane Science* **1999,** *161* (1–2), 67-76.

16. Abate, S.; Genovese, C.; Perathoner, S.; Centi, G., Performances and stability of a Pd-based supported thin film membrane prepared by EPD with a novel seeding procedure. Part 1—Behaviour in H2:N2 mixtures. *Catalysis Today* **2009,** *145* (1–2), 63-71.

17. a: Wang, L.; Yoshiie, R.; Uemiya, S., Fabrication of novel Pd–Ag–Ru/Al2O3 ternary alloy composite membrane with remarkably enhanced H2 permeability. *Journal of Membrane Science* 2007, *306* (1–2), 1-7; b: Ackerman F.J., Koskinas, G.J., Permeation of hydrogen and deuterium through palladium silver alloys. *Journal of Chemical and Engineering Data* 1972, *7*(1), 51-55; c: Collins, J.P., Way, J.D., Preparation and characterization of a composite palladium-ceramic membrane. *Industrial and Engineering Chemistry* 1993, *32*, 3006-3013; d: Li, Z.Y., Maeda H., Kusakabe K., Marooka S., Anzai, H., Akiyama S., Preparation of palladium-silver alloy membranes for hydrogen separation by the spray pyrolysis method. Journal of Membrane Science 1993, *78*, 247-254; e: Jayaraman V., Lin, Y.S., Synthesis and hydrogen permeation properties of ultrathin palladium-silver alloy membranes. *Journal of Membrane Science* 1995, *104*, 251-262; f: Athayde, A.L., Baker, R.W., Nguyen P., Metal Composite membranes for hydrogen separation. *Journal of Membrane Science* 1994, *94*, 299-311.

18. Yun, S.; Ted Oyama, S., Correlations in palladium membranes for hydrogen separation: A review. *Journal of Membrane Science* **2011,** *375* (1–2), 28-45.

19. Pereira, A. I.; Pérez, P.; Rodrigues, S. C.; Mendes, A.; Madeira, L. M.; Tavares, C. J., Deposition of Pd-Ag thin film membranes on ceramic supports for hydrogen purification/separation. *Materials Research Bulletin* **2015,** *61*, 528-533.

20. McCool, B.; Xomeritakis, G.; Lin, Y. S., Composition control and hydrogen permeation characteristics of sputter deposited palladium-silver membranes. *Journal of Membrane Science* **1999,** *161* (1-2), 67-76.

21. Xomeritakis, G.; Lin, Y. S., Fabrication of thin metallic membranes by MOCVD and sputtering. *Journal of Membrane Science* **1997,** *133* (2), 217-230.

22. a: Checchetto, R.; Bazzanella, N.; Patton, B.; Miotello, A., Palladium membranes prepared by r.f. magnetron sputtering for hydrogen purification. *Surface and Coatings Technology* **2004,** *177-178*, 73-79; b: Melendez, J., Fernandez, E., Gallucci, F., van Sint Annaland, M., Arias, P.L. Pacheco Tanaka, D.A., Preparation and characterization of ceramic supported ultra-thin (≈ 1 μm) Pd-Ag membranes. *Journal of Membrane Science* **2017**, *528*, 12-23.

23. a: Alimov, V. N.; Busnyuk, A. O.; Notkin, M. E.; Peredistov, E. Y.; Livshits, A. I., Substitutional V–Pd alloys for the membranes permeable to hydrogen: Hydrogen solubility at 150–400 °C. *International Journal of Hydrogen Energy* **2014,** *39* (34), 19682-19690; b: Paglieri, S. N.; Wermer, J. R.; Buxbaum, R. E.; Ciocco, M. V.; Howard, B. H.; Morreale, B. D., Development of membranes for hydrogen separation: Pd coated V-10Pd. *Energy Materials: Materials Science and Engineering for Energy Systems* 2008, *3* (3), 169-176.

24. Kalantari, N.; Vaezi, M. J.; Yadollahi, M.; Babaluo, A. A.; Bayati, B.; Kazemzadeh, A., Synthesis of nanostructure hydroxy sodalite composite membranes via hydrothermal method: Support surface modification and synthesis method effects. *Asia-Pacific Journal of Chemical Engineering* **2015,** *10* (1), 45-55.

25. Xu, X.; Bao, Y.; Song, C.; Yang, W.; Liu, J.; Lin, L., Microwave-assisted hydrothermal synthesis of hydroxy-sodalite zeolite membrane. *Microporous and Mesoporous Materials* **2004,** *75* (3), 173-181.

26. van Niekerk, A.; Zah, J.; Breytenbach, J. C.; Krieg, H. M., Direct crystallisation of a hydroxy sodalite membrane without seeding using a conventional oven. *Journal of Membrane Science* **2007,** *300* (1–2), 156-164.

27. Xu, X.; Bao, Y.; Song, C.; Yang, W.; Liu, J.; Lin, L., Synthesis, characterization and single gas permeation properties of NaA zeolite membrane. *Journal of Membrane Science* **2005,** *249* (1–2), 51-64.

28. Xu, K.; Yuan, C.; Caro, J.; Huang, A., Silver-exchanged zeolite LTA molecular sieving membranes with enhanced hydrogen selectivity. *Journal of Membrane Science* **2016,** *511*, 1-8.

29. Zah, J.; Krieg, H. M.; Breytenbach, J. C., Single gas permeation through compositionally different zeolite NaA membranes: Observations on the intercrystalline porosity in an unconventional, semicrystalline layer. *Journal of Membrane Science* **2007,** *287* (2), 300-310.

13.Closing remarks and future work

13.1. Closing remarks

The research had the task to evaluate the membrane concept we developed (thin selective layer deposited onto porous ceramic substrate), in all its main aspects (porous ceramic preparation, deposition of thin membrane layer, testing of the membrane to analyse the permeation performance) before the final scaling up in a pilot reactor apparatus, to test membranes in real conditions.

After preliminary tests, which involved the study of partial sintering of alumina and the use of different pore formers, we developed a process to prepare very good porous ceramic substrates, starting from very cheap materials in order to reduce the final cost of the ceramic substrate. Our research pointed out that PMMA 1.5 µm is a suitable pore former, since we could prepare a ceramic substrate with high bulk porosity (> 35%), pores interconnection and a surface porosity closed enough to deposit a selective layer without defects. We met all these targets preparing a starting powder mixture having 65 vol% of PMMA and 35 vol% of aluminium oxide. The optimization of pellets sintering, required in order to avoid pellets deformation during sintering, was performed by dilatometric analyses, and studying the shrinkage behaviour of several pellets the most suitable sintering route was finely tuned. Planar pellets were prepared, and after surface finishing they were available for the selective layer deposition step.

For the deposition of the metallic membranes, we employed for the first time the recent HiPIMS technology and, after a series of preliminary tests dedicated to a fine tuning of the sputtering conditions (targets power, deposition pressure, HiPIMS pulses duration and so on), we achieved good and encouraging coatings. The deposition of a metal layer with the correct stoichiometry and good adhesion to the substrate was the main task. HiPIMS membranes completely outclassed DC magnetron sputtering membranes, and HiPIMS technology revealed as a very competitive technique. In order to apply a bias to the insulating substrate, we split the deposition process into two parts, depositing a thin porous metal layer before the main deposition in order also to create an interlayer that can reduce problems due to

the different thermal expansions. Once all the sputtering parameters were optimized, the preparation of a high number of membranes in a very short time was possible, demonstrating that big production rates can be pursued. This work extended the uses of HiPIMS technology, since we demonstrated that this technique can be used not only to prepare hard coatings (the main HiPIMS application) but even membranes for hydrogen separation, with the requirements of a very fine control of final alloy composition and adhesion to the substrate.

Moreover, in this work we investigated alternative metals to prepare membranes for hydrogen separation and purification, to meet the European Community guidelines concerning the use of critical elements. We investigated two alloys (both vanadium based alloys): a binary alloy and a ternary alloy. These membranes, prepared by HiPIMS and DC magnetron sputtering, were successfully deposited onto ceramic substrates. The binary alloy was deposited by HiPIMS and the experience gathered with palladium-silver alloy was very useful to find the correct parameter combinations. The ternary alloy, prepared by DC magnetron sputtering, was deposited onto the ceramic substrate after a preliminary series of tests performed onto dense stainless steel, to find the best sputtering conditions, which involved the use of low pressures and high bias voltages. Vanadium alloys needed a very thin layer of palladium or palladium alloys on both sides to promote the dissociation and re-association of the hydrogen molecule. This requirement prevented us to thermally treat at high temperatures (> 400°C) the membranes, in order to favour a better crystallization of the alloy or a complete conversion into the desired phase, due to the intermetallic diffusion between palladium protective layers and vanadium core.

As to zeolite membranes, we studied a simplification of the synthetic process, in order to prepare zeolite membranes in only one step. We studied the ageing step of hydrogel and the hydrothermal synthesis, finding suitable experimental conditions to prepare pure hydroxy-sodalite membranes. The fine tuning of the synthesis was not ordinary, since small variations of the experimental parameters brought about the growth of membranes with different characteristics, as to surface coverage of porous substrate and phase. A mixture of zeolite type A and hydroxy-sodalite was the final choice; membranes having the double zeolite phase showed a really good ceramic substrate surface coverage, with nice gastight properties, which made them good candidates for permeation tests.

All membranes were tested in a permeation test station entirely developed at CNR-ICMATE, including design of the apparatus and the Labview interface developed to control the permeation measurements. Palladium based membrane showed promising hydrogen permeance values, once compared to other reference membranes having the same layout and similar thickness (≈ 5 μm). Apparently, membranes did not show defects after the permeation test, but a further study (thicker membranes) is underway in order to improve the selectivity parameter, since it is well below the state-of-the-art palladium membranes.

V-Pd alloy showed promising permeance values, with a good stability for all the duration of the permeation test. No comparison with other similar membranes was possible, since it is the very first time that this alloy is prepared by PVD process; these first results are very encouraging and justify the expectation about this alloy, a really good candidate to develop a new generation of membrane for hydrogen separation. On the other hand, the theoretical alloy V-Ni-Ti, although the as prepared sputtered samples seemed to be promising, showed membrane failure during permeation testing, and no permeance values were collected.

Zeolite membranes showed encouraging permeance performances.

13.2. Future works

The next part of the research involves the gathering of permeation data concerning thicker Pd-Ag(23 wt%) and V-Pd membranes, to better comprehend the mechanisms involved in the permeation process and improve the selectivity parameter and improve selectivity. The alloy preparation onto ceramic substrate is only a part of the entire research work, since, after the deposition, membranes have to be tested to verify their performance and reliable testing conditions must be found and approved.

However, this research demonstrated that our membrane concept prototypes work well and the entire production chain, from the ceramic substrate preparation to the alloy deposition, combines well developed sequential steps with high production rates.

Acknowledgments

This research involved several people (CNR-ICMATE) having different proficiencies and their contributions were fundamental to gather all the information reported in the thesis:

- Supervisor Lidia Armelao and co-supervisor Simona Barison;
- Stefano Fasolin (scientific collaborator);
- Francesco Montagner (technical collaborator);
- Stefano Boldrini (permeation test station development);
- Alberto Ferrario (permeation test station development + Labview interface);
- Valentina Zin (scratch tests);
- Filippo Agresti (helpful discussion about XRD analysis, MAUD training);
- Alessia Famengo (TGA-DSC);
- Monica Fabrizio;
- Rosalba Gerbasi (XRD patterns).

I am really grateful to National Research Council, for the doctoral scholarship and the lab facilities, to the PhD Course of Materials Science and Engineering and the coordinator prof. Gaetano Granozzi.

This work has been funded by the Italian *Industria 2015* project "Production of renewable energy with minimum impact from biomasses and not dangerous special waste mixes by means of innovative processes".